Fall 2021

THE PROPAGATION AND EVOLUTION OF CORONAL MASS EJECTION DRIVEN SHEATH REGIONS: INSIGHT FROM MULTI-SPACECRAFT MEASUREMENTS AND STATISTICAL APPROACHES

Tarik Mohammad Salman
University of New Hampshire, Durham

Recommended Citation

Salman, Tarik Mohammad, "THE PROPAGATION AND EVOLUTION OF CORONAL MASS EJECTION DRIVEN SHEATH REGIONS: INSIGHT FROM MULTI-SPACECRAFT MEASUREMENTS AND STATISTICAL APPROACHES" (2021). *Doctoral Dissertations*. 2635.
https://scholars.unh.edu/dissertation/2635

THE PROPAGATION AND EVOLUTION OF CORONAL MASS EJECTION DRIVEN SHEATH REGIONS: INSIGHT FROM MULTI-SPACECRAFT MEASUREMENTS AND STATISTICAL APPROACHES

BY

Tarik Mohammad Salman
Space Science Center and Department of Physics and Astronomy
University of New Hampshire

THESIS

Submitted to the University of New Hampshire
in Partial Fulfillment of
the Requirements for the Degree of

Doctor of Philosophy
in
Physics

September, 2021

This thesis has been examined and approved in partial fulfillment of the requirements for the degree of Doctor of Philosophy in Physics by:

Dr. Noé Lugaz, Research Associate Professor (Thesis Director)
Space Science Center and Department of Physics and Astronomy
University of New Hampshire

Dr. Antoinette Galvin, Research Professor
Space Science Center and Department of Physics and Astronomy
University of New Hampshire

Dr. Charles Farrugia, Research Professor
Space Science Center and Department of Physics and Astronomy
University of New Hampshire

Dr. Reka Winslow, Research Assistant Professor
Space Science Center and Department of Physics and Astronomy
University of New Hampshire

Dr. Shawna Hollen, Assistant Professor
Department of Physics and Astronomy
University of New Hampshire

On August 10, 2021.

Original approval signatures are on file with the University of New Hampshire Graduate School.

Dedication

To my mom and dad,

to my sister,

to my brother,

for being who they are.

Preface

What started as a short-term summer project has shaped the last four years of my life. Coming from a different background, I was initially hesitant to switch to science's brighter and hotter side (because our Sun is both). Now looking back at the journey of my doctoral studies, I firmly believe that I made the right choice.

My deepest and heartfelt gratitude is reserved for my supervisor, Noé Lugaz. Thanks to you, I got introduced to this captivating world of CMEs. No matter how many famous future researchers you mentor from now on, I can proudly say that I am your first graduate student. You have been the best mentor that I could have hoped for. I will be forever grateful to you for your immense support and affectionate guidance. Without you, this thesis would never have been possible.

A huge thank you to my co-authors Reka Winslow, Charles Farrugia, Antoinette Galvin, Lan Jian, and Nathan Schwadron. From our very first interaction, you all have won over my heart with your humbleness. Your continuous expertise has encouraged me every step of the way and has helped me become a better researcher. The world only knows how exceptionally talented you all are. Still, I hope they also get to know how awesome you all are as people. You all are my source of inspiration. It has been a pleasure working with you.

I am grateful to my pre-examiners, Reka Winslow, Charles Farrugia, Antoinette Galvin, and Shawna Hollen, for your time spent evaluating this thesis. Your comments have clarified my writing and immensely improved the outlook of this work.

I thank all my friends who have had a crucial part in keeping me sane. You all have graced my life with your kindness. Thank you so much for putting up with my shenanigans. You all had kept me going when I was down and out. I couldn't have done this without your love and support.

Last but not least, thanks to my family for constantly supporting me. Even though I am so far away, I always feel your presence, which serves as my caffeine.

Tarik Mohammad Salman
New Hampshire, July 2021

Abstract

The complexities of our nearest star, the Sun, are characterized by its magnetic field. In the absence of a magnetic field, diverse phenomena as the solar cycle, solar eruptions, solar wind, to name but a few, would be unknown to us. Coronal mass ejections, a large form of solar eruption, are an essential mechanism for the evolution of the Sun. CMEs provide a means by which the built-up magnetic flux and solar material over solar cycles are removed from the solar atmosphere into the solar wind. This spectacular phenomenon has repercussions throughout the heliosphere, driving a range of heliospheric, magnetospheric, ionospheric, atmospheric, and ground effects, collectively called "space weather." Each CME structure (shock, sheath, and magnetic ejecta) has distinctive characteristics, but all cause perturbations on different scales within regular solar wind conditions. CME-driven shock is the discontinuous transition from a supersonic (or more accurately faster than the fast magnetosonic speed) to a subsonic (or more accurately slower than the fast magnetosonic speed) solar wind, and the sheath is the region of compressed and heated solar wind plasma with higher power of magnetic field fluctuations. In contrast, the magnetic ejecta is a magnetically-dominated region of lower proton density and kinetic temperature with minimal magnetic field fluctuations.

In this thesis, the characteristics and radial evolution of CME sheaths are investigated with multi-spacecraft observations in the inner heliosphere and single-spacecraft measurements near 1 astronomical unit (AU, the mean distance from the center of the Earth to the center of the Sun). In general, the radial evolution of CMEs is inferred from analyzing different CMEs at different heliospheric distances from the Sun. Such statistical approaches are hindered by the inhomogeneity of CMEs, leading to uncertain estimates. The results presented in this thesis provide observational evidence of the inhomogeneity of CME structures. Especially as the heliocentric distance increases, the exponential decrease of the magnetic field strength within the sheath has less CME-to-CME variability than the CME. The results also indicate that CME expansion near 1 AU does not reflect its expansion in the innermost heliosphere.

However, multi-spacecraft observations can also lead to an erroneous treatment of the radial evolution. Our findings suggest that the primary sources of uncertainties in multi-spacecraft observations are longitudinal separations between the measuring spacecraft.

This thesis sheds new light on the physical processes responsible for the observed variabilities of CME sheaths near-Earth. The results point towards the hypothesis that such observed variabilities of CME sheaths near 1 AU are likely to be governed by the sheath formation mechanisms and intrinsic CME characteristics. One fascinating aspect of our findings is that sheath variabilities tend to be not influenced by the shocks that precede them. On the other hand, preliminary statistics from our threshold-based probabilistic forecasting model demonstrate the importance of shocks, hinting at the solar wind variations in the vicinity of shocks to be a strong indicator of an upcoming intense and prolonged southward magnetic field period.

Contents

List of Acronyms **xiv**

List of Publications **xviii**

1 Introduction **1**

2 The Sun **4**

2.1 The solar interior 5

2.2 The solar atmosphere 6

2.3 The Sun's magnetic field and solar cycle 10

2.4 The solar wind 16

2.4.1 Overview 16

2.4.2 Solar wind structures 21

2.4.3 Outer heliosphere 24

2.5 Geomagnetic impact of solar wind structures 24

2.5.1 Geomagnetic indices 24

2.5.2 Prominent drivers of geomagnetic storms 26

3 Coronal mass ejections: an overview **31**

3.1 Basics of CMEs 31

3.2 Origins of eruption and early phase 32

3.3 Observational aspects 36

3.4 Heliospheric propagation 39

3.5 Modeling of CMEs 46

3.6 CME-driven shocks and sheaths 48

3.6.1 Shocks 49

3.6.2 Sheaths 52

3.6.3 Importance of Sheaths 53

3.6.4 Studies of CME sheaths 58

3.7 STEREO CME list 59

4 Characteristics of CME structures near 1 AU: with and without shocks 60

4.1 Background 60

4.2 Initial classification of CMEs 61

4.3 Automated sheath identification algorithm 63

4.4 Example events from different categories 65

4.4.1 Cat-I (CME with an associated shock and sheath region) 65

4.4.2 Cat-II (CME with a sheath but without a shock) 67

4.4.3 Cat-III (CME with no associated shock and sheath) 68

4.5 The proportion of different categories 68

4.5.1 Variation in terms of the leading-edge speed of the ME 68

4.5.2 Solar cycle variation 69

4.6 Superposed epoch analysis 71

4.7 Average profiles of the structures 75

4.7.1 MEs 75

4.7.2 Sheaths 77

4.7.3 Comparison of Cat-II sheaths and Cat-I sheaths driven by slower MEs 78

4.8 Correlation analysis between the sheath and ME 80

4.8.1 Correlation between the average sheath and ME properties 80

4.8.2 Correlation of the sheath size with ME Properties 81

5 **Categorization of ME-driven sheath regions near 1 AU** **85**
5.1 Background 85
5.2 Sheaths categorized by formation mechanisms 86
5.3 Sheaths categorized by variations in speeds 87
5.4 Propagation versus expansion sheaths 90
5.4.1 Comparison of average properties 90
5.4.2 Superposed epoch analysis 91
5.5 Analysis of sheaths with distinct speed variations 94
5.5.1 Solar cycle dependence 94
5.5.2 Superposed epoch analysis 95
5.5.3 Statistical relationships in terms of shock parameters 99
5.5.4 Statistical differences in terms of sheath and ME parameters 101
5.5.5 Influence of ME parameters in driving distinct speed variations . . . 102
5.5.6 Comparison of the multivariate method with in-situ observations . . . 104

6 **Multi-spacecraft measurements of CME structures** **107**
6.1 Background 107
6.2 Identification of probable CME candidate/s for a conjunction event 109
6.3 Estimation of impact speeds at Mercury and Venus 111
6.4 Conjunction events with three-point observations 113
6.5 Database 114
6.6 Speed profile 115
6.7 CME deceleration/acceleration 119
6.8 Magnetic field intensity 121
6.9 Sheath duration 127
6.10 Case study of the 3 Nov 2011 CME 128
6.10.1 CME propagation 128
6.10.2 Sheath and CME 135

6.10.3 CME expansion 135
6.11 Inconsistencies between local and global measures of CME expansion 138
6.11.1 Average values of global and local expansion metrics 141
6.11.2 Comparison of local and global measures of CME expansion 142

7 Prediction of southward B$_z$ **144**

7.1 Background 144
7.2 Examining the proportion of strong southward B$_z$ periods 146
7.3 Identification of closest matches 151
7.4 Probabilistic forecast and error of forecast 152
7.5 Modifications to the model 153
7.5.1 Training window weighting constant pair (TWWCP) 154
7.5.2 Varying weights of parameters 155
7.5.3 Threshold-based forecast 156
7.6 Example of the model 157
7.7 Results from the model 167
7.7.1 Best probabilistic forecast for all 100 reference events 167
7.7.2 Threshold-based probabilistic forecast 169

8 Summary and discussions **171**

8.1 Paper-I 171
8.2 Paper-II 173
8.3 Paper-III 175
8.4 Paper-IV 176
8.5 Paper-V 177

9 Concluding remarks and future proceeding **179**

Bibliography **183**

A CME conjunction catalog 204

B CMEs with and without shocks and sheaths 207

C Propagation and expansion sheaths 216

List of Acronyms

ACE	Advanced Composition Explorer
AE	Auroral Electrojet
ANOVA	Analysis of Variance
AR	Active Region
ASIA	Automated Sheath Identification Algorithm
AU	Astronomical Unit
CACTus	Computer Aided CME Tracking Software
CDAW	Coordinated Data Analysis Workshops
CH	Coronal Hole
CIR	Corotating Interaction Region
CME	Coronal Mass Ejection
DKIST	Daniel K. Inouye Solar Telescope
Dst	Disturbance Storm Time
ES	Expansion Sheath
EUHFORIA	EUropean Heliospheric FORecasting Information Asset
EUV	Extreme Ultraviolet

EUVI	Extreme Ultraviolet Imager
FOV	Field of View
FR	Flux Rope
FW	Forecast Window
GS	Geomagnetic Storm
GSE	Geocentric Solar Ecliptic
GSM	Geocentric Solar Magnetospheric
HCS	Heliospheric Current Sheet
HGI	Heliographic Inertial
HI	Heliospheric Imager
HMI	Helioseismic and Magnetic Imager
HSD	Honestly Significant Difference
HSO	Heliophysics System Observatory
HSS	Heidke Skill Score
IBEX	Interstellar Boundary Explorer
IMF	Interplanetary Magnetic Field
IMPACT	In-situ Measurements of Particles and CME Transients, an instrument suite onboard STEREO
IP	Interplanetary
LASCO	Large Angle and Spectrometric Coronagraph, instrument on SOHO

LISM	Local Interstellar Medium
LS	Longitudinal Separation
MC	Magnetic Cloud
ME	Magnetic Ejecta
MESSENGER	MErcury Surface, Space ENvironment, GEochemistry, and Ranging
MFI	Magnetic Field Investigation, an instrument onboard *Wind*
MHD	Magnetohydrodynamic(s)
ML	Machine Learning
MR	Magnetic Reconnection
PC	Polar Cap
PLASTIC	Plasma and Suprathermal Ion Composition, an instrument suite onboard STEREO
PS	Propagation Sheath
PSP	Parker Solar Probe
RH	Rankine-Hugoniot
SC	Spacecraft
SCy	Solar Cycle
SDO	Solar Dynamics Observatory
SECCHI	Sun Earth Connection Coronal and Heliospheric Investigation, an instrument suite onboard STEREO

SEP	Solar Energetic Particle
SIR	Stream Interaction Region
SSN	Sunspot Number
SO	Solar Orbiter
SOHO	Solar and Heliospheric Observatory
STEREO	Solar Terrestrial Relations Observatory
SWE	Solar Wind Experiment, an instrument onboard *Wind*
RMS	Root-Mean-Square
RTN	Radial-Tangential-Normal
TW	Training Window
TWWCP	Training Window Weighting Constant Pair
UV	Ultraviolet

List of Publications

Paper-I: **Salman, T. M.**, Lugaz, N., Farrugia, C. J., Winslow, R. M., Jian, L. K., and Galvin, A. B., Properties of the sheath regions of coronal mass ejections with or without shocks from STEREO in-situ observations near 1 AU, *The Astrophysical Journal*, 904, doi.org/10.3847/1538-4357/abbdf5, 2020.

Paper-II: **Salman, T. M.**, Lugaz, N., Winslow, R. M., Farrugia, C. J., Jian, L. K., and Galvin, A. B., Categorization of Coronal Mass Ejection Driven Sheath Regions: Characteristics of STEREO Events, *The Astrophysical Journal*, 2021 (accepted for publication).

Paper-III: **Salman, T. M.**, Winslow, R. M., and Lugaz, N., Radial evolution of coronal mass ejections between MESSENGER, Venus Express, STEREO, and L1: Catalog and analysis, *Journal of Geophysical Research: Space Physics*, 125, doi.org/10.1029/2019JA027084, 2020.

Paper-IV: Lugaz, N., **Salman, T. M.**, Winslow, R. M., Al-Haddad, N., Farrugia, C. J., Zhuang, B., and Galvin, A. B., Inconsistencies between local and global measures of CME radial expansion as revealed by spacecraft conjunctions, *The Astrophysical Journal*, 899, doi.org/10.3847/1538-4357/aba26b, 2020.

Paper-V: **Salman, T. M.**, Lugaz, N., Farrugia, C. J., Winslow, R. M., Galvin, A. B., and Schwadron, N. A., Forecasting periods of strong southward magnetic field following interplanetary shocks, *Space Weather*, 16, 2004-2021, doi.org/10.1029/2018SW002056, 2018.

CHAPTER 1

Introduction

From prehistoric petroglyphs to modern satellite missions, the effects of the Sun on its sphere of influence, the "heliosphere" that encloses the planets of the solar system, has been our long-standing curiosity. Since the beginning of the "Space Age" in the 1950s, the interest in the Sun's activity has increased by leaps and bounds in the modern era driven by technology.

Space weather, a term first used in the 1990s, refers to the time-varying disturbances driven by solar activity, manifesting as disruptions to systems and technologies in orbit and on the Earth. The origins of space weather can be traced back to the middle of the 1800s when Richard Carrington made the first documented connection between solar activity and space weather (Carrington, 1859).

Coronal mass ejections (CMEs) are considered to be the primary drivers of space weather. In essence, CMEs are large-scale eruptions of solar plasma and magnetic fields from the Sun (Webb & Howard, 2012). From the "Carrington Event" in 1859 to the "Halloween" storms of 2003, CMEs have been at the forefront of disturbances in the Sun-Earth system. The quasi-dipolar geomagnetic field of Earth has a northward orientation (relative to the ecliptic plane). If the magnetic orientation of a CME is opposite to the Earth's magnetic field, this will trigger a rearrangement of magnetic connections, known as "magnetic reconnection." Magnetic reconnection (MR) is the breaking and reconnection of opposite magnetic field lines, converting magnetic energy into thermal and kinetic energy (Biskamp, 1996). MR exposes the Earth's magnetosphere to the solar wind by opening closed field lines, allowing the transfer of energy and momentum from the solar wind to the near-Earth space. MR in association with the compression of magnetosphere can induce significant variations to the currents and magnetic fields in geospace, resulting in damage on satellites, disruptions in navigation systems, voltage fluctuations in power grids, to name a few.

The consequences mentioned above are most often associated with the magnetic ejecta (ME). This exemplifies the concentrated focus put on the CME by the space physics community. Indeed, the formation of CMEs and their subsequent propagation and evolution in the heliosphere are essential considerations for heliospheric physics (Manchester et al., 2017). However, two other unique solar wind transients, shocks, and sheaths, often preceding the CME, further add to a CME's geoeffective potential. Regardless of the magnetic structure of the corresponding CMEs, both shocks and sheaths are capable drivers of significant geomagnetic disturbances (see Lugaz et al., 2016b). The shock is a discontinuity separating two distinct plasmas. In a scenario when the CME front propagates in the solar wind frame with a speed that exceeds the local characteristic speeds of the medium (sonic, Alfvén), a shock develops in front of the CME. The sheath is composed of compressed and turbulent plasma that can form in the presence or absence of shocks. The critical importance of sheath can be underlined because it provides a much shorter lead time for forecast and is also more complex compared to the CME.

The overarching goal of this thesis is to advance the current understanding of CME sheaths, the period of enhanced density and magnetic field ahead of most but not all CMEs when they reach Earth. This thesis is centered on a two-fold approach, investigating the heliospheric propagation of CME sheaths with in-situ measurements from multiple radially aligned spacecraft (SC) and near 1 AU with single-SC measurements. In this way, this thesis aims to coalesce two unique perspectives of research. The first one investigates the radial evolution of CME sheaths in the inner heliosphere with the same sheath measured at multiple vantage points. Such an approach is valuable in capturing the complex nature of CME sheaths. However, the intrinsic drawback of this approach is that no global trends are identified, and there are only a limited number of events available for study. The second approach specializes in this particular aspect as this involves analysis of CME sheaths at a specific heliocentric distance with a robust statistic. Working in tandem, the scientific questions (SQ) these two approaches mainly address are:

- How different are sheaths not preceded by shocks as compared to sheaths preceded by shocks, even for similar drivers? (SQ-I)
- What are the physical mechanisms contributing to the observed variabilities in CME sheaths near 1 AU? (SQ-II)
- How much do CME features inferred from statistical estimations differ from the individual analysis of CMEs with multi-point observations? (SQ-III)
- Can utilization of prior knowledge of solar wind variations in the vicinity of shocks provide sufficient lead times for space weather forecasting? (SQ-IV)

This thesis comprises an introductory part and integration of five original research articles referred to as Papers I-V. The introductory part is organized as follows. Chapter 2 introduces the structure of the Sun and its complex and swirling magnetic field. Chapter 3 shines a light on odysseys of CMEs, from pre-eruptive structures on the Sun to ranging few tenths of an AU near-Earth. Chapters 4 and 5 review the variabilities of CME sheaths near 1 AU with statistical methods. Chapter 6 provides a context of the radial evolution of CME structures with multi-point observations. Chapter 7 assesses the importance of shocks and sheaths in the probabilistic prediction of intense geomagnetic storms. Chapter 8 summarizes the five research articles. Chapter 9 gives the concluding remarks and a brief review of future science endeavors stemming from this thesis.

CHAPTER 2

The Sun

Our nearest star, the Sun (see Figure 2.1), was born approximately 4.6×10^9 years ago due to the gravitational collapse of a giant gaseous nebula. The Sun, with a radius of (6.96×10^5) ± 65 km (e.g. Emilio et al., 2012), is primarily composed of hydrogen (∼71% by mass), with ∼27% helium, and the rest being heavier elements (originating from the giant molecular cloud from which the Sun was formed).

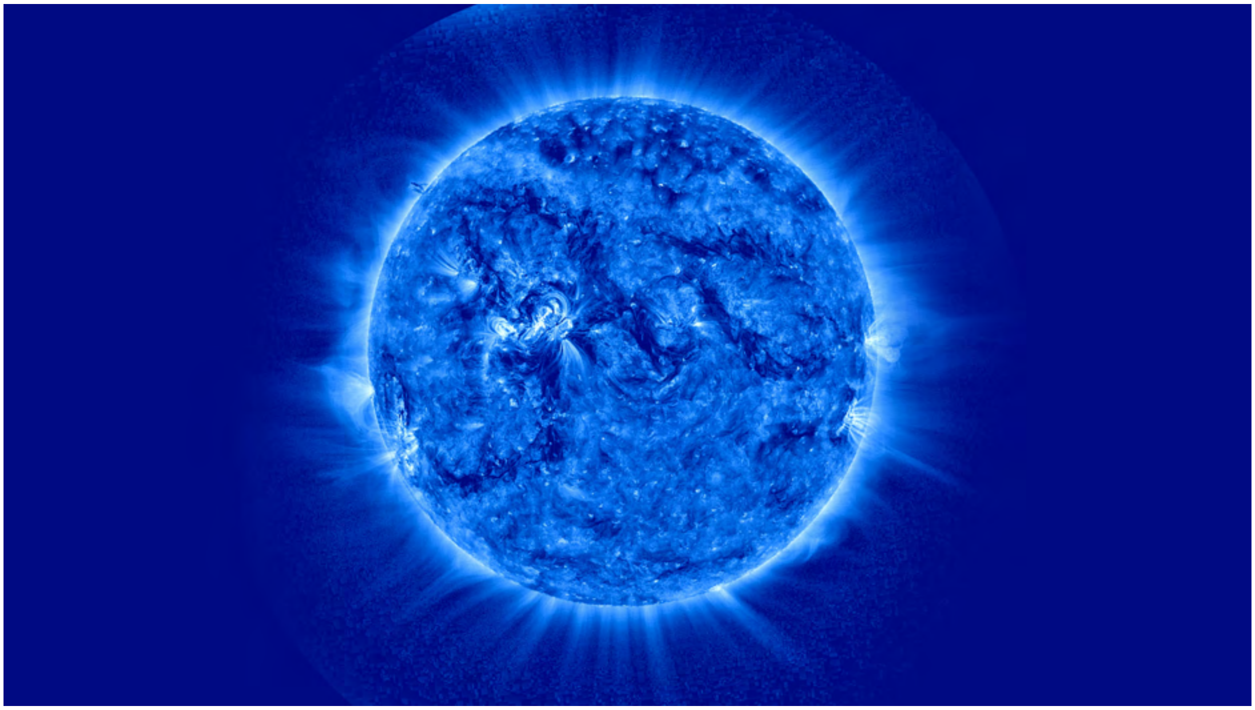

Figure 2.1: The Sun, as seen in 171Å wavelength with the extreme ultraviolet imager (EUVI) instrument from STEREO-A on 9 December 2013. **Image credit: Naval Research Laboratory.**

2.1 The solar interior

The solar interior is so dense that it is impossible to observe its structure with optical instruments (as photons cannot stream out into space). Scientists use a method known as "helioseismology" to probe the structure of the solar interior. The word helioseismology is derived from the words Helios (Sun), seismos (quakes), and logos (study). The modes of the Sun's oscillation are predominantly acoustic. In helioseismology, analogous to geoseismology, observations of waves (acoustic, gravity, and surface gravity) on the Sun's surface are used to probe the solar interior's temperature, density, composition, and motion that influences the oscillation periods.

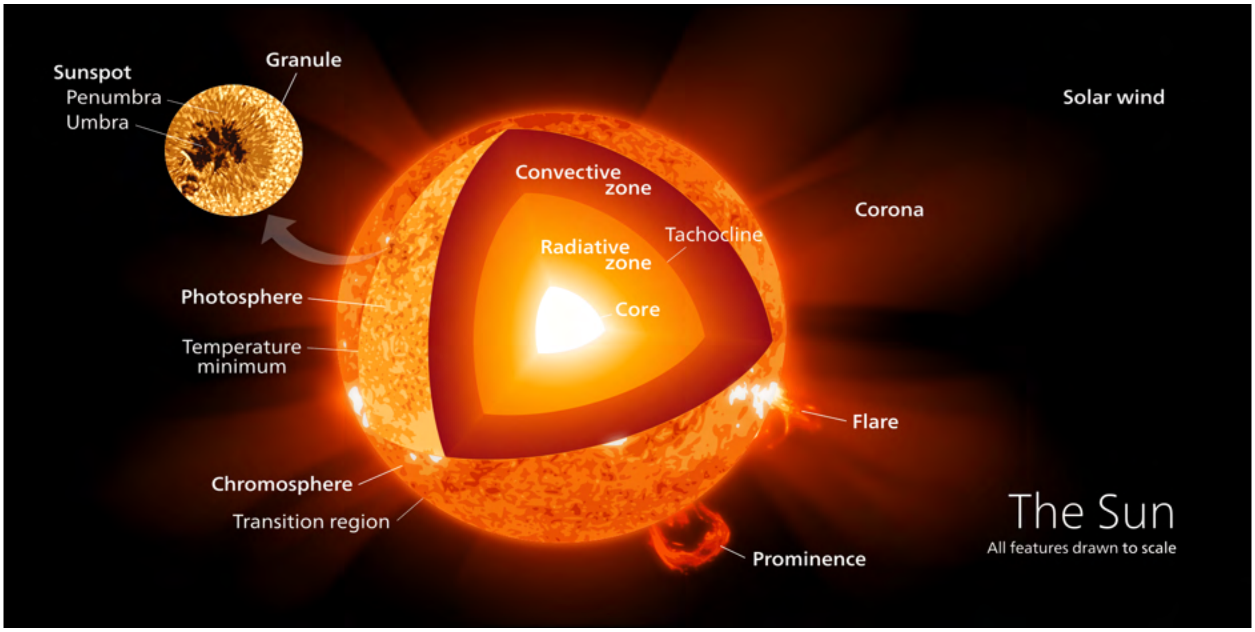

Figure 2.2: The structure of the Sun. **Image credit: universetoday.com.**

The solar interior can be divided into three layers: the core, radiative zone, and convection zone (see Figure 2.2). The Sun's energy is produced in the core through nuclear fusion reactions. 98% of the energy generation occurs over a height range of 0.0 - 0.25 R_s (R_s is the solar radius). The rate of fusion is proportional to both density and temperature. If there is an increase in the fusion rate, this will cause the temperature to rise and the core to expand.

However, an expansion of the core will reduce the density and decrease the rate of fusion. This is how the Sun self-regulates the rate of fusion. In the core, temperatures can reach up to ∼15 MK.

The radiative zone (0.25 - 0.7 R_s) is a spherical shell where the dominant mode of energy transport is radiation (same as the core). In this zone, the temperature drops to 8 MK, such that fusion stops but only free protons and electrons exist. However, the plasma is so dense that photons continuously scatter off free particles. The random walk of photons to reach the outer boundary of the radiative zone, called the "tachocline" takes $\sim 10^5$ years (Mitalas & Sills, 1992).

At the top of the radiative zone, the temperature drops to 1 MK, allowing multi-electron ions to absorb photons more readily, resulting in a dramatic increase in the opacity of the plasma. This increases the temperature gradient and leads to the onset of a convective instability beyond 0.7 R_s, causing plasma to become buoyant and rise relatively quickly to the solar atmosphere (photosphere). The increase in opacity in the convection zone does not allow radiation to go through. Therefore, the mode of energy transport becomes convection in this zone. The temperature reaches ∼6000 K at the upper layer of the convection zone (at 1 R_s).

2.2 The solar atmosphere

The solar atmosphere begins above the visible surface of the Sun (see Figure 2.2). The first layer of the solar atmosphere is the photosphere, where the atmosphere becomes optically thin to visible radiation. The photosphere has a small-scale granular structure with a temperature of ∼5800 K and a density of $\sim 2\times10^{-4}$ kg m^{-3}. The granules are short-lived (lifetime of 5 - 10 minutes) and have typical sizes of ∼1000 km. The compositional signatures of the photosphere are similar to the deeper layers of the Sun.

The most noticeable features in the photosphere are sunspots (see on the left panel in Figure 2.3), regions of concentrated magnetic flux. The sunspots have strong magnetic fields

(∼10000 times that of the Earth's surface magnetic field). The darkness of sunspots can be attributed to the presence of such strong magnetic fields that inhibit convective transport of heat from below, resulting in lower temperatures than the ambient photosphere (∼4000 K). The churning motions of the photosphere stress the magnetic fields, which can cause the magnetic fields to become unstable and erupt violently in the form of solar eruptions. However, the magnetic fields in the photosphere are not only confined to sunspots. There are also weaker fields present, often referred to as the "quiet" Sun.

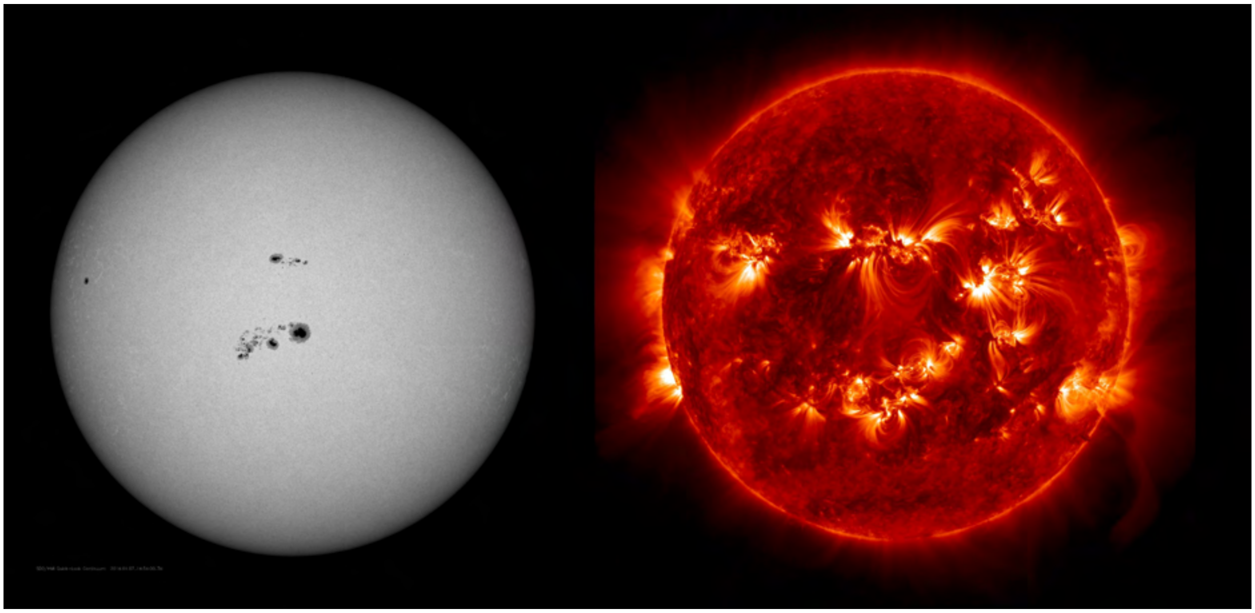

Figure 2.3: A giant sunspot group observed with SDO's helioseismic and magnetic imager (HMI) instrument on 7 January 2013 (left panel, **Image credit: NASA-SDO/HMI**) and active regions observed in 171Å EUV light from SDO on 14 May 2015 (right panel, **Image credit: NASA/SDO**).

The chromosphere is the second layer of the solar atmosphere. The temperature in the chromosphere changes in an unexpected manner, from a temperature minimum of ∼4500 K, to as high as 25000 K at the top of the chromospheric layer. One of the dynamic features associated with the chromosphere is long, narrow jets called "spicules," hurling plasma at speeds of ∼100 km s^{-1} high into the solar atmosphere. Spicules are believed to play a role in heating the solar atmosphere (De Pontieu et al., 2004). Hydrogen-alpha (Hα) observations of the low-temperature region of the chromosphere reveal complex magnetic structures like "filaments" and "prominences" (Mackay et al., 2010). In contrast, the higher temperature region of the chromosphere is visible in ultraviolet (UV) and extreme ultraviolet (EUV) wavelengths. Filaments, composed of large amounts of dense material, appear as dark ribbon structures against the solar disc, lying along magnetic neutral lines (i.e., the demarcation lines between regions of opposite polarity). When seen off the solar limb, filaments appear bright against the dark sky background and are called prominences. Filaments can last from a few hours (active region filaments) to a few months (primarily quiescent filaments). Instabilities in the magnetic fields supporting and overlying filaments and prominences lead to violent solar eruptions.

The layer sandwiched in between the chromosphere and the outer layer of the solar atmosphere (the corona) is the transition region. About ∼100 km thick, this region has the steepest temperature gradient in the solar atmosphere (Gabriel, 1976).

The corona lies above the transition region, ∼2500 km above the photosphere. The temperature in the corona can reach well over 10^6 K (e.g. Fontenla et al., 1988). Such high temperatures are the reason that all elements are ionized in the corona. However, the source of coronal heating remains one of the most elusive problems in solar physics. Another fascinating aspect of the corona is that the solar composition is different in the corona than in the photosphere (Strong et al., 2017).

In a historical context, coronal features have primarily been observed in solar eclipse images (see Figure 2.4 for an example of a more recent observation). At present, the corona is extensively observed with UV and white-light images with an optical system called the "coronagraph," developed by French astronomer Bernard Lyot in 1939 (Lyot, 1939). It creates an artificial eclipse with an occulting disc, suppressing the bright photosphere to image the fainter corona. The corona's white-light radiation is primarily due to the Thomson-scattered photospheric light by free electrons (known as the *Kontinuierlich* or K-corona) and

Rayleigh or Mie scattering of photospheric light from interplanetary dust grains (known as the *Fraunhofer* or F-corona).

Figure 2.4: Coronal features observed during the total solar eclipse in Mitchell, Oregon, USA, on 21 August 2017. **Image credit: Miloslav Druckmüller.**

With UV and X-ray observations, the low corona appears highly structured, showing concentrations of bright coronal loops connecting opposite magnetic polarities on the solar surface. These loops are known as "active regions" (ARs, see on the right panel in Figure 2.3). Coronal loops outline the motion of ionized plasma along the magnetic field lines. ARs are sites of strong heating (making them appear much brighter than their surroundings) with very strong magnetic fields (Sawyer, 1968). Dark sunspots are the most prominent features of ARs. There are also magnetic areas in the corona that connect directly to the interplanetary fields. These open field lines, originating from "coronal holes" (CHs; see Cranmer, 2009), allow the plasma to escape into the heliosphere. Reconfiguration of the unstable coronal magnetic fields can lead to a catastrophic release of excess energy stored in the coronal fields in the form of a solar flare and a CME. Solar flares and CMEs can also occur independently of each other.

2.3 The Sun's magnetic field and solar cycle

The Sun has a complicated magnetic field structure that changes continuously in a quasi-regular way, yielding the solar cycle (see Hathaway (2015) for a review on the solar cycle). Each solar cycle (SCy) has a number attached, starting from SCy 1 in 1755. The complex behavior of the intertwined and dynamic solar magnetic field over an 11-year SCy (there have been SCys as short as 8 years and as long as 14 years), during which the dipole reverses in polarity, is explained by the "solar dynamo" theory (Hathaway, 2015). The temporal and spatial variations of the solar magnetic field primarily occur in response to the drift caused by the "differential rotation". As the Sun is not a solid body, its rotation is not rigid. The Sun rotates at different speeds at different latitudes. This rotation is called the differential rotation. The polar regions rotate more slowly than the equator, and that causes a shearing motion between solar plasma at different latitudes. At the equator, the synodic rotation period (i.e., the rotation period with respect to the Earth) is $\sim$26 days, whereas it is $\sim$36 days at the poles.

The "tachocline" is the interface between the radiative zone with uniform rotation and the convection zone with differential rotation (Spiegel & Zahn, 1992). The initial configuration of the solar magnetic field is poloidal, with field lines parallel to the solar meridians. In the tachocline, the maximum radial and latitudinal shearing occur, generating large magnetic fields. The magnetic fields generated are caught up in the differential rotation of the Sun. The plasma in the tachocline drags the magnetic field with the flow and stretches it about the equator (Babcock, 1961). Over the following rotations, the magnetic field wraps around the

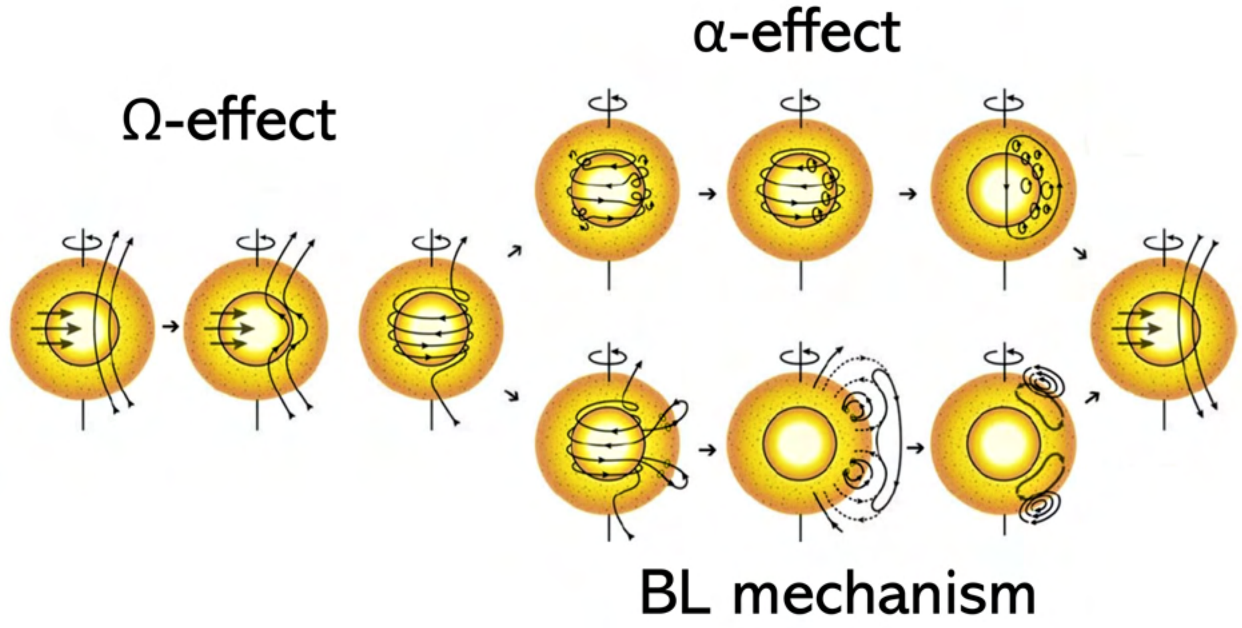

Figure 2.5: Illustrations of the main processes in the solar dynamo. **Adapted from Sanchez et al. (2014).**

solar axis more and more, and the poloidal magnetic field is gradually turned into a toroidal field (known as the "Ω-effect," see Figure 2.5) where the field lines are aligned with the solar parallels. This process also amplifies the magnetic field by converting rotational energy into magnetic energy. The increase in this toroidal field builds up the magnetic pressure near the tachocline in twisted magnetic ropes. When the magnetic pressure exceeds the local plasma pressure, the magnetic ropes become convectively unstable and float towards the solar surface (Fan, 2008). When the complex toroidal field rises through the convection zone, it manifests at the visible surface of the Sun as sunspots and creates a complex magnetic structure in the solar atmosphere known as an AR (see Fan (2009) for a review on the magnetic fields in the convection zone). At the solar activity maximum, the solar magnetic field transitions to a purely toroidal state (i.e., an east-west multi-polar field).

At the solar activity minimum, the solar magnetic field transitions to a purely poloidal state (i.e., a north-south dipolar field). However, there is less consensus regarding how the transition from toroidal field to poloidal field exactly occurs. One envisioned process is the "α-effect." In the convection zone, small-scale helical motions (resulting from convection in the rotating Sun) convert the toroidal field into a large-scale poloidal field (Parker, 1955). This is known as the mean-field α-effect (see Figure 2.5). One other possibility for the poloidal field regeneration is the Babcock-Leighton (BL) mechanism (Babcock, 1961; Leighton, 1969), dependent on diffusion and reconfiguration of the magnetic field. In the BL mechanism (see Figure 2.5), the continuous buildup of the toroidal field in the convection zone makes it susceptible to magnetic buoyancy instability, letting magnetic loops rise into the convection zone. Due to the twisting Coriolis force, the trailing parts of these emerging magnetic loops become closer to the nearby solar poles (that has an opposite polarity to the trailing part). When the magnetic fields near the solar equator in each hemisphere diffuse and reconnect, the solar poles receive a certain amount of opposite polarity fields, which initiate a polarity reversal (see Sanchez et al., 2014). The continuous buildup of magnetic fields at the poles leads to a global reconfiguration of magnetic fields, making possible the return to a poloidal state but with reversed polarity. The newly formed polar magnetic flux is then transported back to the tachocline by the turbulent pumping for the cycle to repeat (Bushby & Mason, 2004).

This natural dynamo mechanism of the Sun is known as the "interface dynamo" model (Parker, 1993). However, there is also the possibility of a shallow "surface layer dynamo" that generates some solar magnetic features.

In recent times, the Sun's "conveyor belt," called the "meridional flow" (see Figure 2.6), has been quoted to also play an essential role in the Sun's dynamo process, producing the 11-year sunspot cycle. At the solar surface, this flow along meridian lines, with arguments for both single-cell (e.g. Gizon et al., 2020) and double-cell (e.g. Zhao et al., 2013) circulations, continuously move material from the equator toward the poles in both the hemispheres. At mid-latitudes, the maximum speed of this flow is $\sim$20 $\mathrm{m\,s^{-1}}$ (e.g. Zhao & Kosovichev, 2004; Ulrich, 2010). As we do not expect the material to be piled up near the poles, near the base of the convection zone, a much slower return flow (~1 - 2 $\mathrm{m\,s^{-1}}$) carry material from the mid-latitudes to the equator in about 11 years (e.g. Giles et al., 1997). The variations in the meridional circulation are important in determining the strength and duration of the SCys (Zhao et al., 2013). The prolonged minimum at the end of SCy 23 (characterized by an unusually large number of days without sunspots during 2007 - 2010) is thought to be associated with meridional flow variations (e.g. Hathaway & Rightmire, 2010; Nandy et al., 2011).

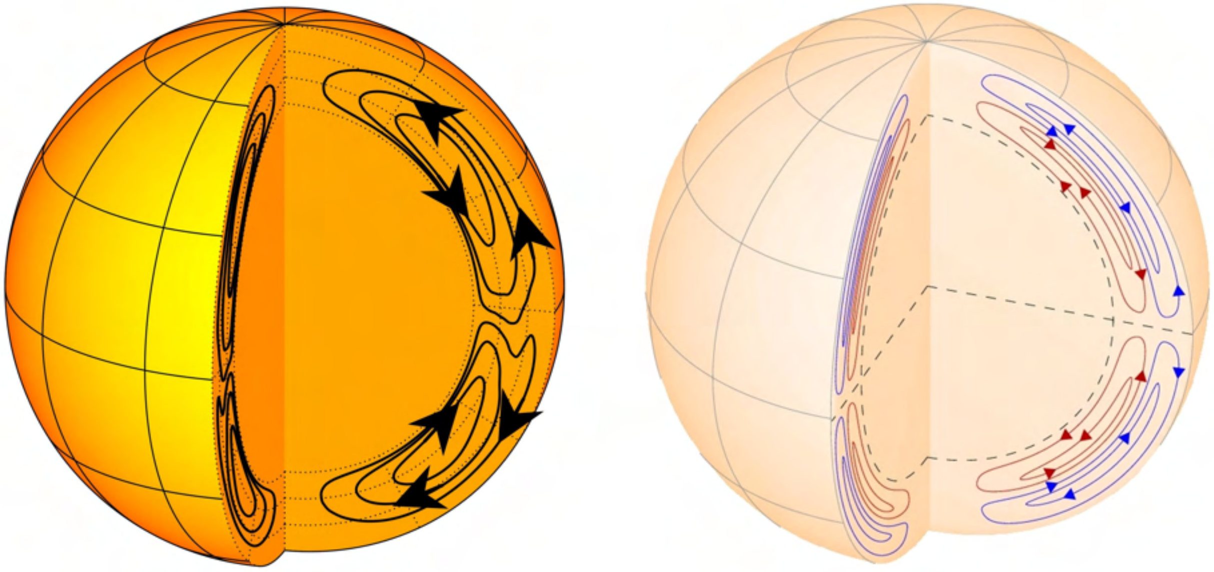

Figure 2.6: Schematic plots of the single-cell (left panel, **Image credit: Z.-C. Liang**) and double-cell (right panel, **Adapted from Zhao et al. (2013)**) meridional circulations in each hemisphere of the Sun.

Sunspots, especially their occurrence rates and positions on the photosphere, are the most evident manifestations of changes in solar magnetic activity. Over 150 years ago, Rudolf Wolf first used sunspot number (SSN) as a characteristic feature to measure solar activity (Izenman, 1985). When SSN is plotted against time, the periodicity in solar activity becomes apparent, which was first discovered by Schwabe (1843). Then, Annie and Edward Maunder first discovered the butterfly pattern of sunspots (Maunder, 1904). At the beginning of a SCy, sunspots tend to form at higher latitudes (with a latitudinal distribution of ±30°) and gradually migrate towards lower latitudes with time until they eventually disappear at the end of a SCy. This recurrent trend gives rise to the famous "butterfly diagram" shown in Figure 2.7.

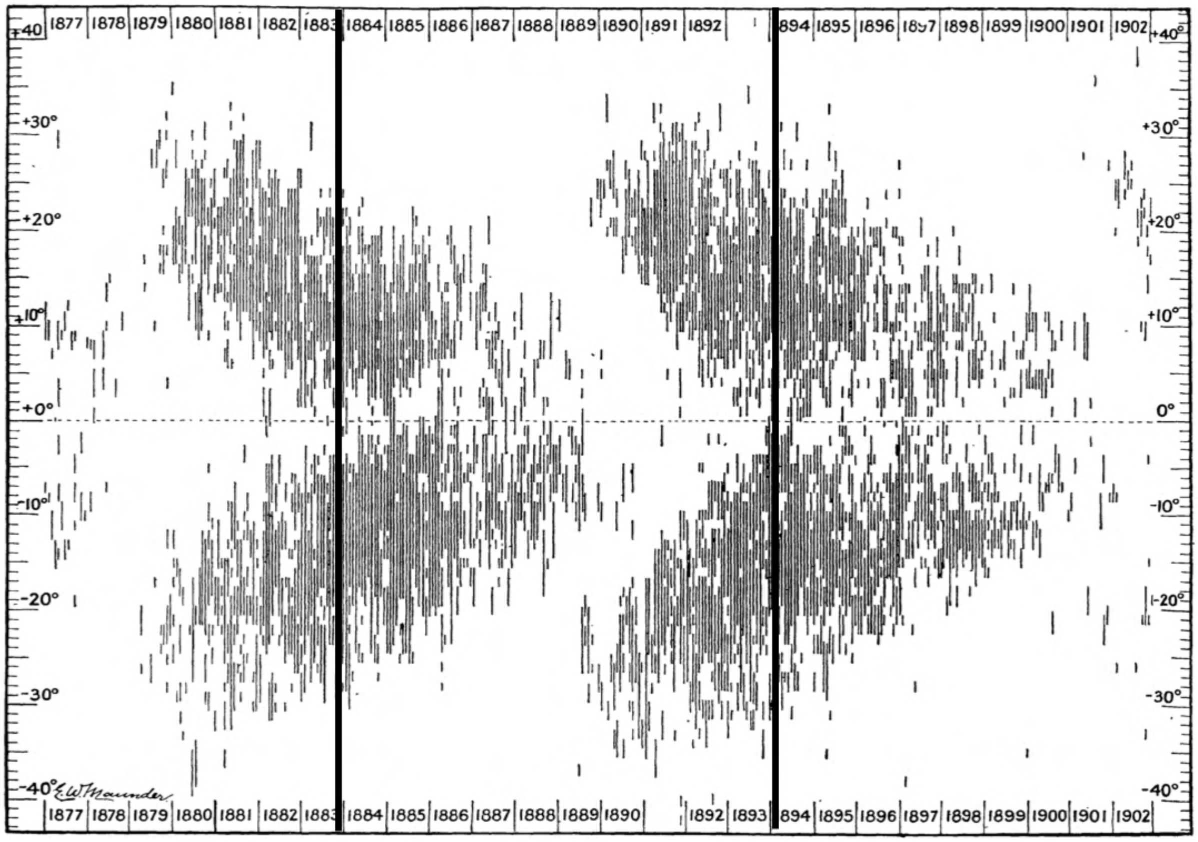

FIG. 8.—DISTRIBUTION OF SPOT-CENTRES IN LATITUDE, ROTATION BY ROTATION, 1877–1902.

Figure 2.7: The original butterfly diagram appearing in Maunder (1904), showing the evolution of the latitudes of sunspots through solar cycles 12 and 13. The two thick lines mark the solar maximum for solar cycles 12 and 13.

During the solar minimum, there are often no sunspots. A few small and short-lived regions from the old cycle may emerge near the solar equator. Such low levels of solar magnetic activity can persist for an extended period, like the "Maunder Minimum" (named after British astronomer Edward Walter Maunder) that lasted from 1645 - 1715 and the "Dalton Minimum" (named after English meteorologist John Dalton) that lasted from 1790 - 1830 (e.g. Usoskin, 2008). When writing this thesis, we are at the minimum phase of a new cycle, SCy 25 (that began in December 2019), and approaching its predicted maximum

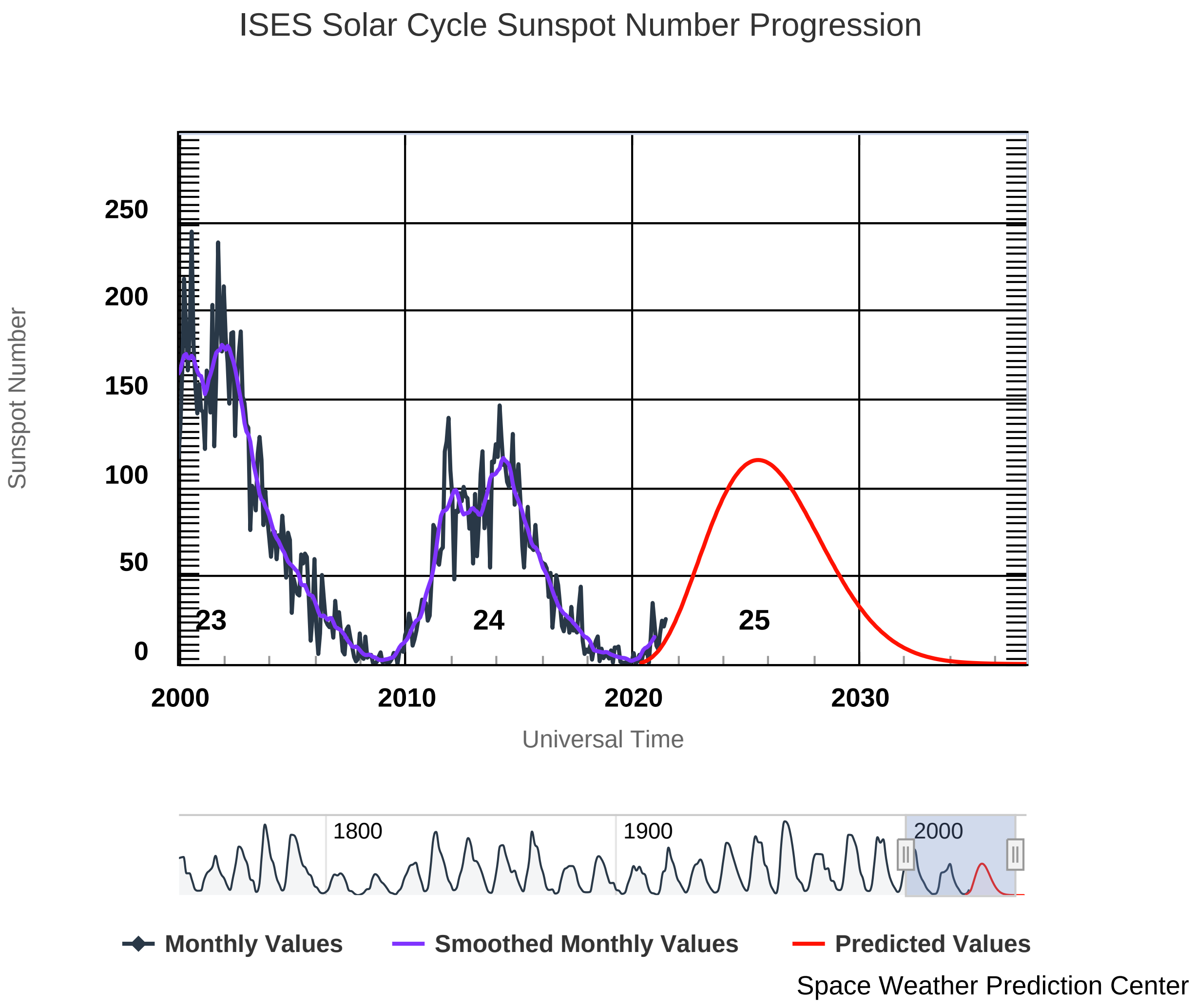

Figure 2.8: Sunspot number predictions for solar cycle 25 (the red line). The black line represents the monthly averaged data, and the purple line represents a 13-month weighted, smoothed version of the monthly averaged data. **Image credit: NOAA/SWPC.**

in July 2025. The predictions regarding the strength of SCy 25 have been varying, with predictions suggesting that SCy 25 will be the weakest SCy in the last 100 years (e.g. Upton & Hathaway, 2018) to a similar or slightly stronger than the previous cycle, SCy 24 (e.g. Bhowmik & Nandy, 2018; Sarp et al., 2018). Figure 2.8 shows the SSN predictions for SCy 25, provided by the National Oceanic and Atmospheric Administration (NOAA).

2.4 The solar wind

2.4.1 Overview

A continuous gas flow leaving the Sun, named the "solar corpuscular radiation," was first mentioned in the 1950s (Biermann, 1951). Building on the assumption of L. Biermann that this radiation is happening at the Sun all the time, Eugene Parker first theoretically predicted the existence of a steady, spherically symmetric, and isothermal outflow from the Sun (Parker, 1958). Out of the five possible solutions of the "Parker solar wind equation" (see Equation 2.1), the unique solution favored by Parker hinted that this flow starts subsonically at the base of the corona and accelerates to supersonic speeds after a distance called the "critical radius" (r_c, see Equation 2.2). This transition point is typically thought to be located at a distance of 4 - 8 R_s. Parker named this flow the "solar wind."

$$\frac{1}{u_r}\frac{du_r}{dr}\,(u_r^2 - \frac{2k_BT}{m_pr}) = \frac{4k_BT}{m_pr} - \frac{GM_s}{r^2} \tag{2.1}$$

$$r_c = \frac{GM_sm_p}{4k_BT} \tag{2.2}$$

Here, u_r is the radial flow speed, r is the radial distance from the solar surface, k_B is the Boltzmann's constant, T is the coronal temperature, m_p is the proton mass, G is the gravitational constant, and M_s is the solar mass.

The first experimental confirmation of the solar wind's existence was provided by a Soviet SC in 1959 (Gringauz et al., 1960, 1961). In essence, the solar wind, originating from the corona, is a million mile-per-hour stream of charged particles, propagating radially outward from the Sun into the interplanetary (IP) space due to the hot corona and low pressure in IP space). This supersonic stream of ions and electrons shapes a spherical bubble-like structure in the surrounding local interstellar medium (LISM) called the heliosphere (Davis, 1955). The charged particles primarily include protons, electrons, and alpha particles. However, minor ions (ions heavier than alpha particles) such as ionized oxygen and iron are also present and carry information regarding the formation, acceleration, and transfer of solar plasma from the corona into the solar wind (Bochsler, 2007). The solar wind plasma is quasi-neutral (i.e., almost neutral), in which the positively charged protons almost wholly neutralize the negatively charged electrons. The solar wind is the carrier of coronal magnetic field throughout the heliosphere (termed as the interplanetary magnetic field or IMF), as the field is "frozen-in" to the flow due to the high electrical conductivity of the corona (diffusion of the magnetic field through the plasma is not taken into account). Due to corotations with the Sun, the IMF has the pattern of an Archimedean spiral (see Figure 2.9), known as Parker's spiral (Parker, 1958).

Based on the speeds of the plasma flow, the solar wind can be assumed to have three states: fast, intermediate, and slow (Neugebauer & Snyder, 1966). Origins of the fast, intermediate, and slow solar winds are associated with different source regions at the Sun. The fast solar wind, with speeds of $\sim$700 - 800 $\mathrm{km\,s^{-1}}$ (e.g. Neugebauer & Snyder, 1966; Gosling et al., 1976) originates from CHs (both polar and local), associated with open magnetic field lines, and typically located at higher heliographic latitudes. The intermediate solar wind ($\sim$445 - 700 $\mathrm{km\,s^{-1}}$) primarily emanates from high-density streamer belt regions, associated predominantly with closed magnetic field lines. These streamers, separating regions with opposite polarity magnetic fields, are concentrated near the solar equatorial plane during the years of low solar activity (e.g. Wang et al., 2000; Saez et al., 2005). The source areas of intermediate-speed solar winds mostly remain constant over the SC (see Tokumaru et al., 2010). The origins of the slow solar wind ($\sim$300 - 400 $\mathrm{km\,s^{-1}}$) are still under debate, with

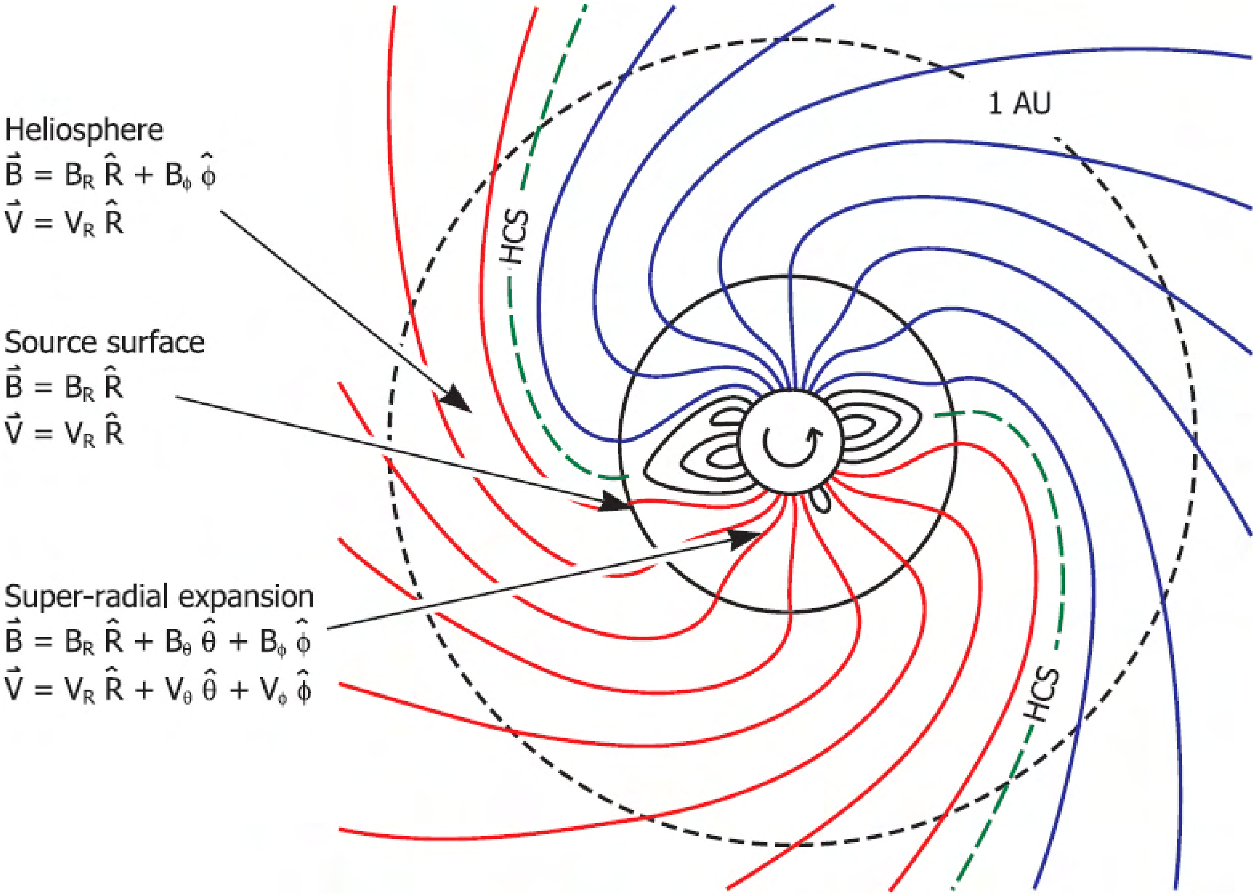

Figure 2.9: A schematic view of the Archimedean spiral pattern of the IMF in the ecliptic plane. Close to the Sun (at $\sim$ 2.5 R_s, known as the "source surface"), the field lines and the solar wind flow are purely radial. In IP space (beyond the solar surface), rotation of the footpoints of the IMF, frozen into the radial solar wind, leads to a spiral geometry. The green dashed line is the heliospheric current sheet (HCS) that separates regions of opposite IMF polarities (shown as red and blue lines). **Adapted from Owens & Forsyth (2013).**

arguments for origins at the boundaries of CHs (e.g. Wang & Sheeley Jr., 1990) or the boundaries between open and closed field lines (e.g. McComas et al., 2008). Source regions, including both open and closed loop-like magnetic field configurations, are found to be the source of flows with the lowest speeds (Lotova et al., 2000).

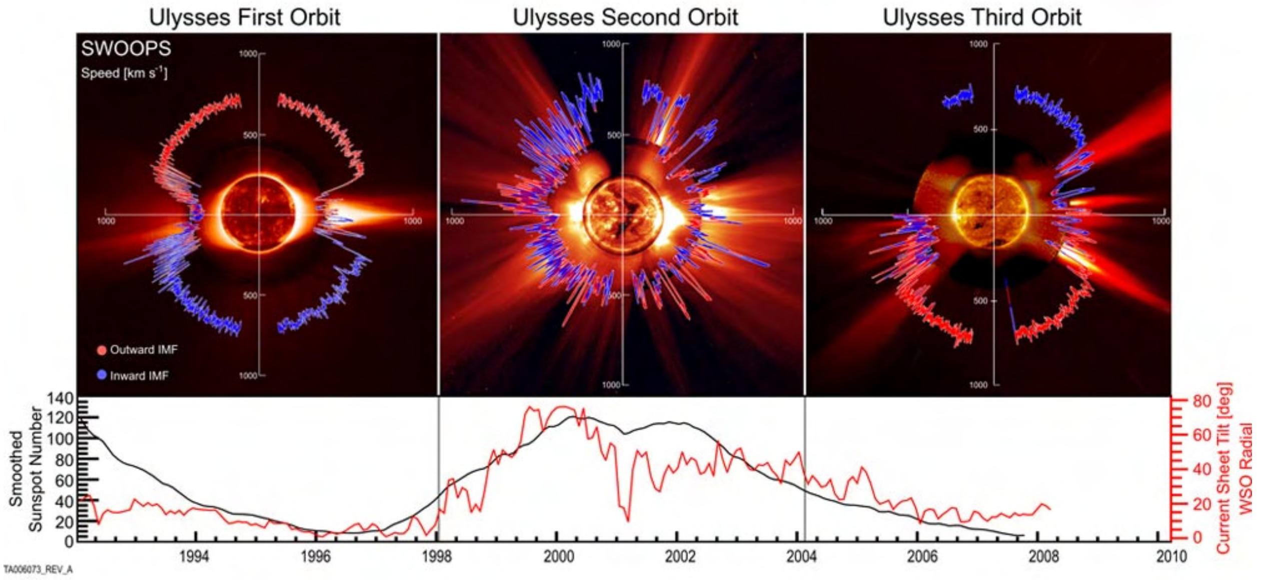

Figure 2.10: The Sun's magnetic field and solar wind speed as observed by Ulysses over all three of its orbits. The blue-colored lines represent the outward IMF, and the red-colored lines the inward IMF. A timeline and line graphs showing sunspot frequency are shown at the bottom. **Adapted from: McComas et al. (2008).**

Figure 2.10 shows the radial plots of the solar wind speeds from all three of Ulysses' (Wenzel et al., 1992) polar orbits of the Sun. The first orbit of Ulysses occurred during the solar minimum phase and showed slow wind streams over the equator and fast wind streams over the poles (McComas et al., 2008). The second orbit showed an intermix of fast and slow winds at all latitudes, consistent with solar maximum activity (McComas et al., 2008). Three-quarters of the third orbit was completed during the minimum of the next SCy.

The solar wind is highly structured as its characteristics vary with heliospheric latitude and longitude. Previous missions like Helios 1 and Helios 2, with Helios 2 achieving perihelion at

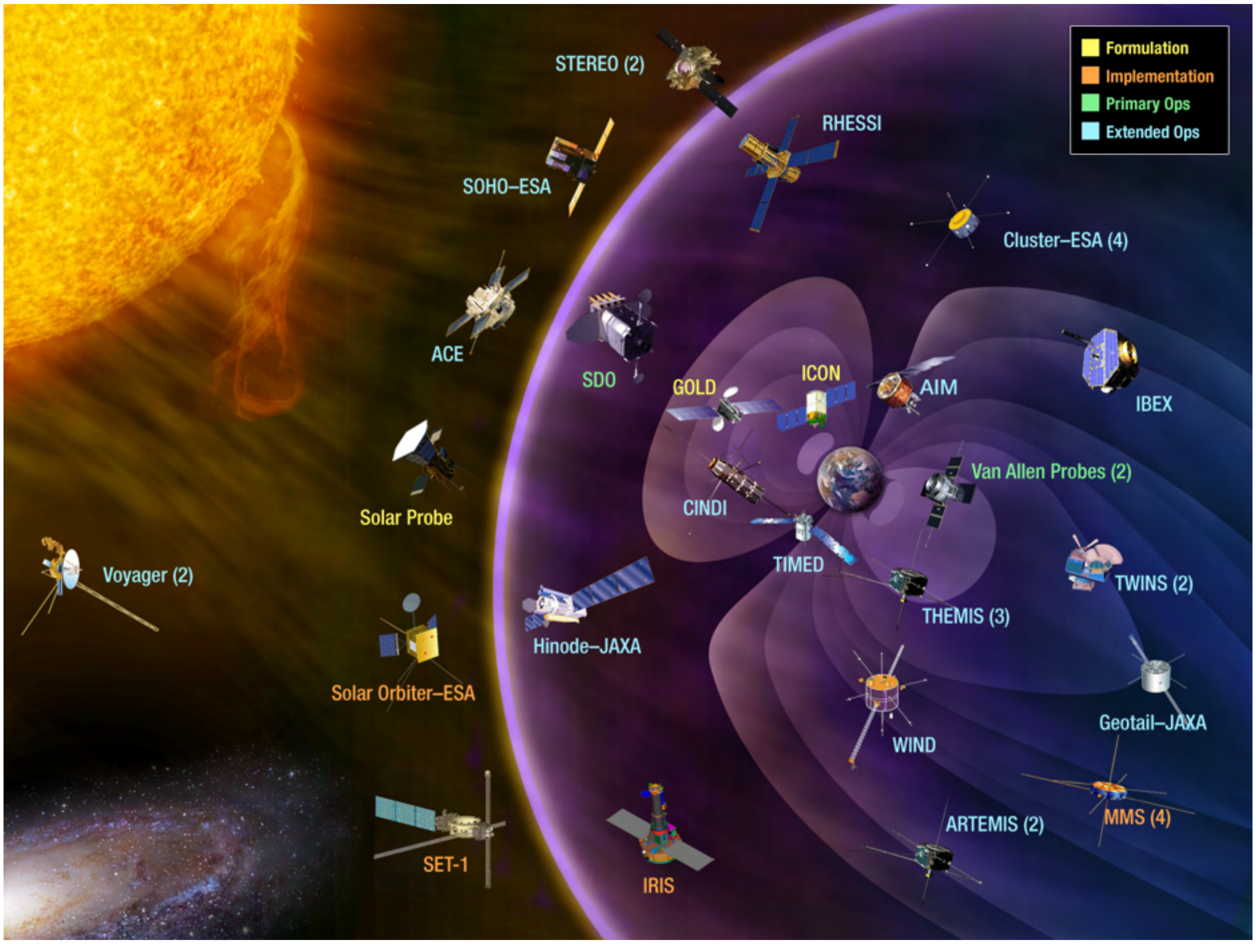

Figure 2.11: The Heliophysics System Observatory (HSO). **Image credit: NASA.**

a distance of 0.29 AU (slightly inside the orbit of Mercury), provided valuable information about the solar wind close to the Sun (Schwenn et al., 1975; Rosenbauer et al., 1977). The solar wind characteristics are currently sampled in-situ by a small fleet of SC at specific locations, primarily in orbits near the ecliptic plane and around planets. In addition, historic missions such as the Parker Solar Probe (PSP; Fox et al., 2016) and Solar Orbiter (SO; Müller et al., 2013) have solar wind plasma measurements that will be able to decode long-sought mysteries of the solar wind. Figure 2.11 shows the Heliophysics System Observatory (HSO), which can be thought of as a single observatory comprising a fleet of satellites that have recently performed or are currently performing heliophysics science investigations.

2.4.2 Solar wind structures

The large-scale structure of the solar wind is dominated by two types of flows: transient disturbances (i.e., CMEs, an example is seen in Figure 2.12) and corotating flows (i.e., corotating interaction regions or CIRs) (Gosling, 1996). Corotating flows are consequences of the spatial variability in the coronal expansion and solar rotation, which radially aligns solar wind flows of different speeds (e.g. Gosling & Pizzo, 1999), whereas transient disturbances, interrupting the quasi-stationary solar wind are associated with episodic ejections of solar material into IP space (e.g. Neugebauer, 1991).

Stream interaction regions (SIRs) form when faster solar wind streams originating from CHs catch up with the preceding slower solar wind streams (see Figure 2.13), resulting in a density pile-up of compressed plasma upstream of the stream interface (e.g. Pizzo, 1978; Richardson, 2018). This happens because the slower streams are more curved in the Parker spiral, whereas faster streams are more radial (less tightly wound). Therefore, the faster streams can overtake the slower streams ahead of them.

A rarefaction region follows the compression in the fast wind because the slow wind cannot reach the fast wind. As the faster and slower solar wind plasma is magnetically separated

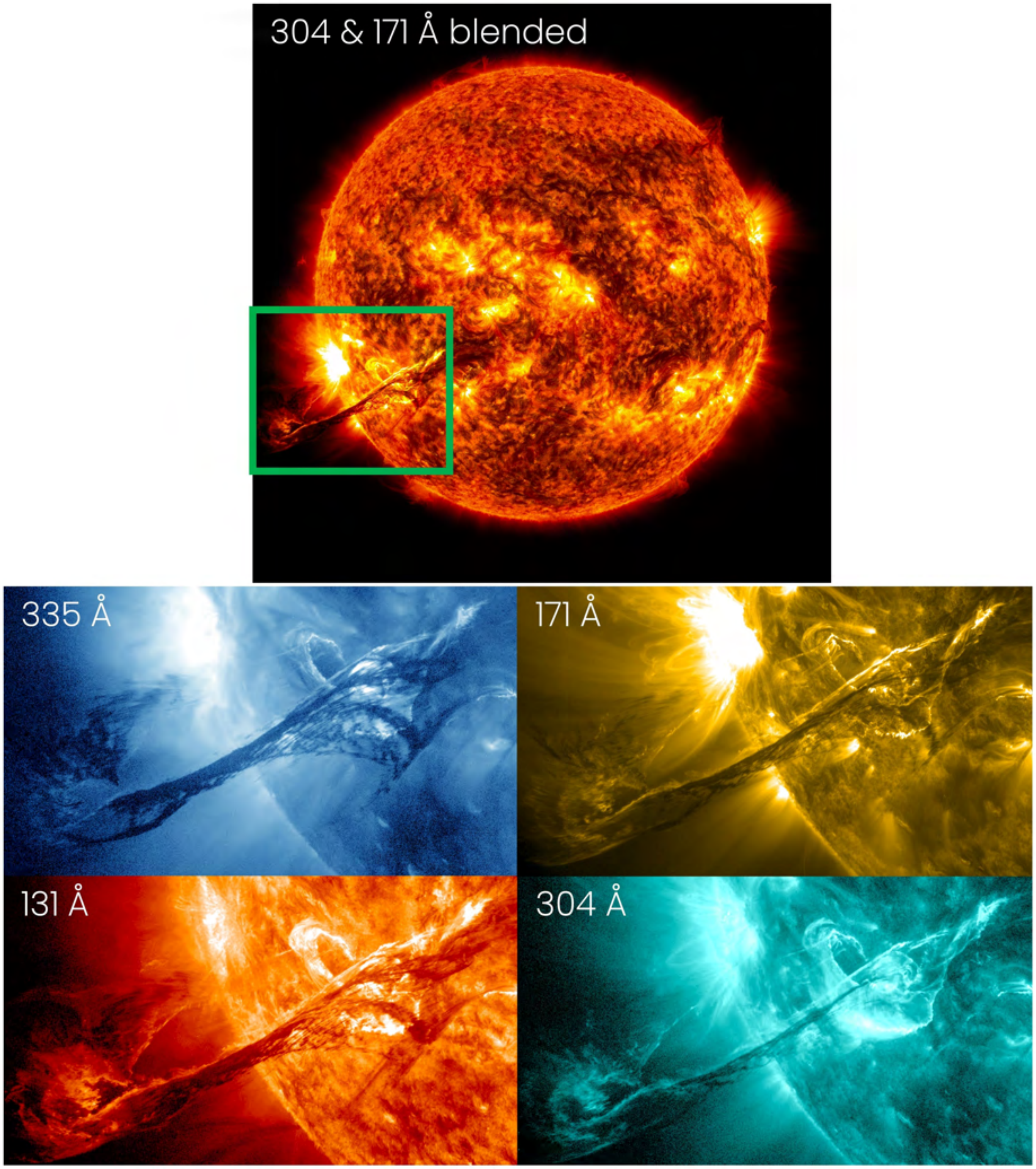

Figure 2.12: Filament eruption of a CME on 31 August 2012 at 19:49 UT in different EUV wavelengths, captured by SDO. **Image credit: NASA/SDO.**

and can not pass through the stream interface, the compression can lead to the formation of a forward shock at the leading-edge that propagates away from the Sun and reverse shock at the trailing-edge, that propagates towards the Sun (see Richardson, 2018). As CHs (from where fast solar wind originates) rotates around the solar rotation axis, this also results in the rotation of the SIR structure. After a complete solar rotation, the SIR is referred to as a CIR.

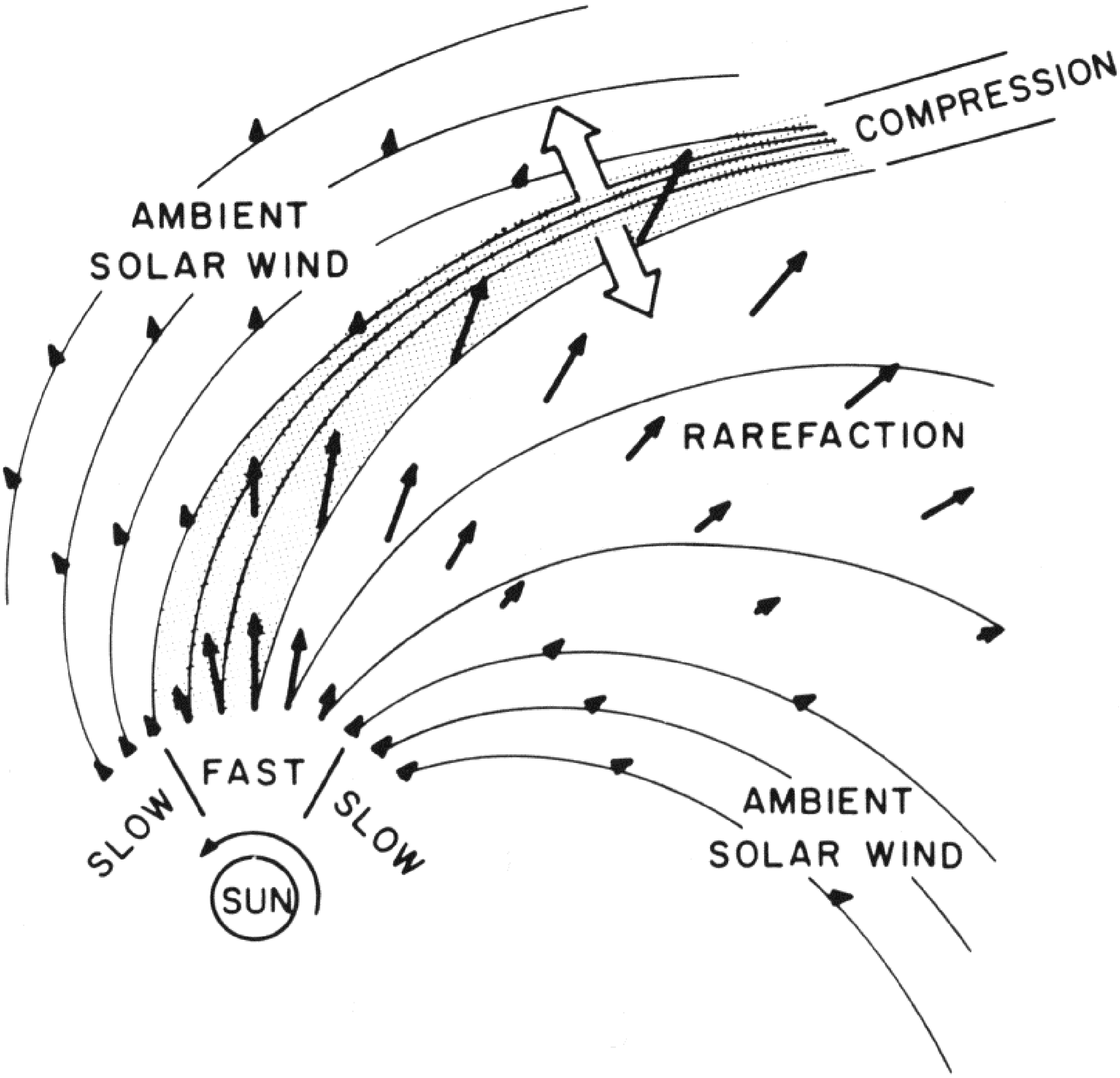

Figure 2.13: Schematic of the formation of a SIR (in the inertial frame) with the interaction between fast and slow solar winds. **Adapted from Pizzo (1978).**

2.4.3 Outer heliosphere

The interplay between supersonic solar winds of different origins shapes the IP space. The supersonic solar wind becomes subsonic at the "termination shock," located at ∼80 - 100 AU (e.g. Stone & Cummings, 2001), see Figure 2.14) because of interactions with the LISM. Then, at the edge of the heliosphere, where the heliosphere meets the interstellar medium, termed as the "heliopause" (see Figure 2.14), located at ∼119 AU (e.g. Stone et al., 2019), the solar wind achieves pressure balance with interstellar plasma. However, the existence of a "bow shock" (as seen in Figure 2.14) in front of the heliosphere is still under debate. The hypothesized bow shock is the region where the heliosphere is believed to ram into the interstellar medium. With analysis of data from the Interstellar Boundary Explorer (IBEX), scientists have argued that the transition from the heliosphere to the interstellar medium is not as abrupt as previously thought, forming a "bow wave" rather than a bow shock at the interface (see McComas et al., 2012).

2.5 Geomagnetic impact of solar wind structures

2.5.1 Geomagnetic indices

The intensity of geomagnetic disturbances driven by solar wind structures is quantitatively defined with various "global" indices, such as Kp, AE (Auroral Electrojet), PC (Polar Cap), Dst (Disturbance Storm Time), etc. Geomagnetic disturbances can be characterized as temporary distortions in the Earth's magnetic field induced by solar wind structures. Two of the most extensively used geomagnetic indices are Kp and Dst.

The planetary Kp index, introduced by Bartels (1949), is a measure of the sub-auroral geomagnetic disturbance on a global scale (Matzka et al., 2021). It is derived based on 3-hour measurements from the standardized K index (or Ks) of 13 ground-based magnetic observatories around the world. Ranging from 0 - 9, values of the Kp index highlight the disturbance of the Earth's magnetic field caused by the solar wind structures.

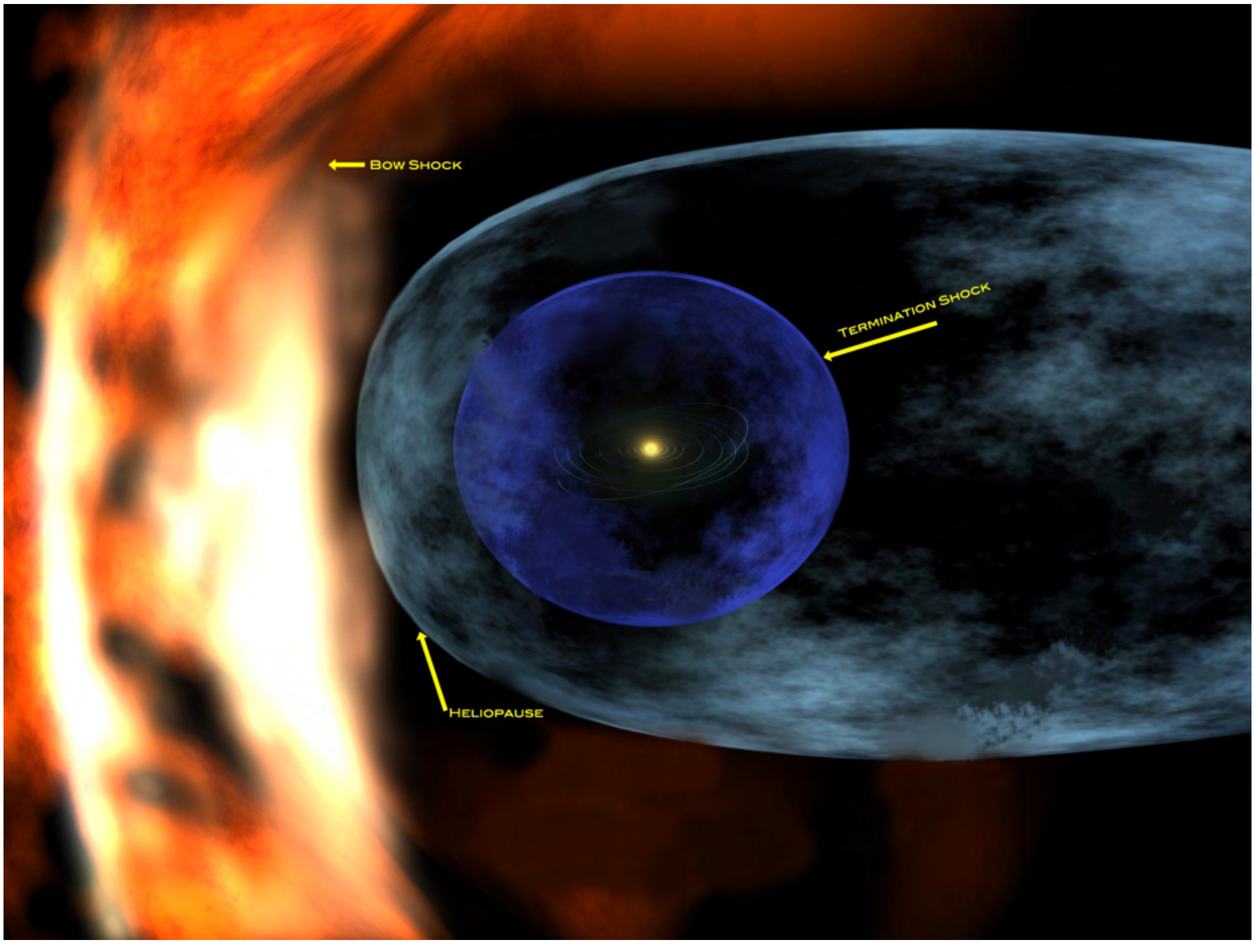

Figure 2.14: Artist's impression of the solar system's boundaries. **Image credit: NASA/GSFC.**

The Dst index provides a measure of the weakening or strengthening of the Earth's equatorial magnetic field. The index measures the growth and recovery of the ring current in the Earth's magnetosphere due to particle injection. Dst is measured in nT and calculated once per hour, based on the average value of the horizontal component of the Earth's magnetic field at four near-equatorial ground-based magnetic observatories. Lower values of Dst indicate a higher amount of energy stored in the Earth's magnetosphere. Gonzalez et al. (1994) defined the intensity of geomagnetic storms (GSs) with the Dst index (weak or minor storm: minimum Dst falls between -30 and -50 nT, moderate storm: minimum Dst falls between -50 and -100 nT, and strong storm: minimum Dst is -100 nT or less). A typical GS manifests in three phases. The onset or initial phase is characterized by an abrupt increase in Dst, also called "storm sudden commencement" (SSC; e.g. Joselyn & Tsurutani, 1990). This is followed by a sharp decrease in Dst (as the ring current intensifies) during the storm's main phase. As the ring current starts to recover (the recovery phase), it is associated with the Dst value gradually returning to its quiet time value (± 20 nT).

2.5.2 Prominent drivers of geomagnetic storms

CMEs and their subset magnetic clouds (MCs) are responsible for the most extreme geomagnetic disturbances (e.g. Zhang et al., 2004; Denton et al., 2006; Echer et al., 2008; Richardson & Cane, 2012). MCs are CMEs that feature enhanced magnetic fields, smooth rotations of the magnetic field vectors, low plasma beta (β, ratio of the plasma thermal pressure to the magnetic pressure), and low proton temperatures (Burlaga et al., 1982).

It was at least one (possibly more) CME, in association with a solar flare that was responsible for one of the most famous and extreme solar events, the "Carrington" event on 1 September 1859 (Carrington, 1859). This massive CME caused one of the largest GSs on record, with estimates suggesting that the Dst amplitude might have been larger than 1000 nT (e.g. Siscoe et al., 2006). Another extreme space weather event on 23 July 2012, observed in-situ by STEREO-A, was caused by interactions between consecutive CMEs. This event would possibly have driven Dst to under -1200 nT had this impacted Earth (e.g. Baker et al., 2013).

The reasons why a CME can drive an intense GS are the following: the southward component of the CME magnetic field may be non-fluctuating, especially strong, and may last for several hours (e.g. Gosling et al., 1990; Brueckner et al., 1998; Huttunen et al., 2005; Ontiveros & Gonzalez-Esparza, 2010). MR of the southward component of the CME's magnetic field with the northward geomagnetic field causes an injection of energized particles into the magnetosphere. Magnetospheric and ionospheric variations triggered through this effect can cause substantial damage to satellites and disruptions of radio communications and air travel. Geomagnetically induced currents (GICs) on the Earth's surface, a byproduct of significant variations of electric currents in the magnetosphere and ionosphere, also pose a serious threat to modern power transmission systems. Figure 2.15 highlights the consequences of solar eruptions in both space and Earth. Important to note that CME-induced disturbances are not only limited to the Earth, as CME-related space weather events have also been observed at Mercury (e.g. Winslow et al., 2017, 2020) and Mars (e.g. Lee et al., 2017).

The occurrence and intensity of CMEs and GSs at various phases of SCys have previously been studied (e.g. Le et al., 2013; Gopalswamy et al., 2015; Li et al., 2018; Alexakis & Mavromichalaki, 2019). As seen in Figure 2.16, CMEs follow the SSN in SCy 23 (1996 - 2008), as the highest number of CMEs occur near the solar maximum of the SSN in 2001, and the lowest number of CMEs correspond to the solar minimum in 2008. For SCy 24, the number of CMEs peak near the double-peak solar maximum in 2012. The number of GSs does not exactly follow the SSN as CMEs. The largest number of GSs are observed to occur in the years 2003 and 2015, not coinciding with the maximums of the SCys. However, during the rising phases of both SCys, GSs tend to follow CMEs, indicating a strong correlation of CMEs and GSs with the SSN in this phase.

Even though SCy 24 represents a significant reduction in the number of CMEs compared to SCy 23, the fraction of MCs in SCy 24 (60%) is significantly larger compared to SCy 23

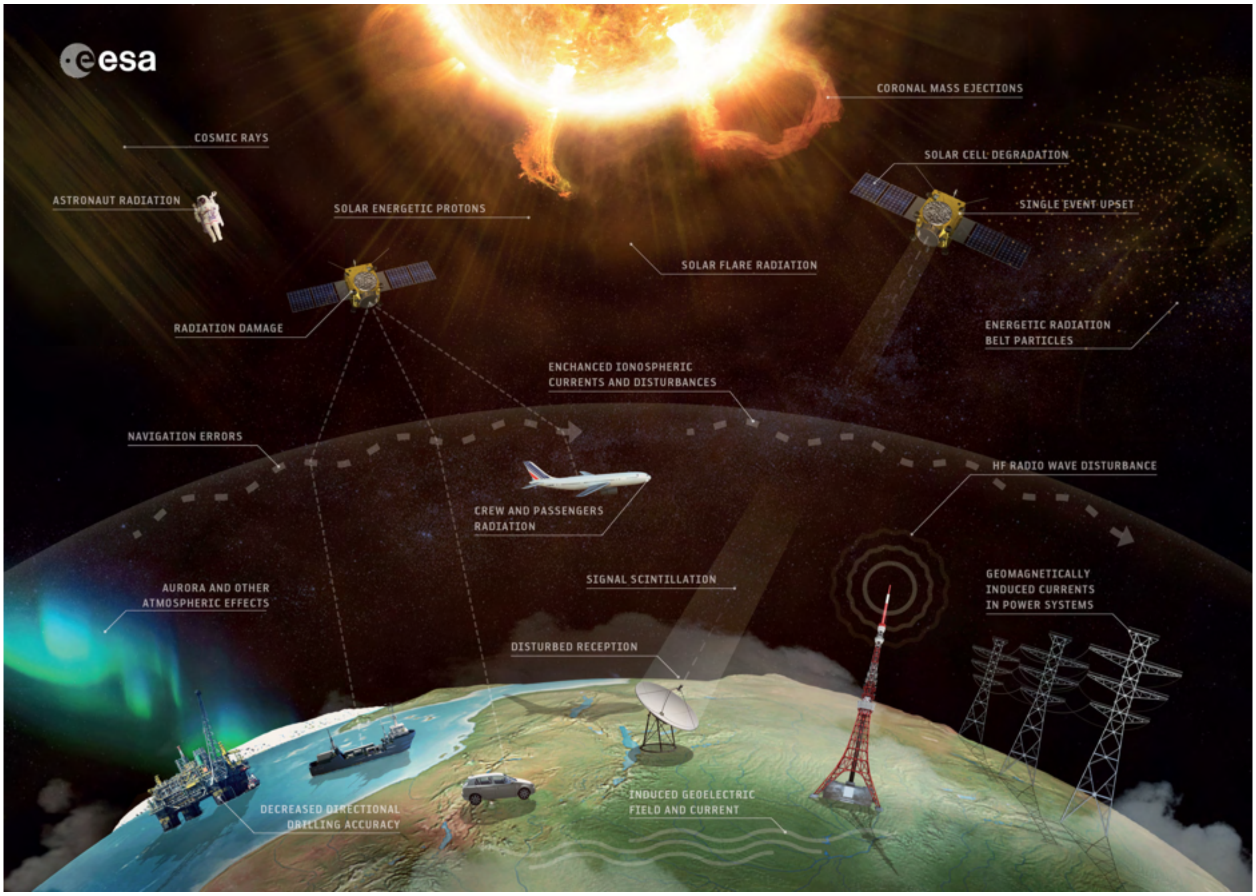

Figure 2.15: Effects on space and ground-based technologies and infrastructures as consequences of solar eruptions. **Image credit: ESA.**

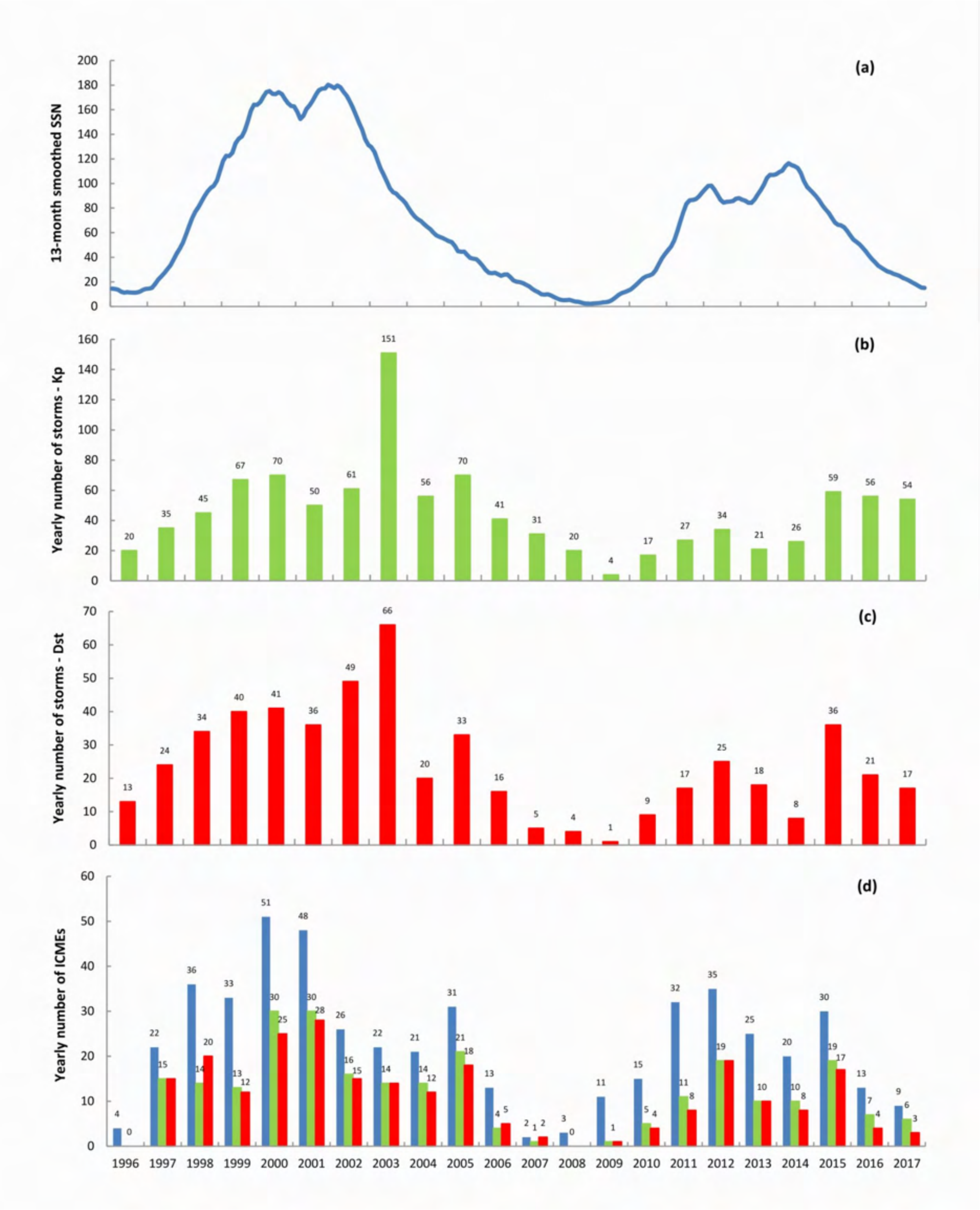

Figure 2.16: Solar cycle evolution of the 13-month smoothed SSN (top panel), the annual number of storms based on the Kp and Dst indices (middle panels), and the yearly counts of CMEs (in blue, bottom panel). In the bottom panel, CMEs associated with geomagnetic storms based on the Kp index are in green, and the Dst index are in red. **Adapted from Alexakis & Mavromichalaki (2019).**

(41%) (see Syed Ibrahim et al., 2019).

SIRs/CIRs are the other notable drivers of geomagnetic disturbances. SIRs/CIRs correspond to weak or moderate storms due to their fluctuating magnetic and velocity fields in the overtaking high-speed stream, consistent with Alfvénic waves (e.g. Tsurutani, 1995; Borovsky & Denton, 2006). SIRs/CIRs with their longer durations and hotter plasma sheets can be more hazardous to SC (i.e., stronger charging), particularly at the geosynchronous orbit than CMEs (e.g. Borovsky & Denton, 2006). The geosynchronous orbit is a low inclination orbit about Earth, located at about $\sim$6.6 R$_e$ (R$_e$ is the Earth's radius), with an orbital period matching the Earth's rotation on its axis. SIRs/CIRs can be associated with several magnetospheric phenomena (i.e., acceleration of radiation belt electrons) as well (see Tsurutani et al., 2006). In addition, interactions with CMEs (i.e., compression at the back of the CME by the following SIR/CIR) can strengthen the southward fields inside CMEs, leading to intense GSs (e.g. Zhang et al., 2007; Richardson, 2018).

CHAPTER 3

Coronal mass ejections: an overview

3.1 Basics of CMEs

Originally termed as “coronal transients,” CMEs are manifestations of instabilities in the corona, leading to eruptions of plasma (on average 10^{15} - 10^{16} g) from the solar atmosphere (e.g. Webb & Howard, 2012; Green et al., 2018). CMEs remove the built-up magnetic flux and helicity over the SCy (Chen, 2017). CME ejected material in the solar wind is a crucial link between solar activity and disturbances in the heliosphere (Liu et al., 2010). CMEs are also one of the most spectacular and energetic forms of solar phenomena, with kinetic energies potentially exceeding 10^{25} joules (e.g. Hudson et al., 2006). The largest kinetic energy related to a CME has been approximated to be 10^{26} joules for the Halloween CME on 28 October 2003 (Gopalswamy et al., 2005). Depending on the phase of the SCy, on average, 1 (solar minimum) to 5 (solar maximum) CMEs can form per day at the Sun (Webb & Howard, 2012). It can take 1 - 5 days for a CME to reach Earth. In IP space, CMEs can be identified with a range of in-situ signatures, like enhanced magnetic fields (>10 nT) and rotations (>30°) of the field components (e.g. Burlaga et al., 1982), discontinuities (tangential) at CME boundaries (e.g. Janoo et al., 1998), reductions in the magnetic field variability (e.g. Klein & Burlaga, 1982), low proton temperatures and densities (e.g. Richardson & Cane, 1995), enhanced ion charge states (e.g. Lepri et al., 2001), etc. Even with such a plethora of signatures, the exact definition of a CME structure in the solar wind is unambiguous, as these characteristic signatures do not co-occur for every CME. There can also be CMEs that lack some of the most ubiquitous signatures. Therefore, CME identification “is still something of an art" (Gosling, 1997).

3.2 Origins of eruption and early phase

The eruptions of CMEs are associated with magnetic structures that span a range of spatial scales (see Green et al. (2018) for a review on observations and physical mechanisms behind CME eruptions). CMEs can originate from both quiescent regions (in associations with filament eruptions) and ARs (in close associations with solar flares) in the corona (e.g. Gosling et al., 1974; Manchester et al., 2017). The origins of CMEs manifest signs of SCy dependence. At solar minimum, CMEs erupt more often from streamer blowouts and quiescent filament eruptions at low latitudes. In contrast, at solar maximum, the source regions of high latitude eruptions are likely to be ARs (see Manchester et al., 2017).

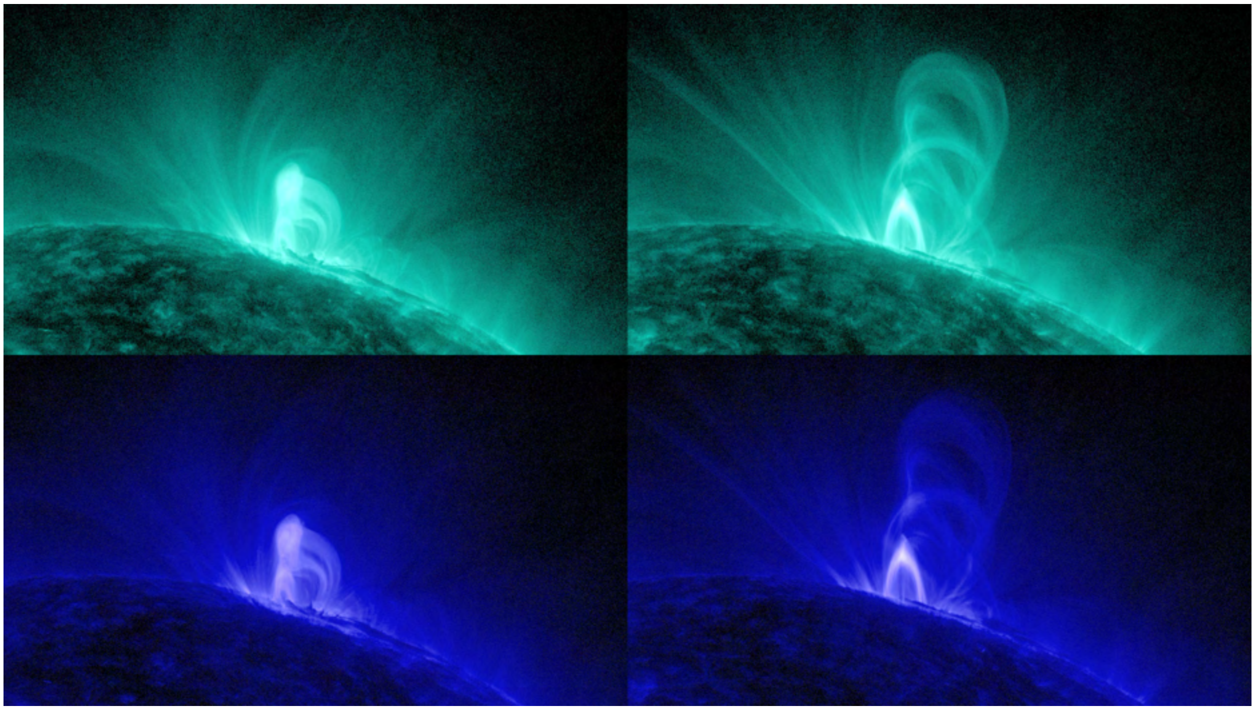

Figure 3.1: Formation and temporal evolution of a FR responsible for the CME eruption on 19 July 2021, in 131 Å wavelength standard coloration (top panels) and hue-shifted images (bottom panels). **Image credit: NASA/SDO.**

The current consensus is that CMEs erupt from the solar atmosphere as helical magnetic structures called "flux ropes" (FRs; e.g. Vourlidas et al., 2013; Green et al., 2018), see an example in Figure 3.1. Due to interactions with the background solar wind during propagation and large crossing distances of the measuring spacecraft from the center of the FRs (e.g. Kilpua et al., 2011), clear FR configurations may not always be unambiguously observed in-situ. However, there is less consensus regarding the exact onset mechanism of CMEs. Over many decades, numerous initiation mechanisms have been explored with observations and numerical simulations. Such observations of the onset and evolution of the eruption have formed the basis of a standard model for a CME or an eruptive flare, called the "CSHKP model" (Carmichael, 1964; Sturrock, 1966; Hirayama, 1974; Kopp & Pneuman, 1976). This model connects MR to the eruptions of solar flares and CMEs.

The general concept of CME eruption is attributed to a coronal magnetic arcade (series of arch-like magnetic field lines), embedding a sheared arcade or FR (e.g. Chen, 1989; Török & Kliem, 2005). The destabilization of the coronal magnetic arcade essentially triggers the onset mechanism (see Biskamp & Welter, 1989). This destabilization can occur as a result of instabilities, like the "kink" instability (e.g. Török et al., 2004; Török & Kliem, 2005) or the "torus" instability (e.g. Aulanier et al., 2010). This results in an outwards expansion of the arcade and the formation of a radial current sheet (see an example in Figure 3.2). MR at this current sheet builds poloidal flux around the erupting arcade and cuts the tethers of the overlying restraining field (e.g. Moore et al., 2001; Lynch et al., 2004) initiating the eruption of the formed twisted FR structure.

The eruption is preceded by a slow rising motion of the pre-eruptive structure (initiation phase), continued by a rapid increase in its speed as the free magnetic energy accelerates the large-scale structure into the upper corona (acceleration phase), that is followed by a smooth propagation phase as the CME is ejected from the corona (see Zhang & Dere, 2006). However, for more compact AR structures, the slow rising phase can be rapid, taking as little as just a few minutes (e.g. Zharkov et al., 2011).

The Lorentz force governs the early stages of CME propagation close to the Sun, which results

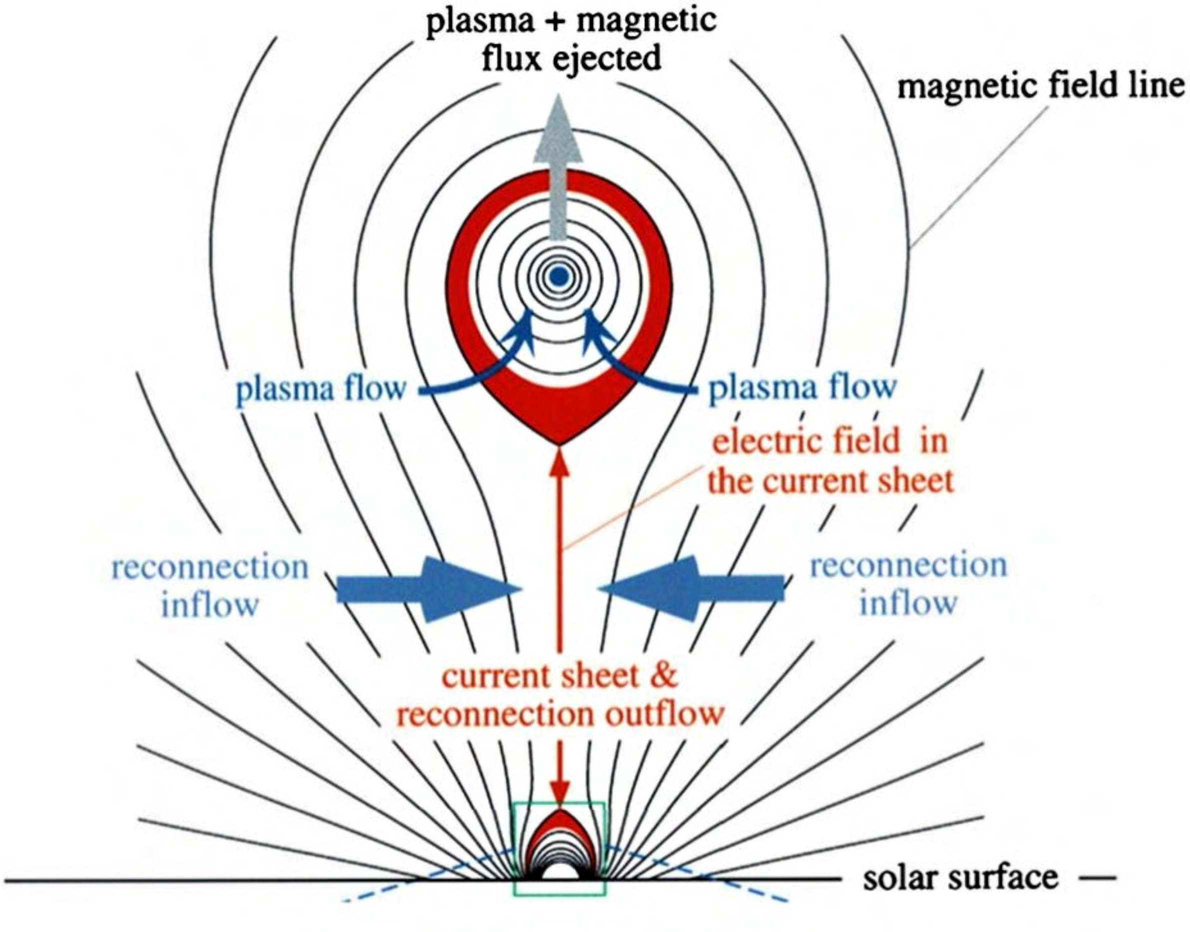

Figure 3.2: Schematic of the formation of a current sheet and magnetic reconnection beneath the erupting FR structure. **Adapted from Webb & Vourlidas (2016).**

from the non-uniform expansion of the magnetic field in high pressure-stratified atmosphere (Manchester, 2007). This Lorentz force (see Equation 3.1) is also responsible for launching and accelerating the CME (e.g. Vršnak et al., 2004).

$$\mathbf{j} \times \mathbf{B} = \frac{1}{\mu_0}\,(\nabla \times \mathbf{B}) \times \mathbf{B} = \frac{1}{\mu_0}\,(\mathbf{B} \cdot \nabla)\mathbf{B} \text{ - } \nabla\,\frac{B^2}{\mu_0} \tag{3.1}$$

Here, $\mathbf{j}$ is the electric current density, $\mathbf{B}$ is the magnetic field vector, μ_0 is the magnetic permeability of vacuum. The first term on the right is the magnetic tension that acts as a restoring force against the bending of magnetic field lines, and the second term is known as the magnetic pressure. In Equation 3.1, any gradient in the field will produce a force (expanding or compressing). These two components of the Lorentz force play an essential role in the CME eruption.

Close to the Sun, CMEs have typical latitudinal widths of 30 - 65°, with radial speeds in the range of 200 - 3000 $\mathrm{km\,s^{-1}}$ (speeds range from 300 - 1000 $\mathrm{km\,s^{-1}}$ near 1 AU), and accelerations of the order of 0.1 - 10 $\mathrm{m\,s^{-2}}$ (e.g. Vourlidas et al., 2010). A CME's angular width, estimated from remote-sensing observations is only the projected width in the sky plane. Therefore, it can be constrained by projection and geometric effects and does not represent its actual width (see Zhao et al., 2017; Lamy et al., 2019). Impulsively ejected CMEs, originating from ARs with strong magnetic fields start accelerating at low heights (e.g. Vršnak et al., 2007; Bein et al., 2011) and may accelerate up to speeds of $\sim$3000 $\mathrm{km\,s^{-1}}$ (e.g. Möstl et al., 2014). CMEs originating from huge quiescent prominences can also reach higher speeds of $\sim$1000 $\mathrm{km\,s^{-1}}$ (Vršnak et al., 2005). However, it has been argued that it is impossible for CME speeds to exceed $\sim$4000 $\mathrm{km\,s^{-1}}$ because of the limit on the maximum free energy that can be stored in solar ARs (e.g. Gopalswamy et al., 2010).

3.3 Observational aspects

Compared to geomagnetic storms (discovered in the 1700s) and solar flares (discovered in the 1800s), CMEs are a recently discovered phenomenon (at the beginning of the 1970s) (Gopalswamy, 2016). However, before the first detection of a CME on 14 December 1971 with the seventh Orbiting Solar Observatory (OSO-7) of the Naval Research Laboratory, ejections of magnetized plasma from the Sun were hypothesized with the detection of radio bursts and shock waves.

Early knowledge of CMEs was mainly accumulated with white-light coronagraph observations. In coronagraphs, CMEs are detected via Thomson-scattered photons as outward moving structures with a higher electron density than the background corona (Gosling et al., 1974). CMEs entered the modern era of observations with the "Apollo Telescope Mount" (ATM) coronagraph onboard Skylab (Gosling et al., 1974). After that, the Solwind coronagraph onboard the Air Force satellite P78-1 (Howard et al., 1985) provided an early detailed view (with observations of $\sim$1700 CMEs), including the discovery of the "Halo" CME. Halo CMEs are interpreted as CMEs that form near the center of the solar disc, either in the front or back hemisphere of the Sun (Howard et al., 1982). Some other CMEs, named "stealth" CMEs, originate at altitudes higher than 0.1 R_s in the corona without noticeable signatures and show no observational white-light signatures in the lower atmosphere (see Robbrecht et al., 2009). Apart from coronagraphs, CME signatures are also observed in radio bursts, EUV and X-ray wavelengths, and other non-coronagraphic observational techniques (see Hudson & Cliver, 2001).

Some other CMEs, named "stealth" CMEs, originate at altitudes higher than 0.1 R_s in the corona without noticeable signatures and show no observational white-light signatures in the lower atmosphere (see Robbrecht et al., 2009).

Exponential progress in the observational aspects of CMEs (see Webb & Howard (2012) for a review on CME observations) have been made possible by the unprecedented observations

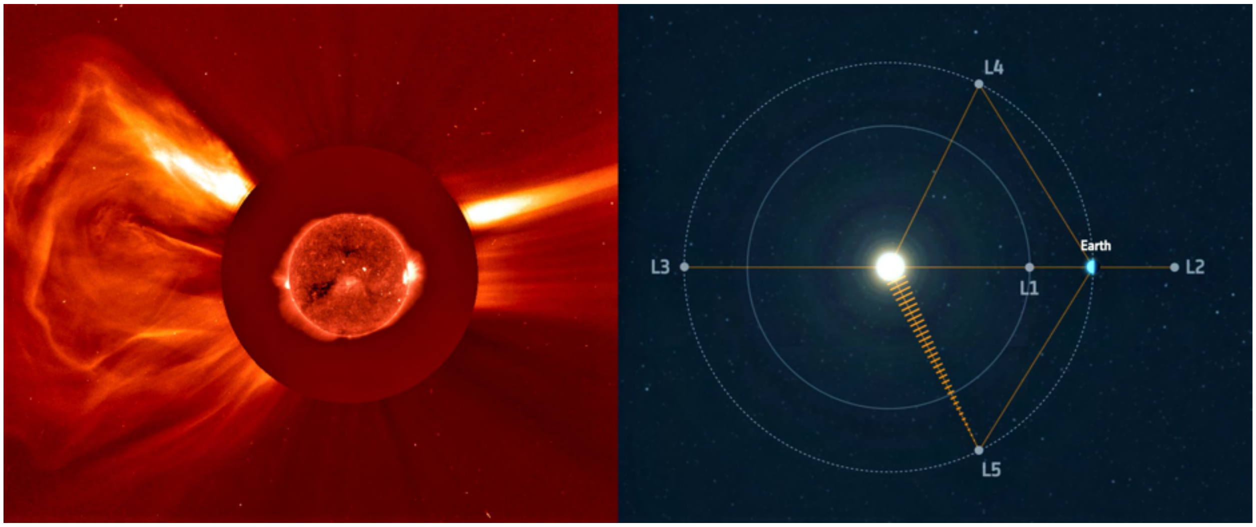

Figure 3.3: Left panel: A CME seen in SOHO's LASCO C2 coronagraph on 24 January 2006 **Image credit: NASA.** Right panel: The five Lagrangian points of gravitational stability (SOHO is located at L1) in the Sun-Earth system. **Image credit: ESA.**

provided by the Large Angle Spectroscopic Coronagraph (LASCO; Brueckner et al., 1995), onboard the Solar and Heliospheric Observatory (SOHO) spacecraft (see an example of CME observation with the LASCO coronagraph on the left panel in Figure 3.3) and the Sun Earth Connection Coronal and Heliospheric Investigation (SECCHI; Howard et al., 2008) that includes the inner coronagraph COR1, the outer coronagraph COR2, and the two heliospheric imagers (HIs; see Harrison et al. (2017) for a review on heliospheric imaging), on board the two Solar Terrestrial Relations Observatory (STEREO; Kaiser, 2005) spacecraft. In the pre-SOHO era, the simplest configuration of a CME in remote-sensing images was the so-called three-part structure (see Figure 3.4), with a bright frontal rim enclosing a dark low-density cavity that contains a high-density bright core of prominence material (e.g. Hundhausen, 1993). CME-driven shock fronts are not included in this traditional structure, which is now routinely identified with the improved sensitivity of SOHO and STEREO coronagraphs.

Before the launch of STEREO, most modern-day CME observations were primarily constrained to two domains: near-Earth spaceborne observations extending out to 30 R_s and in-situ measurements near L1 (the first Lagrangian point, located on the Sun-Earth line,

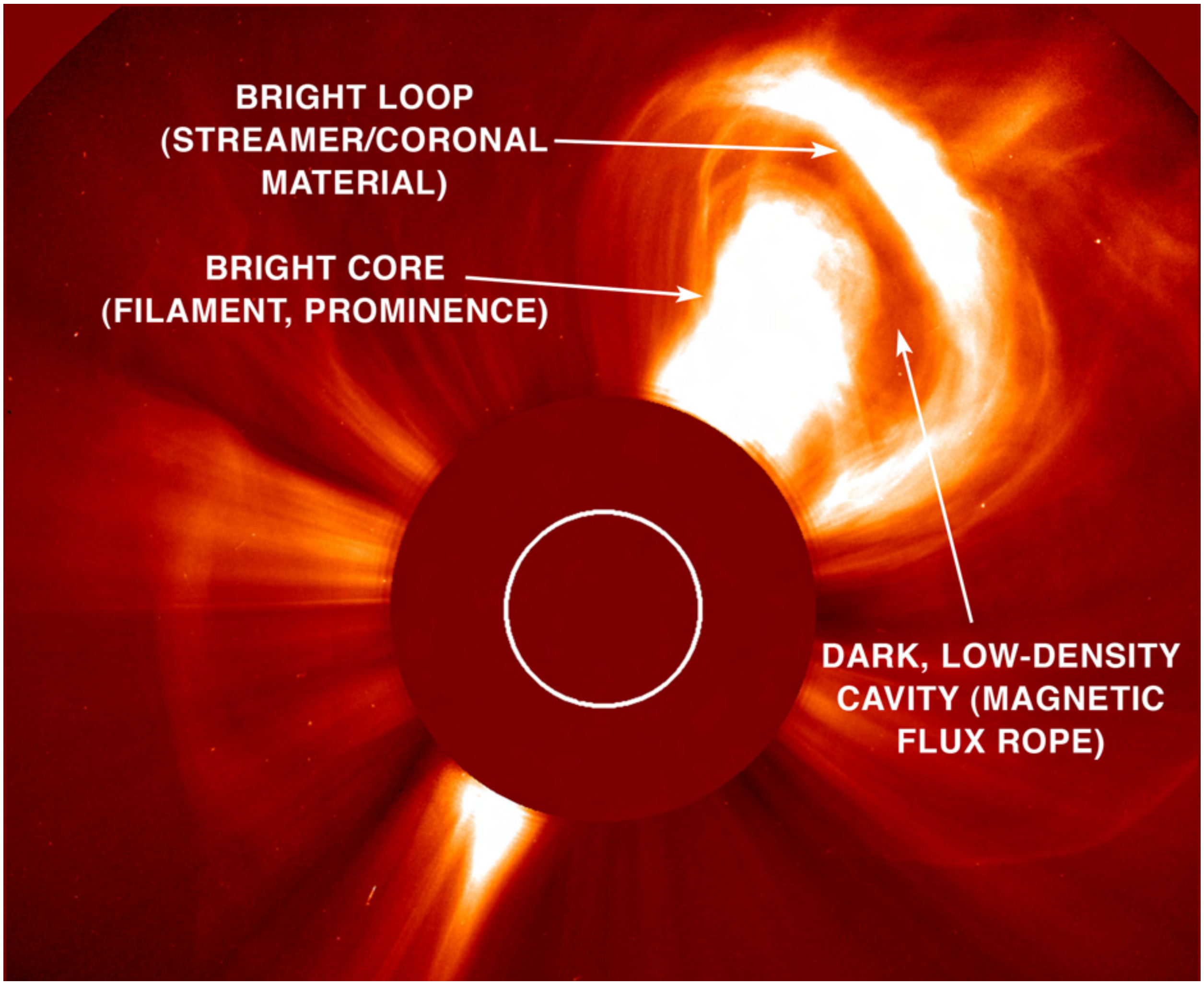

Figure 3.4: A classic three-part structure of a CME. **Image credit: Naval Research Laboratory.**

at a distance of 1.5×10^6 km from the Earth's center, see on the right panel in Figure 3.3). With the launch of STEREO in 2006, CMEs have been routinely observed from the Sun to the Earth, combining observations from extreme ultraviolet imager (EUVI: range of 1 - 1.7 R_s), coronagraphs (COR1: observes white-light ranging from 1.5 - 4 R_s and COR2: observes white-light ranging from 2.5 - 15 R_s, see on the left panel in Figure 3.5 for an example of CME observation with COR2), and HIs (HI-1: range of 15 - 84 R_s and HI-2: range of 66 - 318 R_s, see on the right panel in Figure 3.5 for an example of CME observation with HI-1) onboard the twin STEREO spacecraft (Harrison et al., 2005; Howard et al., 2008; Davis et al., 2009; Harrison et al., 2018). Therefore, these instruments, coronagraphs, and HIs can image a CME in its entirety, all the way from the Sun to 1 AU.

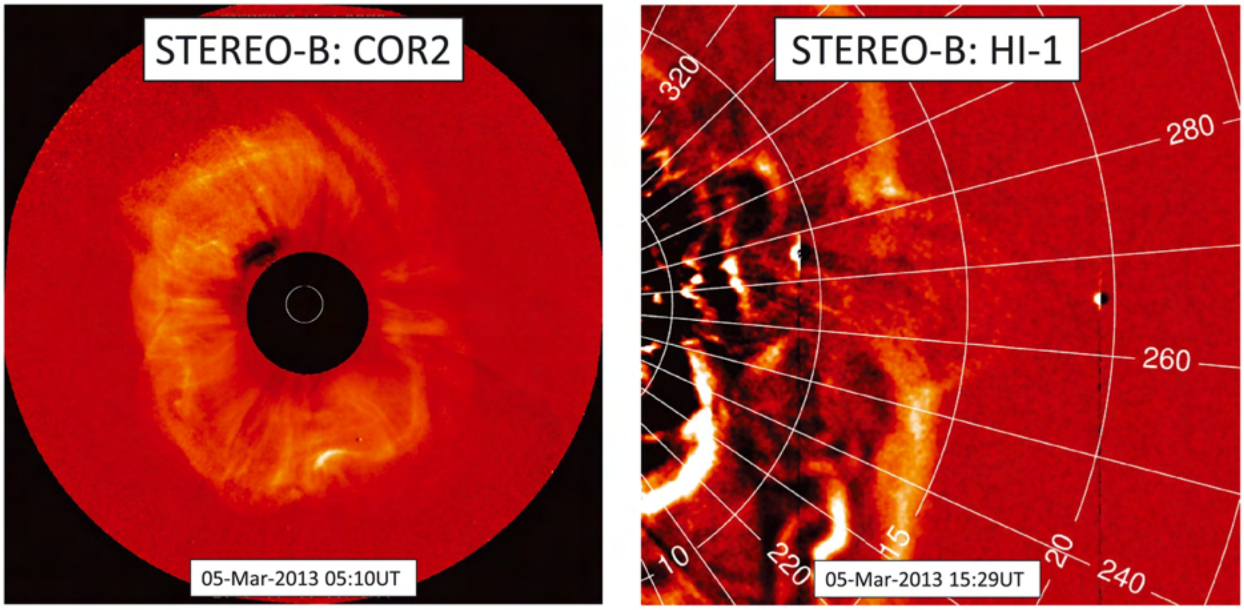

Figure 3.5: STEREO-B observation of a Halo CME on 5 March 2013 with a COR2 difference image at 05:10 UT (left) and a HI-1 difference image of the western portion of the halo event at 15:29 UT (right). **Adapted from Harrison et al. (2017).**

3.4 Heliospheric propagation

As the CMEs propagate anti-sunward in the heliosphere, they are observed to maintain approximately constant angular widths (Zhao et al., 2017). The heliospheric environment significantly influences CMEs that they propagate in (e.g. Temmer et al., 2011; Kilpua et al., 2012), leading to changes in speeds, shapes, and orientations. Global features of CMEs in the heliosphere can significantly deviate from their initial configurations, owing mainly to the interactions with the structured background solar wind (e.g. Owens, 2006; Savani et al., 2010). However, the biggest changes in CME speeds and orientations are thought to occur in the corona (e.g. Vourlidas et al., 2011; Isavnin et al., 2014).

CME propagation in the heliosphere is shaped by two dynamic processes: the expansion of the CME and its interaction with the background solar wind (see Manchester et al. (2017) for a review on the heliospheric evolution of CMEs). As the solar wind pressure decreases with heliocentric distance, the approximate pressure balance between the CME with its surrounding solar wind induces CME expansion (Démoulin & Dasso, 2009; Gulisano et al., 2010). In IP space, CME expansion is characterized by an almost linear decrease in the solar wind speed during the spacecraft passage through the CME (e.g. Lepping et al., 2008; Gulisano et al., 2010; Masías-Meza et al., 2016; Rodriguez et al., 2016). However, the lateral expansion of the CME can happen at a faster rate than the radial expansion (e.g. Russell & Mulligan, 2002; Leitner et al., 2007; Gulisano et al., 2012; Nieves-Chinchilla et al., 2018), which can lead to the deformation of the CME cross-section (see Vršnak et al., 2019).

Deformations of CME shapes can also occur because of the interactions with the solar wind. The spherical geometry of the solar wind gives rise to pressure gradients that make FRs develop a convex-outward "pancake" shape (see Riley & Crooker, 2004). Numerical ideal magnetohydrodynamic (MHD) simulations have also seen the magnetic field structure of MCs to kink and deform (e.g. Manchester et al., 2004). Furthermore, in many instances, CME expansion in the non-radial direction may be faster than the local Alfvén speed, leading to localized deformations, as the information of interaction on a given CME segment does not reach its distant segments (e.g. Temmer et al., 2014; Ala-Lahti et al., 2020; Owens, 2020).

Interaction with the background solar wind can cause CME speed to change significantly (e.g. Temmer et al., 2011; Liu et al., 2013). The Lorentz force becomes negligible at larger heliocentric distances, and the MHD drag mainly drives the CME dynamics. The acceleration caused by this MHD drag (a, see Equation 3.2) has a quadratic dependence on the CME speed relative to the background solar wind (e.g. Vršnak & Gopalswamy, 2002; Cargill, 2004).

$$a = -\ \gamma\ (v\ \text{-}\ w)\ |v - w| \tag{3.2}$$

Here, "γ" is the drag parameter, v is the CME speed, and w is the background solar wind speed (see Vršnak et al., 2013).

The drag parameter can be expressed as the following:

$$\gamma = \frac{c_d A \rho_w}{M + M_V} \tag{3.3}$$

Here, c_d is the dimensionless drag coefficient (see Cargill, 2004), A is the CME cross-sectional area, ρ_w is the ambient solar wind density, M is the CME mass, and M_V ($\sim \rho_w V/2$, V is the CME volume) is the so-called virtual CME mass.

As seen in Equation 3.3, the MHD drag depends on the CME geometry and density (see Vršnak et al., 2010). The influence of MHD drag results in fast CMEs, those with propagation speeds above that of the background solar wind to decelerate, whereas slow CMEs, with propagation speeds below the solar wind get accelerated up to the solar wind speed (e.g. Vršnak et al., 2004; Maloney et al., 2009).

Kinematic interactions in the heliosphere can also affect the radial propagation of CMEs by causing longitudinal deflections. CME deflection can be characterized as a departure from an expected radial trajectory. Even though CME FR deflection predominantly occurs below 10 R_s (e.g. Kay et al., 2015; Isavnin et al., 2014), a significant amount of deflection can also occur in the IP space (e.g. Rodriguez et al., 2011; Isavnin et al., 2014). The influence of deflection on an otherwise radial trajectory is important because a deflection toward the Sun-Earth line can make a CME more geoeffective (Gopalswamy, 2016). The global magnetic patterns surrounding the eruption regions (e.g. Filippov et al., 2001; Kilpua et al., 2009; Gui et al., 2011; Kay et al., 2013; Möstl, 2015) and the background solar wind flow patterns (e.g. Cremades et al., 2006) can be attributed to CME deflections near the Sun. In IP space, kinematic interactions are primarily responsible for longitudinal deflections (e.g. Wang et al., 2004, 2014; Manchester et al., 2017). Wang et al. (2004) suggested that longitudinal deflections of CMEs can be explained by the interactions with the Parker-spiral-structured solar wind.

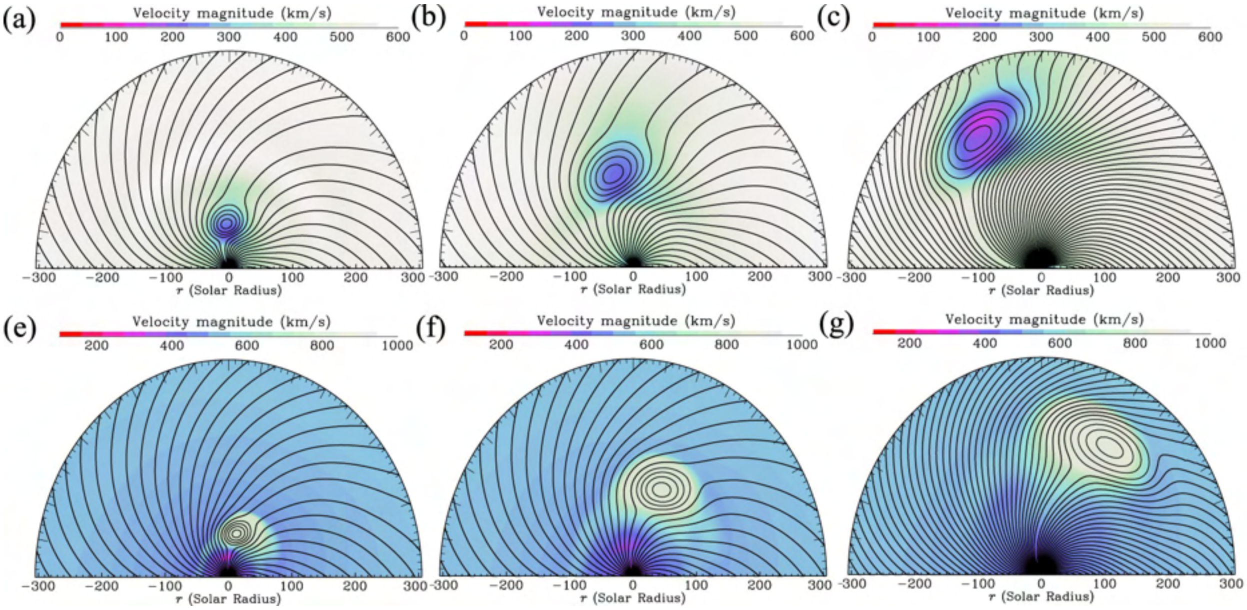

Figure 3.6: 2.5D ideal MHD simulation showing (in the laboratory frame) westward deflection of a slow FR, propagating with a constant radial speed of 300 $\mathrm{km\,s^{-1}}$ (top panels, a-c) and eastward deflection of a fast FR, propagating with a constant radial speed of 1500 $\mathrm{km\,s^{-1}}$ (bottom panels, e-g). Panels (c) and (g) plot the background magnetic field lines with denser contour curves. The closed lines plot the flux rope structure, and the open lines show the background magnetic field. The false-color shows the flow velocity magnitude. **Adapted from Zhuang et al. (2019).**

Slow CMEs are deflected westward when pushed from behind by the faster solar wind, whereas fast CMEs deflect eastward as they are decelerated by the slow solar wind ahead (e.g. Gosling et al., 1987). The same has also been reported by (Zhuang et al., 2019) with an ideal 2.5 MHD simulation (see Figure 3.6). In addition to longitudinal deflections, CMEs can be deflected in latitudinal directions (e.g. Kilpua et al., 2009; Zhou & Feng, 2013; Isavnin et al., 2014; Manchester et al., 2017). Deflection in latitude primarily occurs close to the Sun, in the proximity of the streamer belts (Manchester et al., 2017). At the Sun, latitudinal deflections can occur due to the polar CH fields, guiding CMEs from high-latitude source regions towards the equator (e.g. Kilpua et al., 2009).

Another aspect of CME propagation in the heliosphere is CME-CME interaction that involves a faster CME overtaking a slower CME (see Lugaz et al. (2017b) for a review on the interactions of CMEs). CME-CME interactions can be responsible for delayed arrivals as consequences of interactions with preceding CMEs (e.g. Manoharan et al., 2004; Temmer et al., 2012). CME-CME interactions are also responsible for longitudinal deflections in the heliosphere (e.g. Lugaz et al., 2012; Shen et al., 2013). The resulting structures at 1 AU as a result of CME-CME interactions can be a multiple-MC event (see on the top left panel in Figure 3.7) where a denser sheath precedes the multiple distinct MCs (e.g. Farrugia et al., 2006), long-duration event (see on the top right panel in Figure 3.7), possessing many of the characteristics of an individual CME (e.g. Dasso et al., 2009; Lugaz & Farrugia, 2014), complex event (see on the bottom left panel in Figure 3.7) where the interacting CMEs cannot be distinguished in-situ (e.g. Burlaga et al., 2003), to name a few. In addition, extreme geomagnetic effects are expected to be related to interacting CMEs occurring in close succession (e.g. Liu et al., 2014; Lugaz et al., 2017b). A different form of interaction often seen in IP space is shown on the bottom right panel in Figure 3.7 where a fast shock propagates within a CME. Such shocks are often observed at the back of the CME.

During propagation, CMEs can also interact with high-speed streams (HSSs), SIRs/CIRs, and the HCS (e.g. Burlaga et al., 1987; Farrugia et al., 2011; Temmer et al., 2011; Vršnak et al., 2013; Winslow et al., 2016; He et al., 2018; Heinemann et al., 2019; Liu et al., 2019; Winslow et al., 2021a,b). HSSs are much faster than the typical solar wind. They can

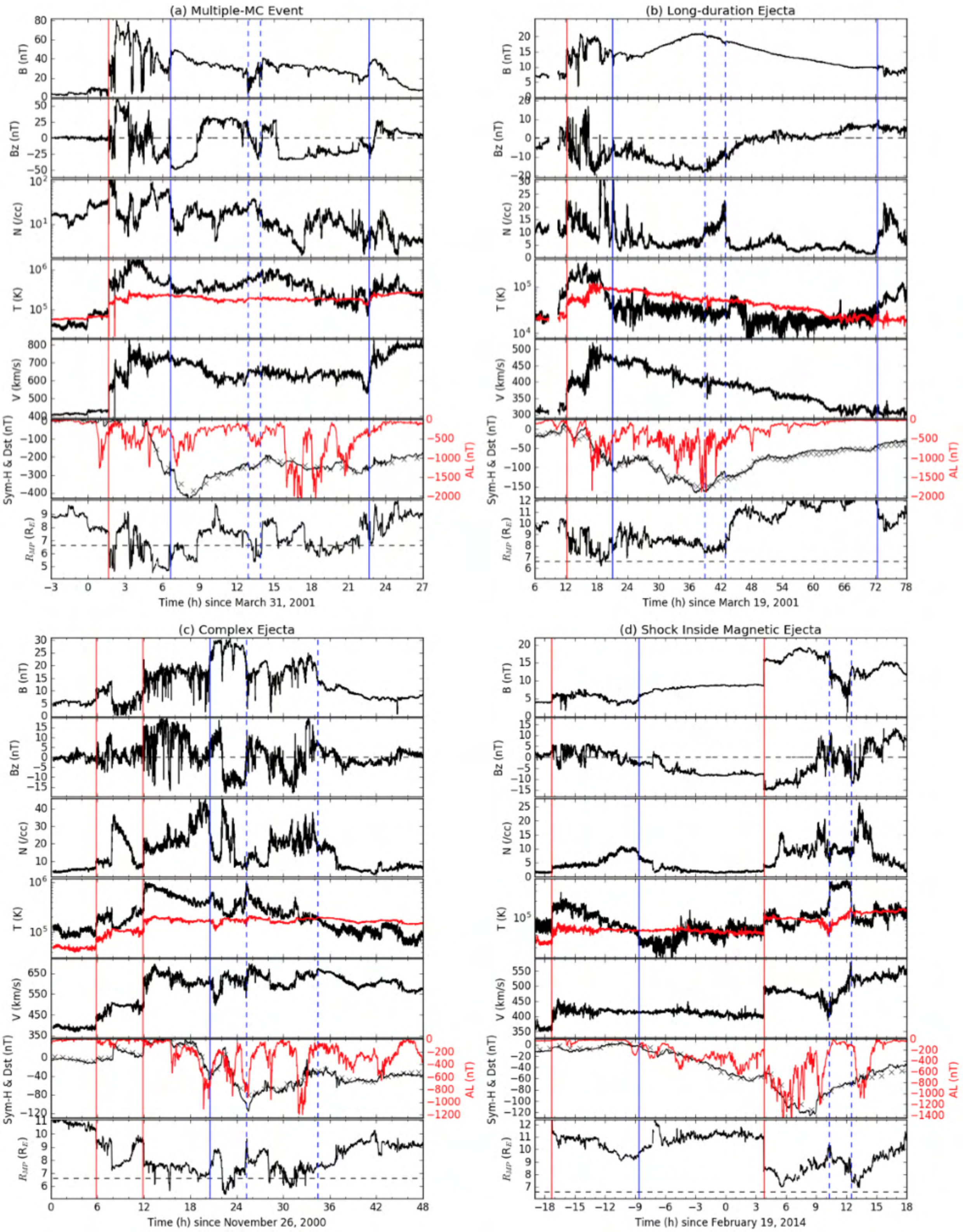

Figure 3.7: In-situ measurements of CME-CME interaction. Shocks are marked with red lines, and CME boundaries with blue lines (dashed for internal boundaries). **Adapted from Lugaz et al. (2017b).**

significantly affect the motion and shape of CMEs, weakening the drag and consequent deceleration for fast CMEs and strengthening the drag and consequent acceleration for slow CMEs (e.g. Temmer et al., 2011; Winslow et al., 2021a). Compound streams due to interactions with SIRs and HCS can also lead to substantial complexities in CME in-situ signatures (e.g. Winslow et al., 2016, 2021b) and intensified geomagnetic activity (e.g. Burlaga et al., 1987; Farrugia et al., 2011).

Apart from the aforementioned consequences of interactions, MRs between the front of the CMEs and the ambient IMF can peel off the outer magnetic flux of CMEs, causing the magnetic topology at the back of the CMEs to differ from the rest of the CME substantially (see McComas et al., 1998; Dasso et al., 2006; Ruffenach et al., 2012; Lavraud et al., 2014; Ruffenach et al., 2015). Such erosion can also lead to a decrease in the geoeffectiveness of a CME with the removal of southward oriented magnetic flux (e.g. Lavraud et al., 2014). However, erosions can also occur at the rear boundaries of CMEs (see Ruffenach et al., 2015).

The last aspect of the coronal and heliospheric propagation of CMEs is rotation. The estimate of CME rotation is obtained by comparing the orientation of the pre-eruptive structure on the Sun and the orientation of the axis of its IP counterpart (Manchester et al., 2017). CME rotation is primarily expected to occur in the low corona (e.g. Thompson, 2011), but it can persist at larger coronal heights or even in IP space (e.g. Lynch et al., 2010; Vourlidas et al., 2011; Nieves-Chinchilla et al., 2012; Thompson et al., 2012). Moderate rotations ($\sim$10°) are a common context in erupting FRs (e.g. Török et al., 2010). However, significantly larger values of CME rotations ($\sim$100°) have also been reported (e.g. Isavnin et al., 2014; Liu et al., 2016), including a rotation of almost 180° with a 3-Dimensional (3D) MHD simulation (see Fan, 2016). Since the interaction with the Earth's magnetosphere depends on the magnetic orientation of a CME, it is important to understand the physical mechanisms behind CME rotations to estimate the amount of rotation a CME can undergo during its propagation. Observational and numerical studies have suggested a substantial number of mechanisms, such as external shear (e.g. Isenberg & Forbes, 2007; Kliem et al., 2012), straightening of an initially strong FR (S-shape) during its eruption (e.g. Török et al., 2010; Kliem et al., 2012), MR (e.g. Cohen et al., 2010; Lugaz et al., 2011; Winslow et al., 2016), alignment of the CME FR with the HCS (e.g. Yurchyshyn, 2008), that can be responsible for a CME to rotate about its direction of propagation.

3.5 Modeling of CMEs

In a hypothetical timeline, with hundreds of spacecraft around the heliosphere, especially on the Sun-Earth line, modeling of CMEs will be considered an afterthought. Coming back to reality, with a limited number of spacecraft in the heliosphere and an even lesser number focused on the science of CMEs, mathematical modeling provides a virtual reality of CMEs. CME models have transitioned from qualitative "cartoon" models to analytical and semi-analytical and then to idealized MHD models in the past few decades. In the future, with machine learning (ML) algorithms (see Camporeale (2019) for a review on future challenges of ML) and parallel computing, hopefully, CME modeling approaches will be able to catch up with the predicted advancement in CME observations.

A broad spectrum of models is employed to model and forecast the heliospheric propagation of CMEs (see Vourlidas et al. (2019) for a review on the current status and open issues regarding CME modeling). Empirical methods in the pre-STEREO era were based on relationships between the measured CME parameters by remote observations and in-situ measurements (e.g. Brueckner et al., 1998; Gopalswamy et al., 2000, 2001; Vršnak & Gopalswamy, 2002; Manoharan et al., 2004; Michalek et al., 2004; Schwenn et al., 2005). This method was based on an average CME deceleration or acceleration between the Sun and the Earth, derived from the estimated CME speed via coronagraph observations and in-situ measured CME speed and transit time. However, this method was constrained by projection effects of white-light observations and uncertainties of CME evolution beyond the coronagraphic field of view (FOV, see Vourlidas et al., 2019). In the STEREO era, empirical methods are primarily based on 3D reconstructions of Earth-directed CMEs throughout the full SECCHI

FOV, although other modeling techniques are also used (e.g. Colaninno et al., 2013; Möstl et al., 2014; Rollett et al., 2016; Hess & Zhang, 2017; Möstl, 2017).

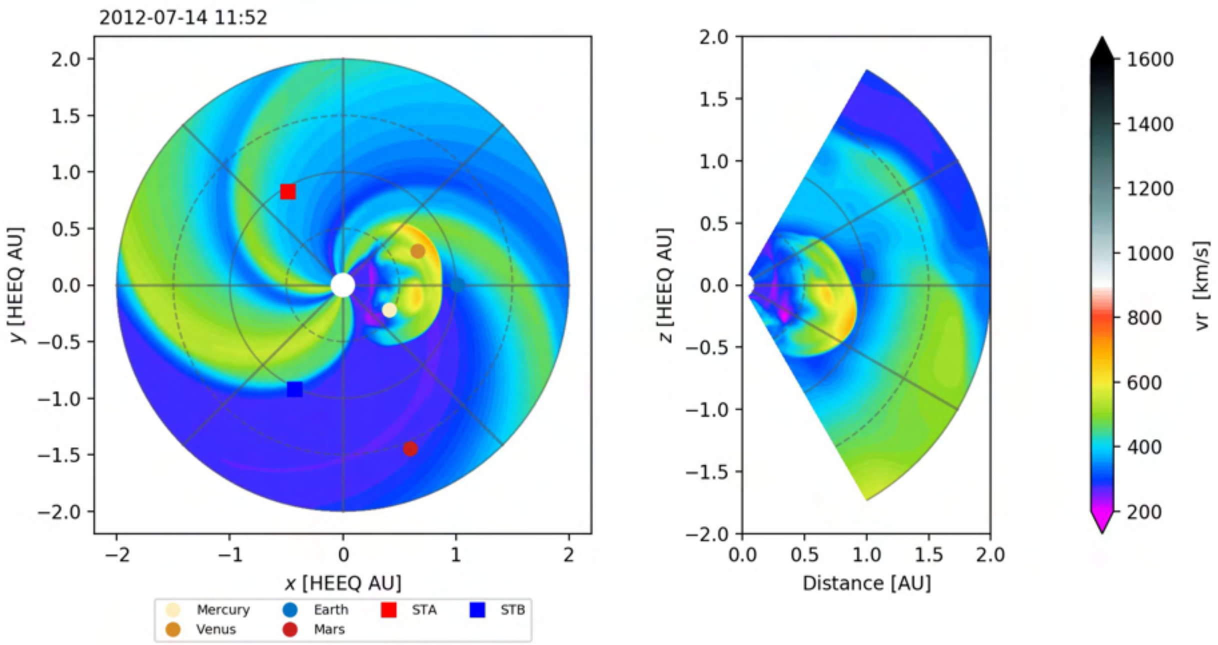

Figure 3.8: Snapshot (on 14 July 2012 at 11:52 UT) of the radial speed simulation of the 12 July 2012 Earth-directed CME with EUHFORIA (using the linear force-free spheromak CME model) in the heliographic equatorial plane (left) and in the meridional plane that includes the Earth (right). **Adapted from Scolini et al. (2019).**

A drawback of empirical methods is that these methods can not consider the background heliosphere's state, which is possible with MHD models (see Vourlidas et al., 2019). The majority of the MHD-based methods model the heliospheric propagation of CMEs or CME-driven shocks through a pre-determined inner heliospheric state, using CME input parameters close to the Sun (e.g. Groth et al., 2000; Fry et al., 2003; Odstrčil et al., 2003; Manchester et al., 2004; Odstrčil et al., 2004; Lugaz et al., 2005; Odstrcil et al., 2005; Taktakishvili et al., 2009; Shiota & Kataoka, 2016; Pomoell & Poedts, 2018; Riley, 2018; Wold et al., 2018; Scolini et al., 2019). Figure 3.8 illustrates a MHD model of CME simulation, EUropean Heliospheric FORecasting Information Asset (EUHFORIA, see Pomoell & Poedts, 2018) that uses parameters derived from remote-sensing observations for the model initiation.

In between the empirical and computational-expensive numerical MHD-based models, there is a class of “semi-empirical” models that combine CME parameters derived from observations with geometrical and physics-based approaches, like the 3DCORE (Möstl et al., 2018), to either model the full propagation of the CME FR (e.g. Isavnin, 2016; Möstl et al., 2018) or to simulate the Earth’s trajectory through the FR structure (e.g. Savani et al., 2015; Kay et al., 2017) by using remote observations to fit the FR type (e.g. Bothmer & Schwenn, 1998; Palmerio et al., 2017). The most commonly used semi-empirical model is the Wang-Sheeley-Arge (WSA; Wang & Sheeley Jr., 1990) model.

There is also a class of analytical, MHD- or HD-based, kinematical models of CME propagation, based on the drag forces (viscous, aerodynamic, hybrid) that a CME experiences in IP space (e.g. Cargill, 2004; Owens & Cargill, 2004; Subramanian et al., 2012; Vršnak et al., 2013; Hess & Zhang, 2015; Sachdeva et al., 2015; Dumbović et al., 2018b; Napoletano et al., 2018; Braga et al., 2020). Most of these models rely on the hypothesis that in IP space, CME dynamics are solely governed by the interaction of the CME with the background solar wind and can be simplified into a “drag term” (see Eqs. (3.2) and (3.3). In recent times, ML algorithms have also been introduced to refine empirical approaches in forecasting the propagation of CMEs (e.g. Sudar et al., 2016; Liu et al., 2018).

3.6 CME-driven shocks and sheaths

The IP manifestation of a fast CME typically involves three distinct features (see Figure 3.9): a shock wave compressing and deflecting the upstream solar wind flow, the region of compressed solar wind bounded by the shock front and the leading-edge of the ME, called the sheath, and a cold, magnetically-dominated region behind the sheath, called the ME (see Kilpua et al. (2017) for a review on CME structures in IP space).

3.6.1 Shocks

The eruption speeds of CMEs often can exceed the local magnetosonic wave speeds in the corona, resulting in a magnetic field and pressure enhancements forming a bow shock ahead of the CME. Apart from detections in white-light observations, CME-driven shocks can also be detected in radio emissions (known as type-II and type-III bursts, see Wild, 1950; Wild & Smerd, 1972; Mann et al., 1996; Lengyel-Frey et al., 1997) and UV spectral line profiles (e.g. Ciaravella et al., 2006; Gallagher & Long, 2011).

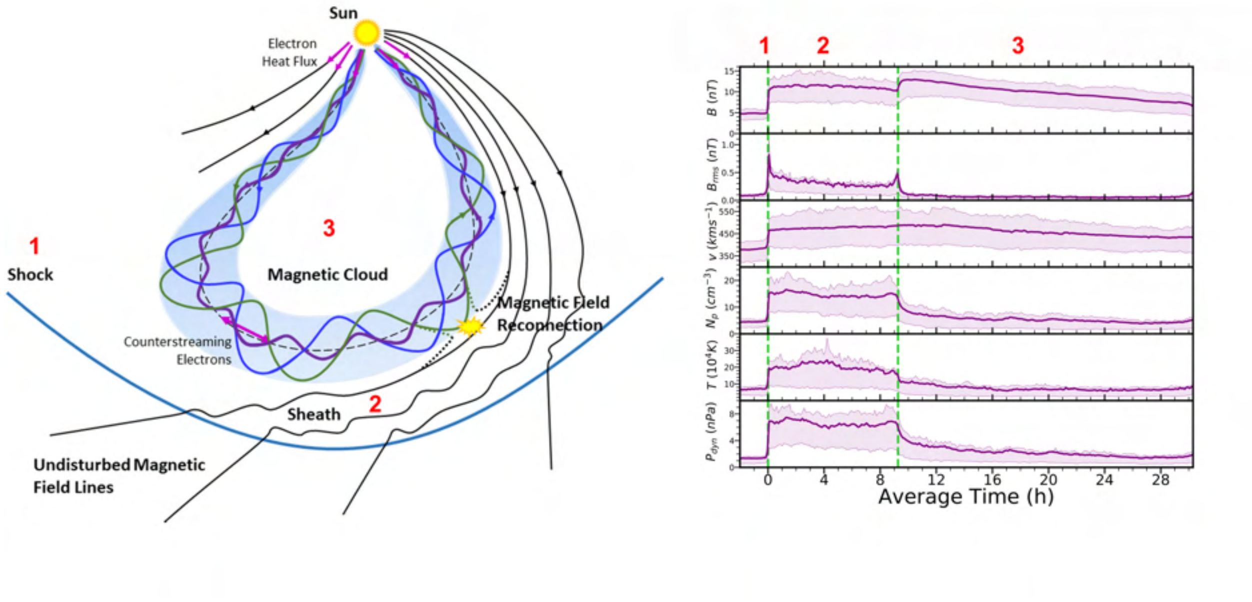

Figure 3.9: Schematic diagram of a typical MC in IP space (left panel). **Adapted from Wang et al. (2018).** Superposed epoch profile of a typical CME (with shock, sheath, and ME) near 1 AU, based on in-situ measurements of 106 CMEs (right panel). **Adapted from Paper-I.**

The magnetosonic speed decreases with radial distance from the Sun. As a result, the shock can be formed at larger distances from the Sun under favorable conditions (see Žic et al., 2008). In addition, radial expansion can also play an important role in shock formations beyond the corona for slower CMEs (e.g. Liu et al., 2016; Lugaz et al., 2017a). During their propagation from the Sun to the Earth, the shocks can undergo substantial distortions due to interactions with the background solar wind (e.g. Manchester et al., 2004).

In space physics and astrophysics, shocks are usually considered "collisionless," indicating that the transition from the pre-shock to post-shock states occurs on a length scale much smaller than the mean free path. However, the changes in plasma conditions across the shock, in response to the advancing shock wave can be described using a similar mathematical framework as neutral shocks in a collisional plasma, known as the "Rankine-Hugoniot (RH) jump conditions." The RH conditions (see Eqs. (3.4) to (3.9) in x and y components) define the conservation of mass, linear momentum, and energy across the shock front within the framework of MHD (see Oliveira (2017) for a review on MHD discontinuities), even though the MHD approximation breaks down at the transition region.

$$[\rho u_x] = 0 \tag{3.4}$$

$$[\rho u_x^2 + p + \frac{B_y^2}{2\mu}] = 0 \tag{3.5}$$

$$[\rho u_x v_y - \frac{B_x B_y}{\mu}] = 0 \tag{3.6}$$

$$[\frac{1}{2}u^2 + \frac{\gamma p}{(\gamma - 1)\rho} + \frac{B_y(u_x B_y - u_y B_x)}{\mu \rho u_x}] = 0 \tag{3.7}$$

$$[B_x] = 0 \tag{3.8}$$

$$[u_x B_y - u_y B_x] = 0 \tag{3.9}$$

Here, the flow velocity (**u**) and the magnetic field (**B**) is considered in the x-y plane, the square bracket for any quantity X has the meaning: $[X] = [X_1]$ - $[X_2]$, where the 1 and 2 subscripts represent upstream (unperturbed) plasma and downstream (perturbed or shocked) plasma, ρ is the mass density, p is the thermal pressure, and γ is the ratio of specific heats. The strength of the shock is characterized by the dimensionless upstream magnetosonic Mach number (M_{ms}), which is the ratio of the solar wind flow speed to the magnetosonic speed in the shock frame of reference.

In IP space, a CME-driven shock is identified in in-situ solar wind measurements, which show an abrupt enhancement in the magnetic field strength, proton density, speed, proton temperature, and dynamic pressure at the shock boundary (see an example in Figure 3.10).

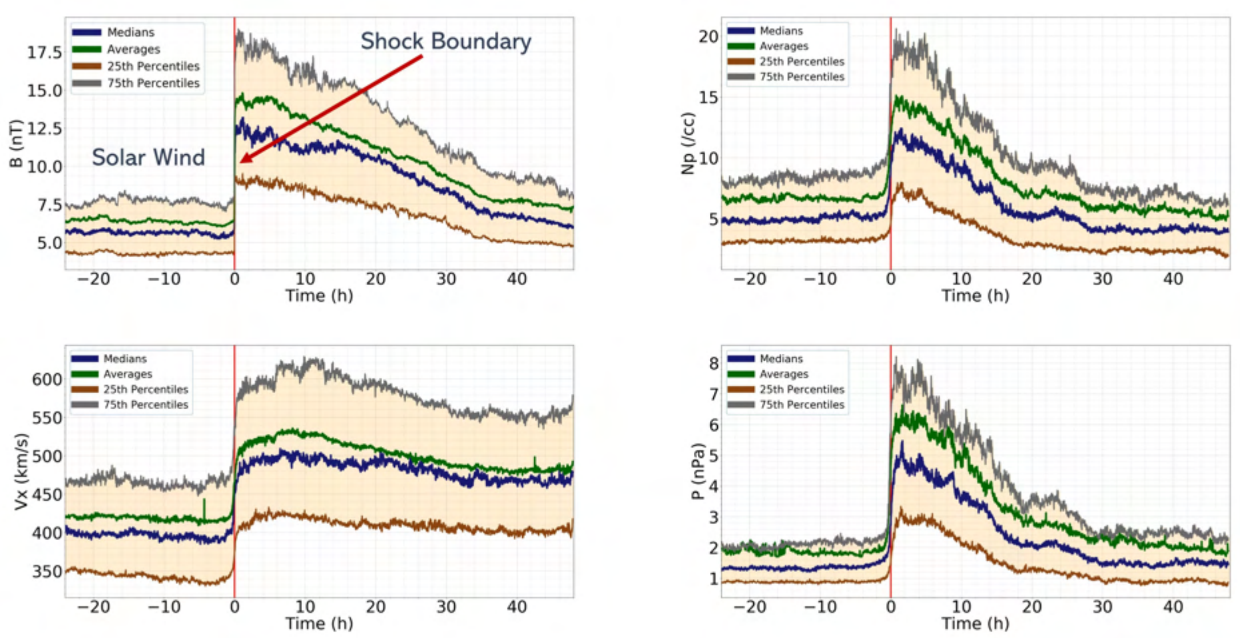

Figure 3.10: A typical CME-driven shock (t=0) showing the jumps (clockwise from upper left) in the magnetic field strength, proton density, dynamic pressure, and speed at the shock boundary, based on the superposed epoch analysis of 183 CME-driven shocks observed by the *Wind* spacecraft from 1995 to 2016. The green curves show the average values, the blue curves show the median values, and the shaded regions indicate the interquartile ranges.

3.6.2 Sheaths

In earlier times, the term “sheath” was not in common usage. Instead, this region was typically referred to as a “post-shock flow” (e.g. Borrini et al., 1982; Tsurutani et al., 1984), which was changed to “sheath” later on (e.g. Galvin et al., 1987).

In the presence of a shock, the region consisting of compressed and heated plasma with a stretched and turbulent magnetic field, bounded by the shock front and leading-edge of the ME is identified as the sheath (Kaymaz & Siscoe, 2006). However, sometimes the ME is preceded by a dense sheath even in the absence of shocks, such as in, for example, the well-studied 12 December 2008 CME (see DeForest et al., 2013) or the 17 January 2013 CME, studied by Lugaz et al. (2016a). In addition, databases of CMEs measured near 1 AU (Jian et al., 2018) and at 1 AU (Richardson & Cane, 2010; Nieves-Chinchilla et al., 2018) include CMEs without shocks but with a start time several hours before the beginning of the CME, often corresponding to a period of dense and disturbed solar wind that can be identified as the sheath region.

CME-driven sheaths are often compared to planetary magnetosheaths, as the solar wind tries to flow around the magnetic obstacle, just like the solar wind flows around the Earth’s magnetosphere. However, as CMEs propagate through the IP medium and expand into it, sheaths upstream of MEs significantly differ from planetary magnetosheaths (Siscoe & Odstrcil, 2008; Démoulin & Dasso, 2009). CMEs expand at significant speeds in many cases, although the expansion is typically slower than the local fast magnetosonic speed (Klein & Burlaga, 1982). This expansion results in the continuous accumulation of solar wind plasma and magnetic field upstream of the ME (Takahashi & Shibata, 2017). The layers in sheaths are not simple stacks of compressed solar wind plasma along the radial line from the Sun because the layers can also slide laterally by different amounts as they are compressed. As a result, CME-driven sheaths are often associated with complex formations, and the sheath field appears to be highly variable and turbulent (Kataoka et al., 2005;

Moissard et al., 2019), for example, the north/south direction of the magnetic field does not present any clear relationship between the sheath region and the ME (Jian et al., 2018). This can make understanding their global configurations and predicting their geoeffectivity particularly challenging (e.g. Palmerio et al., 2016).

One possible two-way mechanism for sheath formation involves propagation of the CME through the solar wind (where the solar wind is deflected sideways at the nose of the magnetic obstacle) with no ME expansion and the expansion of the ME (where the magnetic obstacle expands but does not propagate with respect to the background solar wind). When the lateral deflection speed at the nose of the ME is comparable or less than the ME expansion speed, the solar wind may not be able to flow around the ME (Siscoe & Odstrcil, 2008), resulting in the pile-up of solar wind in front of it (Siscoe & Odstrcil, 2008; Owens et al., 2017a). However, pure propagation sheaths and pure expansion sheaths are rare since the formation of most sheaths is the result of these two mechanisms acting simultaneously (Siscoe & Odstrcil, 2008). Expansion sheaths are unique to CMEs and differ from the most commonly studied sheaths, planetary magnetosheaths (see Figure 3.11), since planetary magnetosheaths are almost pure propagation sheaths (e.g. Kaymaz & Siscoe, 2006; Siscoe & Odstrcil, 2008). The other possible two-way mechanism for sheath formation involves the shock and its associated compression.

3.6.3 Importance of Sheaths

Though CMEs and their subset MCs are the primary drivers of intense geomagnetic disturbances (Farrugia et al., 1997; Zhang et al., 2007; Richardson & Cane, 2012), a substantial amount of moderate-intense geomagnetic disturbances are associated with sheath plasma and magnetic field behind shocks (Kamide et al., 1998; Richardson et al., 2001; Huttunen & Koskinen, 2004; Yermolaev et al., 2010; Echer et al., 2013). For a significant fraction of the GSs, the peak of the geomagnetic index is reached within the sheath. In addition, geoeffective sheaths (see Ontiveros & Gonzalez-Esparza, 2010; Lugaz et al., 2016b) provide

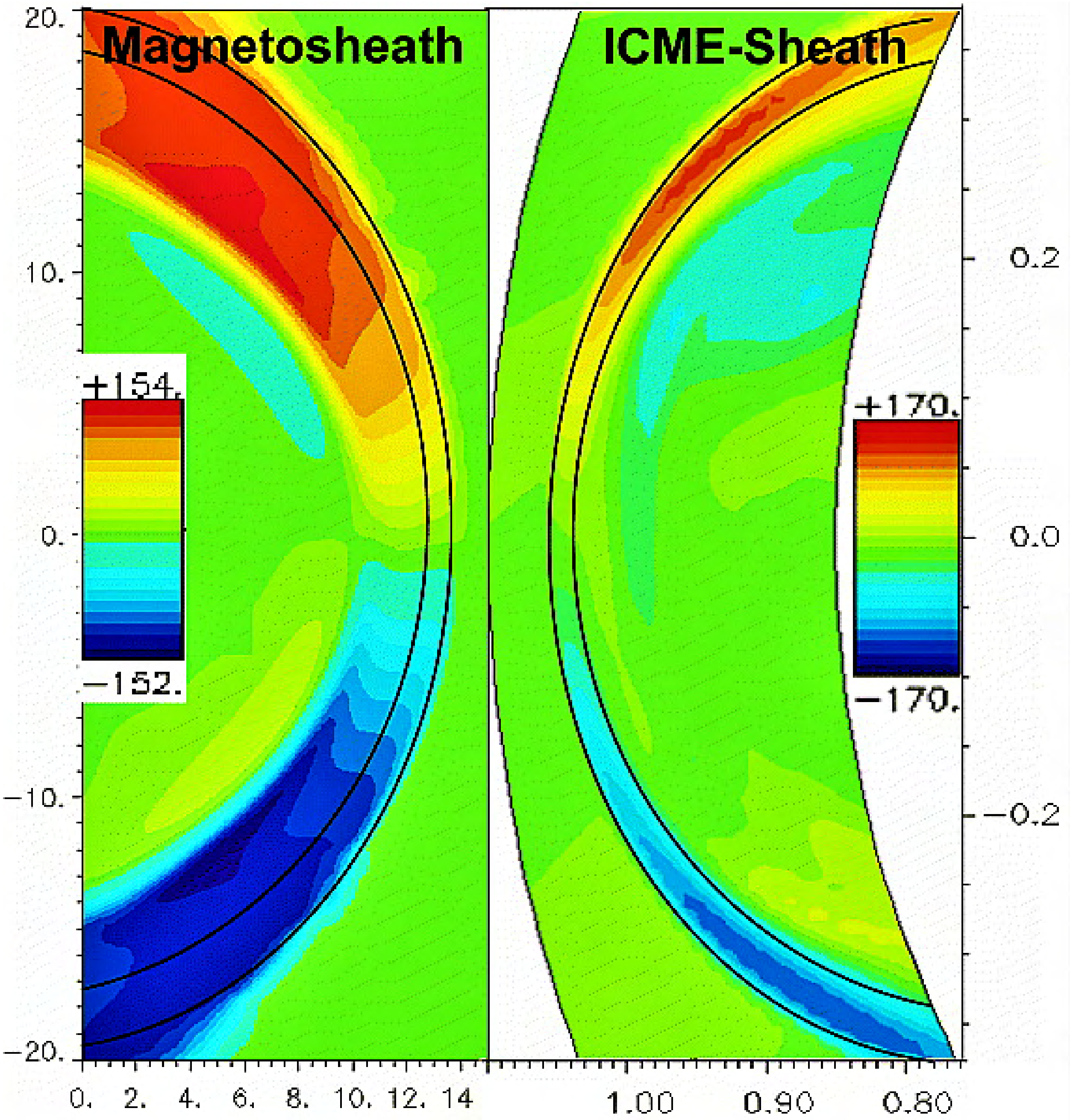

Figure 3.11: MHD simulations showing the deflected component of solar wind velocity in the equatorial plane (i.e., y-component) in Earth's magnetosheath, with the x-axis representing the distance in R_E (left) and in the 8° latitude plane in a CME sheath, with x-axis representing distance in AU (right). The ranges on the speed scales are the maxima in the magnetosheath case and the theoretical maximum for propagation sheaths in the CME case. The distance scales are normalized. This figure illustrates that the CME sheath is thinner than the magnetosheath (relative to the radius of curvature of the body) and has a slower deflection speed relative to the incident flow speed (i.e., flow speed perpendicular to the upstream solar wind flow) than has the magnetosheath. **Adapted from Siscoe & Odstrcil (2008).**

even shorter lead times for forecasts than CMEs.

Embedded magnetic fields (with strong southward B_z) in sheath regions have significant potential to impact the northward geomagnetic field (e.g. Tsurutani et al., 1988; Lugaz et al., 2016b). Such out-of-ecliptic fields in the sheath regions are a byproduct of two possible mechanisms: compression of pre-existing southward B_z at the boundary of a shock (see on the left panel in Figure 3.12), with a normal close to the ecliptic (Lugaz et al., 2016b) or magnetic field line draping upstream of the CME (McComas et al., 1989; Gonzalez et al., 1994). Planar magnetic structures, where the magnetic field is ordered into laminar sheets (Farrugia et al., 1991; Jones et al., 2002; Savani et al., 2011), are commonly found within shock-driven sheath regions (see on the right panel in Figure 3.12). Palmerio et al. (2016) showed that these planar parts of the sheath, in all likelihood, are more geoeffective than non-planar parts. In rare instances, a preceding CME stuck inside the sheath of the following CME can simultaneously enhance solar wind parameters and cause large GSs (see Liu et al., 2020).

CME-driven shocks and sheaths are significant in solar-terrestrial studies as shocked plasma in the immediate downstream of the shock may contribute to the acceleration of solar energetic particles (SEPs; e.g. Reames, 1999; Manchester et al., 2005), and significantly compress and distort the magnetosphere (Joselyn & Tsurutani, 1990; Kim et al., 2010), enhancing the geoeffective potential of CMEs. Due to enhanced solar wind dynamic pressures, sheath regions are capable of compressing the magnetosphere (the magnetic bubble surrounding the Earth that is created by the Earth's terrestrial magnetic field), pushing the dayside magnetopause down to below the geosynchronous orbit (Hietala et al., 2014; Lugaz et al., 2015, 2016b; Kilpua et al., 2019). The magnetopause (see in Figure 3.13) is the outer boundary of separation between the solar wind plasma and the Earth's confined geomagnetic field (Chapman & Ferraro, 1931; Ferraro, 1952), with the subsolar point of the magnetopause located at about ∼10 R_e from the Earth under normal solar conditions (e.g. Spreiter & Stahara, 1985; De Keyser et al., 2005). One of the effects on the outer Van Allen radiation belts of

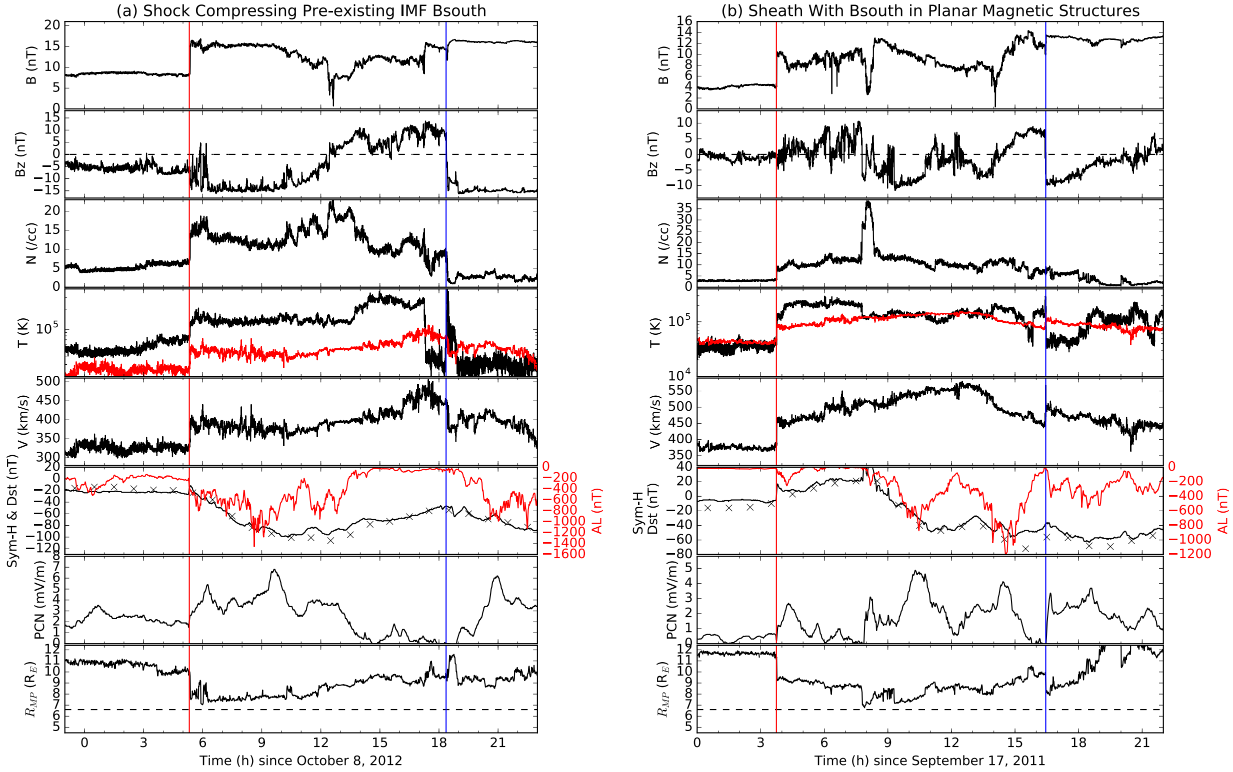

Figure 3.12: *Wind* observations of the shock and geoeffective sheaths on 8 October 8 2012, *Wind* shifted by 70 min (left) and 17 September 2011, *Wind* shifted by 48 min (right). The panels show from top to bottom, the magnetic field strength, GSM B_z component, proton density, the proton velocity and temperature (in red, the expected proton temperature), the proton speed, the Dst index (crosses), and SYM-H index (in red, the AL index), and the PCN index. The ME boundaries are shown with blue lines and the shock with a red line. **Adapted from Lugaz et al. (2016b)**

such magnetospheric compression involves the drastic depletion of relativistic electron fluxes over a broad range of energy, equatorial pitch angle, and radial distance (Pulkkinen et al., 2007; Turner et al., 2012; Hietala et al., 2014; Hudson et al., 2014; Kilpua et al., 2015b; Alves et al., 2016; Lugaz et al., 2016b; Xiang et al., 2017).

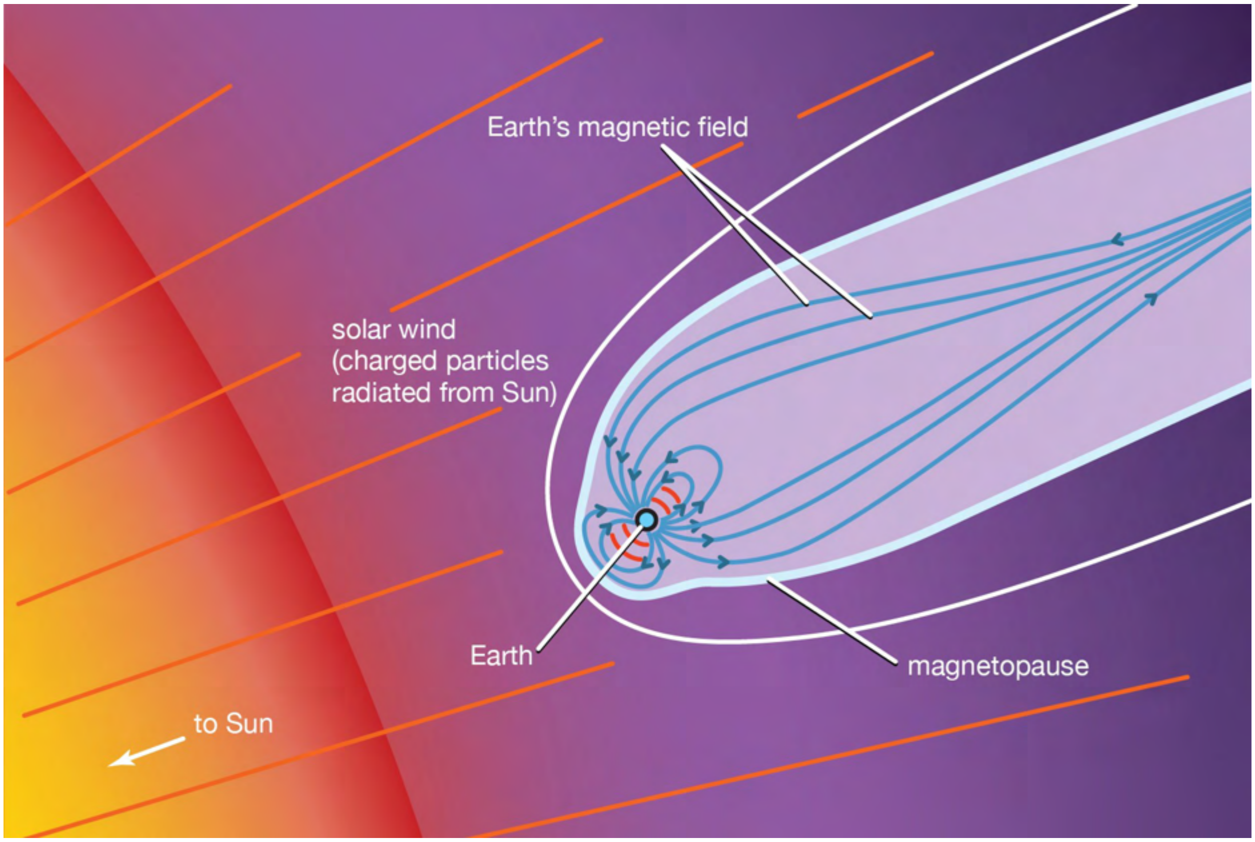

Figure 3.13: Schematics of the Earth's magnetosphere. **Image credit: Encyclopædia Britannica, Inc.**

The relevant importance of CME-driven sheaths is not only limited to its contribution to the effects mentioned above. The layers of CME-driven sheaths contain information about the interaction of the CME with the background solar wind, since these layers are accumulated through the CME journey from the Sun (Kaymaz & Siscoe, 2006). Sheath plasma measured near 1 AU can be composed of material with coronal origins (see Lugaz et al., 2020b), which can provide insight into the early phase of CME evolution. Sheath interfaces are also suitable for searching for plasma discontinuities and reconnection exhausts (e.g. Feng & Wang, 2013).

In addition, time series of solar wind plasma and IMF corresponding to the front of the sheath can serve as a precursor for an upcoming intense southward IMF period (see Salman et al., 2018). Magnetic fluctuations within sheaths can also provide insight into the formation of coherent structures (Kilpua et al., 2020).

3.6.4 Studies of CME sheaths

Different statistical methods have been used to understand the complexity of sheaths. A first method uses observations of the same CME-driven sheath by multiple spacecraft at different heliocentric distances that are nearly radially aligned (e.g. Good et al., 2020; Lugaz et al., 2020b; Salman et al., 2020b). This type of research method has been performed during the completion of this thesis and presented in Chapter 6. This method sheds light on the radial growth of the sheath and the decline in the sheath magnetic field as the CME propagates away from the Sun. This method is mainly limited to case studies because of the rarity of CMEs measured in perfect radial conjunction. In addition, small longitudinal separations between the measuring spacecraft can result in significant variations (e.g. Kilpua et al., 2011; Lugaz et al., 2018). The relative lack of plasma measurements in the inner heliosphere critically constrained the applicability of this method until the recent launches of PSP and SO.

A second method analyzes in-situ measurements of different CME sheaths at different radial distances from the Sun (e.g. Winslow et al., 2015; Janvier et al., 2019). This method is convenient for determining the average properties at different heliocentric distances. However, such a method does not consist of measurements of the same CME sheath (at two or more distinct heliocentric distances) like the previous method. As a result, inherent CME-to-CME variability makes the unambiguous interpretation of radial dependency extremely difficult (e.g. Lugaz et al., 2020a; Salman et al., 2020b).

A third method is focused on in-situ measurements of an extensive list of CME-driven sheaths near-Earth (Guo et al., 2010; Kilpua et al., 2013; Mitsakou & Moussas, 2014; Masías-Meza et al., 2016; Rodriguez et al., 2016; Kilpua et al., 2017; Jian et al., 2018; Kilpua et al., 2019; Regnault et al., 2020; Salman et al., 2020a). This type of research method has also been carried out during the completion of this thesis and presented in Chapters 4 and 5. This method provides the opportunity to examine the correlation between the sheath and the CME and the geoeffectiveness of CME structures statistically. These studies are based on the assumption that analyzing a large number of CME sheaths can possibly cancel out the individual sheath properties (e.g. Démoulin et al., 2020).

3.7 STEREO CME list

Chapters 4 to 6 have extensively used the STEREO CME list compiled by Jian et al. (2018). This list is a compilation of 341 CMEs (192 CMEs with distinguishable sheath regions), measured by one of the two STEREO spacecraft between 2007 - 2016. For the identification of CMEs, the following standard set of features are used: stronger than ambient magnetic field, relatively quiet magnetic field, smooth rotations of the magnetic field over a relatively long time, declining solar wind speed, low proton temperature, low β, increased total pressure (P_t), and bidirectional suprathermal electron (BDE) strahl.

In this list, CMEs are ranked with a quality index ranging from 2 to 0. CMEs with an index of 2 are the closest to the MC criteria (21%). CMEs with a quality index of 1 are MC-like (23%), with the quality index 0 corresponding to non-MCs (56%). In addition, CMEs are sorted into three groups based on the temporal variations of P_t profile: (1) Group 1 with a central maximum in P_t profile (20%), (2) Group 2 with a plateau-like P_t profile (35%), and (3) Group 3 with a monotonic decrease in P_t (32%) after a shock and/or sheath.

CHAPTER 4

Characteristics of CME structures near 1 AU: with and without shocks

This chapter is formed from the publication Salman et al. (2020a). Magnetic field measurements from the magnetometer of the IMPACT (In-situ Measurements of Particles and CME Transients; Luhmann et al., 2008) instrument with a 1/8 s resolution and plasma measurements from the PLASTIC (Plasma and Suprathermal Ion Composition; Galvin et al., 2008) instrument with a 1-min resolution, onboard the twin STEREO SC have been used in this work.

4.1 Background

Compared to the shock and ME, the sheath is the less studied structure in solar-terrestrial physics. In addition, studies of such sheaths, associated with shocks, come mostly from simplified numerical simulations (often hydrodynamic) or similarities with the Earth's bow shock. However, numerous studies of ME-driven sheaths based on in-situ measurements have also been carried out, focusing on the generic profile and/or correlation/comparison with the driving ME (Mitsakou et al., 2009; Guo et al., 2010; Mitsakou & Moussas, 2014; Kilpua et al., 2017; Jian et al., 2018; Kilpua et al., 2019), superposed epoch analysis or SEA (Kilpua et al., 2013; Masías-Meza et al., 2016; Rodriguez et al., 2016; Janvier et al., 2019), and radial evolution (Lugaz et al., 2020b; Good et al., 2020).

At the conceptualization stage of this work, to the best of our knowledge, there was no specific study of sheaths driven by MEs that did not drive shocks. The concentrated focus in past studies have been on the geoeffectiveness of sheath regions associated with only fast and shock-driving MEs. This prompted us to study this unexplored class of sheaths. The objective was to examine the distinctness of CME sheaths with pure measurements, especially the distinguishability of ME-driven sheaths with and without shocks near 1 AU. We also extended the analysis to MEs that did not drive a shock and a sheath near 1 AU. In a recent study, Regnault et al. (2020) investigated the diversity of CME profiles for different groups of CMEs at L1, which included an analysis of CMEs with and without sheaths based on a SEA. However, the authors did not differentiate between CME sheaths with and without shocks.

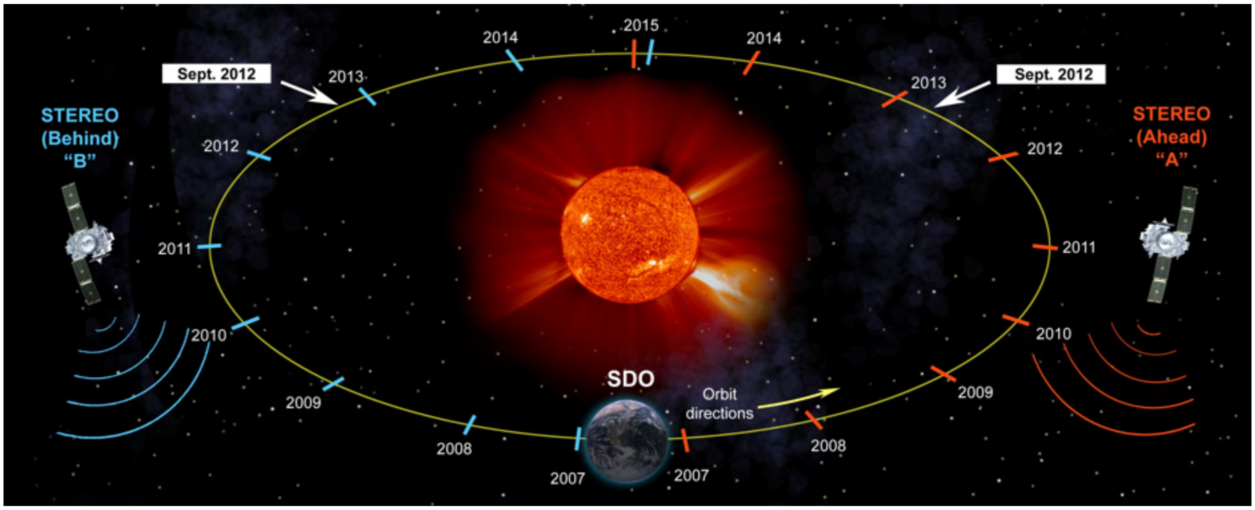

Figure 4.1: Relative orbital positions of both STEREO spacecraft for each year from June 2007 to June 2015 (not to scale). Communications with the STEREO-B spacecraft were interrupted on 1 October 2014. **Image credit: NASA/GSFC.**

4.2 Initial classification of CMEs

In this work, we examined 188 CMEs and 142 ME-driven sheaths measured by one of the twin STEREO SC during 2007 - 2016. We classified the CMEs, as reported in Jian et al. (2018) into three main categories, focusing on whether a ME drives both a shock and sheath, or only a sheath, or neither, near 1 AU. We defined the sheath as a region with a significant increase in density and magnetic field strength for at least 2 hours above the background solar wind and directly preceding a ME.

For each CME, Jian et al. (2018) lists the start time of the CME, the start time of the ME, and the end time of the ME at the measuring SC. When the start time of the CME differs from the start time of the ME, there exists a sheath region upstream of the ME. For MEs driving shocks, the CME start time corresponds to the arrival of the shock at the measuring SC.

The first category (Cat-I) included MEs driving a shock near 1 AU and with a clear sheath region upstream of the ME. We used the Heliospheric shock database of Kilpua et al. (2015a), generated and maintained at the University of Helsinki (can be found at `http://ipshocks.fi/`) and STEREO shock list (available at `https://stereo-ssc.nascom.nasa.gov/`) for identifying shocks associated with these CMEs. The former database is referred to as IPshocks database from now on. We only included shocks listed in both of the databases mentioned above or only listed in one of them but had M_{ms} greater than 1. For this category, we initially identified 105 CMEs. The second category (Cat-II) included CMEs with associated sheath regions but with no shock signatures or sometimes associated with shock-like discontinuities. This category also included CMEs with shocks listed in the IPshocks database with $M_{ms}<1$. We excluded 13 potential Cat-II CMEs as the sheath boundaries for these CMEs were not properly defined due to considerable data gaps. Therefore, initially, through visual inspection, we identified 17 Cat-II CMEs. The third category (Cat-III) included CMEs with no shocks and sheaths. The CME and ME start times listed in Jian et al. (2018) for this specific category were the same. Initially, we identified 66 Cat-III CMEs from the STEREO CME list. We excluded 21 CMEs through visual inspection as these CMEs were associated with "driverless shocks" or shocks that were not followed by their drivers (see Gopalswamy et al., 2009). These driverless shocks were those for which the start time of the CME corresponded to a shock and was listed as the same time as the start of the ME, so that these CMEs had a shock and no sheath or more reasonably, a shock, a sheath, but no driver.

4.3 Automated sheath identification algorithm

In addition to the visual search described above, we devised an automated sheath identification algorithm (ASIA) to identify any possible sheath region upstream of the ME. The algorithm provided a quantitative basis to confirm the initial classification and reclassify a few unclear events as needed. The sheath region, in general, features elevated levels of density and magnetic field strength over the background. In our approach, we approximated the sheath to be 1.5 times more compressed and 1.3 times more magnetized than the unperturbed solar wind. The rationale for these specific ratios was that the weakest shocks measured near 1 AU have jumps of ∼1.3 in the density and magnetic field strength at the shock, but the density in the sheath is often more elevated than just downstream of the shock (Manchester et al., 2005), which led to our criteria of 1.5 for the density and 1.3 for the magnetic field strength. Although enhancements in the solar wind speed, temperature, and dynamic pressure are also considered characteristic evidence for the identification of sheaths associated with shocks, such enhancements are not universally associated with sheaths not preceded by shocks. Therefore, for better optimization, we limit the ASIA to only search for predefined enhancements in density and magnetic field strength over the quiescent solar wind to identify sheaths.

We initially started with a preliminary sheath, extending up to the ME leading-edge and with a duration of 2 hours (blue shaded region in Figure 4.2), and we approximated the 2-hr interval before this preliminary sheath as the background solar wind (pink shaded region in Figure 4.2). The reason behind starting with this predefined sheath interval of 2 hours was that ∼97% of the sheaths in our database were longer than 2 hours in duration. Therefore, we approximated a 2-hr interval to be the minimum threshold for any preliminary sheath. However, this resulted in the algorithm inherently not identifying the 4 sheaths in our database that were shorter than 2 hours. Then, for each following iteration of the ASIA, we extended this preliminary sheath by 5-min steps but always limit the background solar wind as a 2-hr interval before this

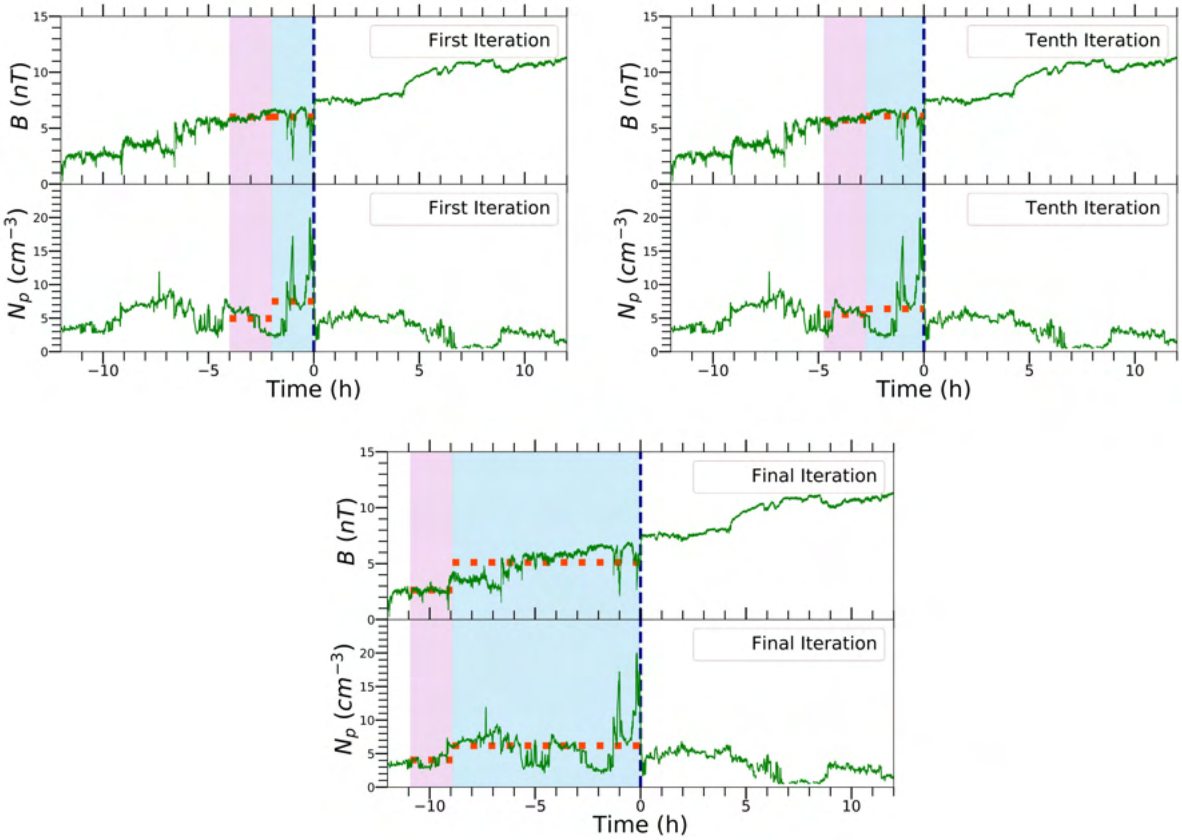

Figure 4.2: Visual representation (selected iterations) of the ASIA based on the average proton density and magnetic field strength criteria. The blue shaded region is the approximated sheath for each iteration, and the pink shaded region is the approximated upstream solar wind. The horizontal red dotted lines in each region indicate the averages within that region. The vertical navy dashed line marks the start of the ME leading-edge.

We carried out the iterations in a recursive manner. We extended this preliminary sheath up to 30 hours before the start of the ME (allowing identification of extremely long sheaths) and each time compared the average density and magnetic field strength in this preliminary sheath with that of the background. As there can be substantial fluctuations of the solar wind plasma and IMF within the sheath, it was quite possible to have an interval that satisfied our average criteria, only for the region enclosed by the immediate next time step to violate one or both of them. To negate that, our goal was to find the time step after which both of the ratios were satisfied for a prolonged interval. The interval enclosed by this specific time step upstream of the ME was identified as the probable sheath. However, as our ratios were somewhat subjective, we did not entirely rely on the ASIA to identify probable sheaths and no sheaths. The start of the ME (especially for a non-MC) can be ambiguous. Therefore, for disagreements between the initial classification of CMEs, solely based on the STEREO CME list of Jian et al. (2018) and ASIA, we carried out our visual inspection of the CME boundaries (for ∼200 CMEs), looking at both the magnetic field and plasma parameters and changed the start times of MEs (as listed in Jian et al. (2018)) accordingly.

We ran this algorithm for each and every event of our database. For the Cat-III events, the algorithm identified 20 events to have sheaths. We visually inspected these 20 events and identified them to have sheaths as well. We then looked for upstream shock signatures within the previous 30-hr period before the start of the ME in both of the shock databases to determine whether to move those events to Cat-I or Cat-II. Based on the findings, we moved 1 event to Cat-I and 19 to Cat-II. In summary, the ASIA accurately identified 172 out of the 188 CMEs. Therefore, after the application of the ASIA along with thorough visual inspection, our final database was composed of 106 Cat-I, 36 Cat-II, and 46 Cat-III CMEs (see Appendix B for the list of CMEs in each category).

4.4 Example events from different categories

4.4.1 Cat-I (CME with an associated shock and sheath region)

The Cat-I event presented here (see the top left panel in Figure 4.3) was driven by an expanding ME near 1 AU, with an expansion speed of 71 $\mathrm{km\,s^{-1}}$. The expansion speed was taken as half the difference between the leading and trailing-edge speeds (see Owens et al., 2005). The shock propagated in an upstream solar wind speed of 315 $\mathrm{km\,s^{-1}}$. The upstream fast magnetosonic speed was 63 $\mathrm{km\,s^{-1}}$. Here, the upstream solar wind and fast magnetosonic speeds were taken as the average of the 2-hr interval before the arrival of the shock. The associated shock was listed in the IPshocks database (M_{ms} of 2) and the STEREO shock

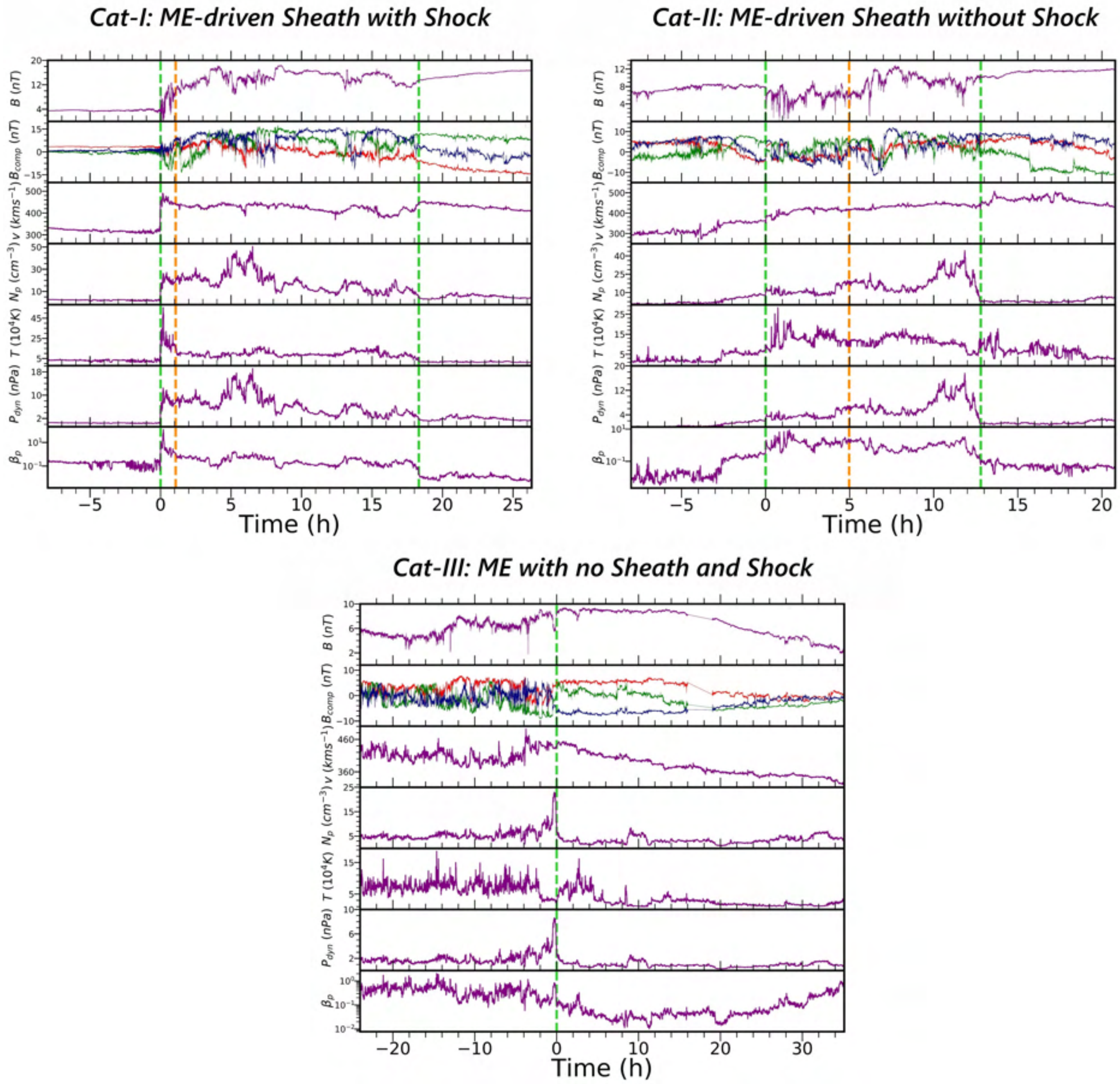

Figure 4.3: IMF and plasma measurements of three example CMEs. The seven panels show the magnetic field strength, components in RTN coordinates (red: radial, green: tangential, blue: normal), solar wind speed, proton density, proton temperature, dynamic pressure, and proton beta (from top to bottom). The two vertical green dashed lines bound the sheath, with t=0 corresponding to the start of the sheath and the vertical orange dashed lines denote the start of the sheath, as identified by the ASIA (top panel). For the bottom panel, the start of the ME is denoted by the green dashed line, with t=0 corresponding to the start of the ME. *Top left*: STEREO-B measurements of the Cat-I CME starting on 12 April 2014 at 2:27 UT, *Top right*: STEREO-B measurements of the Cat-II CME starting on 29 October 2011 at 04:12 UT, *Bottom*: STEREO-A measurements of the Cat-III CME starting on 28 April 2011 at 09:00 UT.

list (M_{ms} of 2.6). The shock arrived at STEREO-B on 12 April 2014 at 2:27 UT. The SC encountered the sheath for a relatively long period of 18.32 hours, with the leading-edge of the ME arriving on 12 April 2014 at 20:46 UT. The ASIA also identified a sheath region upstream of the ME. For this particular event, the sheath interval identified by the ASIA was 17.25 hours, slightly shorter.

4.4.2 Cat-II (CME with a sheath but without a shock)

Our example Cat-II event revealed an interesting discontinuity. The start of this sheath coincided with a sharp decrease in the magnetic field strength (see the top right panel in Figure 4.3). The discontinuity, which probably was a slow-mode shock/wave, arrived at STEREO-B on 29 October 2011 at 04:12 UT. According to the STEREO CME list of Jian et al. (2018), the SC encountered the sheath for 7 hours. The ASIA also identified a sheath region extending out to 7.83 hours upstream of the ME. However, with a visual inspection, we approximated the sheath to start at 12.80 hours before the start of the ME to accomodate the enhancements of the solar wind speed, proton density, temperature, and dynamic pressure. The driving ME expanded at a much slower rate compared to the Cat-I ME mentioned above, with an expansion speed of $\sim$47 $\mathrm{km\,s^{-1}}$. Here, the upstream solar wind speed of 357 $\mathrm{km\,s^{-1}}$ might have been an overestimation because of the compression region right before the sheath. The upstream fast magnetosonic speed was 72 $\mathrm{km\,s^{-1}}$, slightly higher than in the previous example. The region upstream of the ME was a typical sheath-like structure as the physical parameters (proton density, temperature) within the sheath was enhanced by a factor of 2 than the background solar wind, while this factor was 3 for the dynamic pressure. The average speeds of the structures (sheath and ME) were also comparable to each other, indicating that the ME was driving the sheath.

4.4.3 Cat-III (CME with no associated shock and sheath)

The example Cat-III ME presented on the bottom panel in Figure 4.3 arrived at STEREO-A on 28 April 2011 at 9:00 UT. The SC encountered the ME for ∼35 hours before it ended on 29 April 2011 at 20:07 UT. The ME propagated in a moderately fast solar wind of 440 $\mathrm{km\,s^{-1}}$. The upstream fast magnetosonic speed was 55 $\mathrm{km\,s^{-1}}$. This ME, with a leading-edge speed of 441 $\mathrm{km\,s^{-1}}$, was expanding near 1 AU with an expansion speed of ∼58 $\mathrm{km\,s^{-1}}$. The ASIA identified no sheath region upstream of the ME. There were some notable enhancements and fluctuations in the magnetic field upstream of the ME. However, they did not coincide with any notable enhancements in the plasma parameters and might correspond to Alfvén waves. The sharp increase in proton density just before the start of the ME, coinciding with a simultaneous sharp decrease in the magnetic field strength might have been a product of magnetic reconnection. Also, the change in proton beta (β_p) across the boundary was small, which is a condition favorable for MR (Phan et al., 2013). This certainly was not an anomaly, as 8 out of the 46 Cat-III MEs exhibited such signatures.

4.5 The proportion of different categories

4.5.1 Variation in terms of the leading-edge speed of the ME

We examined the proportion of different categories based on the leading-edge speed of the ME near 1 AU (see the top left panel in Figure 4.4). We first arranged all the MEs by the increasing order of leading-edge speeds. We excluded 3 MEs because the leading-edge portions for these MEs had considerable data gaps. The leading-edge speeds ranged from 301 $\mathrm{km\,s^{-1}}$ (a Cat-III ME) to 949 $\mathrm{km\,s^{-1}}$ (a Cat-I ME). Then, we binned the leading-edge speeds into 8 intervals, each containing 23 MEs except the last one, which contained 24. For each interval, we normalized the count from each category by the total number of MEs in that interval.

We observed that, for small leading-edge speeds, the number of MEs not driving shocks

(Cat-II and Cat-III) outweigh the number of MEs driving shocks (Cat-I). For leading-edge speeds below 400 $\mathrm{km\,s^{-1}}$, only 42% of MEs were able to drive shocks, confirming the results of the study by Lugaz et al. (2017a) based on *Wind*/ACE data. The normalized ratio of Cat-II MEs peaked for leading-edge speeds around 340 - 371 $\mathrm{km\,s^{-1}}$, maybe indicating that they were in the process of forming shocks. As expected, the proportion of shock driving MEs started outweighing the non-shock driving ones with increasing leading-edge speeds. However, the proportion of non-shock driving MEs did not immediately become negligible. Even for higher leading-edge speed intervals, we did find a non-negligible amount of non-shock driving MEs. For example, between leading-edge speeds 590 - 710 $\mathrm{km\,s^{-1}}$, 26% of MEs still did not drive shocks. According to our database, MEs with leading-edge speeds >598 $\mathrm{km\,s^{-1}}$ all drove sheaths and MEs with leading-edge speeds >701 $\mathrm{km\,s^{-1}}$ all drove shocks near 1 AU and had associated sheaths.

4.5.2 Solar cycle variation

In this section, we examined the annual variation of ME counts of the three categories. Different phases of two SCys were sampled: the solar minimum of SCy 23 and transition to SCy 24 (2007-2008), the rising phase of SCy 24 (2009-2011), and the double-peak solar maximum (2012-2014). For improved statistics, we combined the counts from 2007 - 2009. We then normalized the counts for each temporal bin (2007 - 2009: 28, 2010: 19, 2011: 38, 2012: 40, 2013: 36, 2014: 27, see the top right panel in Figure 4.4). We observed a gradual increase in the proportion of Cat-I MEs from 2009 onwards, coinciding with the rising phase of SCy 24 and peaking near the solar maximum (75% of the MEs in 2012 were Cat-I). During solar maximum, a large proportion of MEs originates from ARs near big sunspot groups. Eruptive events associated with ARs usually give rise to fast MEs (Manchester et al., 2017). Therefore, the increase in the occurrence rate of Cat-I MEs (fastest among the three categories) during the rising phase of a SCy was expected. In contrast, during solar minimum, most MEs originate from streamer blowouts and quiescent

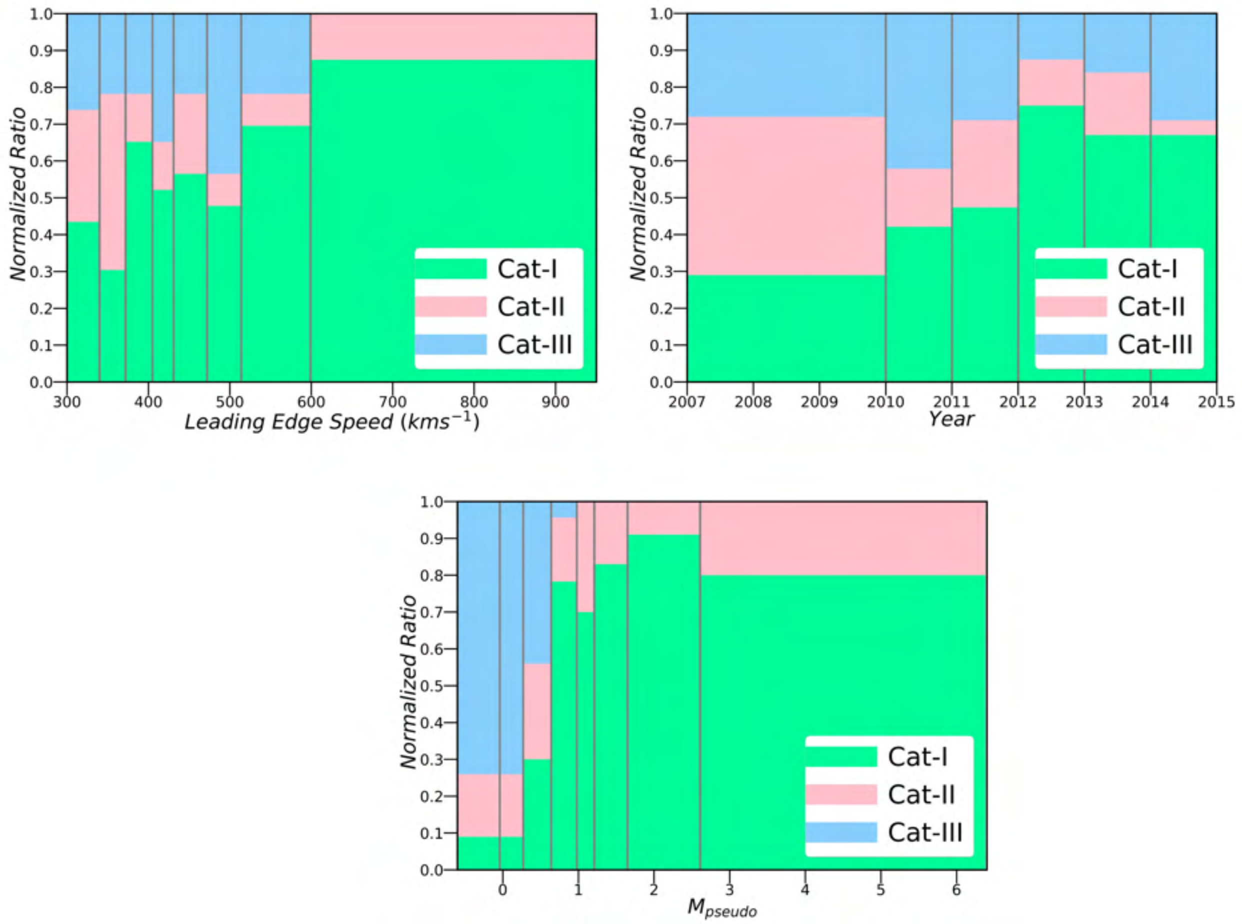

Figure 4.4: *Top panel*: Normalized ratios of leading-edge speeds (left) and annual occurrence rates (right) of the three ME categories, *Bottom panel*: Normalized ratios of "pseudo" Mach numbers (see section 4.7.1) of the three ME categories.

prominences, located far from ARs. Such eruptions usually produce slow MEs (Manchester et al., 2017). Therefore, as expected, the occurrence rate of Cat-II MEs (slowest among the three categories, see Table 4.1 for comparison of average ME speeds of the three categories) peaked at solar minimum (33% of Cat-II MEs occurred during the solar minimum). The proportion of Cat-III MEs was relatively constant with a peak in 2010 during the rising phase of SCy 24. These MEs propagated in the fastest upstream solar wind and may have been associated with slower MEs propagating through SIRs that were more likely to occur outside the solar maximum.

4.6 Superposed epoch analysis

We performed a SEA, also known as Chree analysis (Chree, 1913) to derive the generic profiles of sheaths driven by MEs near 1 AU. SEA is a non-parametric averaging technique that consists of sorting time series data into categories. The basic rationale is that the averaging is done in a way that the common features of the data do not change, and small variabilities tend to average out.

For Cat-I and Cat-II CMEs, we used two characteristic epoch times, the start of the sheath and the start of the ME, so that all events with different timescales but from the same category were perfectly aligned. We primarily used the timings listed in Jian et al. (2018). We used the timings identified with visual inspection only for discrepancies between the STEREO CME list and the ASIA. For each event, the sheath and ME timescales were resampled to the average timescales of each category (average sheath duration: Cat-I is 9.27h, Cat-II is 8.32h). Then, the SEA was performed to analyze the temporal profiles of Cat-I and Cat-II sheaths statistically. This allowed the average temporal profiles to be presented on the average timescales of the sheath and the ME. We used the average sheath to ME interval ratio (0.44 for both Cat-I and Cat-II) to set up the typical timescale of the ME (typical ME duration: Cat-I was 21h, Cat-II was 18.9h). Therefore, the typical ME durations used in the SEA differed from the average ME durations listed in Table 4.1. The sheaths of both categories were binned into 75 time bins and later averaged to get the same number of data points in the sheath interval. As the average ratio between the length of the sheath and ME intervals for both Cat-I and Cat-II MEs were 0.44, we imposed 170 time bins for the ME (for both categories) and 16 (for Cat-I) or 18 (for Cat-II) time bins for the upstream solar wind (by comparing the average sheath duration of 9.27h for Cat-I and 8.32h for Cat-II with the predefined 2-hour interval upstream of the shock/discontinuity/sheath as the solar wind). Lastly, the averaged values from different events but of the same bin number were averaged to determine the average profiles of the physical parameters in the sheath and ME.

For Cat-III MEs, we presented the average timescales in a slightly different manner, as these MEs did not have associated sheath regions. We selected an extended 8.8h solar wind interval upstream of the ME (average of the typical durations of Cat-I and Cat-II sheaths). Similar to Cat-I and Cat-II sheaths, we required this extended pre-ME solar wind interval to have 75 time bins. 211 time bins for the ME (comparing the average ME duration of 24.8h with the 8.8h extended pre-ME solar wind interval) and 17 time bins for the solar wind (2-hour interval upstream of the extended pre-ME solar wind interval) were taken and later averaged.

The goal of the extended 8.8h pre-ME solar wind was to identify, if it existed, any signature in the SEA of Cat-III MEs that may have been missed by visual inspection. It was also used for visualization purposes to present all three categories with a similar format, the ME, preceded by a sheath period of ∼8-9 hours and a 2-hour pristine solar wind.

From the SEA profiles of Cat-I MEs (see the top left panel in Figure 4.5), as expected, we observed an abrupt increase in the magnetic field strength, magnetic field fluctuations, proton density, speed, temperature, and dynamic pressure over the quiescent solar wind at the shock boundary. In the sheath region, the IMF and plasma profiles remained relatively constant (except the magnetic field fluctuations). To quantify the fluctuations of the magnetic field

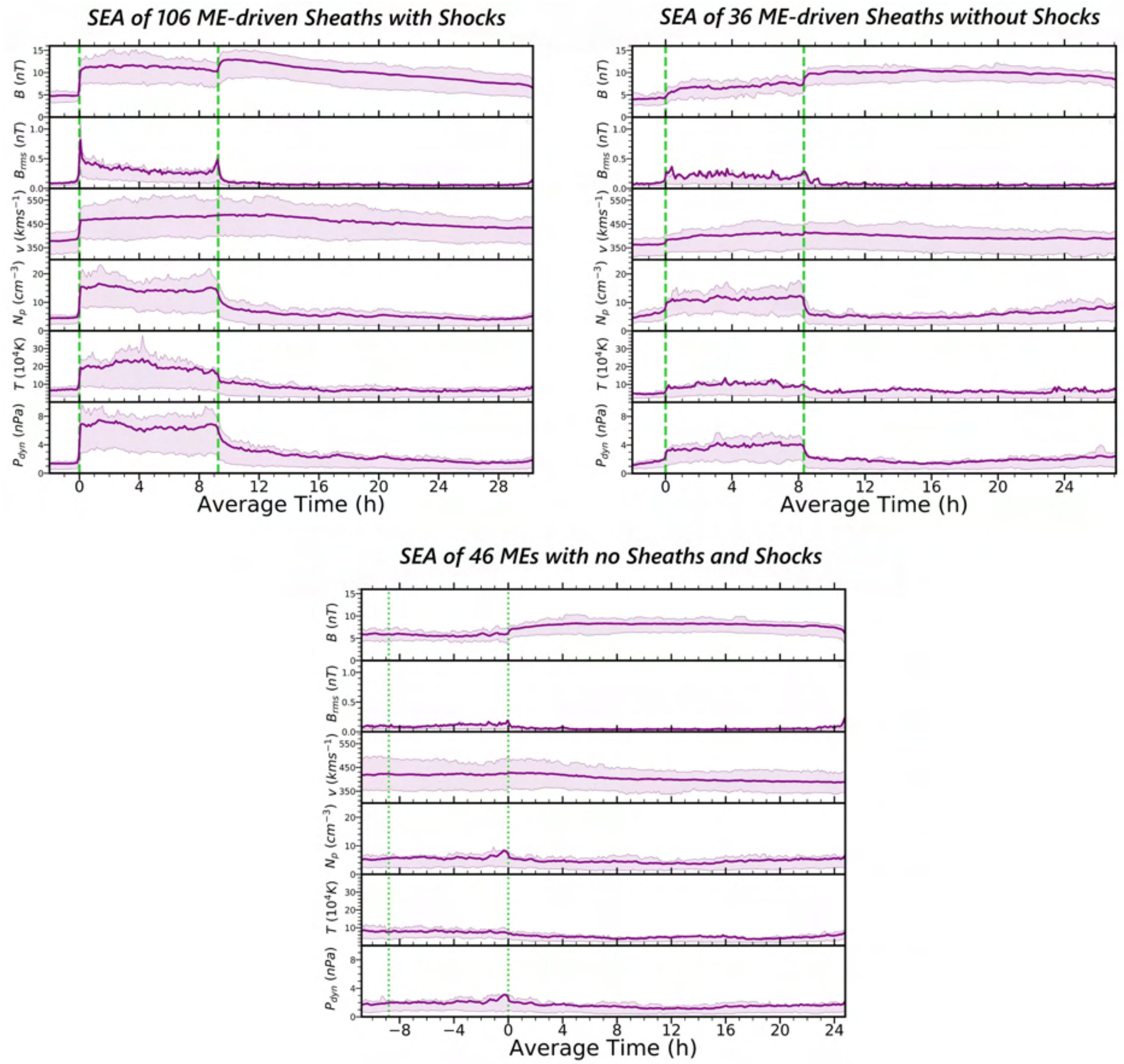

Figure 4.5: Superposed epoch analysis profiles for the 106 Cat-I CMEs (top left), 36 Cat-II CMEs (top right), and 46 Cat-III MEs (bottom). The purple curves show the average values, and shaded regions indicate the interquartile ranges. The panels show distributions (from top to bottom) of the magnetic field strength, total root-mean-square error of the magnetic field strength, solar wind speed, proton density, proton temperature, and dynamic pressure. The vertical green dashed lines (top panel) bound the sheath region. The vertical green dotted lines (bottom panel) bound the extended pre-ME solar wind interval. The region to the left of the vertical green dashed lines represents the unperturbed solar wind, and the region to the right of the vertical green dashed/dotted lines represents the entire ME.

strength (e.g. Masías-Meza et al., 2016; Kilpua et al., 2019), we introduced a total root-mean-square (B_{rms}) that is the sum of root-mean-square-deviations for each 1-min time interval (B_{rms^*}, as defined in Equation 4.1) that makes up the regions (solar wind, sheath, and ME).

$$\mathrm{B}_{rms^*} = \sqrt{\sum_{i=1}^{n} \frac{(B_i - \langle B \rangle)^2}{n}} \tag{4.1}$$

Here, $\langle \mathrm{B} \rangle$ represents the temporal average of magnetic field strength for 1-min intervals.

The field fluctuations peaked right at the shock arrival and then continuously decreased throughout the sheath, consistent with the study of Masías-Meza et al. (2016), before a second peak was observed at the leading-edge of the ME. The piled-up IMF and plasma in the sheath corresponded to the enhanced magnetic field and plasma profiles over the background solar wind. The steady decline in the magnetic field strength and lower proton density and temperature levels in the ME were direct consequences of the typical expansion undergone by the ME near 1 AU. In addition, the magnetic field strength inside the ME was asymmetric, possibly owing to the aging effect (see Démoulin et al., 2008). The magnetic field fluctuations stabilized to lower typical solar wind levels in the ME, a feature characteristic of MCs (Burlaga et al., 1981).

For Cat-II CMEs, at the start of the sheath, we also observed a jump in the parameters compared to the unperturbed solar wind (see the top right panel in Figure 4.5). However, the jumps were significantly less pronounced than for Cat-I CMEs. In addition, the jumps were more extended and smoother, not as abrupt and sharp as Cat-I. Similar to Cat-I sheaths, the magnetic field and plasma profiles remained roughly constant within the sheath. The magnetic field fluctuations peaked slightly after the sheath and were more symmetric than Cat-I fluctuations. Cat-II sheaths also corresponded to elevated IMF and plasma parameters over the background solar wind.

In the case of Cat-III MEs, we observed an enhanced magnetic field in the ME compared to the ambient solar wind (see the bottom panel in Figure 4.5). The magnetic field was roughly steady in the ME with relatively small fluctuations. The proton density and temperature were also low compared to the background solar wind.

4.7 Average profiles of the structures

4.7.1 MEs

In Table 4.1, we compared the average parameters within the MEs for different categories. We also introduced three different types of ME Mach numbers (see Eqs. (4.2) to (4.4)). The "pseudo" Mach number (M_{pseudo}) represented the ratio of the leading-edge speed in the solar wind frame to the upstream fast magnetosonic speed. The "propagation" Mach number (M_{prop}) denoted the ratio of the average ME speed in the solar wind frame to the upstream fast magnetosonic speed. The "expansion" Mach number (M_{exp}) was the ratio of the expansion speed to the upstream fast magnetosonic speed.

$$\mathrm{M}_{pseudo} = \frac{\mathrm{v}_{le} - \mathrm{v}_{sw}}{\mathrm{v}_{ms}} \tag{4.2}$$

$$\mathrm{M}_{prop} = \frac{\mathrm{v}_{ejecta} - \mathrm{v}_{sw}}{\mathrm{v}_{ms}} \tag{4.3}$$

$$\mathrm{M}_{exp} = \frac{\mathrm{v}_{exp}}{\mathrm{v}_{ms}} \tag{4.4}$$

Here, v_{ejecta} is the ME propagation speed, calculated as the average speed of the ME, v_{sw} is the solar wind speed, v_{ms} is the fast magnetosonic speed of the local solar wind, v_{exp} is the ME expansion speed, and v_{le} is the ME leading-edge speed. Both v_{sw} and v_{ms} are calculated as the average in a 2-hr time interval upstream of the shock/ME.

The main results were as follows:

1) MEs driving Cat-I sheaths were the fastest among the three categories, and they had the fastest expansion speeds.

2) MEs driving Cat-II sheaths were the slowest among the three categories and had the slowest expansion speeds. However, they also propagated in the slowest solar wind with the lowest fast magnetosonic speed, i.e., in conditions that would be ideal for driving a shock. The average leading-edge speed of MEs driving Cat-II sheaths was 416 $\mathrm{km\,s^{-1}}$, which was almost identical to the minimum leading-edge speed a Cat-II ME required to drive a perpendicular shock near 1 AU, which was 412 $\mathrm{km\,s^{-1}}$.

Table 4.1: Averages and standard deviations of selected solar wind plasma and IMF parameters in the ME regions of different categories. The standard deviations represent 1σ uncertainty. The values in parentheses are of a subset of Cat-I MEs with leading-edge speeds <516 $\mathrm{km\,s^{-1}}$.

Parameter	Cat-I (Cat-I Subset)	Cat-II	Cat-III
$< t >$ (h)	27±16(27±18)	22±10	25±13
$< N_p >$ ($\mathrm{cm^{-3}}$)	5.4±3.7(6.0±3.8)	5.9±4.2	4.6±3.3
$< v >$ ($\mathrm{km\,s^{-1}}$)	460±112(402±57)	396±88	402±65
$< T >$ (10^4K)	7.4±5.4(6.2±3.6)	6.4±9.6	4.8±3.0
$< B >$ (nT)	9.9±3.9(9.5±3.1)	9.9±2.9	8.0±3.1
$< P_{dyn} >$ (nPa)	2.2±1.7(2.0±1.4)	1.9±2.1	1.5±1.1
$< v >_{Upstream-sw}$ ($\mathrm{km\,s^{-1}}$)	382±81(345±44)	364±68	421±82
$< v >_{Upstream-fms}$ ($\mathrm{km\,s^{-1}}$)	64±26(53±18)	48±18	73±35
v_{LE} ($\mathrm{km\,s^{-1}}$)	483±118(416±56)	416±100	429±80
v_{exp} ($\mathrm{km\,s^{-1}}$)	26±38(12±26)	12±26	17±30
M_{pseudo}	1.7±1.2(1.5±1.1)	1.1±1.1	0.1±0.3
$M_{propagation}$	1.4±1.2(1.2±1.1)	0.7±0.9	-0.3±0.6
$M_{expansion}$	0.4±0.6(0.2±0.5)	0.3±0.5	0.3±0.6
$< \beta >_{Proton}$	0.2±0.2(0.2±0.2)	0.1±0.1	0.1±0.1

3) Cat-III MEs had almost the same average speeds as those driving Cat-II sheaths. However, they propagated in the fastest solar wind with the highest fast magnetosonic speed, i.e., in conditions that were the least ideal for driving a shock. The leading-edge speeds of Cat-III MEs were comparable to the upstream solar wind speed, which was consistent with these CMEs not driving any shocks. In addition, faster solar wind is less dense, and also the average expansion speed of Cat-III MEs was moderate. As a result, it was easier for the deflected solar wind at the nose of the ME to go around it, which is a possible physical explanation as to why these MEs also did not drive sheaths.

4) Except for their faster speeds, another significant difference between MEs associated with Cat-I and Cat-II sheaths was that Cat-I MEs were longer duration.

5) For Cat-I sheaths, the average magnetic field strength in the sheath (see Table 4.2) was higher than that in the ME by 13%, and the peak magnetic field occurred 60% of the time in the sheaths. For Cat-II sheaths, the magnetic field strength in the sheath was lower than that in the ME by 30%, and the peak magnetic field occurred only 25% of the time in the sheaths.

6) While the leading-edge speeds of the MEs organized the three categories reasonably well (see the top left panel in Figure 4.4), it was even better organized when we examined the distribution based on M_{pseudo} (see the bottom panel in Figure 4.4), as defined above. We did the binning of M_{pseudo} in a similar way to section 4.5.1. It was evident that leading-edge speeds of Cat-III MEs in the solar wind frame were considerably lower than the upstream fast magnetosonic speed ($M_{pseudo}<1$). The largest proportion of Cat-II MEs was found in the range of $1<M_{pseudo}<1.2$, whereas ∼57% of Cat-I MEs had $M_{pseudo}>1.2$.

4.7.2 Sheaths

We listed the average sheath parameters driven by Cat-I and Cat-II MEs in Table 4.2. Table 4.3 listed the results from the Welch's t-test (with 95% confidence level) to determine if differences between Cat-I and Cat-II sheaths were statistically different. In this section, we focused on the main differences between Cat-I and Cat-II sheaths, listing only statistically significant ones. We found the following results:

1) The compression in density and magnetic field in the sheath compared to the background solar wind was significantly higher for Cat-I sheaths than Cat-II sheaths. The level of compression (∼4) in density for Cat-I sheaths was unlikely to be explained only by the compression resulting from the associated shock since the shock compression ratio for a typical

Table 4.2: Averages and standard deviations of selected solar wind plasma and IMF parameters in the sheath regions of different categories. The standard deviations represent 1σ uncertainty. The values in parentheses are of a subset of Cat-I sheaths that are driven by MEs with leading-edge speeds <516 $\mathrm{km\,s^{-1}}$. $< Ratio >$: Ratio of the average values within the sheath to that in the upstream solar wind.

Parameter	Cat-I (Cat-I Subset)	Cat-II
$< t >$ (h)	9.3±4.9(9.3±5.2)	8.3±4.0
$< N_p >$ ($\mathrm{cm^{-3}}$)	14.4±8.0(15.8±8.2)	11.3±6.1
$< v >$ ($\mathrm{km\,s^{-1}}$)	477±113(411±57)	404±91
$< T >$ (10^5K)	2.0±1.6(1.2±0.9)	1.0±1.0
$< B >$ (nT)	11.2±4.6(9.8±3.3)	6.9±2.6
$< B_{rms} >$ (nT)	0.3±0.2(0.3±0.2)	0.2±0.4
$< P_{dyn} >$ (nPa)	6.5±4.4(5.4±3.0)	3.8±2.6
$< Ratio >_{N_p}$	3.8±2.3(4.0±2.1)	2.2±1.4
$< Ratio >_v$	1.3±0.2(1.2±0.1)	1.1±0.1
$< Ratio >_T$	3.4±2.6(3.1±2.4)	2.1±1.5
$< Ratio >_B$	2.6±1.4(2.7±1.5)	1.8±0.9
$< Ratio >_{P_{dyn}}$	6.4±4.7(6.0±4.2)	2.8±2.0

ME-driven shock is ∼2. This indicated follow-up compression after the shock, consistent with the numerical simulation of Manchester et al. (2005).

2) Cat-I sheaths were made of denser (by 27%), hotter (by 100%), and more magnetized (by 62%) plasma than Cat-II sheaths. The sheath plasma was faster (by 18%) and had a higher dynamic pressure (by 71%) in Cat-I than Cat-II sheaths. The level of fluctuations in the magnetic field was, however, not statistically different.

3) The average sheath durations for Cat-I and Cat-II sheaths were similar, at ∼8-9 hours. As Cat-I sheaths were faster, their sizes were statistically larger than Cat-II sheaths.

4.7.3 Comparison of Cat-II sheaths and Cat-I sheaths driven by slower MEs

We next investigated if the differences between Cat-I and Cat-II sheaths were due to the different speeds of the drivers, or they were inherently different. To do so, we created a subset of Cat-I MEs, where the leading-edge speeds were <516 $\mathrm{km\,s^{-1}}$ (average leading-edge speed of Cat-II MEs was 416 ± 100 $\mathrm{km\,s^{-1}}$). We listed the average values of this subset

Table 4.3: Measure of statistical difference with 95% confidence level (p-values from the Welch's t-test) between selected solar wind plasma and IMF parameters. P-values representing statistical differences are made bold.

Parameter	Cat-I & Cat-II	Cat-I Subset & Cat-II
$< Size >_{Sheath}$	**0.0020**	0.1253
$< B >_{Sheath}$	**4.2E-10**	**3.1E-06**
$< N_p >_{Sheath}$	**0.0134**	**0.0021**
$< v >_{Sheath}$	**0.0003**	0.6806
$< T >_{Sheath}$	**2.8E-05**	0.2126
$< P_{dyn} >_{Sheath}$	**2.1E-05**	**0.0067**
$< B_{rms} >_{Sheath}$	0.1780	0.6056
$< v >_{Upstream-sw}$	0.2190	0.1326
$< v >_{Upstream-fms}$	**0.0002**	0.1724
v_{LE}	**0.0016**	0.9976
v_{exp}	**0.0156**	0.9134
M_{pseudo}	**0.0065**	0.0952
$M_{propagation}$	**0.0007**	**0.0060**
$M_{expansion}$	0.3111	0.8011

in parentheses in the Cat-I column in Table 4.1 and Table 4.2. From comparing upstream conditions and ME speeds, we approximated that this subset of Cat-I sheaths and Cat-II sheaths were driven by similar MEs, propagating in the similar upstream solar wind (see Table 4.3). We did see that the average properties of Cat-II sheaths and sheaths of this subset were more similar to each other than Cat-I and Cat-II sheaths. This was true for the sheath size, speed, and temperature (see Table 4.3). However, the sheath density, magnetic field strength, and dynamic pressure remained more statistically elevated in Cat-I sheaths driven by slower MEs than in Cat-II sheaths (see Table 4.2 and Table 4.3). This highlighted intrinsic differences in the compression (of the density and magnetic field) associated with the presence or absence of a shock.

We expected the comparison between this subset of Cat-I sheaths and Cat-II sheaths to be statistically less significant, as they were driven by MEs with similar speeds. Except the sheath density and the upstream solar wind speed, we indeed observed higher p-values for all other examined parameters (see Table 4.3). From these p-values, we approximated that this subset of Cat-I sheaths and Cat-II sheaths were similar in many aspects, even though their formation mechanisms were supposed to be different, as Cat-I sheaths were driven by MEs which also drove shocks and Cat-II sheaths were associated with MEs that did not drive shocks.

4.8 Correlation analysis between the sheath and ME

We investigated any potential correlation between the average parameters of the structures. We applied a linear least-squares regression technique to test the correlation of the average parameters (proton density, solar wind speed, and magnetic field strength) within the sheath with that of the driving ME. We used the average ME speed in our correlation analysis to exclude the contribution of the expansion speed, similar to Gopalswamy (2008). For each category, we used two sets to examine the correlation of the sheath with its driver ME. The first set considered all CME types with quality index 0, 1, and 2 (see Section 3.7), and the second set considered CMEs with quality index 1 and 2 (see Table 4.4).

4.8.1 Correlation between the average sheath and ME properties

1) The average proton density of Cat-I sheaths showed modest (Correlation Coefficient or CC=0.50 - 0.75) positive correlation with the average proton density (CC=0.55) and magnetic field strength (CC=0.57, see in Figure 4.6) of the ME, which meant that sheaths driven by denser and stronger MEs tend to be denser as well. However, the average proton density of Cat-I sheaths did not have any sort of relationship with how fast the ME was propagating. This was surprising as the rate at which the ME accumulates solar wind material over its propagation was assumed to be dependent on the speed of the ME. On the other hand, the density and speed of general solar wind are typically anti-correlated, i.e., fast solar wind with lower density while slow solar wind with higher density. Thus, the two effects might have resulted in no clear correlation between the sheath density and ME speed. For Cat-II sheaths, the average proton density did not have any clear correlation with the average parameters

of the ME (see in Figure 4.6 for the correlation with the average magnetic field strength of the CME).

Table 4.4: Correlation coefficients of the linear least-squares regression between the average parameters of the structures (sheath and CME) for different categories. The values in parentheses refer to linear least-squares regression, including MEs with quality index 1 and 2 only. + indicates positive correlation with CC<0.25. - indicates negative correlation with CC<0.25. CCs>0.50 are made bold.

Parameter	Average $N_{p,Ejecta}$ Cat-I	Average $N_{p,Ejecta}$ Cat-II	Average B_{Ejecta} Cat-I	Average B_{Ejecta} Cat-II	Average v_{Ejecta} Cat-I	Average v_{Ejecta} Cat-II
$< N_p >_{Sheath}$	**0.55** (**0.52**)	+ (+)	**0.57** (**0.56**)	0.38 (0.37)	- (-)	- (-)
$< B >_{Sheath}$	+ (-)	+ (-0.25)	**0.64** (**0.62**)	**0.54** (0.34)	**0.60** (**0.63**)	**0.62** (**0.56**)
$< v >_{Sheath}$	-0.30 (-0.36)	+ (-0.32)	+ (+)	0.31 (+)	**0.91** (**0.93**)	**0.93** (**0.97**)

2) The average magnetic field strength of Cat-I sheaths also showed a modest relationship with the magnetic field strength (CC=0.64) and the average speed (CC=0.60, see in Figure 4.6) of the ME. The same was true for Cat-II sheaths. Sheaths of both categories did not have any substantial correlation with the average proton density of the ME.

3) The average speeds of Cat-I and Cat-II sheaths did not have any clear correlation with the average proton density and magnetic field strength of the ME. The average speeds in the sheaths for both categories only depended upon how fast the driving ME was propagating (CC=0.91 for Cat-I, CC=0.93 for Cat-II, see in Figure 4.6), which meant, as expected, a faster ME drives a faster sheath as well.

4.8.2 Correlation of the sheath size with ME Properties

We also examined the linear relationship of the sheath size (in AU) of Cat-I and Cat-II sheaths with the speed profile and associated Mach numbers of the ME (see Table 4.5 and Figure 4.7). The sheath size was approximated as the product of the average speed in the radial direction and the time interval through which the SC measured the sheath. Here,

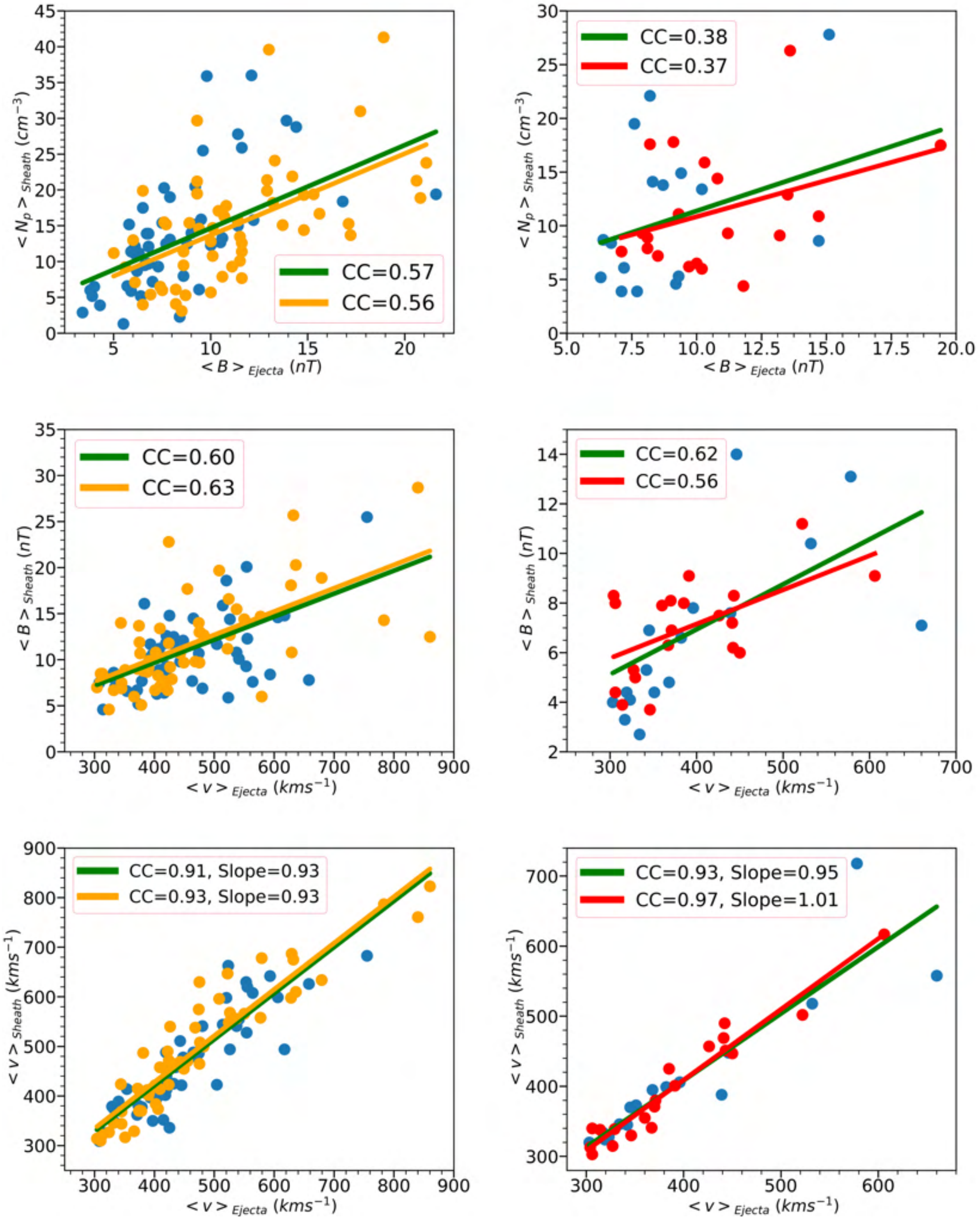

Figure 4.6: Scatter plots of selected average parameters for Cat-I (left panels) and Cat-II (right panels). Blue circles represent observations of CMEs with quality index 0. Orange (for Cat-I) and red (for Cat-II) circles represent observations of CMEs with quality index 1 and 2. The solid green line represents the best linear least-squares fit of the data set for all CME observations (with quality index 0, 1, and 2). The orange (for Cat-I) and red (for Cat-II) lines represent the same but only for observations of CMEs with quality index 1 and 2.

this approximation for the sheath size was dependent on the location where the sheath was crossed with respect to the nose of the ME.

Table 4.5: Correlation coefficients of the linear least-squares regression between the sheath size in radial direction (AU) with specific ME parameters for different categories and different combinations. (+) indicates positive correlation with CC<0.25, (-) indicates negative correlation with CC<0.25. CCs>0.50 are made bold.

Parameter	Sheath Size (AU)		
	Category	All MEs	MEs (Quality Index 1 & 2)
v_{LE} ($\mathrm{km\,s^{-1}}$)	Cat-I	0.39	0.44
v_{LE} ($\mathrm{km\,s^{-1}}$)	Cat-II	(+)	0.38
v_{LE} - $< v >_{Upstream-sw}$ ($\mathrm{km\,s^{-1}}$)	Cat-I	(+)	0.25
v_{LE} - $< v >_{Upstream-sw}$ ($\mathrm{km\,s^{-1}}$)	Cat-II	0.29	**0.65**
$< v >_{Ejecta}$ ($\mathrm{km\,s^{-1}}$)	Cat-I	(+)	0.28
$< v >_{Ejecta}$ ($\mathrm{km\,s^{-1}}$)	Cat-II	(+)	0.33
v_{exp} ($\mathrm{km\,s^{-1}}$)	Cat-I	0.42	0.48
v_{exp} ($\mathrm{km\,s^{-1}}$)	Cat-II	(+)	0.37
M_{pseudo}	Cat-I	(-)	(-)
M_{pseudo}	Cat-II	(+)	0.41
$M_{propagation}$	Cat-I	-0.25	(-)
$M_{propagation}$	Cat-II	0.25	0.39
$M_{expansion}$	Cat-I	0.30	0.35
$M_{expansion}$	Cat-II	(-)	0.25

The sheath size for both Cat-I and Cat-II sheaths showed a weak linear correlation with the speed profiles of the driving MEs. The best correlations for Cat-I MEs were found with the leading-edge speed and the expansion speed (∼0.4). In addition, both these correlations were positive, indicating that faster MEs had thicker sheaths. The correlations, in general, were poorer for Cat-II MEs. There existed similar poor correlations between the sheath size and the three aforementioned Mach numbers for both categories.

This poor correlation between the sheath size and the speed profile and associated Mach numbers of the driving ME was unexpected compared to the results of Russell & Mulligan (2002); Savani et al. (2011), where sheath thickness was approximated to decrease with the shock Mach number, meaning slower MEs tend to have thicker sheaths.

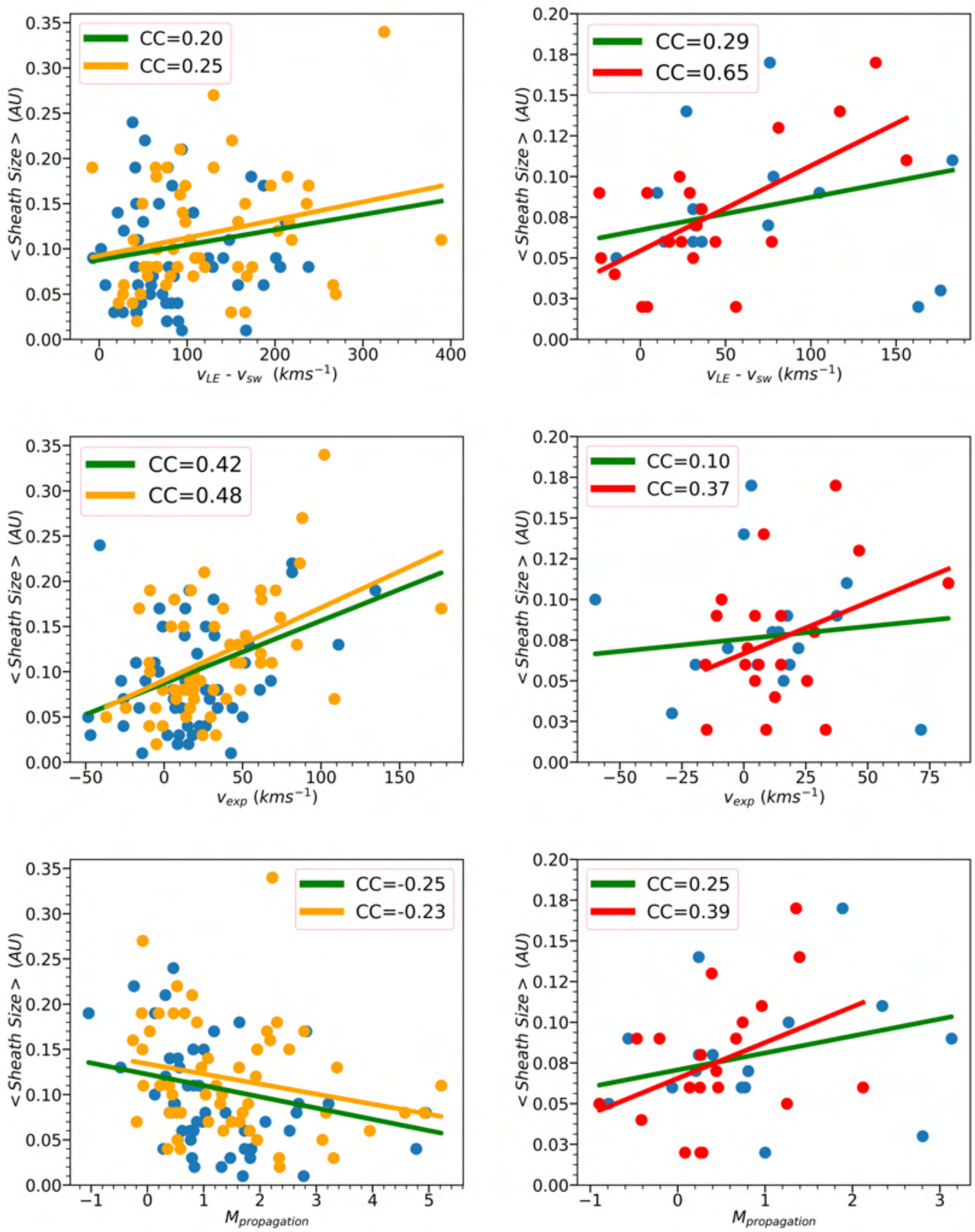

Figure 4.7: Scatter plots of the sheath size in radial direction (in AU) and selected CME parameters for Cat-I (left panels) and Cat-II (right panels). Blue circles represent observations of CMEs with quality index 0. Orange (for Cat-I) and red (for Cat-II) circles represent observations of CMEs with quality index 1 and 2. The solid green line represents the best linear least-squares fit of the data set for all CME observations (with quality index 0, 1, and 2). The orange (for Cat-I) and red (for Cat-II) lines represent the same but only for observations of CMEs with quality index 1 and 2.

CHAPTER 5

Categorization of ME-driven sheath regions near 1 AU

This work has been accepted for publication in *The Astrophysical Journal* on 5 July 2021.

5.1 Background

This work is a follow-up to the previous work (presented in Chapter 4), where we investigated the generic profiles of CME structures near 1 AU. In that work, the CMEs were categorized based on the presence of shocks and sheaths. We also explored statistical relationships between sheaths, preceded and not preceded by shocks, driven by MEs with comparable leading-edge speeds. At the conceptualization stage of this work, aspects of propagation and expansion sheaths were primarily explained with theoretical arguments (e.g. Siscoe & Odstrcil, 2008). This led to the framework of this work, to identify propagation sheaths (PSs) and expansion sheaths (ESs) near 1 AU and probe the physical differences between them with a statistical analysis based on in-situ measurements.

In this work, we followed a similar approach to Salman et al. (2020a) but performed a more in-depth analysis beyond looking at the correlation between the average sheath and ME properties. The focus was to examine the sheath-to-sheath variability and how specific properties of the MEs affect the sheath properties near 1 AU, with an extended analysis of ME-driven sheaths (preceded by shocks), based on two entirely different categorization schemes. The sheath boundaries listed in Jian et al. (2018) were used for the analysis, with minor adjustments for some events based on an ASIA and visual assessment (see Salman et al., 2020a). Data used for this work was the same as in Chapter 4.

5.2 Sheaths categorized by formation mechanisms

For the first categorization, we focused on the potential formation mechanisms of ME-driven sheaths. These sheaths are combinations of a PS, where the solar wind is deflected sideways at the nose of the magnetic obstacle and flows around it, and an ES, where the magnetic obstacle expands but does not propagate along with the background solar wind that causes the plasma to pile-up upstream of the ME (Siscoe & Odstrcil, 2008). In an attempt to quantitatively estimate that either the propagation or expansion of the MEs had a significant contribution in their formations, we categorized the sheaths with three ME Mach numbers, M_{prop}, M_{exp}, and M_{pseudo} (see Section 4.7.1), based on the propagation, expansion, and leading-edge speeds. The propagation speed does not include a contribution from expansion. Therefore, this removed any potential overlap between M_{prop} and M_{exp}. The reason for introducing M_{pseudo} was to ensure that the sheaths of the two groups have similar M_{pseudo} (i.e., similar ratios of the ME leading-edge speeds in the solar wind frame to the characteristic speeds in the solar wind). This ensured that the examined sheath properties of the two groups would only differ due to the relative importance of their potential formation mechanisms (propagation and expansion).

We identified 28 PSs (see Appendix C for the list) for which the $\mathrm{M}_{exp}\leq0.4$ and $\mathrm{M}_{prop}\geq0.6$. Similarly, we identified 18 ESs (see Appendix C for the list) where the reverse is the case, i.e., $\mathrm{M}_{prop}\leq0.4$ and $\mathrm{M}_{exp}\geq0.6$. Although these limits were somewhat subjective, if we observe the average values (see Table 5.1) for PSs ($\mathrm{M}_{prop}>1$ and $\mathrm{M}_{exp}\sim0$) and ESs ($\mathrm{M}_{exp}>1$ and $\mathrm{M}_{prop}\sim0$), this at least quantitatively ensured significant contribution from either propagation or expansion in forming these sheaths. Since the sheath properties are strongly correlated with the ME leading-edge speeds, we imposed one more criterion in categorizing these sheaths, which is $1<\mathrm{M}_{pseudo}<2$. Lugaz et al. (2017a) looked at specific cases of MEs driving shocks at 1 AU for which $\mathrm{M}_{pseudo}>1$ but $\mathrm{M}_{prop}<1$, i.e., where the propagation speed by itself was not sufficient to explain the formation of shocks. Here, we expanded on that study by considering both PSs and ESs. We had 60 sheaths that did not fall in either category, i.e., both propagation and expansion aspects of the ME kinematics played prominent roles in their formations. This provided further confirmation that typical ME-driven sheaths are "hybrid" sheaths, featuring aspects of both propagation and expansion (Siscoe & Odstrcil, 2008).

5.3 Sheaths categorized by variations in speeds

In the second scheme, we categorized the 106 ME-driven sheaths based on their temporal variations of speeds. The rationale behind this categorization was to search for sheath characteristics (based on their speed profiles) and then try to see if we could find differences in the associated shocks and MEs, rather than looking for different driving MEs and seeing if the sheaths were different. The initial grouping relied upon the visual identification of the sheath speed profile. We categorized these sheaths into those with constant (Category-A), increasing (Category-B), decreasing (Category-C), and complex (Category-D) speed profiles, throughout the entire interval of the sheath (see in Figure 5.1). These profiles were not anomalies, with a significant number of sheaths exhibiting these trends. However, this sort of visual categorization can be subjective and introduce selection bias. Therefore, in an attempt for a more rigid categorization, we performed a linear least-squares regression to identify quantifiable criteria for the categorization. We determined that the following two parameters of the regression model inherently categorized these sheaths into four distinct categories: the first parameter was the slope of the regression line relative to the average sheath speed, and the second parameter was the error in the linear fitting of the sheath speed relative to the average sheath speed. The reason behind normalizing these two parameters was to minimize the influence of the sheath speed itself on the categorization.

The speed profiles for three out of the four categories exhibited marked linearities. Therefore, for the quantitative categorization of these three categories, the first criterion was that the error* (error of the regression model relative to the average sheath speed) was less than 4%.

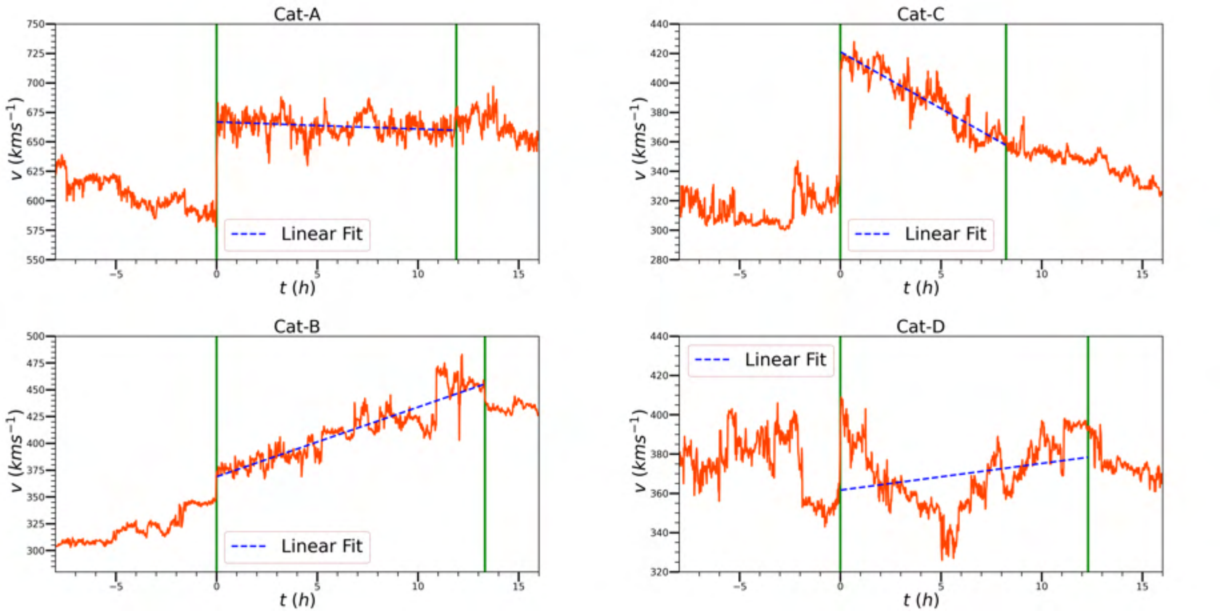

Figure 5.1: Speed variations within ME-driven sheath regions categorized with linear least-squares regression. The vertical green solid lines bound the sheath region. The navy dashed lines represent the best linear least-squares fits of the solar wind speeds within the sheath regions. ME arrival times: Cat-A on 2014 January 29 at 5:20 UT (STEREO-B), Cat-B on 2012 October 5 at 2:51 UT (STEREO-A), Cat-C on 2011 January 17 at 15:46 UT (STEREO-B), and Cat-D on 2014 February 25 at 12:16 UT (STEREO-A).

The second criterion was reliant upon the slope of the regression line. For Cat-A sheaths (constant speed profiles, the top left panel in Figure 5.1), the slope* (slope relative to the average sheath speed and in units of h^{-1}) fell within this range: $-0.4\%\ h^{-1} < \text{slope}^* < 0.4\%\ h^{-1}$. For Cat-B sheaths (increasing speed profiles, the bottom left panel in Figure 5.1), the slope* was greater than $0.4\%\ h^{-1}$. For Cat-C sheaths (decreasing speed profiles, the top right panel in Figure 5.1), the slope* was negative and less than $0.4\%\ h^{-1}$. The quantity $0.4\%\ h^{-1}$ can be explained in this way: for a typical sheath duration of 10 hours and an average sheath speed of 500 $\mathrm{km\,s^{-1}}$, a Cat-A sheath must have variations less than $\sim$20 $\mathrm{km\,s^{-1}}$, whereas larger variations would be categorized as a Cat-B or Cat-C sheath. For the last category or Cat-D sheaths (complex speed profiles, the bottom right panel in Figure 5.1), we only relied on the error* for categorization since their speed profiles did not exhibit any single definite linear trend. Therefore, the error of the regression model was expected to be significant. Cat-D sheaths, therefore, had values of error* that were greater than 4%. In total, we identified 26 Cat-A sheaths, 24 Cat-B sheaths, 20 Cat-C sheaths, and 36 Cat-D sheaths. We also examined whether these speed profiles correspond to PSs or ESs but found both PSs and ESs to be intermixtures of all these speed profiles. Regnault et al. (2020) categorized MEs into three groups based on Δv (the average ME speed in the solar wind frame). The SEA profiles for the speed within sheaths of their three ME groups resembled the speed profiles within sheaths of our categorization. They grouped the MEs based on Δv (similar to M_{prop}) and then looked at the associated sheaths, whereas we categorized the sheaths based on their speed profiles and then tried to find what caused them. In Regnault et al. (2020), superposed epoch profiles of sheaths, driven by MEs with low Δv, medium Δv, and high Δv showed a decreasing speed profile (similar to our Cat-C sheaths), constant speed profile (similar to our Cat-A sheaths), and increasing speed profile (similar to our Cat-B sheaths) respectively.

5.4 Propagation versus expansion sheaths

5.4.1 Comparison of average properties

To examine the statistical relationships between these two types of sheaths, we performed analysis of variance (ANOVA) on the 28 sheaths identified as PSs and the 18 sheaths identified as ESs in Section 5.2. ANOVA is a parametric test that compares the means of two or more independent groups to determine statistical evidence whether or not the associated group means are significantly different. We listed the results from ANOVA in Table 5.1. In Table 5.1, column 1 listed the examined parameters, column 2 listed the p-values from ANOVA that provided the measure of statistical significance (with 95% confidence) of a particular parameter, and columns 3 and 4 listed the average values for PSs and ESs respectively. In column 1, M_{ms} is the shock magnetosonic Mach number, M_{prop}, M_{exp}, and M_{pseudo} are the three ME Mach numbers, S_{sheath} is the sheath thickness (in the radial direction), and θ_{nr} is the angle that the shock normal made with the radial direction, which can be used as an approximation of SC crossing (see Paulson et al., 2012). We used the normal vector of the shock ($\hat{\boldsymbol{n}}$) listed in the IPshocks database (Kilpua et al., 2015a) to calculate this angle. We found the following from ANOVA:

1) Both types of sheaths were driven by MEs with similar magnetic field strengths, and magnetic field strengths within PSs and ESs were also similar.

2) ESs were statistically larger (in the radial direction).

3) In comparison with ESs, PSs were statistically denser, while the same was true for their associated MEs.

4) ESs were statistically faster.

Since θ_{nr} for both types of sheaths were almost identical (see Table 5.1), we emphasized that these differences are not likely byproducts of SC crossings (i.e., SC encountering different

Table 5.1: ANOVA showing the variation between sample means in two categories of ME-driven sheaths. The p-values listed here represent whether the variance between the means of the two categories is significantly different. P-values representing statistical significance (<0.05) are shown in bold. Note: PS=Propagation Sheath, ES=Expansion Sheath.

	ANOVA	Average Value	
Parameter	P-value	PS	ES
B_{ejecta} (nT)	0.11	9.60	8.20
N_{ejecta} (cm^{-3})	**0.00**	5.80	3.00
M_{ms}	0.19	1.37	1.17
M_{prop}	**0.00**	1.20	0.10
M_{exp}	**0.00**	0.00	1.00
M_{pseudo}	0.83	1.30	1.20
v_{sw} (kms^{-1})	**0.00**	351	445
v_{le} - v_{sw} (kms^{-1})	**0.03**	73	99
θ_{nr} (degrees)	0.94	31.1	30.7
S_{sheath} (AU)	**0.00**	0.09	0.15
B_{sheath} (nT)	0.16	9.80	8.70
N_{sheath} (cm^{-3})	**0.00**	16.30	8.40
v_{sheath} ($km\,s^{-1}$)	**0.01**	421	531

portions of sheaths). Characteristic features of PSs and ESs also did not seem to have any visible SCy dependence, as we found that a major proportion (>60%) of both types of sheaths occurred during the maximum phase of SCy 24. The upstream solar wind speed was statistically faster for ESs that could have resulted in lower sheath densities. In addition, the leading-edge speeds of MEs driving these sheaths in the solar wind frame (v_{le} - v_{sw}) were statistically different and could drive some of these differences (i.e., the radial thickness of sheaths).

5.4.2 Superposed epoch analysis

In this section, we examined the average features of PSs and ESs and their associated MEs with a SEA. Provided that variations of distributions are random, an averaging technique like the SEA can reveal common features that are not otherwise readily detectable. However, as these representative values are reductions of the actual distributions and run the risk of being skewed due to extreme outliers, interpretations from this technique need to be done with caution. These average features are only true for the corresponding sets of MEs (28 MEs with PSs and 18 MEs with ESs) that we have analyzed. This was why we plotted the median curves since the median values tend to be less sensitive to extreme outliers (see Regnault et al., 2020).

Since the sheath and the ME durations were different for each ME, we used two characteristic epochs: the start of the sheath and the start of the ME, to rescale individual timescales to the average timescale of each category. The average durations of PSs and ESs were 8.88h and 11.60h respectively. Then, we identified the typical ME timescales based on the average sheath to ME interval ratios (0.53 for PSs and 0.35 for ESs). This led to average ME timescales of 16.75h and 33.14h respectively for PSs and ESs. We selected a 2h time interval upstream of the shock as the background solar wind.

All parameters were binned into 75 time bins for both sheaths. These bins were then averaged to get the same number of data points within sheaths for each event. For PSs (ESs), we imposed 17 (13) time bins for the background solar wind and 142 (215) time bins for the ME. Lastly, the averaged values with the same bin number but corresponding to different MEs were averaged to obtain the generic profiles for the background solar wind, sheath, and ME.

Examining the SEA profiles for both types of sheaths (see Figure 5.2), we observed clear discontinuities for all parameters, accompanied by abrupt enhancements at the start of the sheath (shock boundary). The transitions from the solar wind to the sheath were more pronounced for PSs than ESs, except for the speed. Both types of sheaths featured elevated levels of magnetic field and plasma signatures throughout their intervals compared to the background solar wind, consistent with sheath profiles preceded by shocks (see Janvier et al., 2019; Kilpua et al., 2019; Salman et al., 2020a). The density profile for the expansion sheaths showed compression near the leading-edge, displaying evidence of ME expansion (Owens, 2020).

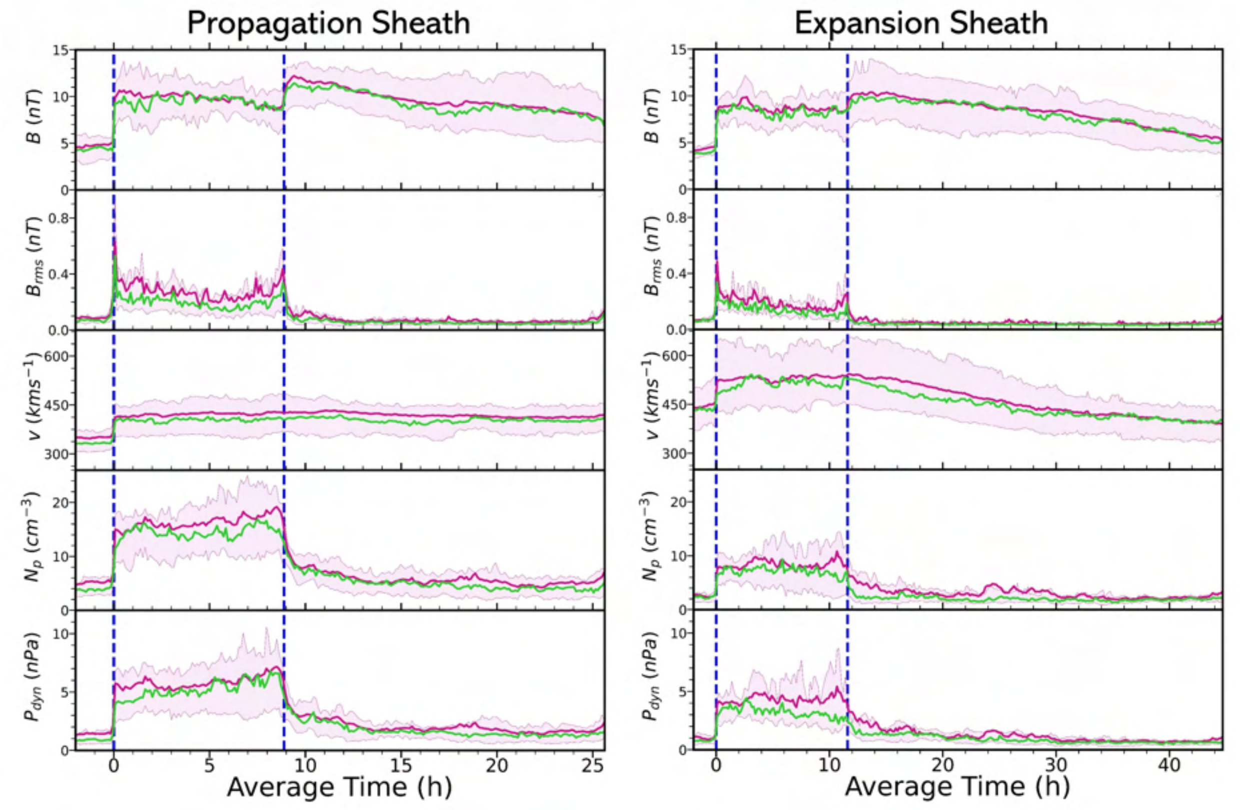

Figure 5.2: Superposed epoch profiles for 28 MEs with propagation sheaths (left panels) and 18 MEs with expansion sheaths (right panels). The panels show (from top to bottom) the magnetic field strength, total root-mean-square of magnetic field fluctuations, speed, proton density, and dynamic pressure. The purple curves show the average values, green curves show the median values, and shaded regions indicate the interquartile ranges. The vertical navy dashed lines bound the sheath region. The region to the left of the first vertical navy dashed line represents the upstream solar wind, and the region to the right of the second vertical navy dashed line represents the ME.

Investigating the signatures of magnetic field fluctuations for both types of sheaths, we observed two prominent peaks: at the start and end of the sheath, consistent with the findings of Masías-Meza et al. (2016); Salman et al. (2020a) for sheaths preceded by shocks. However, the fluctuations differed in trends for the two sheaths. For ESs, the magnetic field fluctuations corresponded to a nearly uniform decrease for the entirety of the sheath. In contrast, the magnetic field fluctuations for PSs were associated with bi-linear trends.

The abrupt transitions in the magnetic field strength, proton density, and dynamic pressure (see first, fourth, and fifth panel in Figure 5.2) at the front of the MEs were also more pronounced for PSs than ESs. For both types of sheaths, the magnetic field strengths at the leading-edges were higher than the rear, leading to asymmetric magnetic field profiles inside the MEs (see Démoulin et al., 2008). Démoulin et al. (2020) suggested that these asymmetric magnetic field profiles could occur due to a stronger compression on one side of the ME. For ESs, the speeds in the MEs monotonically decreased, leading to higher leading-edge speeds than trailing edge speeds (see the third panel on the right in Figure 5.2), in resemblance with the typical expansion undergone by MEs near 1 AU (Gulisano et al., 2010). In contrast, speeds in MEs driving PSs were constant due to minimal expansion.

5.5 Analysis of sheaths with distinct speed variations

5.5.1 Solar cycle dependence

We examined any potential SCy dependence of the occurrence of MEs with distinct speed variations in their sheaths and measured by either of the twin STEREO SC (see Figure 5.3). Since the ME counts for 2007 - 2009 were considerably low, we combined the ME counts in this interval for a more robust statistic. The total ME count (from STEREO-A and STEREO-B) in 2014 had contributions from STEREO-B for the first 9 months only, as communications with STEREO-B were lost on October 1.

During the minimum phase, we only observed the occurrence of MEs associated with Cat-A and Cat-B sheaths.

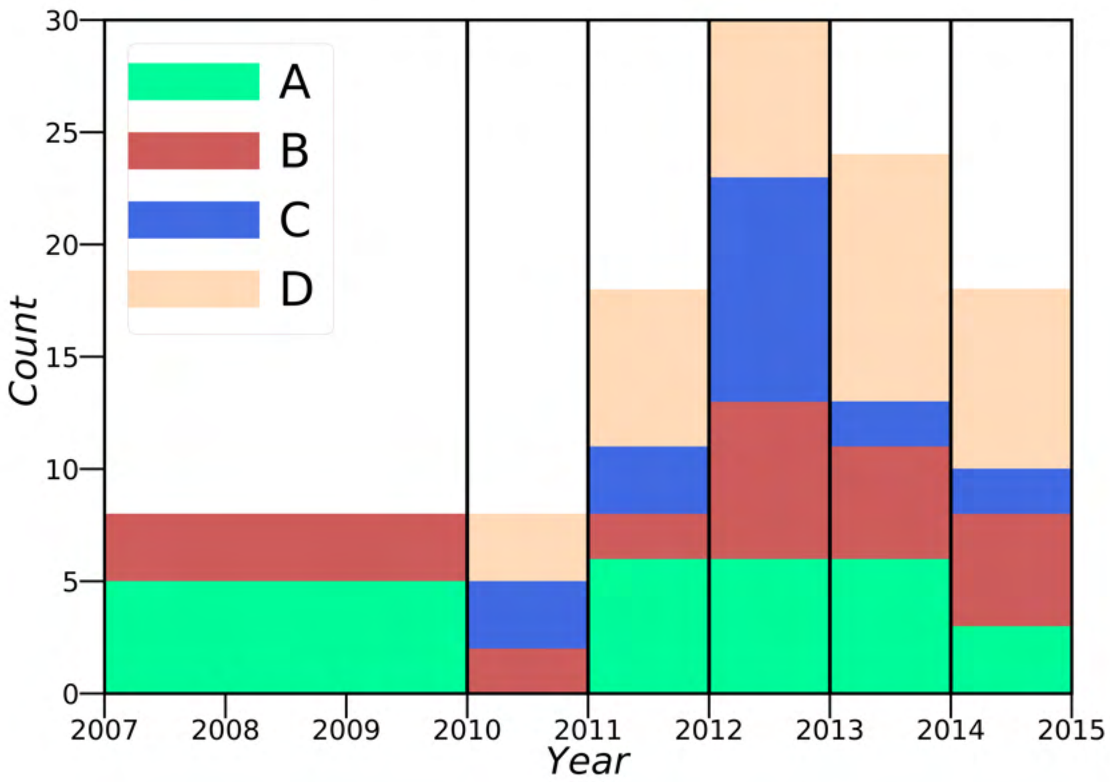

Figure 5.3: Solar cycle evolution of the annual occurrence rates of MEs associated with sheaths exhibiting the four distinct speed variations.

The non-existence of MEs associated with Cat-C and Cat-D sheaths in this time interval was somewhat unexpected. Apart from that, the occurrence rates of MEs associated with all these sheaths somewhat followed similar SCy variations, with increasing trends coinciding with the rising phase and peaking near/at solar maximum. The occurrence rate of MEs associated with Cat-A sheaths mostly remained constant throughout the entire period.

5.5.2 Superposed epoch analysis

Similarly to Section 5.4.2, we also performed SEA for the four categories of sheaths (see Figure 5.4 and Figure 5.5), as categorized in Section 5.3. The average duration of Cat-A, Cat-B, Cat-C, and Cat-D sheaths were 10.38h, 6.64h, 8.00h, and 10.95h respectively. The average sheath to ME interval ratios of 0.47, 0.36, 0.41, and 0.49 (in the same order) led to typical ME timescales of 22.08h, 18.44h, 19.50h, and 22.35h. Here, we also had 75 time bins within sheaths. The number of time bins for the background solar wind for Cat-A, Cat-B, Cat-C, and Cat-D sheaths were 15, 23, 19, and 14 respectively, and the number of time bins for the MEs were 160, 208, 183, and 153 respectively.

The observed higher speeds in the rear than in the front for Cat-B sheaths were consistent with Regnault et al. (2020), who found similar profiles for high Δv MEs. They suggested this occurred due to a fast ME compressing the sheath.

The variations in the magnetic field across the sheaths were similar for all categories. The magnetic field profiles of the MEs for all categories were asymmetric (i.e., stronger magnetic field at the front than in the rear). Even though Cat-A sheaths were associated with slow MEs, their MEs did not have symmetric magnetic field profiles, as found by Masías-Meza et al. (2016) for slow MEs.

For Cat-B sheaths, we observed a density profile with two peaks, one just downstream of the shock and one close to the ME (see Kilpua et al., 2017). Other categories had more monotonic variations of densities, with a nearly constant profile for Cat-A sheaths and decreasing profiles for Cat-C and Cat-D sheaths. The transition from the sheath to the ME for Cat-C sheaths was not as abrupt as expected (see third and fourth panels on the left in Figure 5.5), possibly due to magnetic erosion at the front of the ME (e.g. Ruffenach et al., 2015). The peak in density near the ME leading-edge for Cat-B sheaths was an example of "Pile-Up Compression" (PUC) region (see Das et al., 2011). This PUC region was accumulated near the Sun (Kilpua et al., 2017), primarily due to a larger ME expansion.

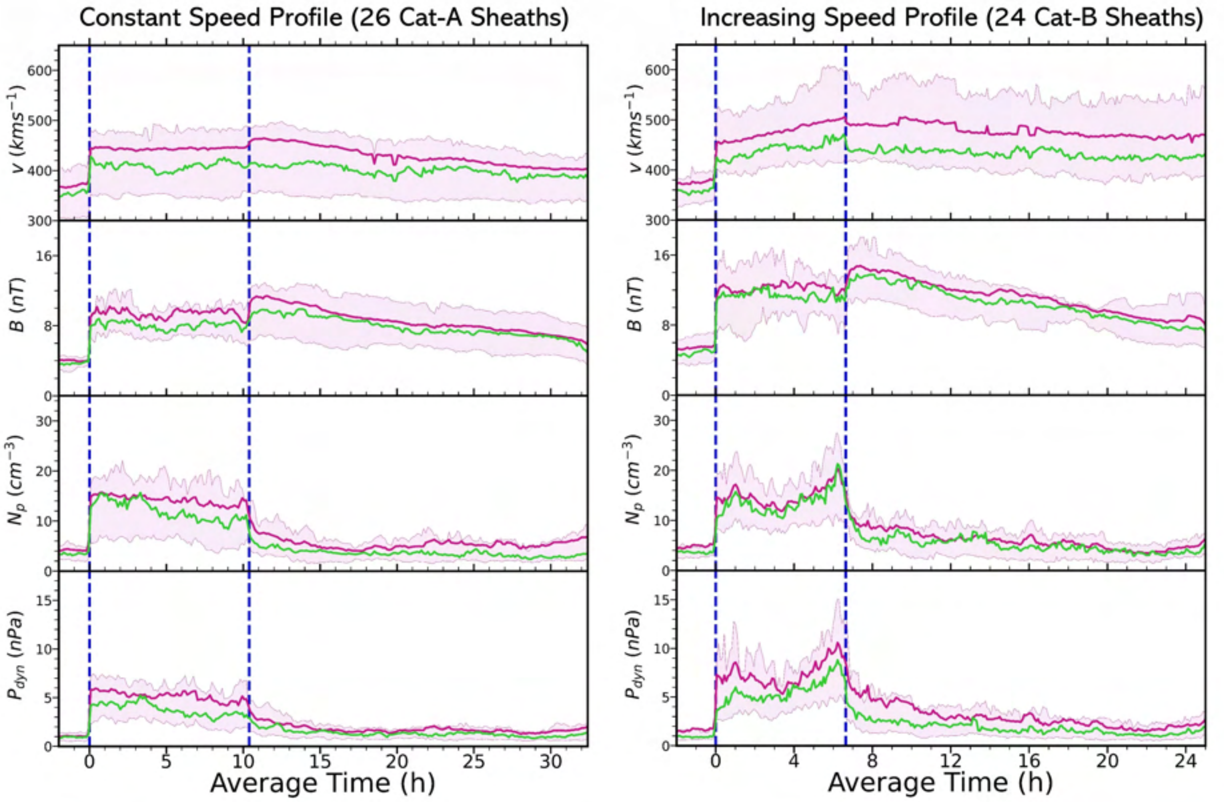

Figure 5.4: Superposed epoch profiles for 26 MEs with Cat-A sheaths (left panels) and 24 MEs with Cat-B sheaths (right panels). The panels show the speed, magnetic field strength, proton density, and dynamic pressure from top to bottom. The purple curves show the average values, the green curves show the median values, and the shaded regions indicate the interquartile ranges. The vertical navy dashed lines bound the sheath region. The region to the left of the first vertical navy dashed line represents the upstream solar wind, and the region to the right of the second vertical navy dashed line represents the ME.

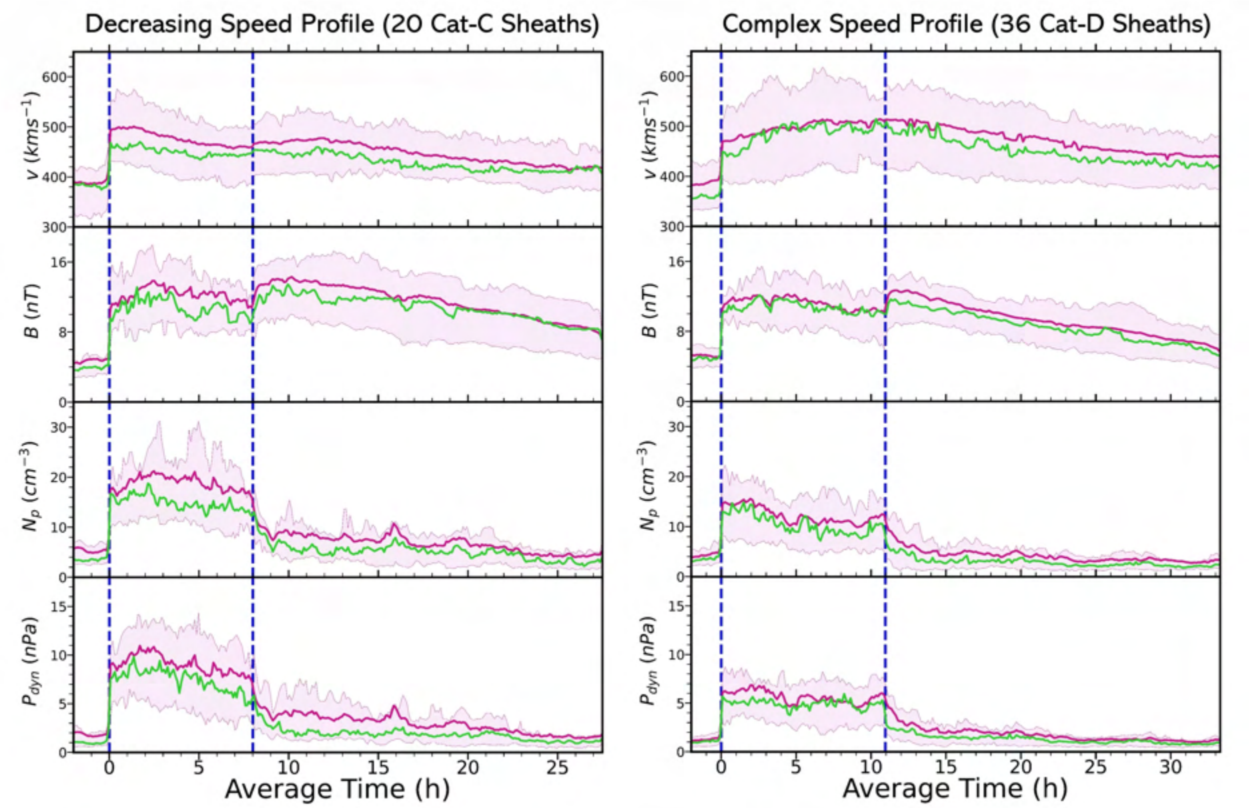

Figure 5.5: Superposed epoch profiles for 20 MEs with Cat-C sheaths (left panels) and 36 MEs with Cat-D sheaths (right panels). The panels show the speed, magnetic field strength, proton density, and dynamic pressure from top to bottom. The purple curves show the average values, the green curves show the median values, and the shaded regions indicate the interquartile ranges. The vertical navy dashed lines bound the sheath region. The region to the left of the first vertical navy dashed line represents the upstream solar wind, and the region to the right of the second vertical navy dashed line represents the ME.

5.5.3 Statistical relationships in terms of shock parameters

In this section, we investigated whether the shock parameters could determine or significantly affect the properties of the following sheaths. Since the sheaths analyzed in this work were all preceded by shocks, the sheaths were composed of shocked and compressed solar wind plasma. Therefore, one could expect the sheath properties to correlate with the properties of the preceding shocks strongly. However, some sheath portions might have only contained compressed (not shocked) solar wind plasma, depending on the radial distance where the shock formed. Similar to Section 5.4.1, we performed ANOVA to identify statistically significant relationships between these four categories of sheaths, in terms of the shocks that preceded them.

In Table 5.2, B_{down}/B_{up} and N_{down}/N_{up} are the downstream-to-upstream ratios of the magnetic field strength and proton density respectively, v_{shock} is the shock speed in a rest frame, Δv is the solar wind speed jump, M_{ms} is the shock magnetosonic Mach number, θ_{Bn} is the angle between the shock normal and the upstream magnetic field, and θ_{nr} is the angle between the shock normal and the radial direction. The upstream and downstream values were calculated as averages in 8-min time intervals upstream (from 9 minutes to 1 minute before the shock arrival) and downstream (from 2 minutes to 10 minutes after the shock arrival) of the shocks. These parameters (except θ_{nr}) were listed from the IPshocks database Kilpua et al. (2015a).

It was an unexpected result that the shocks of the four categories were similar in almost all measured aspects (see Table 5.2), and thus, shock parameters were not a useful distinguishing feature for these sheaths. However, ANOVA revealed that some of these speed variations could be possible manifestations of the nature of SC measurements (characterized by θ_{nr}), depending on the portion of the sheath encountered by the measuring SC. As this was the only relationship that we found to be statistically significant (p-value=0.01), we ran Tukey's honestly significant difference (HSD) post hoc test. Tukey's HSD post hoc test compares all possible pairs of means and controls the experiment-wise error rate (α=0.05). From this test, we saw that sheaths with linear trends of speed variations (Cat-A, Cat-B, and Cat-C) were not statistically different from one another in terms of SC measurements (the three p-values for pairwise comparisons were >0.9). This test also showed that only two pairs had statistically significant differences: i) Cat-B and Cat-D, with p-value=0.03, and ii) Cat-C and Cat-D, with p-value=0.04.

Table 5.2: Average values of selected parameters associated with shocks preceding the four categories of ME-driven sheaths. The p-values listed here represent whether the variance between the means of the four categories is significantly different (from ANOVA). P-values representing statistical significance (<0.05) are shown in bold.

	Average Value				ANOVA
Parameter	Cat-A	Cat-B	Cat-C	Cat-D	P-value
B_{down}/B_{up}	2.31	2.14	2.55	2.44	0.59
N_{down}/N_{up}	3.96	3.02	3.72	3.75	0.29
v_{shock} ($\mathrm{km\,s^{-1}}$)	423	464	478	402	0.10
Δv ($\mathrm{km\,s^{-1}}$)	76	75	98	77	0.45
M_{ms}	1.35	1.55	1.72	1.40	0.37
θ_{Bn} (degrees)	57	67	60	64	0.53
θ_{nr} (degrees)	26	24	24	37	**0.01**

As Cat-A, Cat-B, and Cat-C sheaths were not statistically different for θ_{nr}, the distances from the noses of the shocks at which the SC crossings occur were presumably not the primary drivers of the differences described in this section. In this sense, it differed from the analysis of Paulson et al. (2012), which attributed Cat-B sheaths (increasing speed profiles) to the possibility of crossings away from the noses. Only Cat-D sheaths, which were sheaths that did not fit with linear trends of speeds, may be associated with SC crossings further away from the noses of the shocks (as was clear from the larger θ_{nr}). This analysis also pointed towards the hypothesis that complex speed profiles within sheaths (Cat-D) were more likely for crossings at larger distances from the noses of the shocks.

5.5.4 Statistical differences in terms of sheath and ME parameters

In this section, we attempted to identify whether the speed variations within sheaths were associated with intrinsic differences of the CME structures. As shown in Table 5.3, we found that there were several statistically significant differences between the four categories. ANOVA revealed that:

Table 5.3: Average values of the selected sheath and ME parameters associated with the four categories of ME-driven sheaths. The p-values listed here represent whether the variance between the means of the four categories is significantly different (from ANOVA). P-values representing statistical significance (<0.05) are shown in bold.

	Average Value				ANOVA
Parameter	Cat-A	Cat-B	Cat-C	Cat-D	P-value
B_{ejecta} (nT)	8.5	11.2	11.5	9.2	**0.02**
N_{ejecta} (cm^{-3})	5.5	6	6.8	4.2	**0.04**
v_{ejecta} ($km\,s^{-1}$)	429	482	446	475	0.27
M_{pseudo}	1.45	1.94	1.33	2.09	0.07
v_{exp} ($km\,s^{-1}$)	25	14	21	34	0.11
S_{sheath} (AU)	0.11	0.08	0.09	0.13	**0.00**
B_{sheath} (nT)	9.4	12.3	12.3	11.1	0.10
N_{sheath} (cm^{-3})	14.2	14.8	18.7	12.4	**0.04**
v_{sheath} ($km\,s^{-1}$)	444	478	477	500	0.30

1) The magnetic field strength and density of the MEs had statistically significant differences between the categories. For both these parameters, we ran Tukey's HSD post hoc test for pairwise comparisons. We only found the density of the MEs, associated with Cat-C and Cat-D sheaths to be statistically different from one another (with p-value=0.04).

2) The ME propagation and expansion speeds were similar between the categories. Therefore, these sheaths exhibited such distinct trends of variations, despite the driving MEs propagating with similar average and expansion speeds.

3) The radial thickness and density of the four categories of sheaths were statistically different. With Tukey's HSD post hoc test, we found that the radial thickness of Cat-B and

Cat-D sheaths (with p-value=0.00) and density within Cat-C and Cat-D sheaths (with p-value=0.02) were statistically different from one another.

The findings presented in this section pointed out the fact that sheaths with linear trends of speeds were statistically similar to one another. The statistical differences only existed between sheaths with non-linear trends of speeds (Cat-D) and sheaths with linear trends of speeds (Cat-B and Cat-C).

5.5.5 Influence of ME parameters in driving distinct speed variations

In this section, we measured the significance of the four ME parameters with the lowest p-values (B_{ejecta}, N_{ejecta}, M_{pseudo}, and v_{exp}, see Table 5.3) for a sheath to be identified as a specific category, with logistic regression (LR). LR is a predictive linear algorithm and explains the relationship between a dependent (or response) variable that is dichotomous and one or more independent (or predictor) variables. Therefore, LR can be used for classification purposes. In our case, we used the LR analysis to assess the dependency of the binary outcome of the response variable (whether a sheath will be identified as a specific category or not) on the predictor variables (the four ME parameters, see Table 5.4), in a similar manner to Riley & Richardson (2012). They also used LR analysis to identify the likelihood for a ME to be classified as a MC or not based on several predictor variables.

Table 5.4 summarized the LR analysis. The estimated regression coefficients (column 2 in Table 5.4) for the predictor variables represented the effect of a unit change in a predictor variable (when the other predictor variables were held constant) in the log odds of the response variable, with 95% confidence. The sign of a coefficient represented the direction of the relationship between a predictor variable and the response variable. A positive coefficient would generally indicate that the event was more likely to happen with the increase in a predictor variable (when the other predictor variables in the model did not change). The p-values (column 5 in Table 5.4) provided the measure of statistical significance (with 95%

confidence) of a particular ME parameter. The intercepts in Table 5.4 represented the log of the odds of the response variables when all the predictor variables were 0.

Table 5.4: Logistic regression models for categorization of ME-driven sheaths. Column one lists the predictor variables, column two gives the estimated value of the regression coefficient for each predictor variable, column three gives the standard errors for these estimates, column four gives the results of the Chi-squared test, and column five lists the p-values. P-values representing statistical significance (<0.05) are shown in bold.

Parameter	Estimate	Std. Error	Chi-Square	P-value
For log odds of Cat-A/Not Cat-A				
Intercept	0.3502	0.765	0.21	0.6471
B_{ejecta} (nT)	-0.1691	0.0858	3.88	**0.0489**
N_{ejecta} (cm^{-3})	0.0936	0.0781	1.44	0.2308
M_{pseudo}	-0.2446	0.2414	1.03	0.3109
v_{exp} ($km\,s^{-1}$)	0.0003	0.0068	0.00	0.9600
For log odds of Cat-B/Not Cat-B				
Intercept	-2.1423	0.7413	8.35	0.0039
B_{ejecta} (nT)	0.0828	0.0639	1.68	0.1948
N_{ejecta} (cm^{-3})	0.0028	0.0677	0.00	0.9666
M_{pseudo}	0.1487	0.2081	0.51	0.4749
v_{exp} ($km\,s^{-1}$)	-0.0134	0.0082	2.66	0.1029
For log odds of Cat-C/Not Cat-C				
Intercept	-2.8609	0.8585	11.1	0.0009
B_{ejecta} (nT)	0.1802	0.0784	5.28	**0.0215**
N_{ejecta} (cm^{-3})	0.1624	0.0818	3.95	**0.0470**
M_{pseudo}	-1.0790	0.4091	6.96	**0.0084**
v_{exp} ($km\,s^{-1}$)	0.0083	0.0086	0.95	0.3296
For log odds of Cat-D/Not Cat-D				
Intercept	-0.0426	0.7140	0.00	0.9524
B_{ejecta} (nT)	-0.0701	0.0646	1.18	0.2781
N_{ejecta} (cm^{-3})	-0.1900	0.0874	4.72	**0.0297**
M_{pseudo}	0.5164	0.2063	6.27	**0.0123**
v_{exp} ($km\,s^{-1}$)	0.0037	0.0063	0.34	0.5587

From the LR analysis, we inferred that the following ME parameters had marked influences on the categorization: B_{ejecta}, N_{ejecta}, and M_{pseudo}. This provided clues as to which physical processes caused such speed variations. However, it is important to note that LR only provides statistical evidence since higher p-values do not mean that a particular parameter (e.g. ME expansion speed) is not significant. It only represents the absence of statistical evidence or undetected evidence by the statistical technique used (see Riley & Richardson, 2012). From the LR analysis, the likelihood of the categorization depended on:

a) MEs with strong magnetic fields were less likely to drive Cat-A sheaths.

b) None of these parameters had any statistical influence for a sheath to be categorized as Cat-B.

c) MEs with strong magnetic fields and high densities were likely to drive Cat-C sheaths. In addition, MEs with high Mach numbers (M_{pseudo}) were less likely to drive Cat-C sheaths.

d) MEs with high Mach numbers (M_{pseudo}) were likely to drive Cat-D sheaths. In addition, MEs with high densities were less likely to drive Cat-D sheaths.

To summarize, LR analysis suggested that the physical reasons for the categorization were considerably coupled to the magnetic field strengths and the leading-edge speeds in the solar wind frame (computed as M_{pseudo}) of the associated MEs. The reason for not including N_{ejecta} here was that even when this parameter was statistically significant (in the categorization of Cat-C and Cat-D sheaths), it was still the least influential among the other parameters (higher p-values).

5.5.6 Comparison of the multivariate method with in-situ observations

In the previous section, we used LR to assess the statistical influences of four ME parameters on our categorization. However, the LR analysis relied on our categorization in the first place. Therefore, it was important to identify whether the parameters M_{pseudo} and B_{ejecta} could distinguish the MEs from one another or the predictions from the LR analysis were simply outcomes of selection bias.

To address this, we presented the four categories of sheaths as a function of the magnetic field strengths and Mach numbers (M_{pseudo}) of the associated MEs (see Figure 5.6). Although the plot did not fully separate the four sheath categories, with considerable overlaps

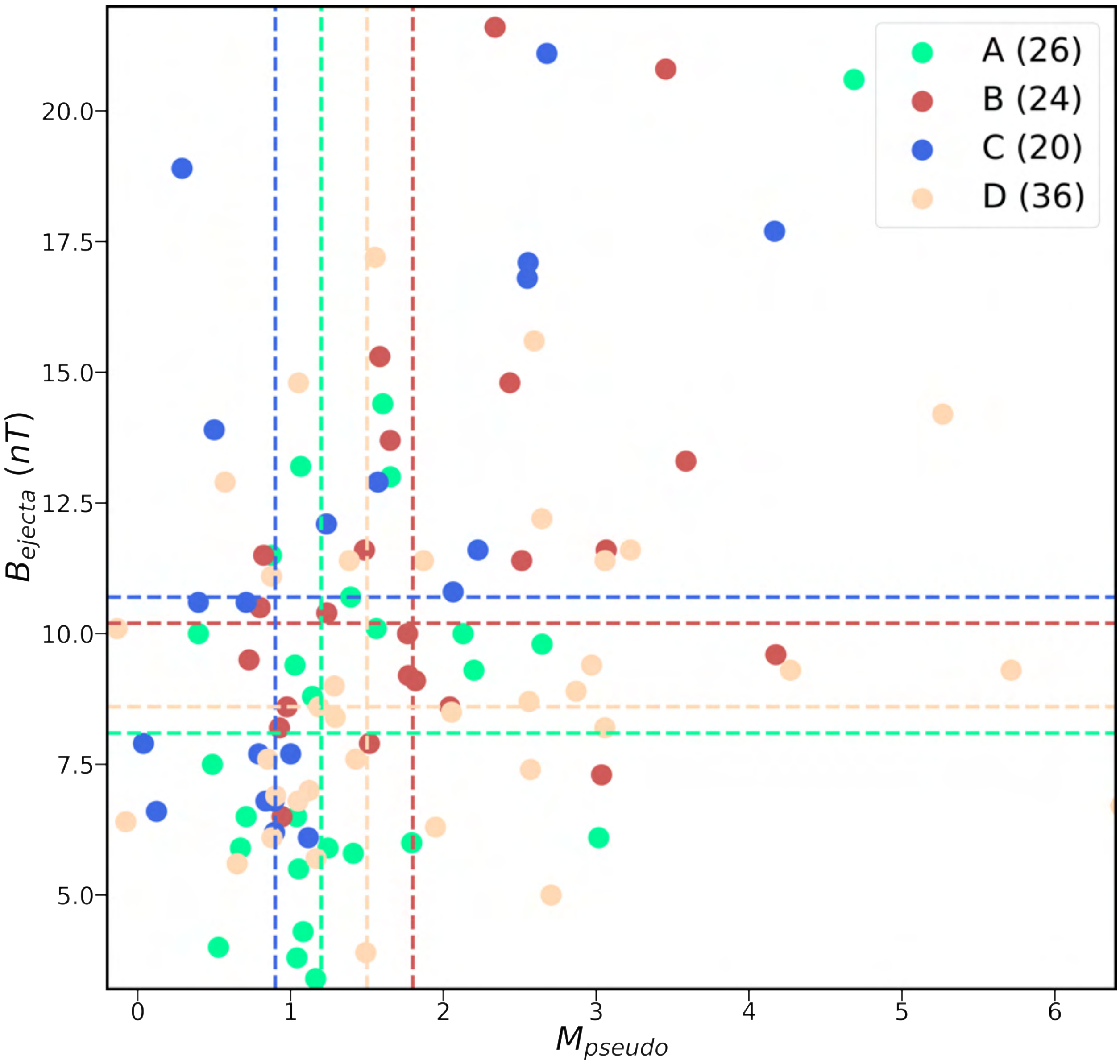

Figure 5.6: Distribution of the 106 MEs (driving both shocks and sheaths near 1 AU) measured by either of the twin STEREO spacecraft from 2007-2016, as a function of the magnetic field strength and Mach number (M_{pseudo}) of the associated MEs. The MEs are color-coded according to the four sheath categories. The horizontal and vertical dashed lines represent the medians of the magnetic field strength and Mach number (M_{pseudo}) of each category.

between the distributions, the trends (represented with horizontal and vertical dashed lines in Figure 5.6) were noticeable. This plot demonstrated that statistical predictions mirror the actual distributions well, with an apparent dependence on M_{pseudo} and B_{ejecta} for the categorization. We observed the following:

a) Cat-A sheaths were likely to be driven by MEs with moderate M_{pseudo} and weaker magnetic fields.

b) Cat-B sheaths were likely to be driven by MEs with a higher M_{pseudo} and stronger magnetic fields.

c) Cat-C sheaths were likely to be driven by MEs with a lower M_{pseudo} and stronger magnetic fields.

d) Cat-D sheaths were likely to be driven by MEs with moderate M_{pseudo} and weaker magnetic fields.

CHAPTER 6

Multi-spacecraft measurements of CME structures

This chapter is formed from the publications Salman et al. (2020b) and Lugaz et al. (2020a).

6.1 Background

Coronal magnetic field and plasma carried by a CME in the heliosphere has distinctive signatures with a large amount of variation. However, except for a few studies that used multi-point SC observations, CME measurements are largely restricted to single-point observations in space (see also discussion in Lugaz et al., 2018). Given the localized nature of CME observations, global configuration of a CME can be difficult to extrapolate as it is not always clear which part of the CME is being sampled, as a single SC can only sample a narrow trajectory through the larger CME structure (e.g. Reinard et al., 2012). Also, the motion of a CME in the solar wind depends on the heliospheric environment it encounters during its propagation (e.g. Kilpua et al., 2012; Temmer et al., 2011). Therefore, CME signatures observed with near-Earth in-situ instruments can drastically change from its coronal counterpart or other measurements in the inner heliosphere, because of the effects (but not limited to) mentioned in Section 3.4 of Chapter 3.

As a result, tracking signatures of the same CME over multiple heliocentric distances can provide the best insight to the governing physics behind CME propagation and radial evolution in the heliosphere. Understanding the nature of this radial evolution can provide important information about the propagation and interaction of CMEs as MHD structures in the heliosphere and how these structures interact with other planets' space environments

(Bothmer & Schwenn, 1998; Liu et al., 2005; Good et al., 2015; Winslow et al., 2015). However, radial coalignment of multiple SC observing the same CME at different heliocentric distances is inherently rare (Vršnak et al., 2019). At the conceptualization stage of this work, multi-SC analysis of CMEs were few and far between (e.g. Burlaga et al., 1981; Cane et al., 1997; Farrugia et al., 2011; Good et al., 2015, 2018; Janvier et al., 2019; Kilpua et al., 2011; Möstl et al., 2009a,b; Möstl, 2015; Prise et al., 2015; Wang et al., 2018; Winslow et al., 2016, 2018), primarily focused on case studies and statistical approaches to infer the radial evolution of CMEs. To the best of our knowledge, there was no comprehensive catalog of CMEs observed in conjunction. The objective of this work was to fill this vacuum and provide the community with a comprehensive catalog of radially aligned CMEs. We listed 47 CMEs in radial alignment, observed with at least two SC (MESSENGER, *Venus Express*, STEREO, and/or *Wind*/ACE) in the inner heliosphere. Recent studies, focused on multi-SC observations of CMEs at varying SC separations have expanded the number of aligned CMEs (e.g. Good et al., 2019; Vršnak et al., 2019) and provided newer insights into the comprehension of the heliospheric evolution of CMEs (even beyond Earth's orbit). In addition, present missions such as PSP, SO, and BepiColombo already have (see an example multi-SC observation of a CME in Figure 6.1) and will present more opportunities to complete the catalog of multi-point detected CMEs.

In this work, we combined two distinct classes of research: multi-SC measurements of the same CME with the SC at the same radial distance (e.g. Burlaga et al., 1981; Möstl et al., 2009a; Kilpua et al., 2011) and multi-SC measurements of the same CME with the SC at the same longitude (e.g. Farrugia et al., 2011; Good et al., 2015; Möstl, 2015; Prise et al., 2015; Winslow et al., 2016; Good et al., 2018; Wang et al., 2018; Winslow et al., 2018). An extensive catalog also meant less reliance on statistical techniques to examine the evolution of CME structures, as was the case for previous studies (e.g. Winslow et al., 2015; Janvier et al., 2019). This also enabled us to evaluate significant deviations of individual CMEs from overall statistical trends.

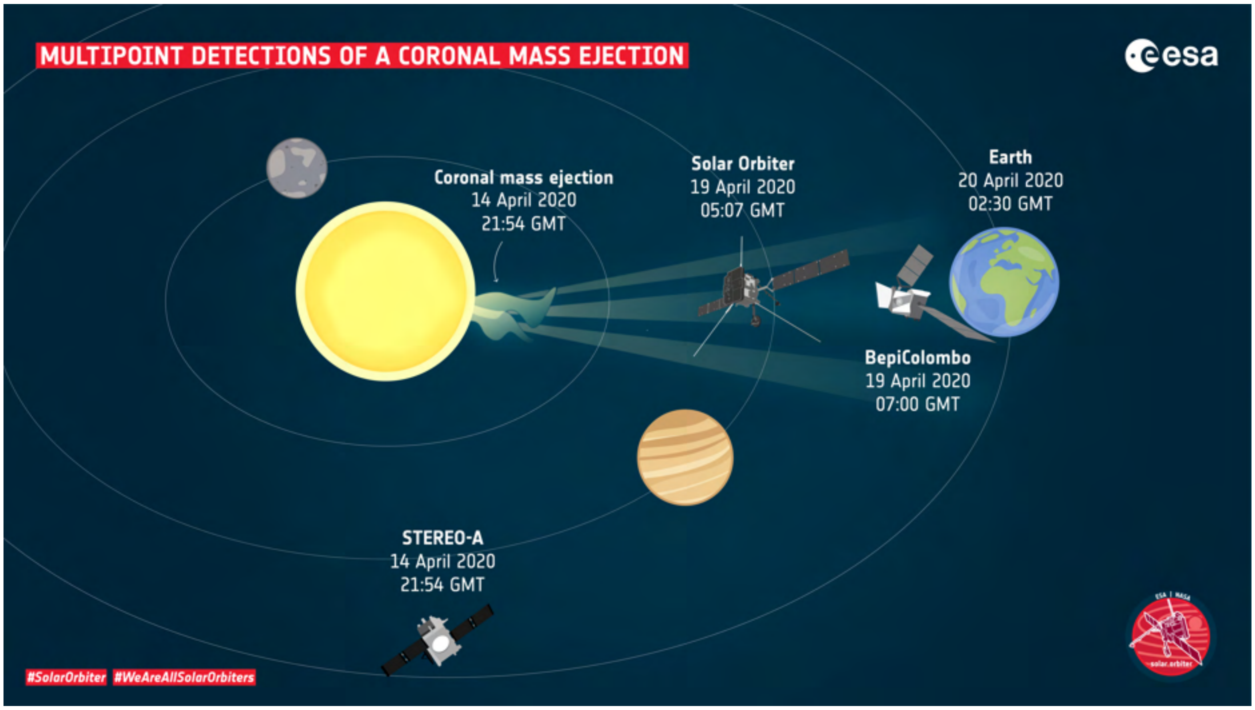

Figure 6.1: Multi-point detection of a CME at SO, BepiColombo, and the Earth. **Image credit: ESA**.

6.2 Identification of probable CME candidate/s for a conjunction event

For a CME to be listed as a possible conjunction between two or more SC, we first required the longitudinal separation (LS) between the SC to be less than 35° in Heliographic Inertial (HGI) Coordinates during the event. We started by examining the CMEs observed by the MESSENGER Magnetometer between 2011 and 2015. For each CME observed by MESSENGER during this time span, we listed the LSs between MESSENGER and *Venus Express*, STEREO, and *Wind*/ACE. For any LS greater than 35°, we removed that specific event from consideration. Then, we searched for CME signatures measured by *Venus Express*, STEREO, and *Wind*/ACE SC in their corresponding databases within an expected interval after the CME was initially measured at MESSENGER. Any CME satisfying this criterion was listed as a possible conjunction between the SC. We repeated the same procedure using the *Venus Express* CME catalog spanning 7.5 years (2006 - 2013) to list possible conjunctions between *Venus Express* and STEREO and *Venus Express* and *Wind*/ACE. Therefore, the conjunction database inherently splits into three groups: CMEs observed in conjunction by MESSENGER and *Venus Express* between 2011 and 2013, MESSENGER and STEREO or *Wind*/ACE between 2011 and 2015, and *Venus Express* and STEREO or *Wind*/ACE between 2006 and 2013.

For each conjunction event, we identified the date and time of the CME's first appearance in the LASCO/C2 FOV. As we lacked plasma measurements of the CMEs encountered by MESSENGER and *Venus Express*, with the help of the Drag-Based model (DBM), formulated by Vršnak et al. (2013), we estimated impact speeds at Mercury and Venus. As an input for this estimate, we used the ambient solar wind speed measured near 1 AU. To determine the date and time of the likely CME's first C2 appearance, we used the CDAW (Coordinated Data Analysis Workshops) CME catalog (Yashiro et al., 2004) and SECCHI CME lists (Robbrecht et al., 2009), automatically generated by CACTus (Computer Aided CME Tracking software). To identify a potential CME candidate, we searched for agreement between the CME launch direction and positioning of the corresponding SC during the event interval. We approximated the CME propagation direction (halo, west/east limb, and backsided) using three different FOVs: the CME observed from SOHO (LASCO observations) and the two STEREO SC (COR2 observations). This was achieved by comparing the relative heliographic longitudes of the SC on the day of interest. We performed this for each CME upto a period of 3 - 5 days (3 if SC 1 was MESSENGER and 5 if SC 1 was *Venus Express*) before the CME was observed at SC 1. After this initial process of elimination, we used the DBM to estimate the CME arrival time at the SC in consideration and matched them with the timings listed in their corresponding catalogs. If the arrival time predicted by the DBM was in reasonable agreement with the listed timing, we listed the CME as a possible candidate for the conjunction event.

For a two SC conjunction, SC 1 (MESSENGER or *Venus Express*) represented the first SC to observe the signatures of the CME during its propagation and SC 2 (*Venus Express* or STEREO or *Wind*/ACE) represented the second SC to observe signatures of the same CME later on. In the case of a three SC conjunction event, we had a third SC where the same CME, which was observed at SC 1 and 2, was also observed.

In our catalog, we had 18 events for which the LSs between the observing SC were 0 - 9.9°, 14 events for which the LSs were 10 - 19.9°, 9 events for which the longitudinal separations were 20 - 29.9°, and 6 events for which the LSs were 30 - 44.2°. The average LS of our catalog events was 16.2°. The 6 events for which the LSs were >30°, two of them had LSs >35° (37.6° and 44.2°) and they were for the same CME. The reason for including this event with such a large LS is explained in Section 6.4.

6.3 Estimation of impact speeds at Mercury and Venus

We calculated the average transit speeds between the Sun and SC 1 (V_{S-SC1}), SC 1 and SC 2 ($V_{SC1-SC2}$), and the Sun and SC 2 (V_{S-SC2}), using the CME take-off time at the Sun and listed arrival times at SC 1 and 2. For consistency, we used the shock/discontinuity arrival times if available at all SC for the calculation of average transit speeds. We used the CME arrival time if shock arrival time was not available at one of the SC in consideration (e.g. due to the SC being inside the magnetosphere). In 12 out of 47 cases, we observed disagreement ($V_{SC1-SC2} > V_{S-SC1}$) in the expected average transit speeds. The discrepancies could be due to the fact that the CMEs were still accelerating in the low corona. In such cases, we used the CME time at 20 R_s rather than the CME take-off time at the Sun to calculate the average transit speeds. However, using the CME time at 20 R_s only fixed 2 out of the 12 discrepancies. Such trends were not entirely unexpected from slow CMEs, where the CMEs actually go through acceleration further away from the Sun. Checking the CME counterparts for these 12 events, we did indeed observe that most of these discrepancies (10 out of 12) were features of slow CMEs (initial speeds less than 700 $\mathrm{km\,s^{-1}}$).

We used the DBM for an estimate of impact speeds at Mercury and Venus. The DBM relies on the assumption that the driving Lorentz force, which launches a CME, ceases in the upper corona and after this propagation distance (20 R_s), the sole dominant force governing the CME propagation is the MHD equivalent of the aerodynamic drag. This model treated CMEs as single expanding bodies, propagating through an isotropic environment to which Newton's second law was applied. This model provided analytical solutions of the equation of motion where the drag acceleration had a quadratic dependence on the CME relative speed (see Equation 3.2). Under the assumptions of constant drag coefficient and constant solar wind flow, with no CME-CME interaction, this model provided predictions for the arrival of the CME front and its impact speed. However, the DBM had certain intrinsic drawbacks that could result in significant amount of uncertainties for events in which the CME still considerably accelerated beyond 20 R_s, the ambient solar wind regime did not remain constant throughout the CME propagation, when there was CME-CME interaction, etc. (Vršnak, 2001; Vršnak et al., 2010, 2013; Žic et al., 2015).

For a given set of seven input parameters (CME start date, CME start time, starting radial distance of the CME, speed of the CME at the starting radial distance, drag parameter with unit of 10^{-7} km^{-1}, asymptotic solar wind speed, and target heliocentric distance), the DBM provided the impact speed for any target in the heliosphere. We used 20 R_s as the starting radial distance (to minimize the effects of Lorentz force) and the 2nd-order speed at 20 R_s (second-order polynomial fit to the height-time measurements evaluated when the CME was at a height of 20 R_s) listed in the CDAW catalog as the CME speed. For the asymptotic solar wind speed, we used the solar wind speed from in-situ measurements at STEREO or *Wind*/ACE before they encountered the CME. For MESSENGER and STEREO/L1 and *Venus Express* and STEREO/L1 conjunctions, we performed a three-step measurement process to get the estimated impact speeds at Mercury and Venus using the DBM. In the first step, we changed the only variable (drag parameter) in the DBM to match the CME arrival time at STEREO or L1. Then, we used that same drag parameter to get an estimated impact speed at Mercury or Venus. In the second step, as we had in-situ plasma measurements available at STEREO and L1, we changed the drag parameter to match the maximum CME speed measured at STEREO or L1. After that, we used that drag parameter to get the second estimated impact speed at Mercury or Venus. The third estimated impact speed at Mercury or Venus was obtained by matching the listed CME arrival time at MESSENGER or *Venus Express* using the DBM. These three estimated impact speeds were then averaged. It is important to highlight here that with large LSs, there was a significant probability of different parts of the CME/sheath impacting different observing SC at different times. This is specifically discussed for our case study (in Section 6.10.2 and Section 6.10.3). Without knowing the true CME shape, it was impossible to fully estimate the errors of these estimates. However, these three estimates gave us an estimate of the error of the procedure.

For any conjunction between only MESSENGER and *Venus Express*, we adopted a slightly modified technique since there were no in-situ measurements available at both the SC. In the first step, we tried to match the listed CME arrival time at MESSENGER by changing the drag parameter in the DBM. It provided an estimation of the impact speed at Mercury and using the same drag parameter, we got an estimated impact speed at Venus. In the second step, we simply reversed the technique by using the DBM to match the listed CME arrival time at *Venus Express*.

6.4 Conjunction events with three-point observations

We had two events with three-point observations (MESSENGER, *Venus Express*, and STEREO) in our catalog which were the most promising for studies of CME evolution in the inner heliosphere. The first event appeared three times in our catalog: as a MESSENGER-*Venus Express* conjunction event (1-2011, number tags explained in Section 6.5), a MESSENGER-STEREO A conjunction event (6-2011), and a *Venus Express*-STEREO A conjunction event (34-2011). The LS between Mercury and Venus was 6.6°, Mercury and STEREO-A was 44.2°, and Venus and STEREO-A was 37.6°. The heliocentric distances of MESSENGER, *Venus Express*, and STEREO-A were 0.32 AU, 0.72 AU, and 0.96 AU respectively at the CME onset time. Though the LSs between Mercury-STEREO A and Venus-STEREO A exceeded our pre-defined criterion, the CME in question was a really fast CME, with substantial angular extent and non-linear speed at 20 R_s approaching 2281 $\mathrm{km\,s^{-1}}$ (listed in the CDAW catalog). Therefore, we approximated this CME to be observerd at the three SC in consideration.

The second event also appeared three times in our catalog: as a MESSENGER-*Venus Express* conjunction event (3-2011), a MESSENGER-STEREO B conjunction event (8-2011), and a *Venus Express*-STEREO B conjunction event (35-2011). The LS between Mercury and Venus was 23.1°, Mercury and STEREO-B was -4.8°, and Venus and STEREO-B was -27.2°. The heliocentric distances of MESSENGER, *Venus Express*, and STEREO-B were 0.44 AU, 0.73 AU, and 1.09 AU respectively at the CME onset time. Analysis of the second conjunction event was presented in Section 6.10. Previouly, radial evolution of this event had been extensively studied by Good et al. (2015, 2018).

6.5 Database

The full database is listed in Appendix A. The arrival times at MESSENGER were listed from Winslow et al. (2015), *Venus Express* from Good & Forsyth (2016), STEREO from Jian et al. (2018), and L1 from Richardson & Cane (2010). We placed a number tag on each conjunction event (e.g. 1-2011, 2-2011 etc.,) to recall it if necessary. The heliocentric distances and LSs (in HGI coordinates) were listed from HelioWeb (`https://cohoweb.gsfc.nasa.gov/coho/helios/heli.html`). For the initial speed, we selected the coronagraph which observed the CME closest to a limb event. When LASCO observed the CME as a limb event, we used the second-order CME speed at 20 R_s listed in the CDAW catalog. For STEREO observations, we used the maximum speed as listed in the CACTus catalog.

In most of the cases, we were able to find one CME candidate in coronagraphic observations which satisfied the temporal and directional requirements of a specific conjunction event. If there were more than one potential CME candidate, we tried to isolate one candidate based on the estimated arrival time at the corresponding SC using the DBM. We understood that there were some uncertainties in determining the CME counterpart based on arrival time agreements. As a result, if there were more than one CME candidate for a single conjunction event and all of them appeared to be suitable matches, we listed them all (conjunction events with number tags 31-2011, 35-2011, 37-2011, 40-2012). For the 31-2011 event, we highlighted two potential CME counterparts on 9 April 2011 with LASCO onset times of 15:48 UT and 18:00 UT. We believed that the consequent CME signatures observed at *Venus Express* and STEREO-A were either due to an interaction between these two CMEs or the first one was the more suitable candidate. There were, however, two events in our CME catalog that did not have a well-defined CME counterpart. The first one was event: 30-2011 for which we did not identify a corresponding CME at the Sun (due to LASCO data gap). We had three events bearing number tags 28-2010 for which we were not confident in their CME counterparts. These events corresponded to three CME measurements at *Venus Express* within a day (1 August 2010 - 2 August 2010). The LSs between *Venus Express* and STEREO-B was 16.5° on 1 August 2010 and 17.3° on 2 August 2010 in HGI coordinates. However, in the expected arrival interval at STEREO-B, only two CMEs were measured (both of these CMEs did not drive shocks and had no sheaths). Therefore, we had two potential conjunction events. We listed the CMEs observed at 3:39 UT and 8:24 UT on 1 August 2010 as the suitable CME counterparts. However, without the availavility of plasma measurements at *Venus Express*, we were not able to link in a unique manner the *Venus Express* and STEREO-B events with a particular CME counterpart at the Sun.

6.6 Speed profile

The basic characteristics of CME propagation is, CMEs that are faster than the ambient solar wind are decelerated, whereas those slower than the solar wind are accelerated by the ambient flow (Gopalswamy et al., 2000; Lindsay et al., 1999). Figure 6.2, Figure 6.3, and Figure 6.4 showed the propagation speed profiles of the CMEs from the Sun to SC 2. The initial speed mentioned here was either the second-order CME speed at 20 R_s listed in the CDAW catalog or the maximum speed listed in the CACTus catalog. For MESSENGER-STEREO/L1 conjunction events, we had the initial CME speed, average estimated impact speed at Mercury from the DBM, and the maximum CME speed measured at STEREO/*Wind*/ACE. For *Venus Express*-STEREO/L1 conjunction events, we had the initial CME speed, average estimated impact speed at Venus using the DBM, and the maximum CME speed measured at STEREO/*Wind*/ACE. For MESSENGER-*Venus Express* conjunction events, we had the initial CME speed and average estimated impact speeds at Mercury and Venus from the DBM. For coronagraphic observations, we used the speed obtained from the best observing SC, for which the CME was close to a limb event. Limb views significantly minimize projection effects as compared to halo views and provide a better estimate of CME speeds. While we chose the best observing SC to minimize any projection effects, using speeds obtained from catalogs came with large error bars. Typical uncertainty range for these catalogs had been reported to be of the order of ~150 - 200 $\mathrm{km\,s^{-1}}$, both for individual events and for the difference between the two catalogs themselves (see Michalek et al., 2017). We also cannot rule out the possibility of different parts of the CME being sampled at different observing SC due to a large longitudinal extent. To further highlight the importance of LSs, in the propagation speed profiles, we binned the CMEs based on the LSs between the SC observing the conjunction event to qualitatively represent potential scenarios concerning higher uncertainties due to large LSs. The four shaded regions in Figure 6.2, Figure 6.3, and Figure 6.4 represented the following domains (from left to right): i) region closer to the Sun extending out to 20 R_s, ii) region of MESSENGER measurements (0.31-0.44 AU), iii) region of *Venus Express* measurements (0.72-0.73 AU), iv) region of in-situ measeurements near 1 AU with STEREO and *Wind*/ACE (0.96-1.09 AU). Each line connecting the three individual CME speeds at different heliocentric domains represented the propagation profile of the same CME in the inner heliosphere after its eruption and are color-coded depending on the LS between the two measuring in-situ SC. The CMEs were separated into three categories based on their initial speeds as measured by coronagraphs: fast (initial speeds greater than 900 $\mathrm{km\,s^{-1}}$, see Figure 6.2), slow (initial speeds less than 700 $\mathrm{km\,s^{-1}}$, see Figure 6.4), and intermediate (initial speeds between 700-900 $\mathrm{km\,s^{-1}}$, see Figure 6.3).

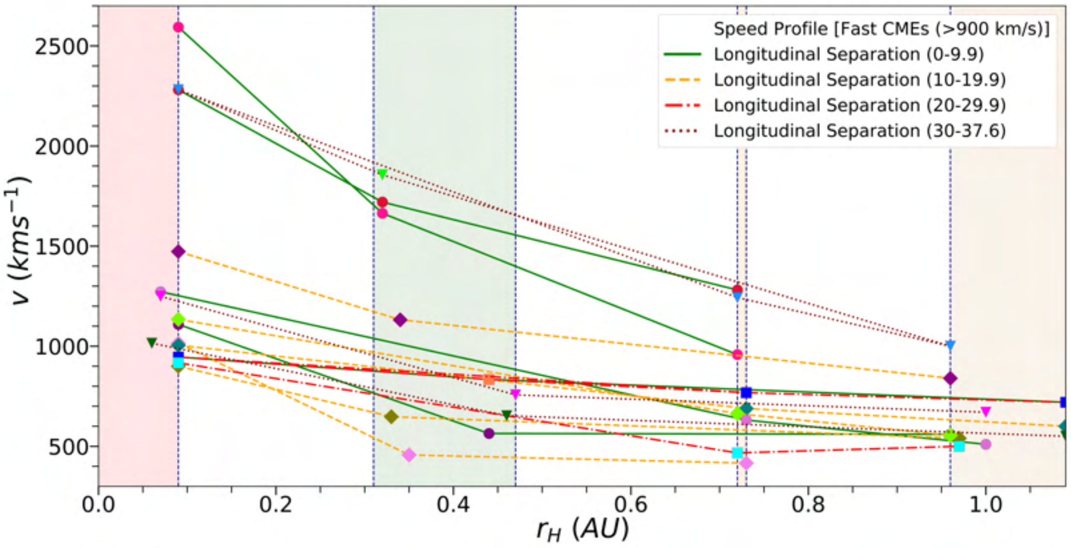

Figure 6.2: Propagation of fast CMEs with heliocentric distance (in AU). Lines connect measurements of the same CME and are color-coded depending on the LS between the two in-situ SC. Estimates of the errors for the speeds are discussed in the text.

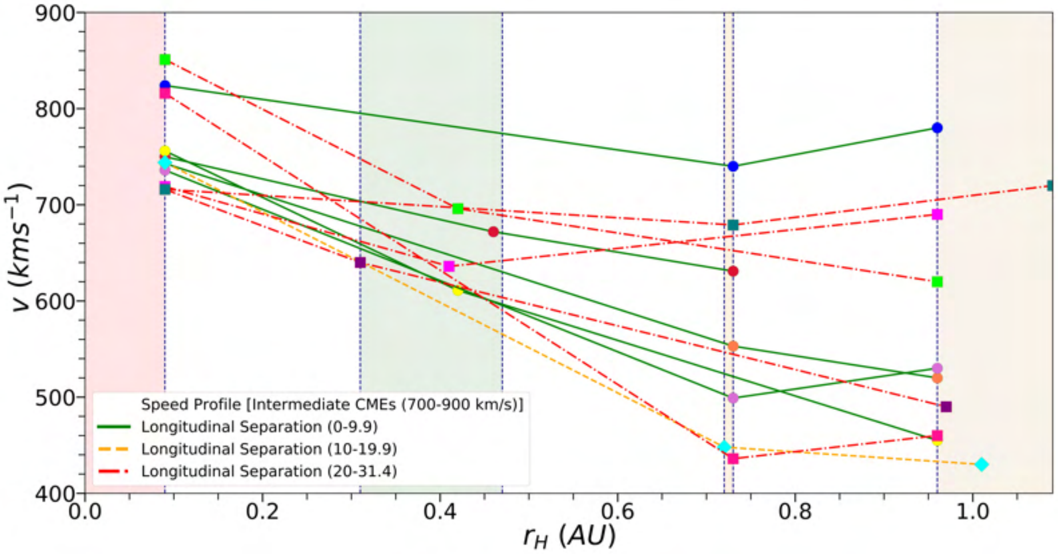

Figure 6.3: Same as Figure 6.2 but for CMEs of intermediate speed.

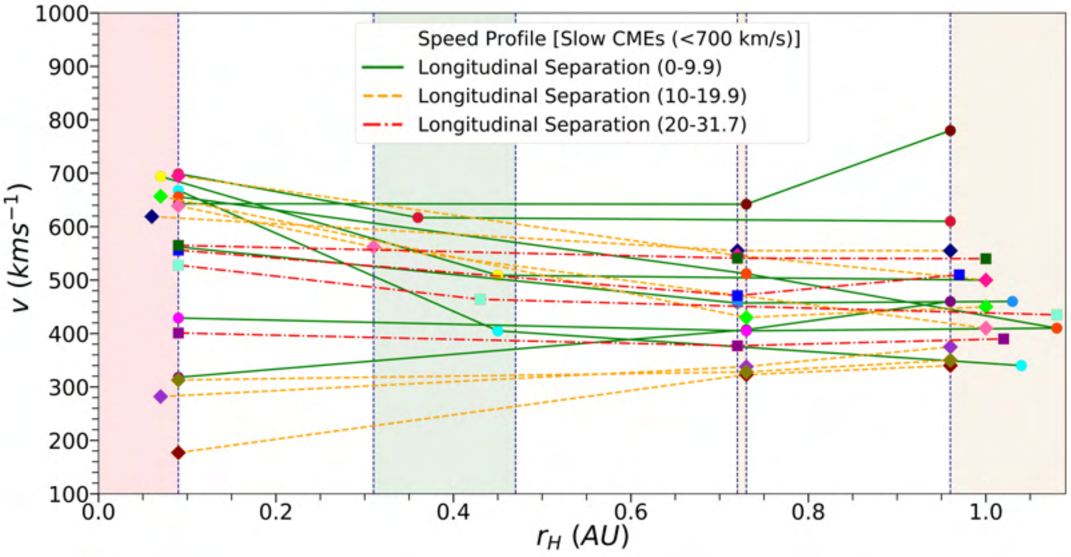

Figure 6.4: Same as Figure 6.2 but for slow CMEs.

For fast CMEs, we observed on average a 45% decrease in speeds through their propagation from the Sun to SC 2 (*Venus Express* or STEREO or *Wind*/ACE). Most of the variation occurred in the innermost heliosphere, within Mercury's orbit, while the rest occurred past 0.44 AU. For intermediate speed CMEs, this average decrease in speeds dropped to 24% through their propagation from the Sun to SC 2. Similar to fast CMEs, most of this variation took place within Mercury's orbit. Slower CMEs were observed to undergo the least amount of variation in speeds during their propagation in the inner heliosphere as the average decrease in speeds for them was only 5%. We found that for CMEs with initial speeds >700 $\mathrm{km\,s^{-1}}$, there were still significant deceleration past Mercury's orbit.

We also examined the radial evolution of the average transit speeds of CMEs. We used the heliocentric distances of the two observation points and the time interval for the transit of the shock/discontinuity (or the CME if shock/discontinuity arrival time was not available at one of the SC) to determine the average transit speeds. The average transit speeds were then assigned to the average heliocentric distances (mid-points between the two observation points used to determine the average transit speeds). Using a multi-linear robust regression fitting technique in logarithmic space, the best fit power law curve to the average transit speeds with average heliocentric distances (see Figure 6.5) was given by: $< v >= 508^{+94}_{-79} < r >^{-0.305\pm0.2}$ where $< v >$ was the average transit speed (in $\mathrm{km\,s^{-1}}$) and $< r >$ was the average heliocentric distance (in AU). The uncertainties represented the 95% confidence interval associated with the fits. The large uncertainty associated with the radial dependency could be a direct consequence of sampling of average transit speeds concerning different portions of the CME. From MESSENGER and ACE observations, using the same fitting technique, Winslow et al. (2015) found a much faster fall-off of the maximum shock speed with heliocentric distance: $< v_{max} >= 464.05^{+23.79}_{-22.63} < r >^{-0.45\pm0.09}$, although their results were not for CMEs measured in conjunction but obtained statistically for all CMEs measured at Mercury and ACE during 2011 - 2014. In addition, they used the transit speeds between the Sun and Mercury as the estimated speed at Mercury, rather than the speed at the mid-point, as done here.

Analyzing the plot, it was evident that CMEs with the highest differences between the initial speeds and solar wind speeds had a steeper fall-off of average transit speed compared to the rest. Our observations also suggested that deceleration does not become negligible past Mercury's orbit, though the rate of deceleration becomes considerably smaller.

6.7 CME deceleration/acceleration

For testing real-time space weather prediction models, it is important to have the exact arrival times of a CME at multiple locations in the inner heliosphere. However, the deceleration/acceleration process is one of the key challenges in predicting the CME arrival at Earth. With scarcity of plasma measurements at sub-1 AU heliocentric distances, it has not yet been possible to construct an average CME deceleration/acceleration profile. That encouraged us to use the estimated impact speeds at Mercury and Venus from the DBM in an attempt to present an average deceleration/acceleration profile of CMEs in the inner heliosphere. CMEs with propagation speeds above that of the ambient solar wind tend to decelerate, while slow ones with propagation speeds below the solar wind speed, get accelerated up to

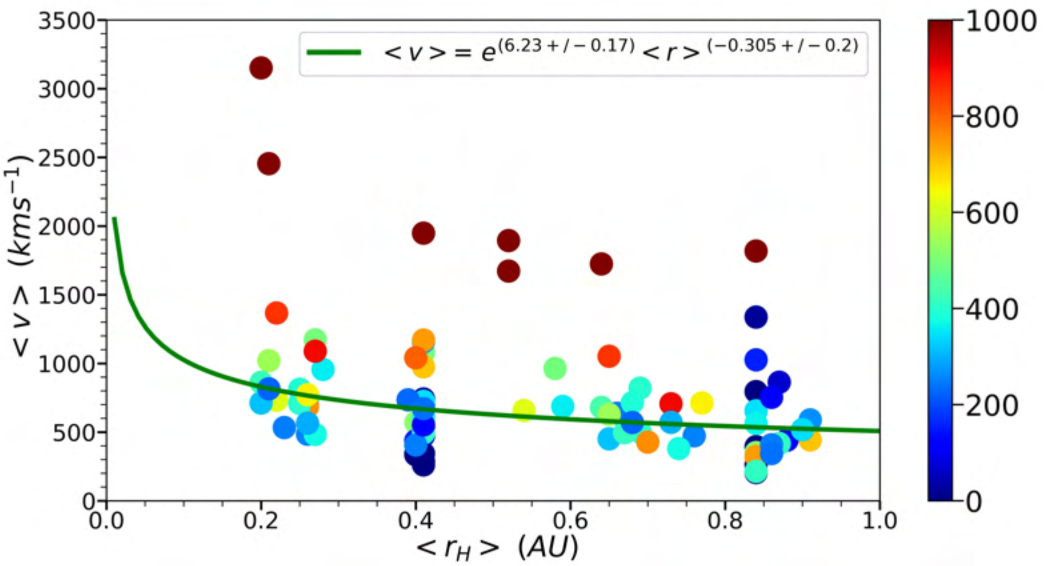

Figure 6.5: Average transit speed (in $\mathrm{km\,s^{-1}}$) versus average heliocentric distance (in AU) plotted along with the best fit power law (green curve) to the data. The relative difference between the initial CME speed and the solar wind speed measured near 1 AU for that specific conjunction event (in $\mathrm{km\,s^{-1}}$) is presented as a second scale in color bar.

the solar wind speed. This general trend was clearly visible by comparing the fast and slow CMEs in Figure 6.2 and Figure 6.4 respectively, although there was significant event-to-event variability. Previous studies have indicated the deceleration to stop at different heliocentric distances: within Mercury's orbit (Liu et al., 2013) or at 0.76 AU (Gopalswamy et al., 2001) or anywhere between 0.3 AU and 1 AU (Reiner et al., 2007; Winslow et al., 2015).

Figure 6.6 showed the distribution of average CME deceleration/acceleration (calculated as $\frac{V_2-V_1}{\Delta t}$) against the average heliocentric distance between the two points where we had speed observations/measurements/estimations, with the relative difference between the initial CME speed and the solar wind speed for that specific conjunction event as a second variable. We used the initial CME speed, average estimated impact speed at Mercury and Venus from the DBM, and the maximum CME speed measured at STEREO/*Wind*/ACE to determine the average deceleration/acceleration of CMEs. The scatter plot highlighted that the rate of deceleration/acceleration was predominantly driven by the relative speed difference between the CME and the solar wind, resembling assumptions from previous studies (e.g. Gopalswamy et al., 2000; Vršnak et al., 2004; Yashiro et al., 2004) that beyond 20 R_s, CME dynamics is solely governed by the drag force. Figure 6.6 used the average heliocentric distance as the mid-point between the two points used to calculate the deceleration/acceleration. For example, a heliocentric distance of 0.27 AU in Figure 6.6 represented the average CME deceleration/acceleration between the first point of CME observation (at the Sun: 0.09 AU) and the second point of in-situ measurement (at MESSENGER: 0.44 AU). We observed the CMEs to undergo the maximum amount of deceleration in their propagation from the Sun to MESSENGER, with an average (median) deceleration of 10.9 (2.5) $\mathrm{m\,s^{-2}}$. With increasing heliocentric distance, this deceleration decreased but did not become negligible, until beyond Venus's orbit, with an average (median) deceleration of 7.4 (1.5) $\mathrm{m\,s^{-2}}$ from MESSENGER to *Venus Express*, and 0.2 (0.1) $\mathrm{m\,s^{-2}}$ from *Venus Express* to STEREO/L1. This provided additional evidence for the argument that CME deceleration continues past the orbit of Mercury (e.g. Winslow et al., 2015), at least to Venus's orbit. In the case of some slow CMEs [with initial (measured CME speeds near 1 AU) CME speeds of 177 (340), 282 (375), 313 (350), 318 (460), and 643 (780) $\mathrm{km\,s^{-1}}$], we did observe an actual increase in speeds during their propagation from the Sun to near-Earth. A similar trend was also observed for one intermediate CME [with initial (measured CME speed near 1 AU) CME speed of 716 (720) $\mathrm{km\,s^{-1}}$].

6.8 Magnetic field intensity

We listed the mean and the standard deviation of the maximum magnetic field intensity within each of the substructures (sheath and ME) measured at MESSENGER, *Venus Express*, and STEREO/*Wind*/ACE in Table 6.1. As expected, the values of the magnetic field intensities decreased from MESSENGER to near 1 AU.

We also listed the ratios between the maximum magnetic field intensity measured in the sheath to that of the ME in Table 6.1. We found the ratios to remain relatively constant,

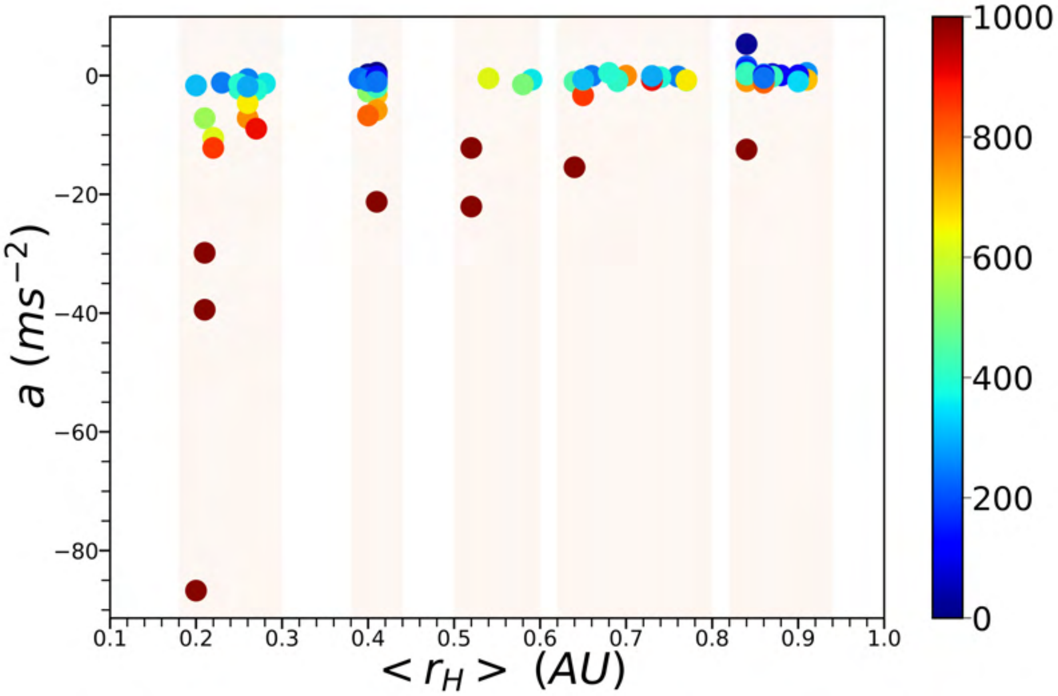

Figure 6.6: Distribution of average CME deceleration/acceleration (in m s^{-2}) versus average heliocentric distance between the two observation points (in AU) with the relative difference between the initial CME speed and the solar wind speed measured near 1 AU for that specific conjunction event (in km s^{-1}) as a second scale in color bar. The heliocentric distance here represents the average distance of the points between which the average CME deceleration/acceleration is estimated. Shaded regions (from left to right): 0.18-0.30 AU [Sun-MESSENGER], 0.38-0.44 AU [Sun-*Venus Express*], 0.50-0.60 AU [MESSENGER-*Venus Express*], 0.62-0.80 AU [MESSENGER-STEREO/*Wind*/ACE], 0.82-0.94 AU [*Venus Express*-STEREO/*Wind*/ACE].

Table 6.1: Mean and the Standard Deviation of the Maximum Magnetic Field Intensities (B_{max}) within the Sheath and the ME at MESSENGER, *Venus Express*, and STEREO/*Wind*/ACE. The Standard Deviations Represent 1σ Uncertainty.

B_{max}	MESSENGER	*Venus Express*	Near 1 AU
Sheath (in nT)	99±63	28±11	18±8
Sheath:Fast CMEs (in nT)	118±84	36±12	24±8
Sheath:Slow CMEs (in nT)	69±26	20±5	14±5
ME (in nT)	95±47	28±18	16±7
ME:Fast CMEs (in nT)	109±64	47±23	20±10
ME:Slow CMEs (in nT)	75±24	20±7	13±4
$B_{max,sheath}/B_{max,ejecta}$	1.04±0.27	1.04±0.41	1.18±0.45

even with increasing heliocentric distance: 1.04 at MESSENGER, 1.04 at *Venus Express*, and 1.18 at STEREO/*Wind*/ACE, consistent with the statistical findings obtained for non-conjunction events by Janvier et al. (2019). It is important to note here that these ratios should only be considered rough estimates, as CME distortion and the possibility of the observing SC traversing through different structures within the CME were not considered. However, interpreting multi-SC observations of the same CME can be really difficult, as seen from the analysis of six possible multi-SC observations by STEREO-A, *Wind*, and STEREO-B, listed by Kilpua et al. (2011). For the CME in the interval of 21-22 May 2007, both STEREO-A and STEREO-B observed this CME at a LS of 9°. Even for this small amount of separation, clear differences were reported in the magnetic field structures from the STEREO observations. At STEREO-B, the FR strucutre was clearly evident, while at STEREO-A, the CME strucutre was more complex. The maximum magnetic field measured at the SC differed by a factor of ∼2 (9.9 nT at STEREO-A and 17.6 at STEREO-B). They presumed that the MC was crossed through the center by STEREO-B, while STEREO-A encountered its flank. However, for the 19 November 2007 CME, even for a large LS of 40.8°, the maximum magnetic field measured at the SC were more comparable (12.3 nT at STEREO-A and 17.2 nT at STEREO-B). Farrugia et al. (2011) conducted a comprehensive analysis of this event and found almost similar fitted magnetic field strength at STEREO-B and *Wind* (21.9 nT at STEREO-B and 23.2 nT at *Wind*). Lugaz et al. (2018) analyzed 35 CMEs with *Wind* and ACE observations and highlighted that differences in the total magnetic field strength from one observing SC to another at 1 AU varies slowly with increasing non-radial separation, compared to the magnetic field components. They indicated that even with non-radial separation of 4 - 7°, almost zero correlation can be expected in the observed magnetic field components, whereas in the case of the total magnetic field strength, this range is clearly higher (14-20°).

We plotted the maximum magnetic field strength measured in the sheath and the CME (Figure 6.7) as a function of heliocentric distance. We used a multi-linear robust regression

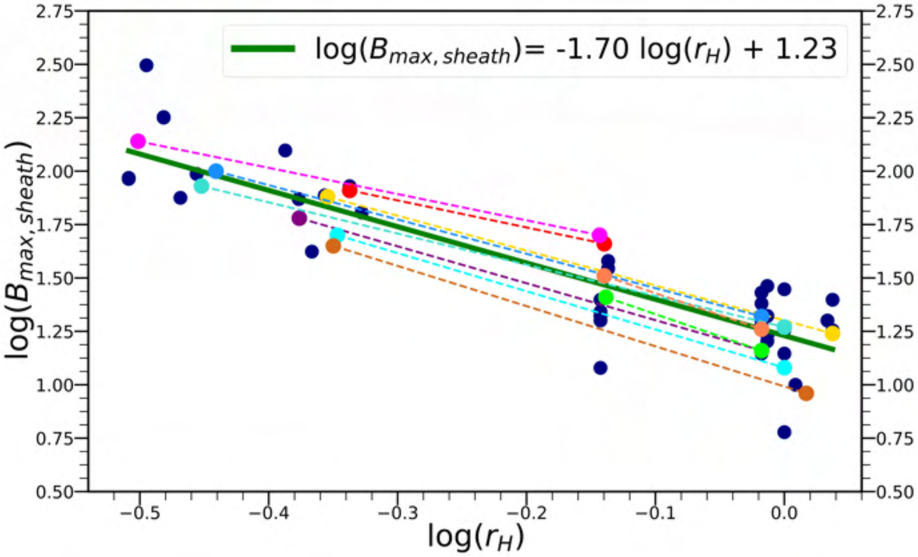

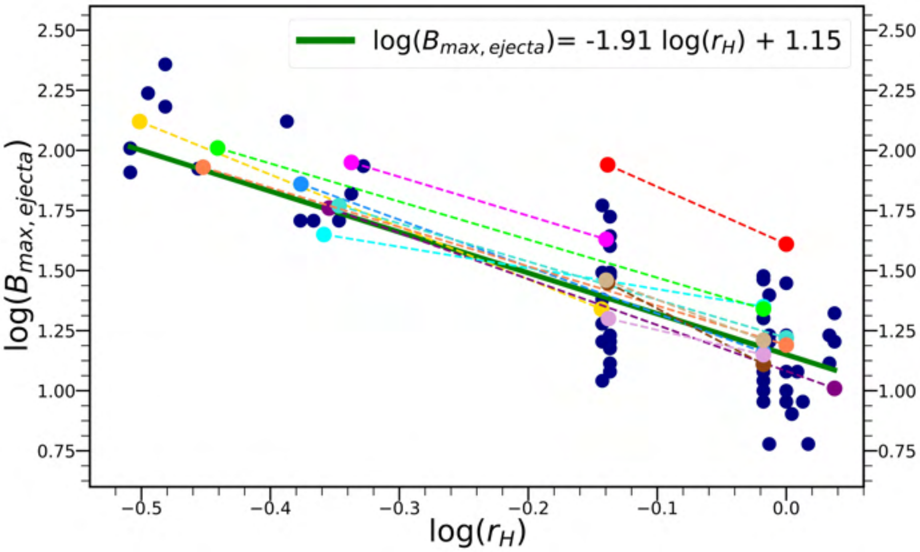

Figure 6.7: Maximum magnetic field strength (in nT) measured at MESSENGER, *Venus Express*, STEREO, and *Wind*/ACE plotted as a function of heliocentric distance (in AU). The green line represents the best linear fit to this data set. (top) Maximum magnetic field strength in the sheath, (bottom) maximum magnetic field strength in the ME. The color-coded lines connect measurements of the same CME at two SC of those events for which the separation was less than 10° (10 events, top panel) or 6° (12 events, bottom panel).

fitting technique in logarithmic space to fit a power law curve to our data set. Robust regression uses iteratively reweighted least-squares with a bi-square weighting function to ensure that less weight is attributed to outliers than in ordinary least-squares fitting. The best fit power law was: $B_{max,sheath} = 17.12^{+2.37}_{-2.09}\ r^{-1.7\pm0.21}$, $B_{max,ejecta} = 14.01^{+1.95}_{-1.71}\ r^{-1.91\pm0.25}$ where $B_{max,sheath}$ and $B_{max,ejecta}$ are the maximum magnetic field strength in nT measured in the sheath and the CME respectively and r is in AU. The uncertainties represented the 95% confidence interval associated with the fits.

The maximum magnetic field strength in the sheath fell off as $\sim r^{\alpha}$ where α is -1.7 ± 0.21. In the case of the CME, the maximum magnetic field strength fell off as $\sim r^{\alpha}$ where α was -1.91 ± 0.25, which was in reasonable agreement with previous theoretical considerations (e.g. Démoulin & Dasso, 2009) and empirical fits (e.g. Farrugia et al., 2005; Leitner et al., 2007; Wang et al., 2005; Winslow et al., 2015).

We also calculated this drop-off not only in a statistical way, as done above, but using the fact that we had conjunction between two SC for each event. Rather than fitting B_{max} vs r_H, we calculated the exponential decrease of $B_{max,sheath}$ and $B_{max,ejecta}$ between the two SC for each conjunction event, similarly to Dumbović et al. (2018a) (see Equation 6.1).

$$\alpha = \frac{log(B_2/B_1)}{log(r_2/r_1)} \tag{6.1}$$

Here, indices 1 and 2 correspond to the first (closer to the Sun) and second (further away from the Sun) SC respectively.

Using this, we found an average (median) α for the sheath to be -1.55 (-1.60). The 25th - 75th percentile range was between -1.85 and -1.29. In the case of the CME, average (median) α was -1.75 (-1.65) and 50% of the α values lied in the range between -2.29 and -1.35. Here, we found that the average behavior (obtained as the fit to the data) was not the same as the typical individual behavior. This highlighted the fact that there might not be one unique behavior for all CMEs, which is masked by performing fits. It also showed that there can be CME-to-CME variability much larger than the typical reported error bar on these fits, as the 95% confidence interval for the CME was -2.16 to -1.66. Such large spread in radial dependencies could be a direct consequence of the LSs between the measuring SC. If LS was indeed the primary influencing factor, we expected larger deviations from the regression line for events with higher separations. In Figure 6.7, we made an attempt to qualitatively represent this correlation between longitudinal separation and CME-to-CME variability. For small LSs (less than 10°), we observed the scaling of the maximum magnetic field strength in the sheath to more or less follow the power law fit equation (see top panel in Figure 6.7). However, in the case of the maximum magnetic field strength in the CME, the trend was not as straightforward. For even smaller LSs (less than 6°), we found the scaling of the maximum magnetic field strength in the CME, for a larger number of events, show significant deviations from the regression line (see bottom panel in Figure 6.7).

This finding prompted us to further explore the possible correlation between LSs and deviations from the regression line. We made an attempt to quantify it in a statistical manner. Using the maximum magnetic field strength measured in the CME at SC 1, we used the scaling constant derived from our robust regression fitting (α= -1.91) to find the expected maximum magnetic field strength in the CME at SC 2, using the following equation: $\mathrm{B}_{max2,expected}=$ $\mathrm{B}_{max1,measured}\ R^{-1.91}$, here R is the ratio of positioning of SC 2 (in AU) to positioning of SC 1 (in AU). Then, we determined the difference between this expected value and the actual measured maximum magnetic field strength at SC 2 and called it ΔB. We normalized the values of ΔB to the measured maximum magnetic field strength in the CME at SC 2. We fit the normalized values against LSs, using a linear-least squares fitting technique in Figure 6.8. The fit results confirmed the randomness of the maximum magnetic field strength in CME (seen in bottom panel in Figure 6.7) and found almost zero correlation with LSs.

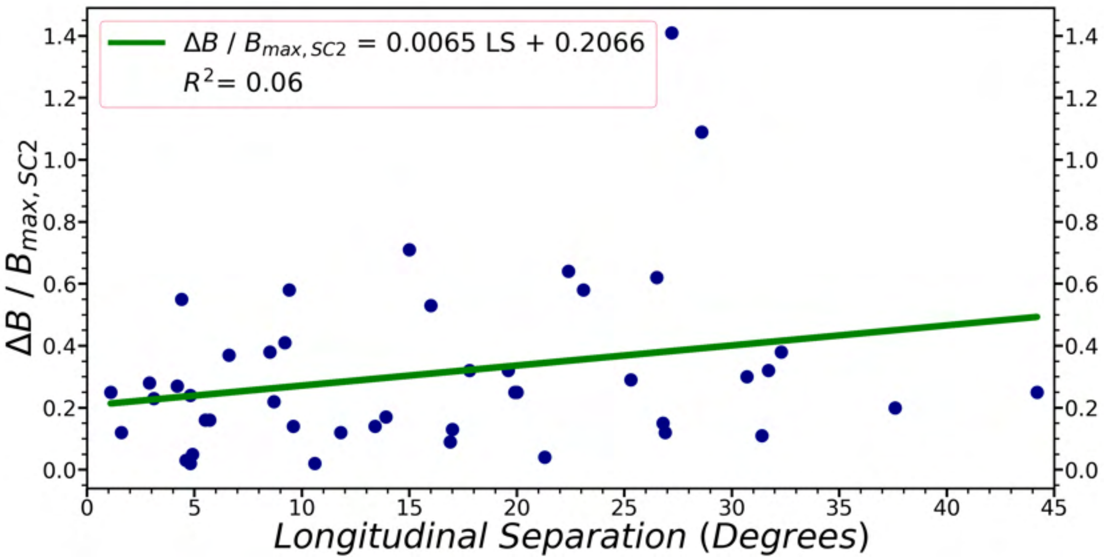

Figure 6.8: Normalized values of ΔB (for the ejecta, details in the text) plotted as a function of LS (in degree). The green line represents the best linear-least squares fit to this data set.

6.9 Sheath duration

We used the CME shock/discontinuity and the CME arrival times to estimate the sheath duration at MESSENGER, *Venus Express*, STEREO, and *Wind*/ACE. We used a linear-least squares fitting of the sheath duration (in hours) against heliocentric distance (in AU) and found the relationship between them to be T_{sheath}= 15.28 r_H - 3.67 (see Figure 6.9). R^2 of the linear regression line was 0.60, which represented a decent correlation between the parameters. The large positive slope indicated a linear increase in sheath duration with increasing heliocentric distance. This confirmed commonly held knowledge that the CME sheath increases with heliocentric distance. We did not have enough data to test whether this increase was anything but linear. We also find the sheath duration on average to be fairly independent of the initial CME speed throughout the inner heliosphere. At Mercury, we found (on average) the sheath duration of fast CMEs to be 1.74 hours and slow CMEs to be 2.22 hours. At Venus, the average sheath duration for fast and slow CMEs increasd by a factor of ~4 and ~3 respectively compared to Mercury, with an avearge sheath duration of 7.30 and 6.57 hours for fast and slow CMEs respectively. Near 1 AU, the average sheath duration for fast and slow CMEs were 13.74 hours and 10.98 hours respectively. This finding ran contrary to commonly held expectation that slower CMEs have larger sheaths than fast CMEs, though our sample size for the analysis was small. This belief is mostly based on comparison with planetary magnetosheaths. However, as explained by Siscoe & Odstrcil (2008), CME sheaths differ in many respects from planetary magnetosheaths. It should also be noted that if sheath thickness was considered rather than sheath duration, according to this finding, fast CMEs would have thicker sheaths. It was an interesting revelation, contradicting the results of Russell & Mulligan (2002); Savani et al. (2011), where stand-off distance of the shock (the separation distance from the magnetic obstacle to the shock) decreased with Mach number (ratio of the speed of the shock in the solar wind frame to the fast-magnetosonic speed), meaning slower CMEs, rather than fast ones should have thicker sheaths. Important thing to note that we did not take into consideration (for lack of measurements) the CME shape, radius of curvature, and the distance to the CME nose.

6.10 Case study of the 3 Nov 2011 CME

6.10.1 CME propagation

Good et al. (2015, 2018) studied this same CME to examine the change in the expansion speed, self-similarity nature, and FR fit. Our primary focus was on the relation between the expansion speed and change of B_{max}, as well as the development of the sheath.

The CME counterpart first appeared in the LASCO C2 FOV on 3 November 2011 at 23:48 UT. This CME emerged from the Sun's western limb at 22:54 UT on 3 November, when viewed from STEREO-A and from the Sun's eastern limb at 23:10 UT on 3 November, when viewed from STEREO-B (Figure 6.10). The listed non-linear speed at 20 R_s for the CME in the CDAW catalog was 946 $\mathrm{km\,s^{-1}}$.

We expected the non-linear speeds listed in the CDAW catalog to produce comparable esti-

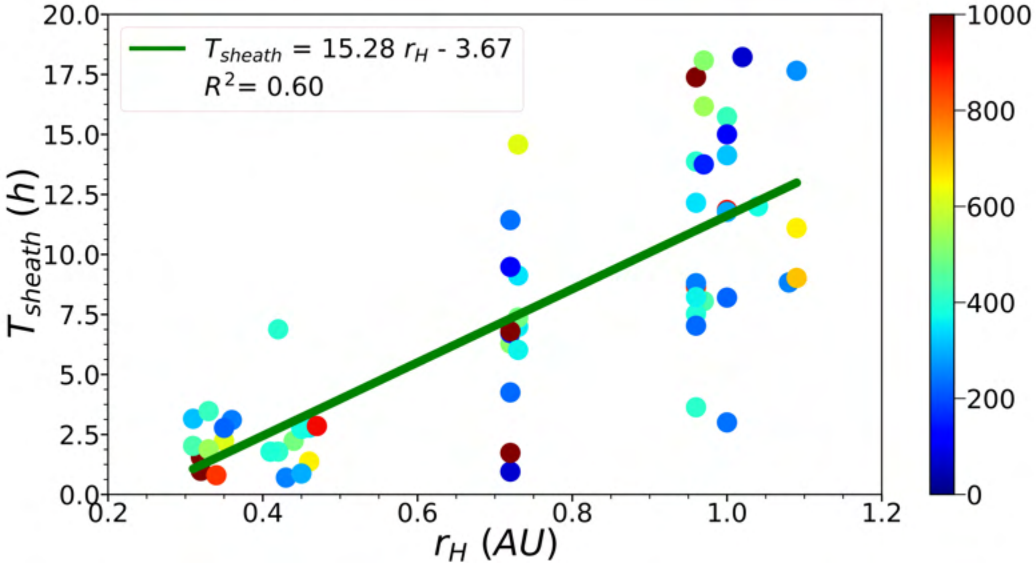

Figure 6.9: CME sheath duration (in h) plotted as a function of heliocentric distance (in AU) from MESSENGER, *Venus Express*, STEREO, and *Wind*/ACE measurements with the relative difference between the initial CME speed and the solar wind speed measured near 1 AU for that specific conjunction event (in $\mathrm{km\,s^{-1}}$) as a second scale in color bar. The coefficient of determination and the best linear least-squares fit (green straight line) to the data are shown.

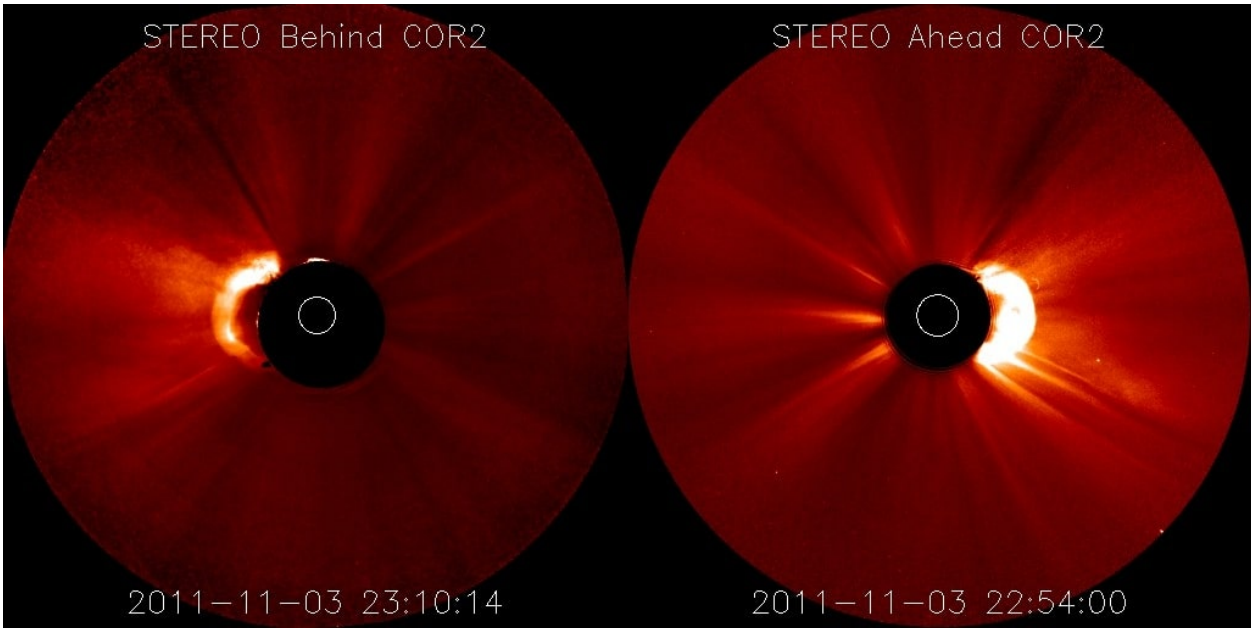

Figure 6.10: COR2 (outer coronagraph) observations of the 3 November 2011 CME event from STEREO-B (left) and STEREO-A (right).

mated arrival times to observed arrival times at different heliocentric distances. Even under the assumption of minimum drag (drag parameter of $0.1 \times 10^{-7}\ km^{-1}$), the DBM estimated arrival time of this CME at MESSENGER was not in reasonable agreement with the listed arrival time at MESSENGER by Winslow et al. (2015). We attributed this discrepancy in timing to the listed non-linear speed at 20 R_s being an estimate from coronagraph observations. As a result, we used two known constraints: listed CME onset time at 20 R_s in the CDAW catalog and the listed shock arrival time at MESSENGER, under the assumption of minimum drag, to estimate the speed of the CME at 20 R_s. Under these conditions, the DBM required the CME speed at 20 R_s to be at least 1140 $\mathrm{km\,s^{-1}}$. With this minimum speed of 1140 $\mathrm{km\,s^{-1}}$ at 20 R_s, we also estimated the arrival time of the CME at *Venus Express*, under the assumption of minimum drag. We found the DBM estimated arrival time at *Venus Express* to be in perfect agreement with the time listed by Good & Forsyth (2016), which verified our assumption about the listed non-linear speed at 20 R_s for this CME in the CDAW catalog to be not entirely accurate. This process also eliminated a second coronagraphic CME candidate (LASCO onset time of 01:25 UT on 4 November 2011, with 716 $\mathrm{km\,s^{-1}}$ as the listed non-linear speed at 20 R_s) as it was considerably slower than the chosen event. However, the observed complex in-situ signatures of the magnetic field at *Venus Express* prompted us to query about possible interactions between these two CME candidates. Interactions of the two candidate CMEs as they propagate were unlikely, especially at MESSENGER and STEREO-B, in light of the clear CME signatures, quite different from the possible in-situ manifestations of CME-CME interactions (see Lugaz et al., 2017b).

Figure 6.11 showed the positioning of the inner heliosphere planets and SC and WSA-ENLIL model with cone extension (Odstrčil et al., 2003, 2004) simulated propagation of the CME at three different time steps of interest: at Mercury, Venus, and STEREO-B. The simulations were illustrations of the CME arrival at the points of interest and were not meant for precise timing of arrival. These simulations were taken from SWRC CATALOG of Space Weather Database Of Notifications, Knowledge, Information (DONKI). Initial CME speed of 1100 km s^{-1} and half angular width of 65° were used for this simulation.

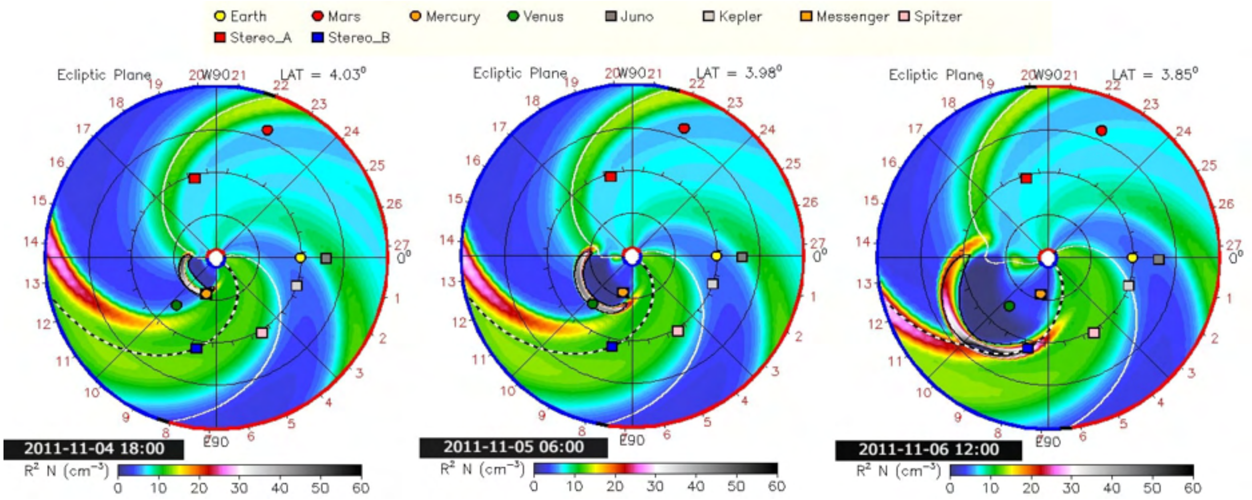

Figure 6.11: WSA-ENLIL model simulation with CME cone extension of the 3 November 2011 CME: when it reached Mercury (left), Venus (middle) and STEREO-B (right).

Due to the close longitudinal alignment of the inner solar system planets, about ∼15 hours after the CME eruption, the shock arrived at MESSENGER on 4 November at 15:09 UT, with an estimated impact speed of 834 km s^{-1} (from the DBM). The heliocentric distance of MESSENGER was 0.44 AU. The signatures of the FRs were observed at MESSENGER from 00:21 UT to 15:21 UT on 5 November with the arrival of the leading edge, ∼9.2 hours after the shock arrival. Using 1-s high-resolution data from the MAG, on board the MESSENGER SC, the magnetic field profile of the sheath and the CME were presented in Figure 6.12. In the plot, t=0 h corresponded to the shock arrival. Intervals when MESSENGER traversed the magnetosphere of Mercury were excluded. The start time and end time of the CME at MESSENGER were estimated to lie at the start period of the B_n rotation (t=9.2 h) to the period after which the magnetic field returned to its pristine condition (t=24.2 h). Our choice of the CME boundaries was consistent with Winslow et al. (2015) except the start time of the CME, which was significantly different. They defined the start of the CME at t=2.23 h and end of the CME at t=24.5 h. The reason behind adjusting the boundaries was that Winslow et al. (2015) defined the boundaries using only magnetic field measurements. In our case, we had the knowledge that this same event was also observed at STEREO-B where we had plasma measurements. So, we used both magnetic field and plasma measurements at STEREO-B to determine the CME sheath and then back-tracked to MESSENGER.

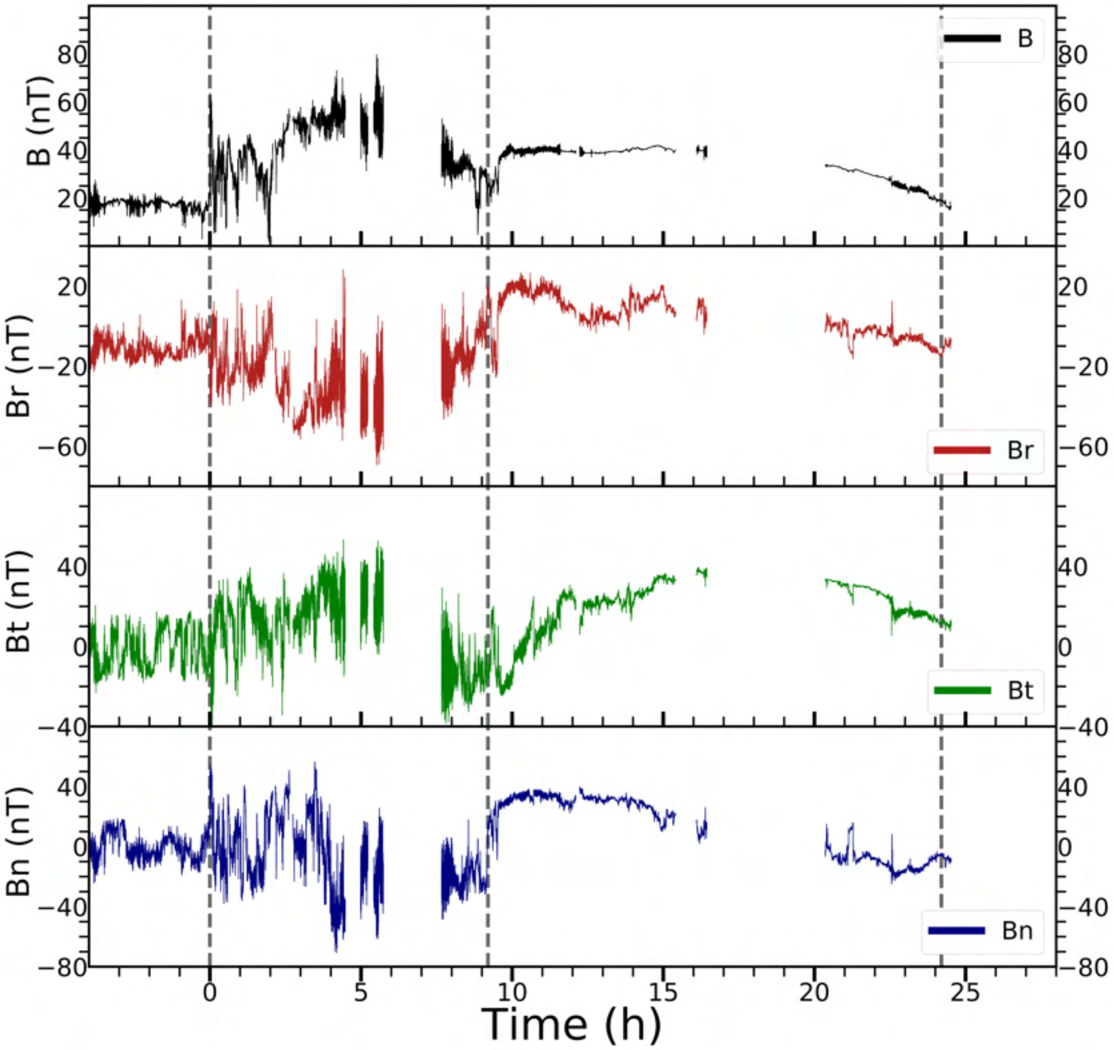

Figure 6.12: MESSENGER measurements of the CME on 4-5 November 2011. The four panels show magnetic field data in RTN coordinates. Vertical grey dashed lines (from left to right) denote the crossing time of the CME shock (t=0 h), ME, and CME end. The data gap corresponds to MESSENGER's passage through Mercury's magnetosphere.

The shock signature was observed in the MAG on board the *Venus Express* SC on 5 November

3:42 UT, with estimated impact speed of 768 $\mathrm{km\,s^{-1}}$ (from the DBM). The heliocentric distance of *Venus Express* was 0.73 AU. We defined the boundaries in the same manner as MESSENGER. The FR was approximated to start at 07:25 UT on 5 November and end at 00:36 UT on 6 November. Figure 6.13 showed the magnetic field measurements in the sheath and the CME at *Venus Express*. In the plot, t=0 h corresponded to the shock arrival. Intervals of induced magnetic field when *Venus Express* was inside the magnetosphere of Venus were shaded. Our choice of the start of the CME was consistent with Good & Forsyth (2016). They approximated the CME to start anywhere between 3.23 and 7.37 hours after the shock arrival, while we defined the boundary to start at t=3.72 h. However, we defined the end of the CME to be at t=20.9 h where they listed the CME to end at t=12.12 h.

A weak shock-like discontinuity was observed at 5:11 UT on 6 November at STEREO-B (in the plasma and magnetic field data). The heliocentric distance of STEREO-B was 1.09 AU. At 22:50 UT on 6 November, ∼47 hours after the arrival of the FR at MESSENGER, the same rope arrived at STEREO-B. The SC encountered the CME for a period of ∼37 hours with the trailing edge arriving on 8 November at 12:11 UT. The leading edge of the FR had a speed of 617 $\mathrm{km\,s^{-1}}$, while the trailing edge had a speed of 446 $\mathrm{km\,s^{-1}}$. The considerable difference between the speeds of the leading edge and the trailing edge represented an expanding CME. Using magnetic field data from the IMPACT instrument and plasma data from the PLASTIC instrument, on board STEREO-B, the sheath and the CME measurements were presented in Figure 6.14. In the plot, t=0 h corresponded to the discontinuity arrival. The boundaries of the CME at STEREO-B were estimated in a similar way to MESSENGER but in this case we also had in-situ plasma data. We defined the FR to start at t=17.67 h and end at t=55h. Our leading edge boundary was consistent with Jian et al. (2018). However, our trailing edge approximation was ∼16 h ahead of them.

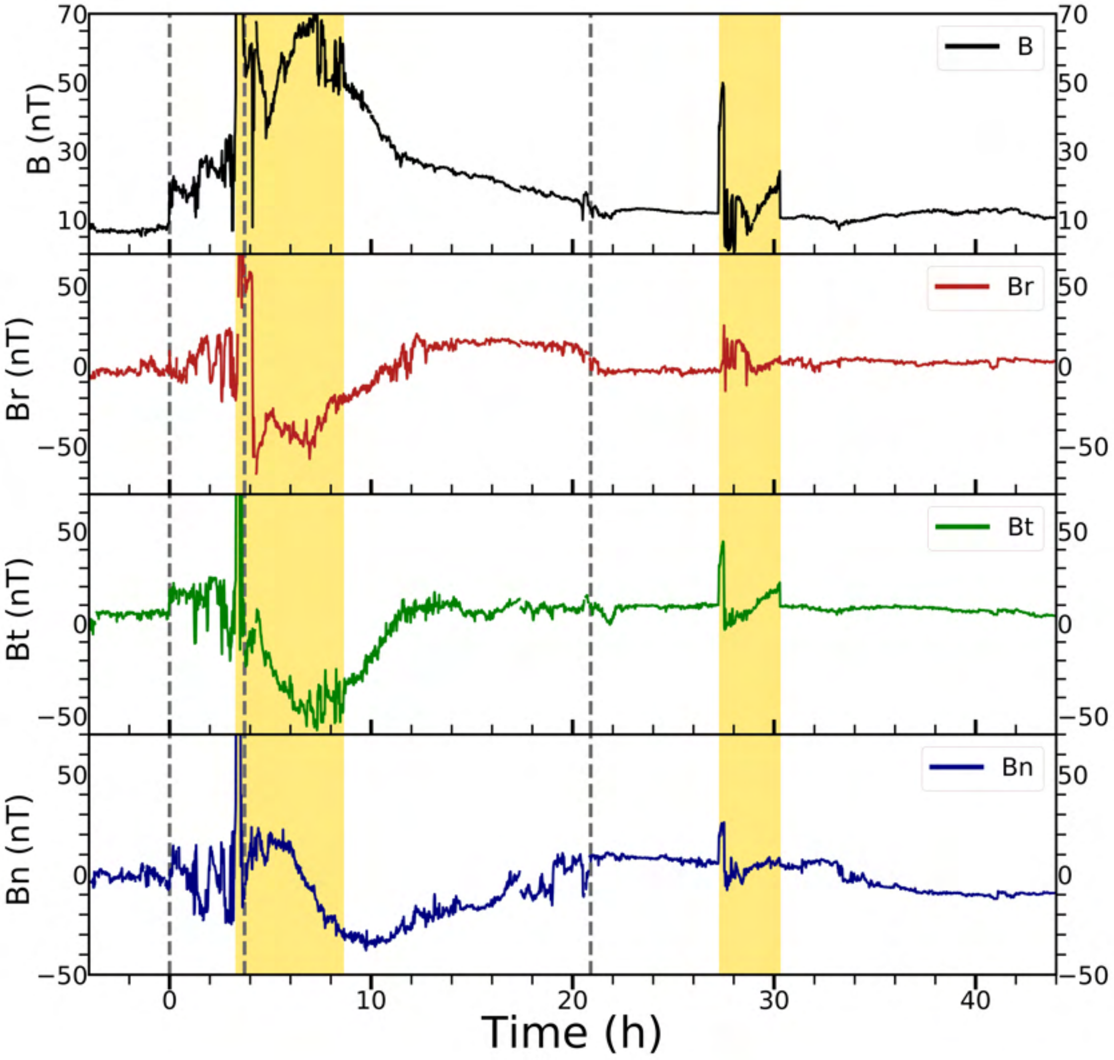

Figure 6.13: *Venus Express* measurements of the CME on 4-6 November 2011. The four panels show magnetic field data in RTN coordinates. Vertical grey dashed lines (from left to right) denote the crossing time of the CME shock (t=0 h), ME, and CME end. Yellow shaded regions represent the two magnetospheric crossings of *Venus Express* during the event.

6.10.2 Sheath and CME

In Table 6.2, we listed the total magnetic field intensities measured at the three SC. The ratio of the measured maximum magnetic field strength in the sheath to the measured maximum magnetic field strength in the CME at MESSENGER, *Venus Express*, and STEREO-B were 1.86, 0.66, and 1.80 respectively. Except at *Venus Express*, this ratio stayed almost constant, which was consistent with our findings (see Table 6.1). At Mercury, the duration of the sheath was ~ 9 h, with MESSENGER observing the CME for a period of ~ 15 h. *Venus Express* spent ~ 4 h in the sheath and ~ 17 h in the CME. The same sheath was observed by STEREO-B for a ~ 18 h period with the CME lasting $\sim$37 h. Looking at the WSA-ENLIL model with cone extension simulated propagation of the CME (see Figure 6.11), it was evident that both MESSENGER and STEREO-B observed the flank of the CME, whereas *Venus Express* observed its nose. We believed this to be the reason for a much shorter sheath period than expected at *Venus Express* and a more magnetized CME than the sheath.

Table 6.2: Total Magnetic Field Intensities within the Sheath and the ME at MESSENGER, *Venus Express*, and STEREO-B. [Note: Avg B_{sh}= Average Magnetic Field Strength Measured in the Sheath, Avg B_{ej}= Average Magnetic Field Strength Measured in the ME, $B_{m,sh}$= Maximum Magnetic Field Strength Measured in the Sheath, $B_{m,ej}$= Maximum Magnetic Field Strength Measured in the ME]

SC	Avg B_{sh} (nT)	Avg B_{ej} (nT)	$B_{m,sh}$ (nT)	$B_{m,ej}$ (nT)
MESSENGER	40	35	80	43
Venus Express	22	25	35	53
STEREO-B	10	8	18	10

6.10.3 CME expansion

We wanted to take advantage of the conjunction to compare the expansion speed measured at 1 AU and the change in the magnetic field strength during propagation. We determined the full expansion speed of the CME at STEREO-B through a linear least-squares fit of the

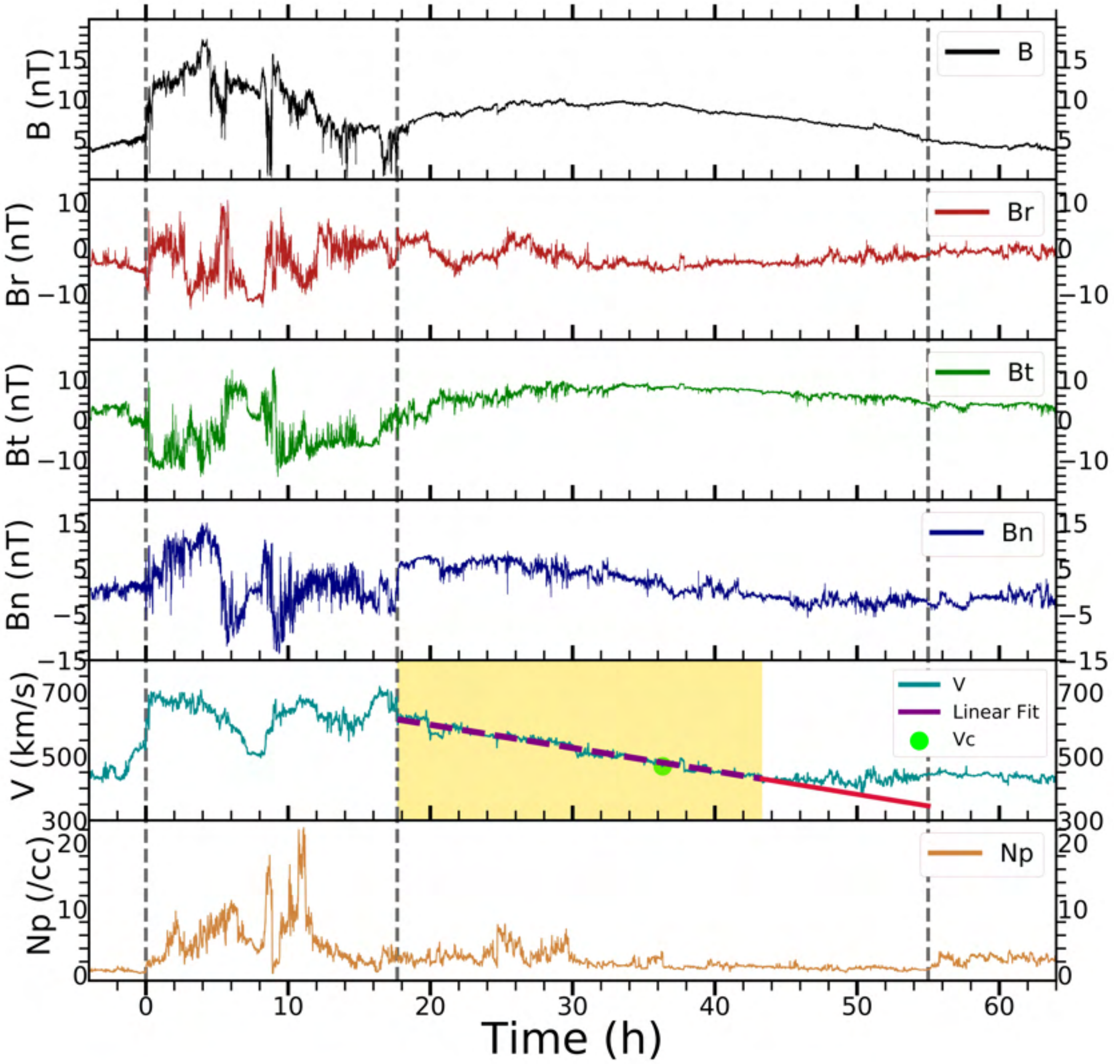

Figure 6.14: STEREO-B measurements of the CME on 6-8 November 2011. The six panels show magnetic field data in RTN coordinates (first four from top) and plasma measurements (last two). Vertical grey dashed lines (from left to right) denote the crossing time of the CME shock-like discontinuity (t=0 h), ME, and CME end. Yellow shaded region in the fifth panel indicate the time interval where a near linear trend in the solar wind speed is observed in the ME.

solar wind speed in the time interval where a near linear trend was present (yellow shaded region on the fifth panel in Figure 6.14), like Gulisano et al. (2010). Then we used the linear fit to define the speeds at the CME boundaries (see Equation 6.2). The expansion speed of the CME at STEREO-B was $\sim$ 135 $\mathrm{km\,s^{-1}}$.

$$\Delta V = \frac{V_{fit}(t_{LE}) - V_{fit}(t_{TE})}{2} \tag{6.2}$$

$$\Delta V = \frac{V_{front} - V_{back}}{2} \tag{6.3}$$

Here, $V_{fit}(t_{LE})$ and $V_{fit}(t_{TE})$ are the CME speeds at the boundaries defined with the linear fit and V_{front} and V_{back} are the CME speeds at the boundaries defined by the database.

Without linear fitting, the expansion speed (see Equation 6.3) was $\sim$86 $\mathrm{km\,s^{-1}}$. This expansion speed was nearly identical to that obtained by using the relation between the leading edge and expansion speed [V_{exp} ($\mathrm{km\,s^{-1}}$)= 0.266V_{LE} ($\mathrm{km\,s^{-1}}$) - 70.6 ($\mathrm{km\,s^{-1}}$), Owens et al. (2005)] which was $\sim$ 94 $\mathrm{km\,s^{-1}}$. Typical expansion speeds at 1 AU are 40 - 60 $\mathrm{km\,s^{-1}}$ (Richardson & Cane, 2010) and this CME was found to be expanding fast based on this metrics.

We also estimated the non-dimensional expansion rate ζ Gulisano et al. (2010) of the CME at STEREO-B (1.09 AU), see Equation 6.4.

$$\zeta = \frac{\Delta V}{\Delta t}\frac{D}{V_c^2} \tag{6.4}$$

Here $\Delta V/\Delta t$ was the slope of the best linear fit, D was the distance to the Sun, and V_c was the plasma speed (469 $\mathrm{km\,s^{-1}}$) measured at the center of the FR (see fifth panel in Figure 6.14).

We found ζ to be 1.5, that represented a very fast expanding CME, as for non-perturbed MCs, typical $\zeta\approx$ 0.8 (e.g. Gulisano et al., 2010), with the typical spread being $\pm$0.19 Démoulin

(2010). We examined the variation of this expansion parameter, as Démoulin & Dasso (2009) showed this parameter to stay relatively constant with distance. According to them, the magnetic field in the CME falls off as $\sim$ r$^{\alpha}$ (see also Dumbović et al., 2018a), where $\alpha \approx$ -2ζ. Thus for this conjunction event, with the value of ζ being 1.5, we expected the magnetic field in the CME to fall off as $\sim$ r^{-3}. The maximum magnetic field strength in the CME at 0.44 AU (Mercury) was 43 nT, it was 53 nT at 0.73 AU (Venus) and 10 nT at 1.09 AU (STEREO-B). The exponent decrease of the magnetic field were therefore $\alpha_{M,VEx}$ = 0.41 between Mercury and Venus, $\alpha_{VEx,STB}$ = -4.16 between Venus and STEREO-B, and $\alpha_{M,STB}$ = -1.61 between Mercury and STEREO-B. We did not consider the α_B values for Venus as it encountered the nose of the CME, whereas Mercury and STEREO-B encountered the flank. The value of α_B between Mercury and STEREO-B was smaller than the median found in section 6.8. This showed that the decrease of B was slower than typical inside this CME. We were left with an unexpected result: the CME was found to expand quickly at 1 AU, but the decrease of the magnetic field was consistent with a weaker-than-average expansion. This might have been due to the fact that the CME flank was encountered at both MESSENGER and STEREO-B.

6.11 Inconsistencies between local and global measures of CME expansion

This section is formed from the publication Lugaz et al. (2020a) on which I am the second author. I performed the analysis of *Venus Express* and STEREO in-situ measurements and participated in analysing the results. Some background of this work:

Radial expansion is one of the fundamental characteristics of CMEs (see Burlaga et al., 1982). In association with this increase in radial size, the magnetic field strength inside the CME decreases as the CME propagates to larger heliocentric distances (e.g. Bothmer & Schwenn, 1998). The knowledge about the increase in radial size and decrease in magnetic field inside CMEs are obtained from statistical studies of in-situ measurements of different MEs at different heliocentric distances. Based on measurements by Helios, ISEE-3, IMP-8, ACE, *Wind*, and Voyager, using different boundaries and different subsets of CMEs, past studies have found that the radial size of a CME increases as $r^{0.6}$ to $r^{0.9}$ and the magnetic field decreases as $r^{-1.4}$ to $r^{-1.9}$ (e.g. Bothmer & Schwenn, 1998; Leitner et al., 2007; Gulisano et al., 2010). This was revisited using STEREO, ACE, and MESSENGER data for SCy 24 by Winslow et al. (2015), yielding a similar index of radial dependency, -1.95 ± 0.19. This approach provides a measure of the average global expansion and assumes that there is a unique typical behavior of CMEs.

Another measure of CME expansion can be obtained from the direct analysis of in-situ measurements at a given location, as the large majority of CMEs have decreasing speed profiles. This is clearly a local measure of expansion where the expansion speed, defined as half the front-to-back speed difference (see Owens et al., 2005). Figure 6.15) shows schematic representations of the various measures of CME expansion.

At the conceptualization stage of this work, only few select studies have investigated the CME size or expansion from multiple in-situ measurements in near conjunction for more than one CME (e.g. Leitner et al., 2007; Good et al., 2019; Vršnak et al., 2019). The goal of this work was to compare the local measures (i.e., the expansion speed) with the global measures (changes in CME size and magnetic field with distance) of CME expansion. In this work, the comprehensive catalog of radially aligned CMEs by Salman et al. (2020b) is adopted to investigate whether the large CME sizes observed near 1 AU are related to a larger expansion near the Sun or simply due to a large front-to-back speed differences near-Earth.

Snippets of the detailed analysis by Lugaz et al. (2020a) are given in the following subsections.

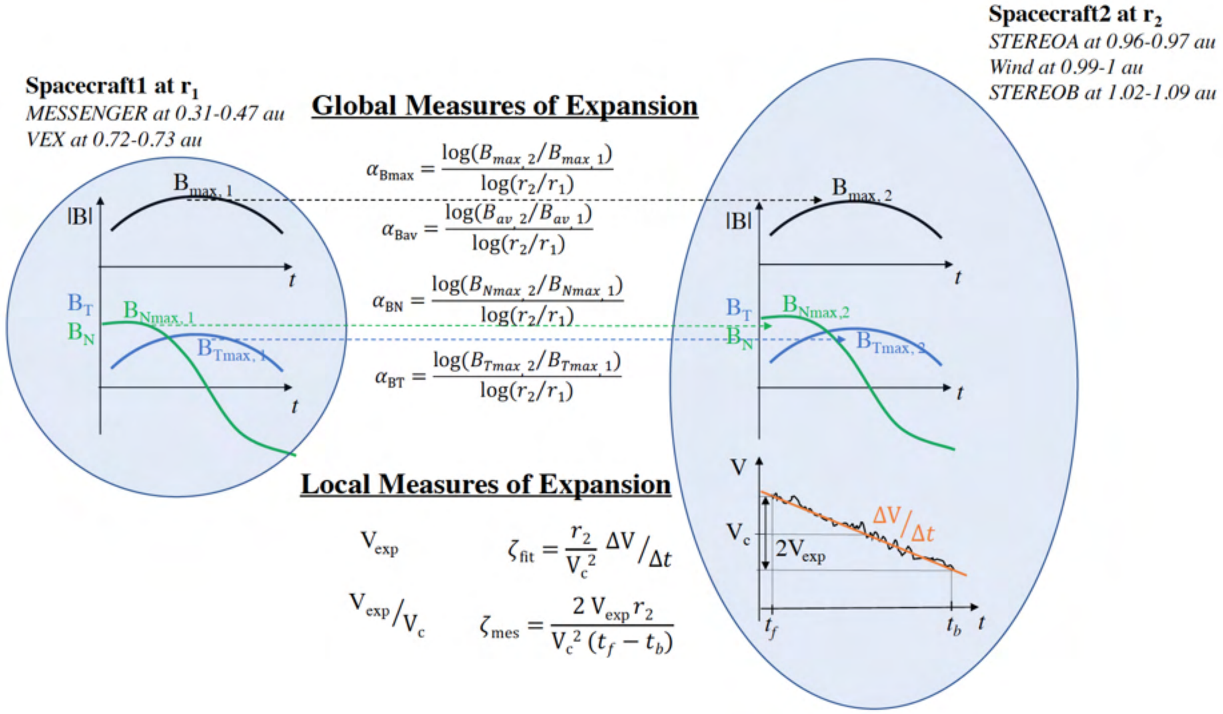

Figure 6.15: Schematic representation and definitions of the global and local measures of ME expansion. The idealized ME cross section and associated magnetic field measurements are shown at two locations at different heliocentric distances. Comparing measurements from these two locations define the global expansion. At the second SC, measurements of the plasma velocity allow the derivation of various measures of the local expansion. **Adapted from Lugaz et al. (2020a).**

6.11.1 Average values of global and local expansion metrics

The average value of α_{Bmax} found for the full data set was -1.81 ± 0.84 but -1.67 ± 0.43 for the conjunctions between MESSENGER and near 1 AU and -1.93 ± 1.06 for the conjunctions between *VEx* and near 1 AU. In all the cases, the average values of α_{Bmax} were similar compared to the results of previous studies based on statistical estimations (-1.73 reported by Farrugia et al. (2005), -1.64 ± 0.40 by Leitner et al. (2007), -1.89 ± 0.14 reported by Winslow et al. (2015), -1.76 ± 0.04 by Good et al. (2019)) but with a much larger standard deviation, for example Winslow et al. (2015) found a 3σ value of ±0.14. Combining all past studies, a range for the exponent decrease of B_{max} can be obtained as -1.75 ± 0.4. Only 20 out of the 42 events studied in this work fell within this range. For α_{Bav}, we found an average of -1.96 ± 0.90 (-1.85 ± 0.07 reported by Gulisano et al. (2010), -1.95 ± 0.19 reported by Winslow et al. (2015)). The average value for ζ was 0.86 ± 0.83, comparable to past studies (0.81 ± 0.19 reported by Démoulin et al. (2008), 0.70 ± 0.61 reported by Gulisano et al. (2010)). We note that we were able to identify a linear trend in the ME speed profile for 82% ± 22% of the ME duration (for 31 events, a trend is identified for more than 60% of the ME duration).

The average expansion speed found was 32 ± 44 $\mathrm{km\,s^{-1}}$ (or 39 ± 35 $\mathrm{km\,s^{-1}}$ if excluding three contracting events) and that of the dimensionless expansion was 0.067 ± 0.09 (0.083 ± 0.06 if excluding these three contracting events). The average size of the MEs near 1 AU was 0.29 ± 0.14 AU, comparable to that found from all ACE MEs by Richardson & Cane (2010). This number was larger than the canonical 0.21 AU from Lepping et al. (2018) but the latter was obtained for a force-free fit to the data, whereas our number and that by Richardson & Cane (2010) were derived by integrating the solar wind speed with time during the ME passage. For all quantities, the average values found were within the typical ranges from past studies, highlighting that our data set was not biased.

6.11.2 Comparison of local and global measures of CME expansion

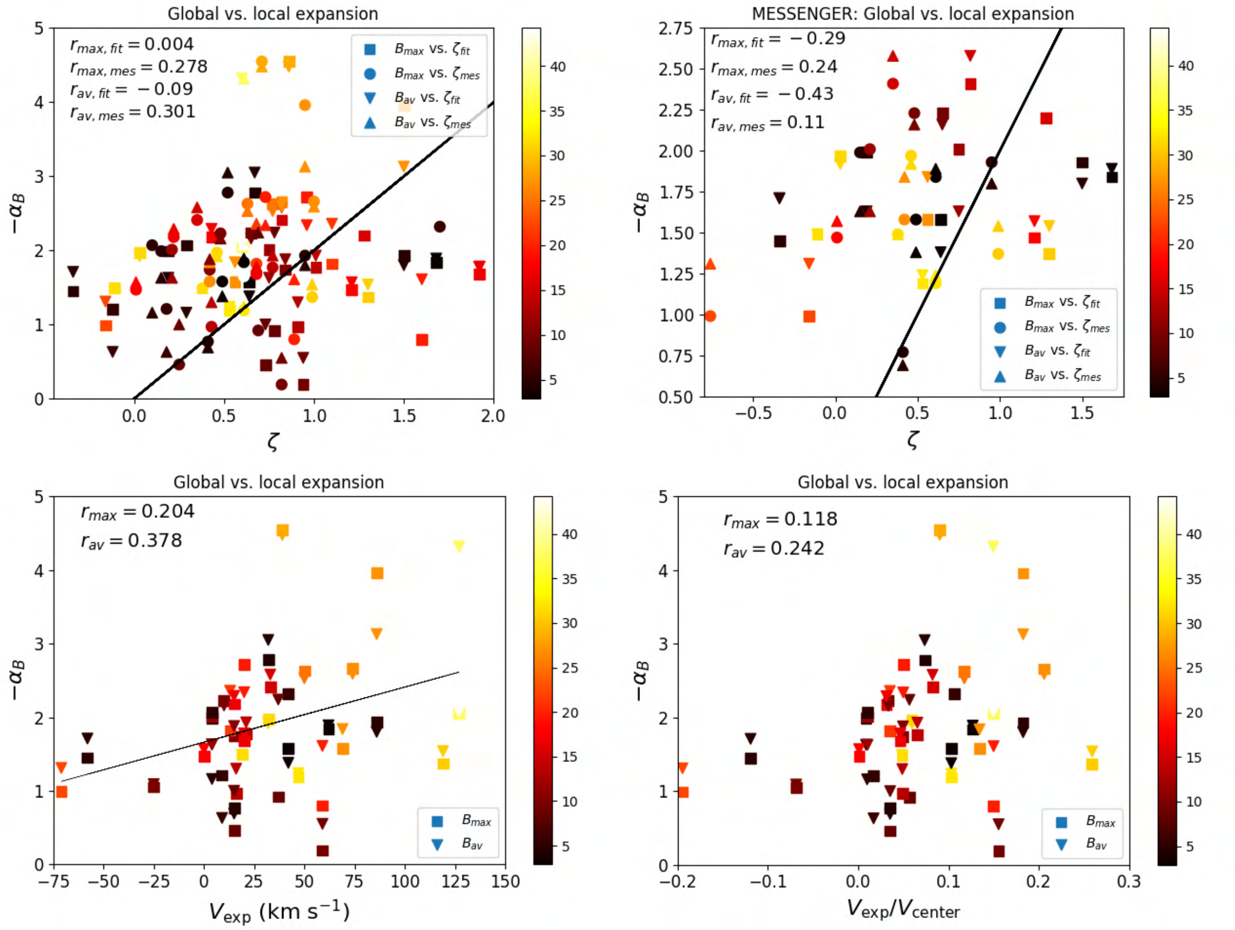

Figure 6.16: Global (y-axis) vs. local (x-axis) measures of CME expansion. The top panels show the index decrease of the magnetic field, α, as compared to the dimensionless expansion parameter near 1 AU, ζ. The line shows the expected value of $\alpha = 2\zeta$. The bottom panels show α as compared to the ME expansion speed near 1 AU (left) and the ratio of the ME expansion to center speeds (right). The thin line shows the linear relation for the best fit: $-\alpha_{Bav} = 1.66 + 0.0075\ V_{exp}$. All data points are color coded with the angular separation between the two SC with the scale in degrees given on the right-hand color bar. **Adapted from Lugaz et al. (2020a).**

In the top panels of Figure 6.16, we showed the plots of α_{Bmax} and α_{Bav} as compared to ζ_{fit} and ζ_{mes}, as well as the values when the first SC is MESSENGER rather than *Venus Express*, since the α values have less variability when the former is the first SC rather than the latter. The symbols were color coded with the SC angular separation and the top panels showed the line $\alpha = 2\zeta$, which was the expected trend. The data was uncorrelated for ζ_{fit}

(obtained by fitting to the slope of the velocity), while there was a very weak correlation with ζ_{mes} (calculated using the measured expansion speed) with the highest correlation coefficient, r=0.3 for the average magnetic field. In the bottom panels of Figure 6.16, α_{Bmax} and α_{Bav} were compared to V_{exp} and V_{exp}/V_{center} (here V_{center} is the speed at the center of the ME). This again compared the global quantities of CME expansion (in the y-axis) to the local quantities of CME expansion near 1 AU (in the x-axis). The largest correlation coefficient was found between the α index for the average magnetic field and the expansion speed (r=0.378). Other correlation coefficients were below 0.25. From these plots and the correlation values, it was evident that, irrespective of the exact quantities being compared, the local and global measures of CME expansion were at best weakly related. In particular, even for the smaller angular separations and large radial separations (the MESSENGER plot), small and large values of α were associated with typical values of ζ, around its average of 0.7.

CHAPTER 7

Prediction of southward B_z

This chapter is formed from the publication Salman et al. (2018). Hourly near-Earth OMNI data (King & Papitashvili, 2005) of B_z component in Geocentric Solar Magnetospheric (GSM) coordinates, extracted from NASA/GSFC's OMNI data set through OMNIWeb has been used in Section 7.2. For the rest of the analysis in this work, 1-minute high resolution data from the *Wind* Magnetic Field Investigation (MFI; Lepping et al., 1995) instrument and 90-second resolution plasma data from the Solar Wind Experiment (SWE; Ogilvie, 1995) instrument have been used.

7.1 Background

Strong interaction of the solar wind with Earth's magnetosphere can give rise to GSs (e.g. Fairfield & Cahill, 1966). Southward B_z opens the subsolar magnetopause through magnetic reconnection that allows the transfer of energy, plasma, and momentum to the magnetosphere. By late 1980s, it was evident that the southward component of the IMF is directly responsible for intense geomagnetic disturbances (Gonzalez & Tsurutani, 1987; Wilson, 1987). Later on, Echer et al. (2008) studied 90 intense GSs (when Dst reached below -100 nT) during SCy 23 (1996-2006) and found all of them to be associated with strong southward B_z.

A criterion for intense GSs is the presence of a long period (>3h) of large, and negative (<-10 nT) IMF B_z (Gonzalez & Tsurutani, 1987). While not infallible, (see Farrugia et al., 1998), this is generally a very useful criterion. Wilson (1987) made the critical connection between CMEs and GSs, that was further validated with future studies (e.g. Zhang et al., 2007; Ontiveros & Gonzalez-Esparza, 2010). However, the driver of such storms can also be the sheath of shocked plasma upstream of a CME, CIR, or a combination of these structures (e.g. Zhang et al., 2007).

Intense GSs are often preceded by storm sudden commencements (SSCs). SSCs serve as an indicator of the first impact of a travelling disturbance, associated with a strong dynamic pressure change on the magnetosphere (Joselyn & Tsurutani, 1990). The disturbance compresses the magnetosphere, resulting in an abrupt increase of the Dst (e.g. Ontiveros & Gonzalez-Esparza, 2010). Shock waves driven by fast CMEs are the primary causes of SSCs (see Russell et al., 1974; Echer et al., 2008). Gold (1955) initially suggested this association of SSCs with interplanetary shocks, which was validated by later studies (e.g. Iucci et al., 1988; Russell et al., 1992).

Due to this existence of a strong correlation between southward B_z and GSs, reliable prediction of B_z can be thought of as a primary basis for accurate space weather forecasting. At the conceptualization stage of this work, several studies were carried out to predict B_z with empirical approaches such as pattern recognition/analogue ensemble (e.g. Owens et al., 2017b; Riley et al., 2017), Bayesian framework (e.g. Chen et al., 1997, 2012), conservation of magnetic helicity (Helicity-CME or H-CME model; Patsourakos, 2016), semi-empirical models such as the The ForeCAT In Data Observer (FIDO; Kay et al., 2017), 3DCORE (Möstl et al., 2018), FRiED (Isavnin, 2016). However, as the IMF frequently fluctuates, predicting southward B_z is full of uncertainties (Jurac et al., 2002). Prediction models based on remote-sensing observations can in theory provide sufficient lead times for forecast (∼2-3 days) but the efficiency of predictions are constrained by numerous uncertainties (i.e., estimation of the initial CME state with white-light observations, heliospheric evolution of CMEs). Prediction models based on near-Earth in-situ measurements do not face such hurdles but the lead times for forecast is critically short (∼1 hour). The purpose of this work was to implement the first iteration of a physics-based statistical approach, based on near-Earth in-situ measurements that could possibly extend the lead times for forecast while minimizing the inherent drawbacks for predictions based on the framework construction.

In this work, we forecasted strong southward B_z periods that are preceded by fast-forward shocks. To do so, we constructed a forecasting model based on pattern recognition (see Riley et al., 2017). It is known that CME speed is somewhat correlated with the CME magnetic field strength (e.g. Möstl et al., 2014). Slow CMEs and minor shock disturbances are not associated with significant geomagnetic activity (see Gosling et al., 1991). Therefore, fast CMEs can be expected to drive the majority of the strong southward B_z periods. Near 1 AU, CMEs are the main drivers of fast-forward shocks (e.g. Berdichevsky et al., 2000). The strong southward B_z periods were therefore likely to be preceded by a fast-forward shock, driven by the CME. This led to our first hypothesis that the majority of strong southward B_z periods were caused by CMEs and as a result we decided to build our ensemble of analogues only from past periods around fast-forward shocks. The level of geomagnetic activity stimulated by the Earth passage of a shock or a CME is related directly to the magnitude of the flow speed, magnetic field strength, and southward field component (e.g. Akasofu, 1981; Baker et al., 1984). This led to our second hypothesis that prediction of these variable solar wind conditions in near-Earth space can be important for space weather forecasting (Owens et al., 2005).

7.2 Examining the proportion of strong southward B_z periods

We first examined the association between fast-forward shocks and subsequent strong and long-duration southward B_z periods to determine if the proposed approach of focusing on periods following fast-forward shocks was appropriate. All instances in the period 01/01/1995-05/27/2017 where B_z<-10 nT for 3 consecutive hours or more were listed. We found 129 such instances. Then, we used two shock databases to match these instances with fast-forward shocks (with M_{ms}>1) observed by the *Wind* spacecraft within the pre-48h interval of an instance. The first database was the IPshocks database (also used in Chapters 4 and 5) and the second one is the shock database of Harvard Smithsonian Center for Astrophysics, which can be found at `https://www.cfa.harvard.edu/shocks/` and referred to as CFASDB from now on. However, we mainly focused on the IPshocks database. Using this, we found that 81 (63%) instances were preceded by at least one fast-forward shock, occurring within the pre-48h interval. Then, we used the CFASDB to look for *Wind* shocks which were not listed in IPshocks database but may be preceding the 48 negative (not preceded by any fast-forward shock occurring within the pre-48h interval) instances. We found that 6 of these negative instances were indeed preceded by a fast-forward shock not listed in IPshocks database but in CFASDB. We then used both IPshocks database and CFASDB to look for ACE shocks which may have preceded the 42 remaining negative instances. We found that 11 of these were preceded by a fast-forward shock observed by the ACE spacecraft at L1. In total we found that, 98 of these instances (76%) were preceded by at least one fast-forward shock, occurring within the pre-48h interval. This validated the assumption that a large portion of the strong and long-duration southward B_z periods were preceded by fast-forward shocks. We also had 2 negative instances on 10/29/2013 and on 10/30/2013 which had been reported as being preceded by shocks but considerable data gaps in the pre-48h interval might have led to a no shock observation.

We then looked at the reverse association in the period 01/01/1995-05/27/2017. We treated multiple southward B_z periods within a 24-h time interval as one. If multiple southward B_z periods were preceded by the same shock, we counted that shock only once. Also, there were instances where a single southward B_z period was preceded by multiple shocks. There were 490 fast-forward shocks (with $M_{ms}>1$ and listed in the IPshocks database) observed by *Wind* spacecraft at L1 and we matched them with the 129 strong and long-duration southward B_z periods. Out of these shocks, 100 were followed by strong and long-duration southward B_z periods. Integration of the CFASDB and inclusion of ACE shocks from the IPshocks database gave us 17 more such shocks (6 *Wind* shocks from CFASDB and 11 ACE shocks from the IPshocks database). So, out of the 507 shocks studied in this time span, 117 (regardless of the spacecraft type) were followed by strong and long-duration southward B$_z$ periods, which accounted for 23% of total. This led to the understanding that, although the large portion of the strong and long-duration southward B$_z$ periods occured within 48 hours after the arrival of fast-forward shocks at L1, only a small portion of fast-forward shocks were actually followed by strong southward B$_z$ periods. We combined our shocks list with the CME list of Richardson & Cane (2010) as done in Lugaz et al. (2017a) and found that 86 (∼74%) of these 117 shocks were CME-driven shocks. So, the majority of shocks followed by southward B$_z$ periods were driven by CMEs, although CME-driven shocks only represented about 72% of all fast-forward shocks at 1 AU (Kilpua et al., 2015b).

The time interval of our study was roughly 22.4 years. The forecast model was constructed to function by monitoring 3-day windows, 1 day training window (TW) and 2 days forecast window (FW) around a fast-forward shock arrival at L1. Removing the fast-forward shock concept from the picture, the forecast model had an uphill task of distinguishing 129 strong southward B$_z$ windows (3.2% of total) from 4088 windows. This forecasting scheme was implemented by Riley et al. (2017) with only moderate success to predict the southward magnetic field. In addition, testing different approaches based on the 22.4-year span of data, and the full range of solar wind plasma and IMF parameters with different weights would have required a dedicated and complex data analysis study, which may not have been a significant improvement over their model. In our current approach, as proposed here, we searched for physics-based constraints to narrow down the total number of windows that were "candidates" as having strong southward B$_z$. We did so by considering those windows preceded by a fast-forward shock. Limiting ourselves to windows around fast-forward shocks enabled to develop a model aimed at distinguishing the 23% positive windows out of 507, instead of 3.2% out of 4088. However, it was achieved at the cost of not being able to predict 24% of strong southward B$_z$ events, those not preceded by a fast-forward shock.

Jurac et al. (2002) examined the influence of shock parameters on geomagnetic disturbances within 48 hours following the shock arrival at the Earth. They studied 107 fast-forward shocks observed by the *Wind* spacecraft from 1995 to 2000. They identified the angle between the shock normal and the upstream IMF, θ_u to be a good indicator of future geoeffectivness of a shock. They found that shocks with θ_u between 70 - 90° were followed by intense storms 38 - 50% of the time. They found an even better correlation using the angle between the shock normal and the downstream IMF, θ_d. They found that shocks with front normals orthogonal to the downstream IMF (θ_d>80°, i.e., perpendicular shocks) were likely to be followed by intense storms 40% of the time. This study highlighted the potential for some fast-forward shocks to provide an "advanced warning" of an incoming strong southward B_z period depending on the shock parameters.

We expanded upon the study of Jurac et al. (2002) by considering the time period 1995-2017 rather than 1995-2000 and we carried out a similar examination of 507 fast-forward shocks during this period. We found 190 shocks with upstream angles between 70 - 90°. However, only 42 of them were followed by an intense southward B_z period within 48 hours after the shock arrival, which accounted for 22% of the total. For another shock parameter, the downstream angle, we found 200 shocks with downstream angles greater than 80° and 50 of them were followed by an intense southward B_z period within 48 hours after the shock arrival, which accounted for 25% of the total. Therefore, the correlation between shock angles and geoeffectiveness seen by Jurac et al. (2002) did not hold true for an expanded interval and increased number of shocks. The proportion we observed for shocks with angles between 70 - 90° was almost identical to the proportion we found for all fast forward shocks (23% of fast-forward shocks were followed by intense storms within 48 hours after the shock arrival at L1, regardless of any parameter criteria). As our probabilistic forecast model was based on periods following fast-forward shocks, this finding led us to consider different combinations of upstream parameters.

By examining the time intervals between fast-forward shocks and the start time of their corresponding strong and long-duration southward B_z periods, we found the mean and median of these intervals to be 13.87 hours and 11.59 hours respectively. This indicated that

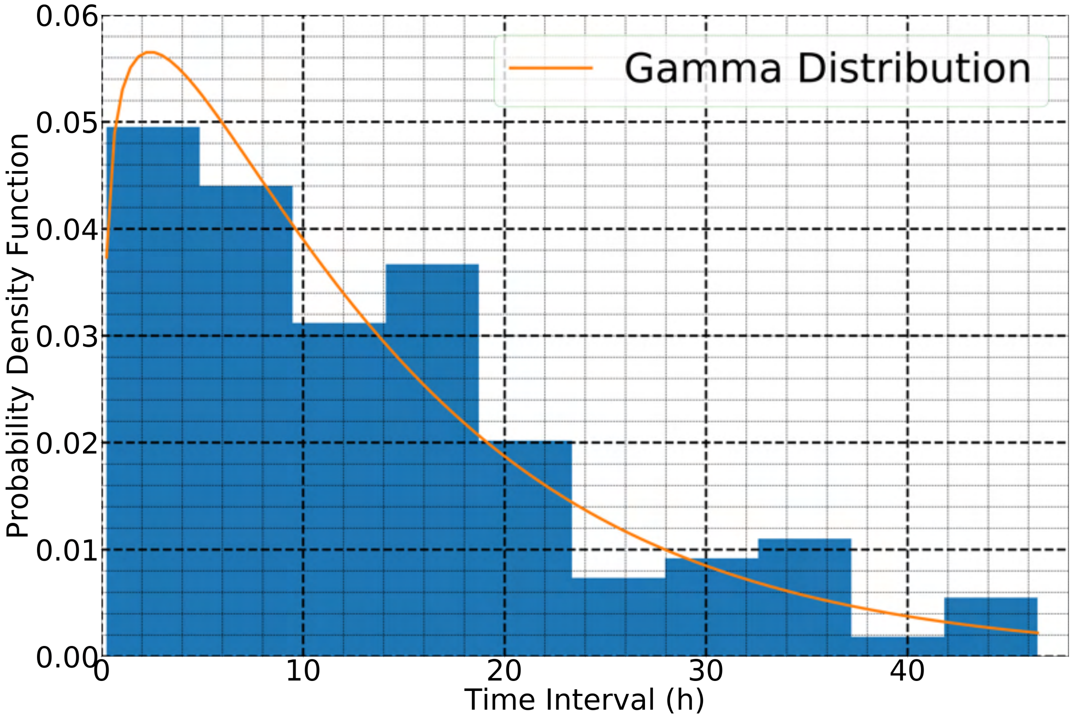

Figure 7.1: Distribution of time intervals between fast-forward shocks and the start time of their corresponding strong and long-duration southward B$_z$ periods.

a forecast of strong and long-duration B_z periods based on shock arrival at L1 may give on average a 14-hour advanced warning. Examining these intervals more precisely, we observed a large range (from a minimum time interval of 15 minutes to a maximum time interval of approximately 47 hours). It was also seen that half of the time intervals lied in the range between 5.19 hours (25th percentile) and 19.15 hours (75th percentile). To first order, this 25 - 75% range corresponded to southward B_z starting towards the back of a sheath or the beginning of the CME (typical sheath duration is $\sim$7.5 hours) to the second half of the CME (after a 7.5-hour sheath and 11.6 hours of the $\sim$20-hour CME). The shortest durations were expected for shocks inside CMEs. The greater than 75% may be at the back of a CME or in the wake or due to multiple CME interaction (Lugaz et al., 2017b). Figure 7.1 showed the theoretical distribution which best fit these time intervals. It was a Gamma distribution with a shape parameter of 1.67 and a scale parameter of 8.30.

7.3 Identification of closest matches

At the core of the forecasting technique was the idea that the shock parameters may contain information related to the driver of the shock. For example, the speed of a CME-driven shock is certainly related to the speed of the CME front. As this method was meant to be used in near-real time, it was simpler and faster not to calculate the shock speed, normal direction, etc. from the RH relationships but instead to rely on data from the shock ramp. As such, our TW, where the closest matches to a reference event were identified, included the period before the shock as well as the shock ramp itself. In details, we used the combination of the pre-shock (23.75 hours) interval and the shock itself (± 0.25 hours around the shock) as the TW and the post-shock (47.75 hours) interval as the FW. As we found from the time intervals that 90% of strong and long-duration southward B_z periods occured at least 1.85 hours after a shock arrival at L1, it enabled us to include the post shock 0.25 hours period in the TW. For any reference event, we used the TW to determine the closest matches to the solar wind conditions to be forecasted and used observations of the corresponding post-shock intervals to make a probabilistic forecast for the reference event (see Section 7.4 for further details).

The closest matches to any reference event were found based on the variations of four solar wind and IMF parameters of the database events (the magnetic field magnitude (B), z-component of the magnetic field (B_z) in GSM coordinates, solar wind proton number density (N_p), and x-component of the solar wind velocity (V_x in GSM coordinates), in comparison with the reference event in the TW. These variations were quantified using the RMSE method. We made the RMSE of a particular parameter dimensionless by dividing it with the average in the TW of that parameter of the reference event. All errors were done on dimensionless values because we did not want the RMSE of one of the parameters to dominate the calculation of TRMSE, as the range of speed for example (250 - 1500 km/s) was very different than that of the magnetic field (2 - 100 nT). The dimensionless RMSE for each of the four parameters (B, B_z, N_p, and V_x) were then added to get the total RMSE (TRMSE, see Equation 7.1).

$$\text{TRMSE} = \sum_{i=1}^{4} Z_i \tag{7.1}$$

Here, Z_i is the dimensionless RMSE of a parameter, and i runs from 1 to 4 (four parameters in consideration).

Based on the values of the TRMSE (the lower the value of TRMSE, the closer was a event to the reference), the closest matches to a reference event were identified.

7.4 Probabilistic forecast and error of forecast

With the closest matches to a reference event identified, we first made a probabilistic forecast for B_z in the FW. Our focus was on B_z reaching a pre-defined threshold, here -10 nT for 3 consecutive hours or more in the FW. If we focused on N number of closest matches, and if M of those had B_z reaching the threshold, a probability of M/N that the reference event may have B_z reaching the threshold in its FW was assigned. For each probabilistic forecast, the error of the forecast was also calculated. If the reference event indeed reached the threshold, the correct forecast was 1 and the probabilistic error was $\sqrt{1-(M/N)^2}$. If the reference event did not reach the threshold, the correct forecast is 0 and the probabilistic error was M/N.

The primary goal of our probabilistic forecast model was to outperform the random (i.e., coin flipping) forecast, which had an error of 0.5, irrespective of whether the reference event reached the threshold or not. A perfect forecasting method would have an error of 0, error of 1 meant no or zero skill. We tried to minimize the error of our probabilistic forecasts. As our statistics showed that 23% of fast-forward shocks were precursors to a strong and long-duration B_z period, the best naive guess was to assign a probability of 0.23 to every fast-forward shock. This best zero-skilled approach led to a RMSE of 0.421. Ideally, we would like to beat this, to show that our forecast model not only had more skill than a random forecast, but also possessed more skill than the best possible average-based forecast.

7.5 Modifications to the model

In order to minimize the error, we randomly selected 100 events from the 496 fast-forward shocks (490 listed in the IPshocks database + 6 additional from CFASDB) observed by the *Wind* spacecraft in the period 01/01/1995-05/27/2017 and removed them from the database. This way the training set was fully different from the events set and cross-contamination was negated. We then randomly sliced these 100 events into four individual sets (24, 25, 25, and 26 events respectively). We used these events to form the basis of our model and referred to them as “reference events” from now on. The goal was to identify how to construct the TRMSE to minimize the error of forecasts.

7.5.1 Training window weighting constant pair (TWWCP)

The TW was split into two intervals: the first interval was the period of 24 hours to 0.25 hours prior to the shock and the second interval was the period of 0.25 hours prior to the shock to 0.25 hours after the shock arrival (it captured the shock jump). For the former interval, we binned the magnetic field and plasma data into 15-minute averages. For the latter one, the 1-minute and 90-second data was used as it is. Figure 7.2 showed the way the time interval was split and averaged.

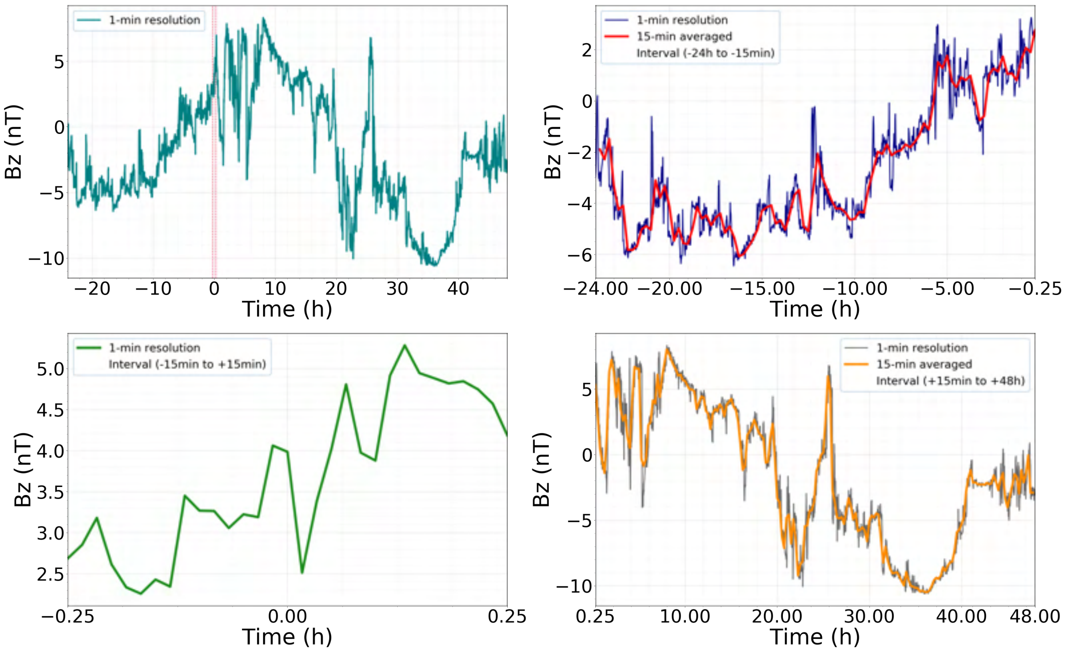

Figure 7.2: *Wind* observations of the fast-forward shock on 25 May 1997. The panels show: i) variation of GSM B_z component (top left) using 1-min resolution data over a 3-day window around the shock, from 24 May 1997 to 27 May 1997. The red dashed lines represent the interval of 0.25 hours prior to the shock arrival and 0.25 hours after the shock arrival ii) variation of GSM B_z component (top right) using 1-min resolution data and 15-min averaged data for the interval of 24 hours to 0.25 hours prior to the shock arrival iii) variation of GSM B_z component (bottom left) using 1-min resolution data for the interval of 0.25 hours prior to the shock arrival to 0.25 hours after the shock arrival iv) variation of GSM B_z component (bottom right) using 1-min resolution data and 15-min averaged data for the interval of 0.25 hours to 48 hours after the shock arrival.

For both intervals, we found the dimensionless RMSE of a parameter individually, multiplied them with a weighting constant pair, and added them to get the RMSE for that particular parameter. Five sets of weighting constant pairs were tried: (1,0), ($\frac{3}{4}$, $\frac{1}{4}$), ($\frac{1}{2}$, $\frac{1}{2}$),($\frac{1}{3}$, $\frac{2}{3}$), and ($\frac{1}{4}$, $\frac{3}{4}$).

A weighting constant pair (m, 1-m) meant that in calculating the RMSE of a parameter in the TW, we were putting $100m\%$ weight into the variations in the -24 h to -0.25 h interval and 100(1-m)% weight into the variations in the -0.25h to +0.25 h interval. Introduction of the weigthing constant pair provided a key insight into the importance of both intervals to the prediction of southward B$_z$ periods. If the probabilistic forecast improved by adding more weight into the variations of a parameter in the -0.25 h to +0.25 h period, it would suggest that what happens in the vicinity of the shocks play the prominent role in the occurrence of southward B$_z$ periods. If the probabilistic forecast did not improve or worsened, it would suggest that the pre-shock interval was the important one.

7.5.2 Varying weights of parameters

Additionally, when the TRMSE was calculated by adding the dimensionless RMSE of the four solar wind and IMF parameters, different weights were assigned to each parameter. For example, a set of weights, a$_1$=1, a$_2$=1, a$_3$=0, a$_4$=0, assigned to B, B$_z$, N$_p$, and V$_x$ respectively indicated that the TRMSE in the TW was calculated with an equal weight for B and B$_z$, whereas the variations in N$_p$ and V$_x$ were neglected. These weights could have values ranging from 0 to 1, with 1 representing the maximum weight. We tried out different sets of weights. In our model, the weight assigned to a particular parameter was the same for both intervals of the TW. As such, the TRMSE was now defined by:

$$\text{TRMSE} = \sum_{i=1}^{4} a_i[mZ_{1i} + (1-m)Z_{2i}] \tag{7.2}$$

Here, Z_{1i} was the RMSE of a particular parameter in the pre-shock 23.75 hours period, Z_{2i}

was the RMSE of a particular parameter in the 0.5 hours period around the shock, and a_i represented the weights assigned to the four parameters.

7.5.3 Threshold-based forecast

In addition to the probabilistic forecasts, it could be interesting to develop dichotomous forecasts (YES/NO) that assigned a probability of 100% or 0% to an event occurring. To do so, we imposed a threshold on our forecasts. As our model provided forecasts based on observations in the FWs of 15 closest matches, we had 15 thresholds to choose from. In our analysis, we extensively tried 5, 10, and 15 closest matches. Using the 15 closest matches to identify a threshold was found to work better than using 5 or 10 closest matches. We did not try to determine if a number of closest matches larger than 15 would have been better. As there were only 106 positive events in our database and many of them having different characteristics, using a larger number of closest matches was unlikely to improve the model in a meaningful manner. We also found that using 10 or 15 closest matches were relatively similar.

Now, the thresholds in consideration could be generalized as $\frac{n}{15}$ where n=1, 2, 3,..........15. Any probabilistic forecast exceeding the threshold would be considered a YES and any probabilistic forecast below the threshold would be considered a NO. Let us assume that the threshold criterion selected for the probabilistic forecasts was 0.4 or $\frac{6}{15}$. So any probabilistic forecast would be considered a YES if it was greater than or equal to 0.4 (number of closest matches satisfying the B_z criterion was ≥ 6) and would be considered a NO if it was lower than 0.4 (number of closest matches satisfying the B_z criterion was < 6).

The skill of our threshold-based forecast model was quantified using the Heidke Skill Score (HSS, see Table 7.1) (Heidke, 1926). Negative skill scores would indicate that the model was fairing worse than the random model, and positive skill scores would indicate that the model was performing better than the random model. The perfect forecast obviously would attain a HSS of 1 and a HSS of 0 would have meant no skill.

Table 7.1: Contingency table for HSS.

Forecast	Observed		
	YES	NO	Marginal Total
YES	a (Hit)	b (False Alarm)	a+b
NO	c (Miss)	d (Correct Negative)	c+d
Marginal Total	a+c (Observed YES)	b+d (Observed NO)	a+b+c+d (Total)
HSS = 2 (ad-bc) / [(a+c)(c+d) + (a+b)(b+d)]			

7.6 Example of the model

We demonstrated the forecasting model for a reference event, observed by the *Wind* spacecraft on 18 June 2003 at 04:42 UT (see Figure 7.3). This reference event corresponded to a shock inside a CME (see Lugaz et al., 2016b). Though it was not a traditional event with a shock impacting the Earth first followed by the CME, our motivation was to present this event as an example because it illustrated the pattern of improving probabilistic forecasts better than any of the other reference events we used in our analysis. Through this event, it was possible for us to showcase how including more than one parameter and putting more weight into the variations closer to the shock significantly improved the forecasts in a clear manner.

For this reference event, the TW extended from 17 June 2003, 04:42 UT to 18 June 2003, 04:57 UT and the FW was the following 47.75 hours. Our goal was to predict the occurence of at least one B_z<-10 nT period of 3 consecutive hours or more within the FW. For this reference event, 17 minutes after the shock arrival, there was the start of a period of four consecutive hours where B_z<-10 nT. Our expectation from the probabilistic model was to generate a probabilistic forecast as close as possible to 1.

Initially, we started with our baseline (only considering B_z variations and no shock info) set of weights: B=0, B_z=1, N_p=0, V_x=0 and choose (1,0) as the training window weighting constant pair (TWWCP). Choice of these weights and TWWCP suggested that only variations of B_z in the -24 h to -15 min interval prior to the shock arrival was considered. This set of

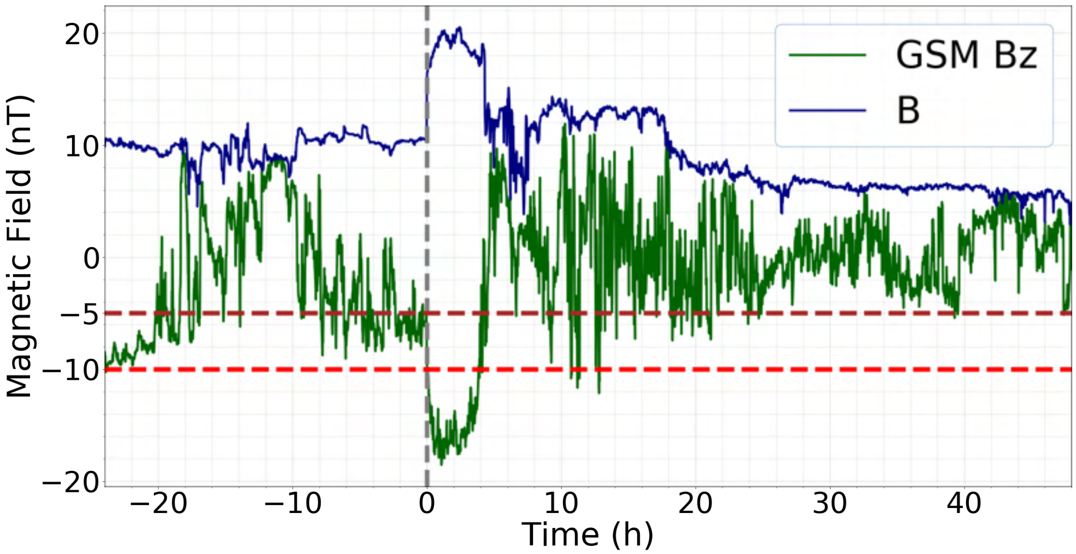

Figure 7.3: *Wind* observations of the fast-forward shock on 18 June 2003. The panel shows the variation of magnetic field strength and GSM B_z component over a 3-day window around the shock, from 17 June 2003 04:42 UT to 20 June 2003 04:42 UT.

weights and TWWCP gave a probabilistic forecast of 0.07 (see in Figure 7.4).

This probabilistic forecast was far from ideal as the prediction was a 7% probability for the occurence of B_z<-10 nT periods of 3 consecutive hours or more in the FW, compared to an observed 100% probability. To improve the probabilistic forecast, the TWWCP was changed from (1,0) to $(\frac{1}{2}\ ,\frac{1}{2})$, keeping the parameter weights fixed. It gave a probabilistic forecast of 0.33. This probabilistic forecast was an improvement for sure. Next, more weight was put into the variations of B_z closer to the shock by selecting TWWCP $(\frac{1}{4}\ ,\frac{3}{4})$ and using the same set of weights. It gave a probabilistic forecast of 0.40 (see in Figure 7.5). This improvement of the probabilistic forecasts from 0.07 to 0.33 and then to 0.4 showed that putting more weight into the variations closer to the shock improved the probabilistic forecast for this particular event.

We then monitored the evolution of probabilistic forecasts by changing the weights and TWWCPs. For each reference event, we accomplished this through numerous combinations of weights and TWWCPs. The goal of these repeated procedures was to identify the pattern

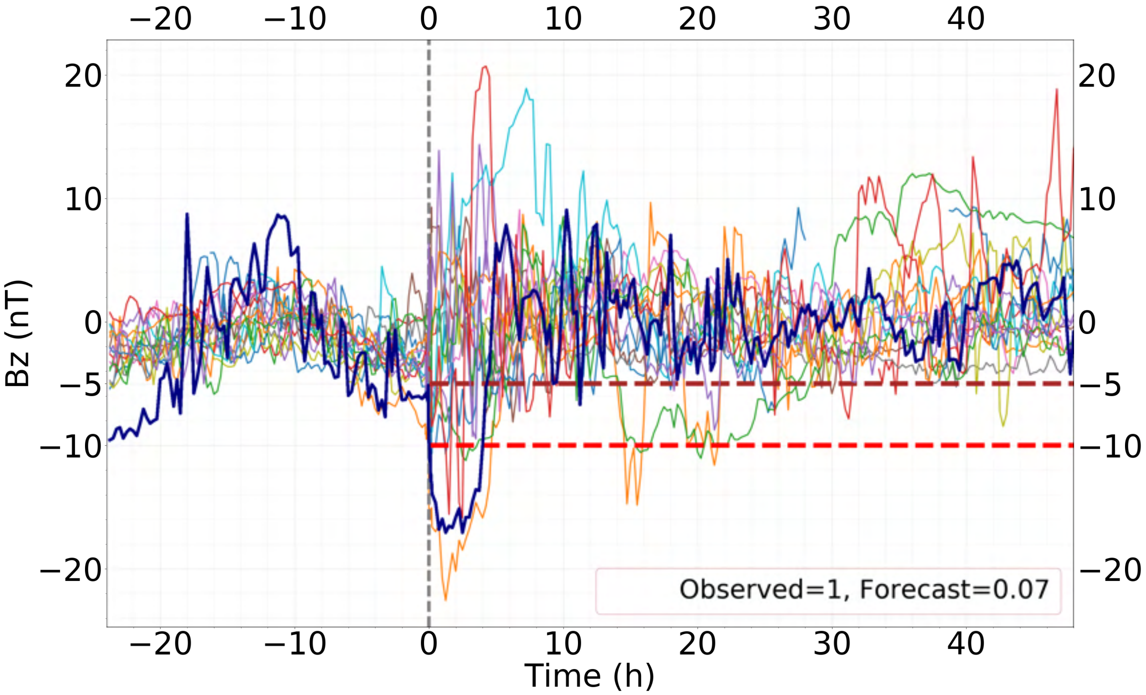

Figure 7.4: Probabilistic forecast for the event following the 18 June 2003 shock shown in Figure 7.3 for TWWCP (1,0) and weights (0, 1, 0, 0) (Navy=reference event, other colors=15 closest matches).

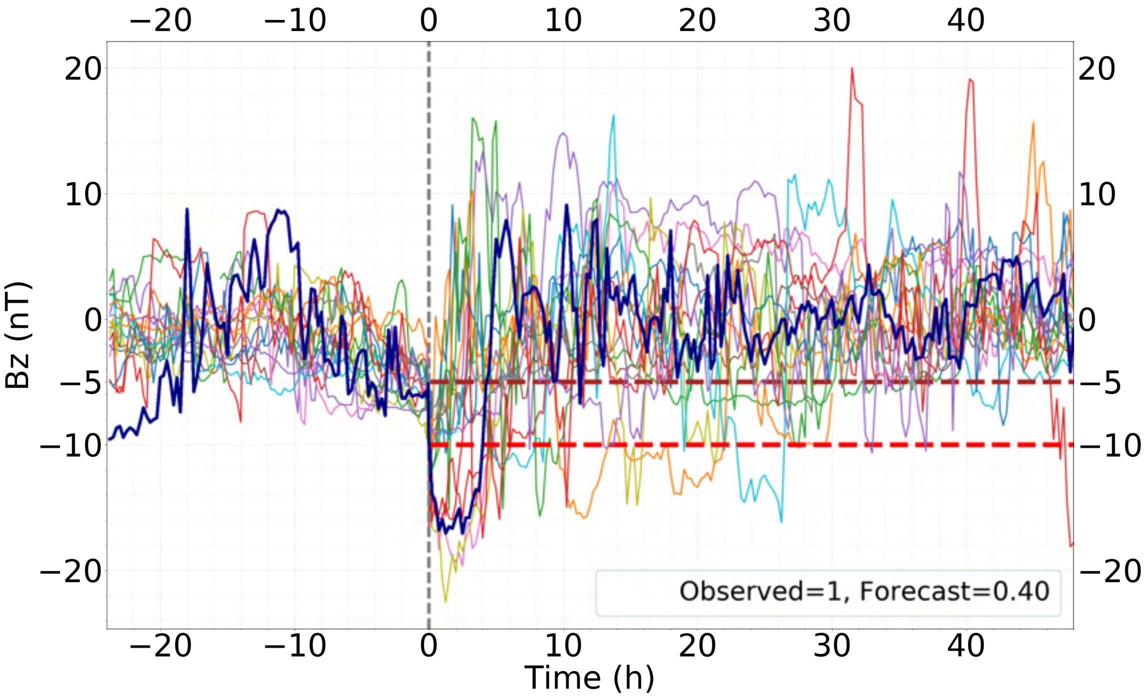

Figure 7.5: Same as Figure 7.4 but for TWWCP ($\frac{1}{4}$, $\frac{3}{4}$).

of improving probabilistic forecasts. Thereby for this reference event, we now considered variations of both B and B_z in the TW. Use of a set of weights (0.5, 1, 0, 0) and TWWCP ($\frac{1}{4}$, $\frac{3}{4}$) gave a probabilistic forecast of 0.53 (see in Figure 7.6).

This improvement in the probabilistic forecast indicated that considering variations of more than one parameter in finding the 15 closest matches supposedly make the forecast better.

This assumption was validated by a probabilistic forecast of 0.13, previously 0.07 for the set of weights (0.25, 1, 0, 0) (previously (0, 1, 0, 0)) with TWWCP (1,0) and a probabilistic forecast of 0.47, previously 0.33 for the set of weights (1, 1, 0, 0) (previously (0, 1, 0, 0)) with TWWCP ($\frac{1}{2}$, $\frac{1}{2}$). We also observed improvements in the probabilistic forecasts by increasing the weights of B.

After that, variations of N_p with the variations of B and B_z in the TW was considered. The set of weights (1, 1, 0.25, 0) with TWWCP ($\frac{1}{4}$, $\frac{3}{4}$) gave a probabilistic forecast of 0.53 (see

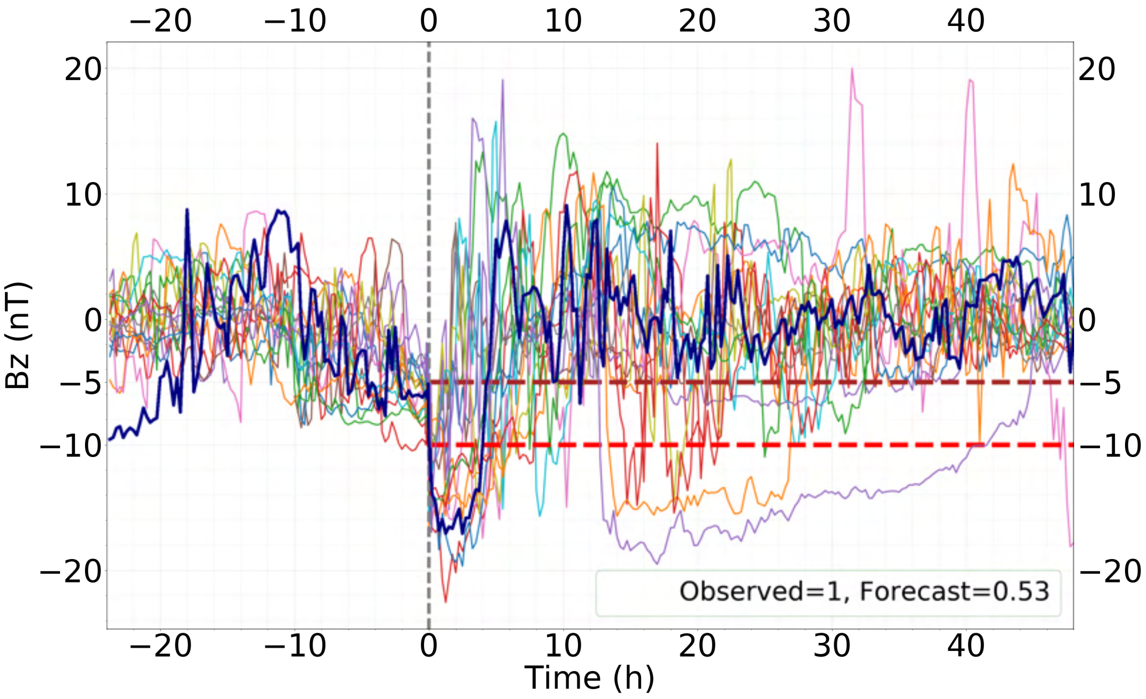

Figure 7.6: Same as Figure 7.4 but for TWWCP ($\frac{1}{4}$, $\frac{3}{4}$) and weights (0.5, 1, 0, 0).

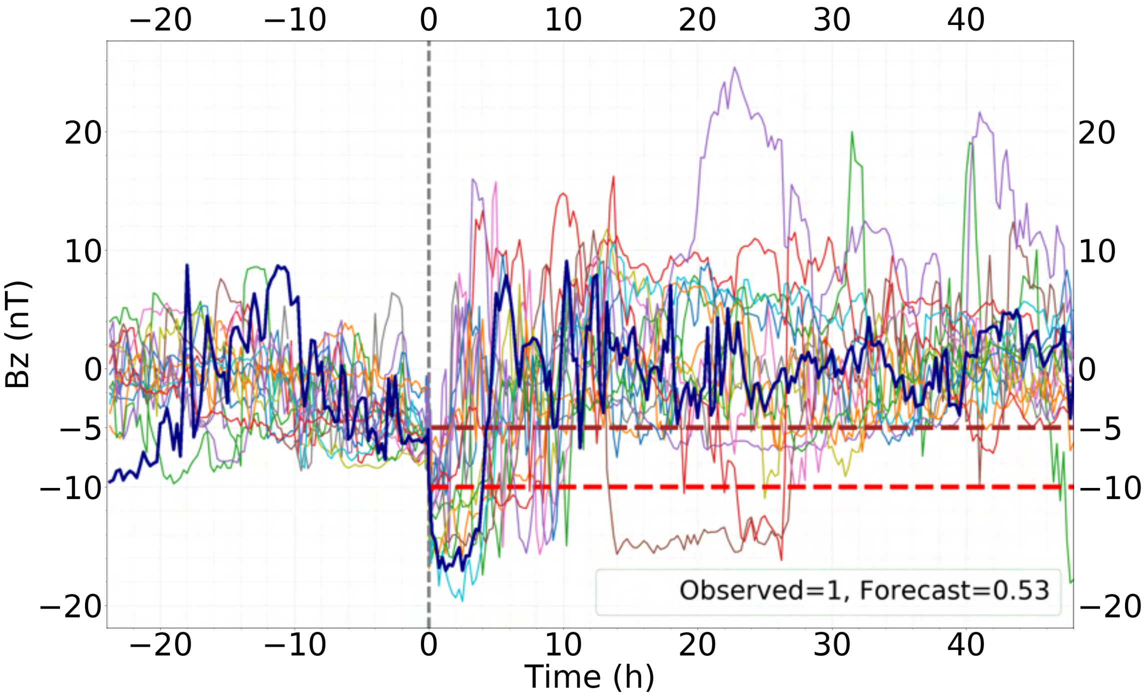

Figure 7.7: Same as Figure 7.4 but for TWWCP ($\frac{1}{4}$, $\frac{3}{4}$) and weights (1, 1, 0.25, 0).

in Figure 7.7) and the set of weights (1, 1, 0.25, 0) with TWWCP ($\frac{1}{2}$, $\frac{1}{2}$) gave a probabilistic forecast of 0.47. The general observed trend was that adding the parameter N_p either kept the forecast constant or improved it.

Finally, the influence of the fourth parameter (V_x) on the probabilistic forecasts was examined. The observed trend was that adding V_x generally worsened the probabilistic forecasts. Two such scenarios were presented for a fixed TWWCP ($\frac{1}{2}$, $\frac{1}{2}$). The probabilistic forecast of 0.47 for the set of weights (1, 1, 0, 0) dropped to 0.2 (see in Figure 7.8) for the set of weights (including V_x) (1, 1, 0, 0.5). Similarly a probabilistic forecast of 0.47 for the set of weights (1, 1, 0.25, 0) dropped to 0.27 for the set of weights (including V_x) (1, 1, 0.25, 0.25). Important thing to note that this model only provided probabilistic predictions for the occurence of strong and long-duration southward B_z periods following a fast-forward shock. The parameter V_x might have influence on the prediction of Kp or Dst.

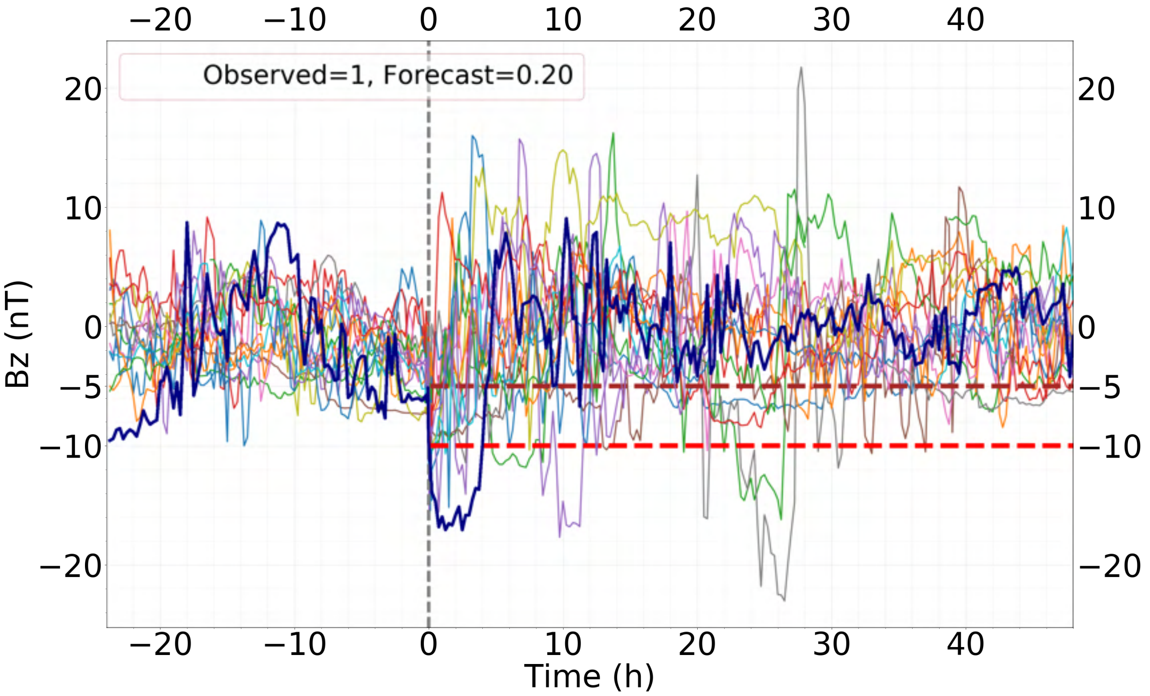

Figure 7.8: Same as Figure 7.4 but for TWWCP ($\frac{1}{2}$, $\frac{1}{2}$) and weights (1, 1, 0, 0.5).

We also highlighted the threshold-based forecast. As shown in Section 7.7, a good criterion was a probabilistic forecast of at least 0.4.

For the reference event discussed above, the set of weights (1, 1, 0.25, 0) with TWWCP ($\frac{1}{4}$, $\frac{3}{4}$) gave a probabilistic forecast of 0.53. So, for a threshold criterion of 0.40, this probabilistic forecast was considered a YES and it correctly predicted the occurence of B_z<-10 nT periods of 3 consecutive hours or more in the FW. Similarly, the set of weights (1, 1, 0, 0.5) with TWWCP ($\frac{1}{2}$, $\frac{1}{2}$) gave a probabilistic forecast of 0.20. So, for the threshold criterion of 0.40, this forecast was considered a NO and the outcome was a missed prediction.

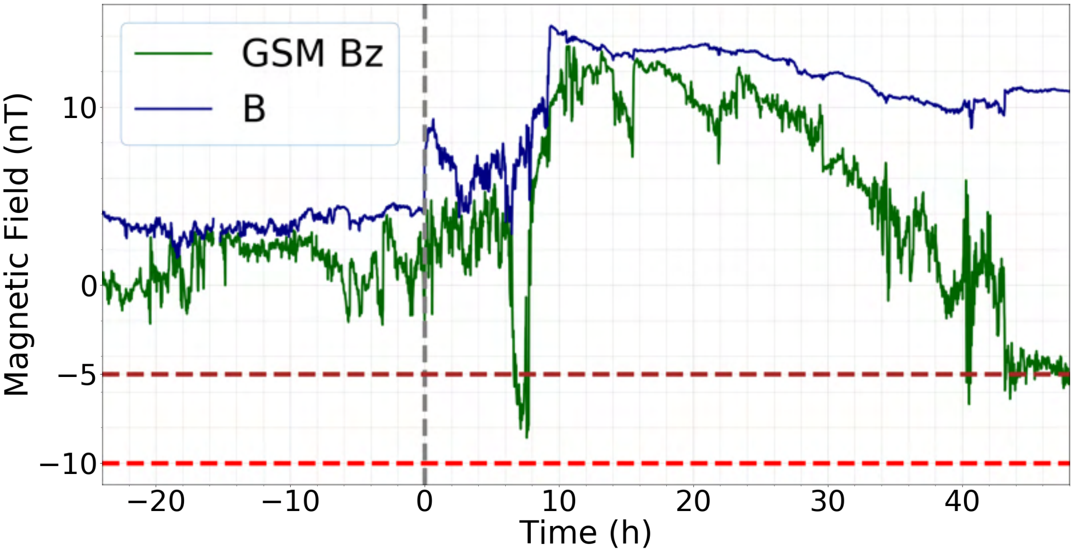

Figure 7.9: *Wind* observations of the fast-forward shock on 29 March 2011. The panel shows the variation of magnetic field strength and GSM B_z component over a 3-day window around the shock, from 28 March 2011 15:09 UT to 31 March 2011 15:09 UT.

Figure 7.9 represented a second reference event for which the model was demonstrated. This event was observed by the *Wind* spacecraft on 29 March 2011 at 15:09 UT. This reference event lied in the opposite side of the spectrum compared to the first reference event, as there was no B_z<-10 nT period of 3 consecutive hours or more in the FW. Thereby, the ideal probabilistic forecast needed to be as close to 0 as possible.

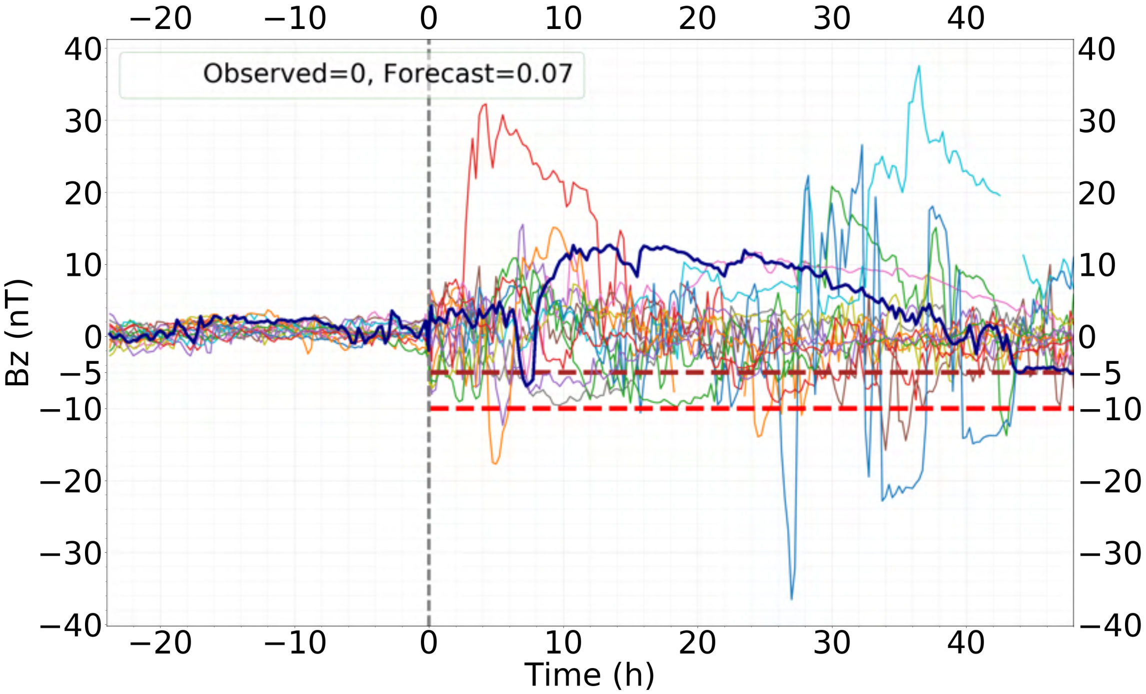

Figure 7.10: Probabilistic forecast for the event following the 29 March 2011 shock shown in Figure 7.9 for TWWCP (1,0) and weights (0, 1, 0, 0).

For the baseline set of weights (0, 1, 0, 0) and TWWCP (1,0), a probabilistic forecast of 0.07 was obtained (see in Figure 7.10). This probabilistic forecast was almost the ideal forecast. However, recognizing the pattern of optimum probabilistic forecast was the primary goal. The trend observed from the first reference event was that adding more parameters and putting more weight into the variations closer to the shock generally improved the probabilistic forecast. However, the probabilistic forecast worsened when the variations of V_x in the TW was considered. These assumptions developed from the analysis of the first reference event were put to the test here. For the set of weights (1, 0.25, 0, 0) with TWWCP (1,0) a probabilistic forecast of 0.07 was obtained (see in Figure 7.11). The probabilistic forecast was not improved by adding a new parameter (B) like the first reference event but did not worsen either.

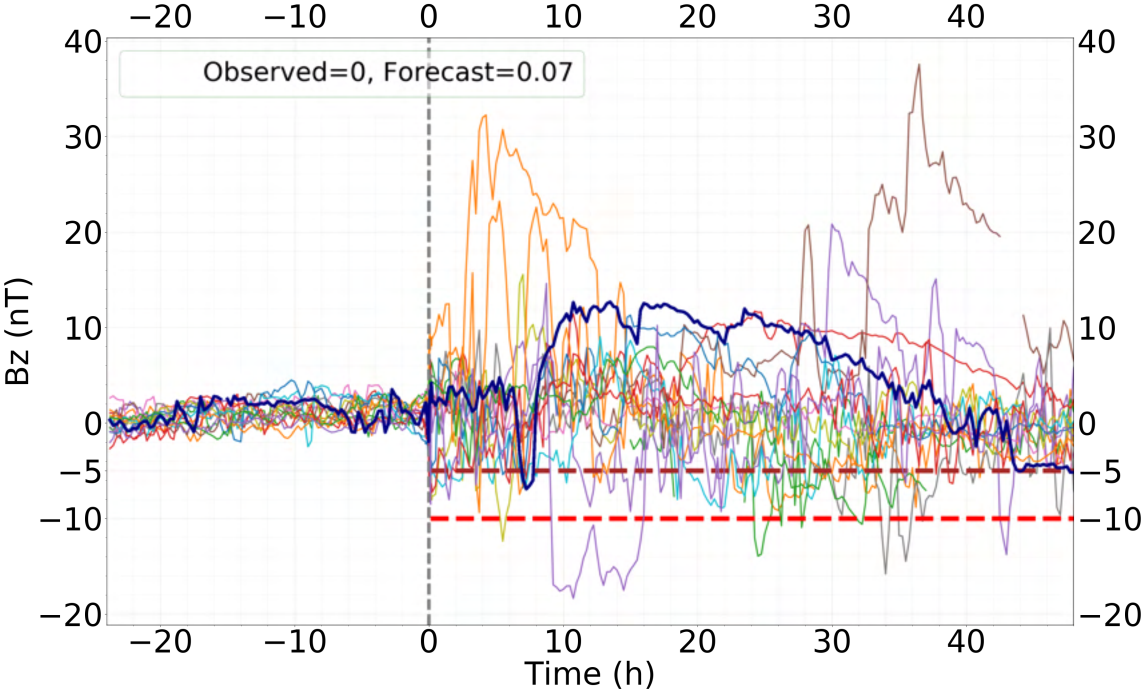

Figure 7.11: Same as Figure 7.10 but for weights (1 , 0.25, 0, 0).

Next, the third parameter N_p was added and more weight was put into the variations closer to the shock. For the set of weights (1, 1, 0.5, 0) with TWWCP ($\frac{1}{3}$, $\frac{2}{3}$) and (1, 1, 0.5, 0) with TWWCP ($\frac{1}{4}$, $\frac{3}{4}$) (see in Figure 7.12), probabilistic forecasts of 0.07 were obtained for both the cases.

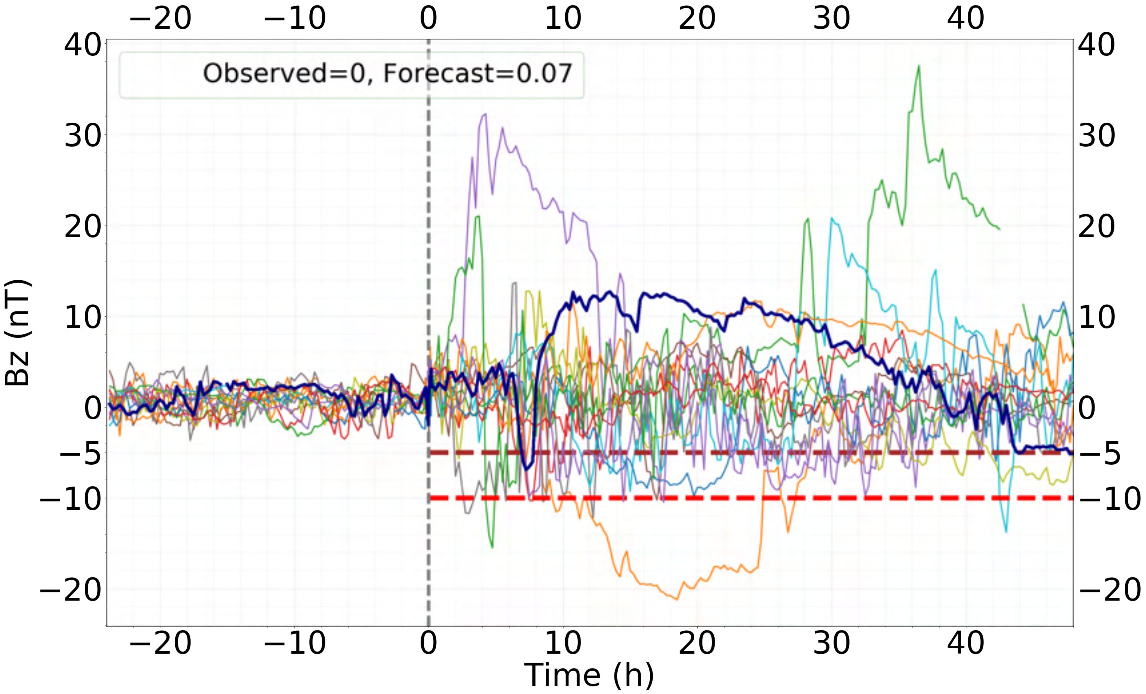

Figure 7.12: Same as Figure 7.10 but for TWWCP ($\frac{1}{4}$, $\frac{3}{4}$) and weights (1, 1, 0.5, 0).

However, for the set of weights (1, 1, 1, 1) with TWWCP ($\frac{1}{2}$, $\frac{1}{2}$), probabilistic forecast of 0.20 was obtained. Similarly for the set of weights including V_x, like (1, 0.5, 0.25, 0.25), (1, 1, 0, 0.5), and (0, 1, 0.25, 0.25) with fixed TWWCP ($\frac{1}{2}$, $\frac{1}{2}$), probabilistic forecasts of 0.20, 0.13, and 0.13 were obtained respectively, which confirmed the assumption that adding the parameter V_x generally makes the forecast worse. Now, for the same selected threshold of 0.40 as the first reference event, all of the predictions discussed above for the second reference event were considered a NO and the outcome was the correct prediction.

The pattern observed through the analysis of reference events (only 2 shown) was consistent for both positive ($B_z<-10$ nT periods of 3 consecutive hours or more in FW) and negative (no $B_z<-10$ nT period of 3 consecutive hours or more in FW) events. The probable best combination corresponded to maximum weights assigned to parameters B and B_z, inclusion of parameter N_p with reduced weight in comparison with B and B_z, exclusion of parameter V_x, and increased weight in the 30 minutes interval around the shocks.

7.7 Results from the model

Based on the construction of our model and selection of sets of weights and TWWCPs, several thousands of different combinations can be used. However, the main goal of this work was to show that such a probabilistic and threshold-based forecast model had skills to define the groundwork for more detailed experimentation in the future.

7.7.1 Best probabilistic forecast for all 100 reference events

We tried out different combinations of sets of weights and TWWCPs for the first set of 24 reference events in a way similar to what is shown for the two events in Section 7.6. We then determined the probabilistic forecast for the forecast parameter ($B_z < -10$ nT for a period of 3 consecutive hours or more). The error of each probabilistic forecast for each reference event was calculated, as well as the RMSEs. This allowed us to select the seven best performing combinations, as well as the baseline forecast based only on B_z and no shock info (see Table 7.2).

Table 7.2: Seven best performing and the baseline combinations of sets of weights and TWWCPs for the first set of reference events and their corresponding RMSE of probabilistic forecasts.

Set of Weights					
B	B_z	N_p	V_x	TWWCP	RMSE (Set-I)
0	1	0	0	1,0	0.387
1	0.5	0	0	1/4,3/4	0.318
1	0.5	0.25	0	1/4,3/4	0.310
1	0.5	0.5	0	1/3,2/3	0.311
1	0.5	0.5	0	1/4,3/4	0.309
1	1	0	0	1/3,2/3	0.303
1	1	0.25	0	1/4,3/4	0.289
1	1	0.5	0	1/4,3/4	0.310

Looking at this list of 8 combinations, it was observed that the highest RMSE of 0.387 belonged to the baseline set of weights (0, 1, 0, 0) with TWWCP (1,0) and the lowest RMSE of 0.289 belonged to the set of weights (1, 1, 0.25, 0) with TWWCP ($\frac{1}{4}$, $\frac{3}{4}$). An important thing to note was that RMSEs for these eight combinations were well below 0.5 which meant each of them was able to provide a probabilistic forecast substantially better than a random forecast. The best non-skilled forecast could be obtained by assigning a probability of 0.23 to all fast-forward shocks, resulting in a RMSE of 0.421. The baseline combination had a RMSE which was 8.08% lower than this, whereas the best RMSE was significantly lower (by 31%).

Then, for each of these eight combinations, we calculated the errors of forecasts (see Table 7.3) for the other three sets of reference events (25, 25, and 26 reference events respectively).

Table 7.3: Seven best performing and the baseline combinations of sets of weights and TWWCPs for the other three sets of reference events and their corresponding RMSE of probabilistic forecasts.

Set of Weights					RMSE		
B	B_z	N_p	V_x	TWWCP	Set-II	Set-III	Set-IV
1	0.5	0	0	1/4,3/4	0.3161	0.3773	0.4716
1	0.5	0.25	0	1/4,3/4	0.3331	0.3795	0.4420
1	0.5	0.5	0	1/3,2/3	0.3564	0.3564	0.4369
1	0.5	0.5	0	1/4,3/4	0.3403	0.3612	0.4287
0	1	0	0	1,0	0.3814	0.3268	0.4427
1	1	0	0	1/3,2/3	0.3128	0.3588	0.4618
1	1	0.25	0	1/4,3/4	0.3435	0.3838	0.4551
1	1	0.5	0	1/4,3/4	0.3356	0.3915	0.4629

Finally, we calculated the average RMSE for each of these 8 combinations for all the 100 reference events (see Table 7.4). Then, we selected 5 combinations from these 8 combinations, 4 in terms of the lowest average RMSEs and the fifth one was the baseline combination. The lowest average RMSE belonged to the set of weights (1, 1, 0, 0) with TWWCP ($\frac{1}{3}$, $\frac{2}{3}$), which had an average RMSE of 0.3592.

Table 7.4: Average RMSE of probabilistic forecasts corresponding to the seven best performing and the baseline combinations of sets of weights and TWWCPs for the four sets of reference events.

Set of Weights					
B	B_z	N_p	V_x	TWWCP	Average RMSE
1	0.5	0	0	1/4,3/4	0.3708
1	0.5	0.25	0	1/4,3/4	0.3662
1	0.5	0.5	0	1/3,2/3	0.3652
1	0.5	0.5	0	1/4,3/4	0.3597
0	1	0	0	1,0	0.3845
1	1	0	0	1/3,2/3	0.3592
1	1	0.25	0	1/4,3/4	0.3678
1	1	0.5	0	1/4,3/4	0.3750

7.7.2 Threshold-based probabilistic forecast

Then, we moved to the second step. For each of these 5 combinations, we tried to find the best threshold criterion out of 15 (see in Section 7.5.3) corresponding to the optimum HSS. To find the optimum HSS, we considered the probabilistic forecasts of the 100 reference events. Looking at the scores (see Table 7.5), we found that the lowest best HSS of 0.31 belonged to the baseline combination for a threshold of 0.33 or $\frac{5}{15}$. The highest best HSS of 0.44 belonged to the set of weights (1, 1, 0, 0) with TWWCP ($\frac{1}{3}$, $\frac{2}{3}$) for a threshold of 0.40 or $\frac{6}{15}$. This HSS represented a 42% improvement over the baseline HSS.

Table 7.5: Threshold criterion corresponding to the optimum Heidke Skill Score for the four best performing and the baseline sets of weights and TWWCPs.

Set of Weights					B_z<-10 nT	
B	B_z	N_p	V_x	TWWCP	Best HSS	Threshold Criterion
0	1	0	0	1,0	0.31	0.33
1	1	0	0	1/3,2/3	0.44	0.40
1	0.5	0.25	0	1/4,3/4	0.42	0.40
1	0.5	0.5	0	1/4,3/4	0.39	0.33
1	0.5	0.5	0	1/3,2/3	0.34	0.33

Now, we used this threshold of 0.40 and the set of weights (1, 1, 0, 0) with TWWCP ($\frac{1}{3}$, $\frac{2}{3}$) to find the HSS for 10 randomly chosen sets, each with 166 reference events (166 events account for slightly more than $\frac{1}{3}$ of our database (see Table 7.6). In this phase, only one forecast was generated at a time by removing only the event in consideration from the database.

Table 7.6: Average contingency table and HSS for 10 randomly chosen sets of 166 reference events each.

	Forecast	Observed		
Average set		YES	NO	Marginal Total
	YES	18 (Hit)	4 (False Alarm)	22
	NO	12 (Miss)	132 (Correct Negative)	144
	Marginal Total	30 (Observed YES)	136 (Observed NO)	166 (Total)
	HSS	0.64		

When we examined these 10 sets, each with 166 threshold-based forecasts (see Table 7.6), the best combination provided (on average) 22 YES forecasts, 18 of them were correct predictions and 4 were false alarms (average False Alarm Ratio of 0.18 indicated that on average in $\frac{2}{11}$ of the forecast for B_z periods, strong and long-duration B_z were not observed). Average Threat Score or Critical Success Index was 0.53, indicating that on average slightly greater than $\frac{1}{2}$ of strong and long-duration B_z periods (observed and/or predicted) were correctly forecast. However, the model correctly predicted (on average) 18 out of the 30 events that occurred (average Probability of Detection Yes was 0.60, indicating that on average 60% of the observed B_z periods were correctly predicted).

CHAPTER 8

Summary and discussions

This thesis is based on the integration of five research articles. A summary and brief discussions on the five articles included in this thesis are given here.

8.1 Paper-I

This paper outlined solar wind plasma and IMF properties in 142 ME-driven sheath regions, measured by one of the twin STEREO spacecraft near 1 AU during 2007 - 2016 (see Chapter 4). The MEs were classified into three categories, based on whether a ME drives a shock and a sheath (106 MEs), or only a sheath (36 MEs), or neither (46 MEs). MEs driving both shocks and sheaths were observed, as expected to be the fastest MEs, propagating through typical solar wind, and MEs driving only sheaths were found to be the slowest MEs, propagating through the slower solar wind.

Our findings suggested that the shock driving rate of MEs varies in phase with the SCy activity (see also Lindsay et al., 1994; Gopalswamy, 2003; Jian et al., 2011, 2018). We found that a ME with a leading-edge speed as low as 316 $\mathrm{km\,s^{-1}}$ drove a shock near 1 AU, whereas another with a leading-edge speed of 701 $\mathrm{km\,s^{-1}}$ did not. Such instances can be subjected to the variation of the background solar wind plasma and IMF conditions for individual cases (e.g. Shen et al., 2007) or the effect of drag during the propagation of MEs in IP space (e.g. Lugaz & Kintner, 2013; Vršnak et al., 2013).

The primary objective of Paper-I was to explore SQ-I (how different are sheaths not preceded by shocks as compared to sheaths preceded by shocks, even for similar drivers?). From our statistical analysis, on average, sheaths preceded by shocks were observed to be hotter, faster, compressed, and magnetized with higher magnetic field fluctuations and dynamic pressure compared to sheaths without shocks. Some of the differences in the sheaths became smaller when sheaths, driven by MEs (with and without shocks) with similar in-situ speeds were compared, though even in this case, the average proton density, magnetic field strength, and dynamic pressure remained statistically higher for sheaths with shocks than sheaths without shocks. These properties are some of the most important ones to determine the effect of solar wind structures on geospace, both in terms of reconnection and compression. Therefore, sheaths preceded by shocks are expected to substantially affect the radiation belt and magnetosphere for a given speed than sheaths not preceded by shocks.

The lack of correlation found between the radial thickness of sheaths and the speed profile and associated Mach numbers of the driving ME, irrespective of the sheath type, was surprising. However, it was in perfect agreement with (see Salman et al., 2020b), who found typical sheath durations throughout the inner heliosphere independent of the initial ME speed. This finding indicated that accumulation of the solar wind before the ME drives a shock is the dominant mechanism that forms sheaths near 1 AU rather than the shock compression. For shock compression, the stand-off distance (the radial separation between the magnetic obstacle boundary and the shock front) is expected to be related to the ME speed or the shock Mach number (e.g. Russell & Mulligan, 2002; Savani et al., 2011). Important to note that this study primarily covered the significantly weak SCy 24 compared to SCy 23 (McComas et al., 2013), where the fraction of fast CMEs was not dominantly high (see Figures 7 and 18 in Jian et al., 2018). Further studies extending this, for example, with ACE or *Wind* data, can allow for improved statistics and the inclusion of more and faster CMEs from the more active SCy 23.

8.2 Paper-II

This paper further categorized the 106 ME-driven sheaths (preceded by shocks) of Paper-I with two different schemes (see Chapter 5). The first categorization was based on their potential formation mechanisms (PSs and ESs). The second categorization was based on observed speed variations within sheaths [constant (Cat-A), increasing (Cat-B), decreasing (Cat-C), and complex (Category-D) speed profiles], quantified with linear least-squares regression.

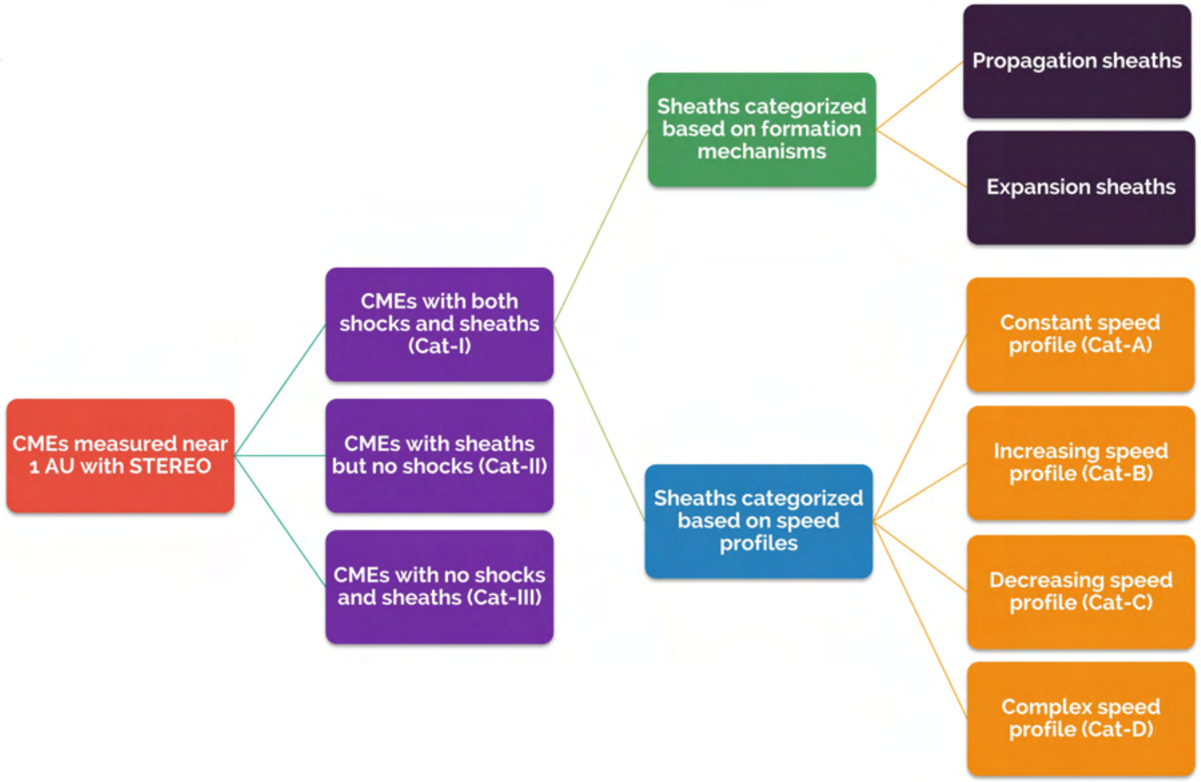

Figure 8.1: Categorizations of CMEs (especially CME sheaths) presented in Chapters 4 and 5.

Statistical differences between 28 PSs and 18 ESs were identified based on in-situ measurements (with ANOVA) and compared with theoretical arguments of previous studies (e.g. Siscoe & Odstrcil, 2008). It was observed that ESs were statistically faster and thicker (in the radial direction). The difference in the radial thickness was presumably not due to SC crossings (see Gopalswamy, 2006) because the shock normal angles with respect to the radial direction (a proxy for the distance of the SC crossing from the shock nose, θ_{nr}) for both sheaths were similar. It was also seen that PSs were statistically denser, a possible consequence of the driving MEs propagating in the denser and slower solar wind (see Temmer et al., 2021).

For the second categorization (26 Cat-A, 24 Cat-B, 20 Cat-C, and 36 Cat-D), it was seen from the results of ANOVA that the associated shock properties and SCy phase do not impact the occurrence of such speed variations within sheaths. The ANOVA results also indicated that SC crossings were presumably not the primary drivers of the observed speed variations, differing from the analysis of Paulson et al. (2012), that attributed Cat-B sheaths (with increasing speed profiles) to the possibility of SC crossing away from the shock nose. The findings also suggested that complex speed profiles (Cat-D) within sheaths were not mere anomalies (seen quite often) and were more likely for SC crossing further away from the nose of the shock.

The possibility of these speed variations being driven by intrinsic ME parameters was examined with LR, similarly to Riley & Richardson (2012), who used LR analysis to identify the likelihood for a CME to be classified as a MC based on several predictor variables. From LR, surprisingly, the ME expansion speed did not seem to influence this categorization. LR suggested that the magnetic field strength and the ME speed in the solar wind frame are the likely drivers of these speed variations.

The rationale behind Paper-II was to inspect SQ-II (what are the physical mechanisms contributing to the observed variabilities in CME sheaths near 1 AU?). The two categorizations of CME sheaths mentioned above lead to the hypothesis that the observed variabilities in CME sheaths near 1 AU are likely to be coupled to the sheath formation mechanisms and properties of the driving MEs, rather than the preceding shock parameters and SCy phases.

8.3 Paper-III

This paper presented a comprehensive list of 47 CMEs observed in conjunction in the inner heliosphere (see Chapter 6). Previously compiled databases of CMEs at MESSENGER, *Venus Express*, STEREO, and L1 were used in association to build the database. Each conjunction event was identified based on strict directional and temporal criteria.

On average, fast CMEs were observed to experience significantly higher speed variations (45%) during their propagation in the inner heliosphere than slow CMEs (5%). Beyond the orbit of Venus, both the variations in propagation speeds and average CME deceleration/acceleration was observed to become negligible. While the use of the DBM to determine the CME impact speeds (at Mercury and Venus) might have influenced this result, it was consistent with past studies (e.g. Gopalswamy et al., 2001; Reiner et al., 2007).

The overarching goal of Paper-III was to probe SQ-III (how much do CME features inferred from statistical estimations differ from the individual analysis of CMEs with multi-point observations?). Multi-linear robust regression fitting showed the maximum magnetic field strength within the ME to scale as $\mathrm{r}^{-1.91}$ in the inner heliosphere, consistent with previous statistical estimations with the same (e.g. Winslow et al., 2015) and different fitting techniques (e.g. Farrugia et al., 2005; Good et al., 2019). It was observed that this decrease of the maximum magnetic field strength within the ME, compared to that within the sheath, showed significant CME-to-CME variability, even for smaller longitudinal separations. A significant number of CMEs (37 out of 45 CMEs in our catalog) had a decrease outside of the 95% confidence interval based on the statistical approach. In addition, the individual analysis revealed a slower rate of decrease ($\mathrm{r}^{-1.75}$) within the ME, leading to the understanding that CME-to-CME variability may not be well represented by fits, such as those performed by Bothmer & Schwenn (1998); Leitner et al. (2007); Gulisano et al. (2010) and should be interpreted with caution.

A decent linear correlation was observed between the sheath duration and heliocentric distance when examined. However, to our surprise, the sheath duration was seen to be reasonably independent of the initial CME speed throughout the inner heliosphere, with comparable sheath durations for fast and slow CMEs at Mercury, Venus, and near 1 AU. Detailed analysis considering CME shapes and SC crossings could provide further insights regarding this.

8.4 Paper-IV

This paper utilized the catalog presented in Paper-III (excluding the 5 CME conjunctions with no plasma measurements at both the measuring spacecraft) to compare the global and local measures of ME expansion in the inner heliosphere during SCy 24 (see Section 6.11).

The underlying motive of Paper-IV was also to investigate SQ-III (how much do CME features inferred from statistical estimations differ from the individual analysis of CMEs with multi-point observations?). The exponent decrease of the magnetic field with heliocentric distance (α) provided a measure of global expansion (see Dumbović et al., 2018a), whereas the local expansion was characterized with the expansion speed and expansion parameter ζ near 1 AU (see Démoulin & Dasso, 2009; Gulisano et al., 2010). The results only indicated a weak correlation between global and local measures of ME expansion. This discrepancy can be attributed to the fact that global measure of ME expansion is primarily governed by the processes occurring below 0.8 AU, with a significant dependence on the initial magnetic field strength, whereas the local measure of ME expansion is primarily controlled by the change in the solar wind pressure (e.g. Démoulin & Dasso, 2009) that does not depend on the initial magnetic field strength of the ME.

8.5 Paper-V

This paper highlighted a two-step threshold-based probabilistic model for forecasting B_z<-10 nT periods of 3 consecutive hours or more, in the 48 hours after a fast-forward shock arrival at L1 (see Chapter 7). The model was constructed with the association between fast-forward shocks and strong and long-duration southward B_z periods as the basis (76 % of such periods occur within 48 hours of a shock arrival at L1). In the first step, a probabilistic forecast was generated based on pattern recognition (see Riley et al., 2017). Closest matches to reference solar wind conditions were found through quantifying variations of four solar wind and IMF parameters (B, B_z, N_p, V_x) in a TW (24 hours before the shock to 0.25 hours after the shock arrival), using a RMSE approach. Historical observations of these closest matches in the post-shock FW (48 hours) were used to achieve a probabilistic forecast. Then, a pre-defined threshold was imposed to generate a dichotomous forecast. Any probabilistic forecast exceeding this threshold was considered a "YES" and any forecast below this threshold was considered a "NO." Different combinations of sets of weights (attached to the parameters and the TW) were tested. The best combination (with the highest HSS) performed 14.7% better than the non-skilled forecast and 28% better than the random forecast.

The model was further evaluated with 10 sets of reference events. Each set consisted of 166 events, randomly chosen from ~500 *Wind* events. On average, the best combination had a False Alarm Ratio of 0.18, indicating that on average, in $\frac{2}{11}$ of the forecast for B_z periods, strong and long-duration B_z were not observed. The average Probability of Detection Yes was 0.60, indicating that, on average, 60% of the observed B_z periods were correctly predicted.

The research goal of Paper-V was to look into SQ-IV (can utilization of prior knowledge of solar wind variations in the vicinity of fast-forward shocks provide sufficient lead times for space weather forecasting?). Preliminary statistics showed that the model based on the association between shocks and strong and long-duration southward B_z periods performed measurably better than a random model. The model also highlighted that solar wind variations near shocks can provide essential information regarding an upcoming intense southward B_z period. Such a model would be able to provide (on average) a 14-hr warning, placing it in between the L1/nowcast forecast (∼30 minutes) and those based on solar/coronal data (1-3 days). However, the model had not been entirely successful in providing accurate and actionable forecasts, leading to the assumption that more parameter combinations and extending the TW to include sheath formation can be utilized in future works.

CHAPTER 9

Concluding remarks and future proceeding

The thesis centers on the global modifications of CME sheaths, manifesting as consequences of their propagation away from the Sun. The impact of this thesis varies from highlighting the large-scale physical mechanisms driving the observed variabilities within sheaths near 1 AU to possible future improvements in space weather predictions with physics-based approaches. This integration of five research articles significantly contributes to the status quo of CME science while providing frameworks for exciting future projects to continue the proceedings set in this thesis.

Paper-I is the first dedicated study of CME sheaths that are not preceded by shocks. Previously, only CME sheaths with shocks have been investigated at this level of detail (e.g. Kilpua et al., 2019). Paper-II underlines statistical differences between propagation and expansion sheaths with in-situ measurements that have been previously done with theoretical arguments and MHD simulations (e.g. Siscoe & Odstrcil, 2008). Thus, Papers-I and II together present an entirely different view of the near-Earth characteristic features of CME sheaths.

Future investigations are required to examine the SQs these papers give rise to. Inspections of the compositional signatures in CME sheaths without shocks can provide insights about the formation of these sheaths in the swept-up solar wind, ahead of the CMEs, before the formation of the shocks. Sheaths with complex speed profiles, especially those 10 - 12 with definite bi-linear trends need to be evaluated in detail to probe the physical mechanisms responsible for such intricacies.

Papers-III and IV emphasize the need to examine the complex observational manifestations of CME dynamics and kinematics in the heliosphere with multi-spacecraft studies. Previous works on this aspect were either focused on case studies (e.g. Good et al., 2015; Winslow et al., 2016; Good et al., 2018) or statistical estimations of the radial evolution from one heliospheric distance to another (e.g. Winslow et al., 2015; Janvier et al., 2019), that did not necessarily mirror the radial evolution within individual CME structures. Paper-III is the first comprehensive study of the radial evolution of CMEs with an extensive list of radially aligned CMEs. Paper-IV provides a detailed outlook of discrepancies in ME expansion identified on local and global scales. Therefore, Papers-III and IV together represent a significant advancement in the radial evolution of CME structures.

Present missions such as the PSP and SO can be utilized in future studies to study the significant variabilities observed in the radial evolution of CMEs in future projects. Equipped with the ability to make plasma measurements, high-resolution data obtained from these missions, closer to the Sun than any previous spacecraft, can provide newer insights into the early evolution of CMEs. In addition, detailed comparisons of longitudinal variations in CME signatures with small and large angular separations between the measuring spacecraft would be valuable in providing a context of the influence of spacecraft crossings on measurements.

Paper-V demonstrates the importance of physics-based approaches in forecasting extreme geomagnetic events. The findings suggest that prior knowledge of the shock and early sheath properties can provide vital information for space weather forecasting. At present, we do have continuous, consistent, and long-ranging observations of the Sun. However, the uncertainties attached to the heliospheric propagation of CMEs and a slender data set of extreme geomagnetic events critically constrain any quantitative forecasting model.

In the future, data assimilation with ML algorithms can be adopted to overcome the limitation of sparse extreme geomagnetic activities and improve the space weather prediction accuracy.

Figure 9.1: Position of a future spacecraft at the L5 point, located ∼60° to the east from Earth. **Image credit: ESA.**

In conclusion, the heliophysics community is ready to embrace data-driven discoveries with future missions and innovative heliospheric modeling. In addition, existing missions still have much life left in them to offer possibilities of expanding our understanding of solar wind transients. In the near future, with a possible L5 mission, as conceptualized in Figure 9.1 (e.g. Vourlidas, 2015) and the world's largest, most powerful solar telescope, the Daniel K. Inouye Solar Telescope (DKIST; see Rimmele et al., 2020) will open the door to a new horizon of solar observations. We are slowly progressing towards the time when we will be able to link remote-sensing observations and in-situ measurements with significant precision. This thesis, hopefully, will contribute, even if small, towards achieving that end goal.

Bibliography

Akasofu, S. I. 1981, Space Science Reviews, 28, 121

Ala-Lahti, M., Ruohotie, J., Good, S., Kilpua, E. K. J., & Lugaz, N. 2020, Journal of Geophysical Research: Space Physics, 125, doi: `10.1029/2020JA028002`

Alexakis, P., & Mavromichalaki, H. 2019, Astrophys. Space Sci., 364, doi: `10.1007/s10509-019-3677-y`

Alves, L. R., Da Silva, L. A., Souza, V. M., et al. 2016, Geophys. Res. Lett., 43, 978, doi: `10.1002/2015GL067066`

Aulanier, G., Török, T., Démoulin, P., & DeLuca, E. E. 2010, The Astrophysical Journal, 708, 314, doi: `10.1088/0004-637X/708/1/314`

Babcock, H. W. 1961, The Astrophysical Journal, 133, 572

Baker, D. N., Li, X., Pulkkinen, A., et al. 2013, Space Weather, 11, 585, doi: `10.1002/swe.20097`

Baker, D. N., Akasofu, S. I., Baumjohann, W., et al. 1984, NASA Ref. Publ., 1120

Bartels, J. 1949, IATME Bull., 12b, 97

Bein, B. M., Berkebile-Stoiser, S., Veronig, A. M., et al. 2011, The Astrophysical Journal, 738, 191, doi: `10.1088/0004-637X/738/2/191`

Berdichevsky, D. B., Szabo, A., Lepping, R. P., Vinas, A. F., & Mariani, F. 2000, J. Geophys. Res., 105, 27289, doi: `10.1029/1999JA000367`

Bhowmik, P., & Nandy, D. 2018, Nat. Commun., 9, 5209, doi: `10.1038/s41467-018-07690-0`

Biermann, L. 1951, Z. Astrophys., 29, 274

Biskamp, D. 1996, Astrophys. Space Sci., 242, 165, doi: `10.1007/BF00645113`

Biskamp, D., & Welter, H. 1989, Solar Phys., 120, 49, doi: `10.1007/BF00148534`

Bochsler, P. 2007, Astron Astrophys Rev, 14, 1, doi: `10.1007/s00159-006-0002-x`

Borovsky, J. E., & Denton, M. H. 2006, J. Geophys. Res., 111, A07S08, doi: `10.1029/2005JA011447`

Borrini, G., Gosling, J. T., Bame, S. J., & Feldman, W. C. 1982, J. Geophys. Res., 87, 4365

Bothmer, V., & Schwenn, R. 1998, Annales Geophysicae, 16, 1, doi: `10.1007/s00585-997-0001-x`

Braga, C. R., Vourlidas, A., Stenborg, G., & Dal Lago, A. 2020, Journal of Geophysical Research: Space Physics, 125, doi: `10.1029/2020JA027885`

Brueckner, G. E., Howard, R. A., Koomen, M. J., et al. 1995, Solar Phys., 162, 357, doi: `10.1007/BF00733434`

Brueckner, G. E., Delaboudiniere, J. P., Howard, R. A., et al. 1998, Geophys. Res. Lett., 25, 3019, doi: `10.1029/98GL00704`

Burlaga, L., Berdichevsky, D., Gopalswamy, N., Lepping, R., & Zurbuchen, T. 2003, J. Geophys. Res., 108, 2, doi: `10.1029/2003JA010088`

Burlaga, L., Sittler, E., Mariani, F., & Schwenn, R. 1981, J. Geophys. Res., 86, 6673

Burlaga, L. F., Behannon, K. W., & Klein, L. W. 1987, J. Geophys. Res., 92, 5725, doi: `10.1029/JA092iA06p05725`

Burlaga, L. F., Klein, L., Sheeley, N. R., et al. 1982, Geophys. Res. Lett., 9, 1317

Bushby, P., & Mason, J. 2004, Astronomy & Geophysics, 45, 4.7, doi: `10.1046/j.1468-4004.2003.45407.x`

Camporeale, E. 2019, Space Weather, 17, 1166, doi: `10.1029/2018SW002061`

Cane, H. V., Richardson, I. G., & Wibberenz, G. 1997, Journal of Geophysical Research: Space Physics, 102, 7075, doi: `10.1029/97JA00149`

Cargill, P. J. 2004, Solar Phys., 221, 135, doi: `10.1023/B:SOLA.0000033366.10725.a2`

Carmichael, H. 1964, NASA Spec. Publ., 50, 451

Carrington, R. C. 1859, Mon. Not. R. Astron. Soc., 20, 13

Chapman, S., & Ferraro, V. C. A. 1931, J. Geophys. Res., 36, 77

Chen, J. 1989, The Astrophysical Journal, 338, 453, doi: `10.1086/167211`

—. 2017, Physics of Plasmas, 24, doi: `10.1068/1.4993929`

Chen, J., Cargill, P. J., & Palmadesso, P. J. 1997, J. Geophys. Res., 102, 14701

Chen, J., Slinker, S. P., & Triandaf, I. 2012, Space Weather, 10, doi: `10.1029/2011SW000740`

Chree, C. 1913, Philosophical Transactions of the Royal Society of London. Series A, Containing Papers of a Mathematical or Physical Character, 212, 75, doi: `10.1098/rsta.1913.0003`

Ciaravella, A., Raymond, J. C., & Kahler, S. W. 2006, The Astrophysical Journal, 652, 774, doi: `10.1086/507171`

Cohen, O., Attrill, G. D. R., Schwadron, N. A., et al. 2010, Journal of Geophysical Research: Space Physics, 115, A10104, doi: `10.1029/2010JA015464`

Colaninno, R. C., Vourlidas, A., & Wu, C. C. 2013, J. Geophys. Res., 118, 6866, doi: `10.1002/2013JA019205`

Cranmer, S. R. 2009, Living Reviews in Solar Physics, 6, doi: `10.12942/lrsp-2009-3`

Cremades, H., Bothmer, V., & Tripathi, D. 2006, Advances in Space Research, 38, 461, doi: `10.1016/j.asr.2005.01.095`

Das, I., Opher, M., Evans, R., Loesch, C., & Gombosi, T. I. 2011, The Astrophysical Journal, 729, doi: `10.1088/0004-637X/729/2/112`

Dasso, S., Mandrini, C. H., Démoulin, P., & Luoni, M. L. 2006, Astron. & Astrophys., 455, 349, doi: `10.1051/0004-6361:20064806`

Dasso, S., Mandrini, C. H., Schmieder, B., et al. 2009, J. Geophys. Res., 114, 2109, doi: `10.1029/2008JA013102`

Davis, C. J., Davies, J. A., Lockwood, M., et al. 2009, Geophys. Res. Lett., 36, L08102, doi: `10.1029/2009GL038021`

Davis, L. 1955, Phys. Rev., 100, 1440, doi: `10.1103/PhysRev.100.1440`

De Keyser, J., Dunlop, M. W., Owen, C. J., et al. 2005, Space Science Reviews, 118, 231

De Pontieu, B., Erdélyi, R., & James, S. P. 2004, Nature, 430, 536

DeForest, C. E., Howard, T. A., & McComas, D. J. 2013, The Astrophysical Journal, 769, 43, doi: `10.1088/0004-637X/769/1/43`

Démoulin, P. 2010, TWELFTH INTERNATIONAL SOLAR WIND CONFERENCE. AIP Conference Proceedings, 1216, 329, doi: `10.1063/1.3395866`

Démoulin, P., & Dasso, S. 2009, Astron. & Astrophys., 498, 551

Démoulin, P., Dasso, S., Lanabere, V., & Janvier, M. 2020, Astron. & Astrophys., 639, A6, doi: `10.1051/0004-6361/202038077`

Démoulin, P., Nakwacki, M. S., Dasso, S., & Mandrini, C. H. 2008, Solar Phys., 250, 347, doi: `10.1007/s11207-008-9221-9`

Denton, M. H., Borovsky, J. E., Skoug, R. M., et al. 2006, J. Geophys. Res., 111, 7, doi: `10.1029/2005JA011436`

Dumbović, M., Heber, B., Vršnak, B., Temmer, M., & Kirin, A. 2018a, The Astrophysical Journal, 860, 12, doi: `10.3847/1538-4357/aac2de`

Dumbović, M., Čalogović, J., Vršnak, B., et al. 2018b, The Astrophysical Journal, 854, 180, doi: `10.3847/1538-4357/aaaa66`

Echer, E., Gonzalez, W. D., Tsurutani, B. T., & Gonzalez, A. L. C. 2008, J. Geophys. Res., 113, A05221, doi: `10.1029/2007JA012744`

Echer, E., Tsurutani, B. T., & Gonzalez, W. D. 2013, J. Geophys. Res., 118, 385, doi: `10.1029/2012JA018086`

Emilio, M., Kuhn, J. R., Bush, R. I., & Scholl, I. F. 2012, The Astrophysical Journal, 750, doi: `10.1088/0004-637X/750/2/135`

Fairfield, D. H., & Cahill, J. L. J. 1966, J. Geophys. Res., 71, 155

Fan, Y. 2008, The Astrophysical Journal, 676, 680

—. 2009, Living Reviews in Solar Physics, 6, 4

—. 2016, The Astrophysical Journal, 824

Farrugia, C. J., Burlaga, L. F., & Lepping, R. P. 1997, Geophysical Monogr. Ser., 98, 91

Farrugia, C. J., Dunlop, M. W., & Elliott, S. 1991, Journal of Atmospheric and Terrestrial Physics, 53, 1039, doi: `10.1016/0021-9169(91)90050-H`

Farrugia, C. J., Jordanova, V. K., Thomsen, M. F., et al. 2006, J. Geophys. Res., 111, doi: `10.1029/2006JA011893`

Farrugia, C. J., Scudder, J. D., Freeman, M. P., et al. 1998, J. Geophys. Res., 103, 17,261

Farrugia, C. J., Leitner, M., Biernat, H. K., et al. 2005, Proceedings of the Solar Wind 11 / SOHO 16, Connecting Sun and Heliosphere Conference (ESA SP-592), 12–17 June 2005 Whistler, Canada, 723

Farrugia, C. J., Berdichevsky, D. B., Möstl, C., et al. 2011, J. Atmos. Sol. Terr. Phys., 73, 1254, doi: `10.1016/j.jastp.2010.09.011`

Feng, H., & Wang, J. 2013, Astron. & Astrophys., 559, A92, doi: `10.1051/0004-6361/201322522`

Ferraro, V. C. A. 1952, J. Geophys. Res., 57, 15

Filippov, B. P., Gopalswamy, N., & Lozhechkin, A. V. 2001, Solar Phys., 203, 119

Fontenla, J., Reichmann, E. J., & Tandberg-Hanssen, E. 1988, The Astrophysical Journal, 329, 464

Fox, N. J., Velli, M. C., & Bale, S. D. 2016, Space Science Reviews, 204, 7, doi: `10.1007/s11214-015-0211-6`

Fry, C. D., Dryer, M., Smith, Z., et al. 2003, J. Geophys. Res., 108, doi: `10.1029/2002JA009474`

Gabriel, A. H. 1976, Royal Society of London Philosophical Transactions Series A, 281, 339

Gallagher, P. T., & Long, D. M. 2011, Space Science Reviews, 158, 365

Galvin, A. B., Ipavich, F. M., Gloeckler, G., Hovestadt, D., & Tsurutani, B. T. 1987, J. Geophys. Res., 92, 12,069

Galvin, A. B., Kistler, L. M., Popecki, M. A., et al. 2008, Space Science Reviews, 136, 437, doi: `10.1007/s11214-007-9296-x`

Giles, P., Duvall, T., & Scherrer, P. 1997, Nature, 390, 52, doi: `10.1038/36294`

Gizon, L., Cameron, R. H., Pourabdian, M., et al. 2020, Science, 368, 1469, doi: `10.1126/science.aaz7119`

Gold, T. 1955, Gas Dynamics of Cosmic Clouds (Proceedings from IAU Symposium), 2, 97

Gonzalez, W. D., Joselyn, J. A., Kamide, Y., et al. 1994, J. Geophys. Res., 99, 5771

Gonzalez, W. D., & Tsurutani, B. T. 1987, Planetary and Space Science, 35, doi: `10.1016/0032-0633(87)90015-8`

Good, S. W., Ala-Lahti, M., Palmerio, E., Kilpua, E. K. J., & Osmane, A. 2020, The Astrophysical Journal, 893, doi: `10.3847/1538-4357/ab7fa2`

Good, S. W., & Forsyth, R. J. 2016, Solar Phys., 291, 239, doi: `10.1007/s11207-015-0828-3`

Good, S. W., Forsyth, R. J., Eastwood, J. P., & Möstl, C. 2018, Solar Phys., 293, 52, doi: `10.1007/s11207-018-1264-y`

Good, S. W., Forsyth, R. J., Raines, J. M., et al. 2015, The Astrophysical Journal, 807, 177, doi: `10.1088/0004-637X/807/2/177`

Good, S. W., Kilpua, E. K. J., LaMoury, A. T., et al. 2019, Journal of Geophysical Research: Space Physics, 124, doi: `10.1029/2019JA026475`

Gopalswamy, N. 2003, Advances in Space Research, 31, 869, doi: `10.1016/S0273-1177(02)00888-8`

—. 2006, Space Science Reviews, 124, 145, doi: `10.1007/s11214-006-9102-1`

—. 2008, J. Atmos. Sol. Terr. Phys., 70, 2078, doi: `10.1016/j.jastp.2008.06.010`

—. 2016, Geosci. Lett., 3, doi: `10.1186/s40562-016-0039-2`

Gopalswamy, N., Lara, A., Lepping, R. P., et al. 2000, Geophys. Res. Lett., 27, 145, doi: `10.1029/1999GL003639`

Gopalswamy, N., Lara, A., Yashiro, S., Kaiser, M. L., & Howard, R. A. 2001, J. Geophys. Res., 106, 29207, doi: `10.1029/2001JA000177`

Gopalswamy, N., Mäkelä, P., Xie, H., Akiyama, S., & Yashiro, S. 2009, J. Geophys. Res., 114, A00A22, doi: `10.1029/2008JA013686`

Gopalswamy, N., Yashiro, S., Liu, Y., et al. 2005, J. Geophys. Res., 110, doi: `10.1029/2004JA010958`

Gopalswamy, N., Yashiro, S., Michalek, G., et al. 2010, Sun and Geosphere, 5, 7

Gopalswamy, N., Yashiro, S., Xie, H., Akiyama, S., & Mäkelä, P. 2015, J. Geophys. Res., 120, 9221, doi: `10.1002/2015JA021446`

Gosling, J. T. 1996, Annual Review of Astronomy and Astrophysics, 34, 35, doi: `10.1146/annurev.astro.34.1.35`

—. 1997, Geophys. Monogr. Ser., 99, 9

Gosling, J. T., Asbridge, J. R., Bame, S. J., & Feldman, W. C. 1976, J. Geophys. Res., 81, 5061, doi: `10.1029/JA081i028p05061`

Gosling, J. T., Bame, S. J., McComas, D. J., & Phillips, J. L. 1990, Geophys. Res. Lett., 17, 901

Gosling, J. T., Hildner, E., MacQueen, R. M., et al. 1974, J. Geophys. Res., 79, 4581

Gosling, J. T., McComas, D. J., Phillips, J. L., & Bame, S. J. 1991, J. Geophys. Res., 96, 7831

Gosling, J. T., & Pizzo, V. J. 1999, Space Science Reviews, 89, 21

Gosling, J. T., Thomsen, M. F., Bame, S. J., & Zwickl, R. D. 1987, J. Geophys. Res., 92, 12399, doi: `10.1029/JA092iA11p12399`

Green, L. M., Török, T., & Vršnak, B. 2018, Space Science Reviews, 214, 52, doi: `10.1007/s11214-017-0462-5`

Gringauz, K. I., Bezrukikh, V. V., Ozerov, V. D., & Ribchinsky, R. E. 1960, Soviet Physics Doklady, 5, 361

—. 1961, Space Res, 2, 539

Groth, C. P. T., De Zeeuw, D. L., Gombosi, T. I., & Powell, K. G. 2000, Advances in Space Research, 26, 793, doi: `10.1016/S0273-1177(00)00008-9`

Gui, B., Shen, C., Wang, Y., et al. 2011, Solar Phys., 271, 111

Gulisano, A. M., Démoulin, P., Dasso, S., & Rodriguez, L. 2012, Astron. & Astrophys., 543, A107, doi: `10.1051/0004-6361/201118748`

Gulisano, A. M., Démoulin, P., Dasso, S., Ruiz, M. E., & Marsch, E. 2010, Astron. & Astrophys., 509, A39, doi: `10.1051/0004-6361/200912375`

Guo, J., Feng, X., Zhang, J., Zuo, P., & Xiang, C. 2010, Journal of Geophysical Research: Space Physics, 115, doi: `10.1029/2009JA015140`

Harrison, R. A., Davies, J. A., Biesecker, D., & Gibbs, M. 2017, Space Weather, 15, 985, doi: `10.1002/2017SW001633`

Harrison, R. A., Davis, C. J., & Eyles, C. J. 2005, Advances in Space Research, 36, 1512, doi: `10.1016/j.asr.2005.01.024`

Harrison, R. A., Davies, J. A., Barnes, D., et al. 2018, Solar Phys., 293, 77, doi: `10.1007/s11207-018-1297-2`

Hathaway, D. H. 2015, Living Reviews in Solar Physics, 12, doi: `10.1007/lrsp-2015-4`

Hathaway, D. H., & Rightmire, L. 2010, Science, 327, 1350, doi: `10.1126/science.1181990`

He, W., Liu, Y. D., Hu, H., Wang, R., & Zhao, X. 2018, The Astrophysical Journal, 860, doi: `10.3847/1538-4357/aac381`

Heidke, P. 1926, Geografiska Annaler, 8, 301, doi: `10.2307/519729`

Heinemann, S. G., Temmer, M., & Farrugia, C. J. 2019, Solar Phys., 294, doi: `10.1007/s11207-019-1515-6`

Hess, P., & Zhang, J. 2015, The Astrophysical Journal, 812, 144, doi: `10.1088/0004-637X/812/2/144`

—. 2017, Solar Phys., 292, 80, doi: `10.1007/s11207-017-1099-y`

Hietala, H., Kilpua, E. K. J., Turner, D. L., & Angelopoulos, V. 2014, Geophys. Res. Lett., 41, 2258, doi: `10.1002/2014GL059551`

Hirayama, T. 1974, Solar Phys., 34, 323

Howard, R. A., Michels, D. J., Sheeley, Jr., N. R., & Koomen, M. J. 1982, The Astrophysical Journal, 263, L101

Howard, R. A., Sheeley, Jr., N. R., Michels, D. J., & Koomen, M. J. 1985, J. Geophys. Res., 90, 8173

Howard, R. A., Moses, J. D., Vourlidas, A., et al. 2008, Space Science Reviews, 136, 67, doi: `10.1007/s11214-008-9341-4`

Hudson, H. S., Bougeret, J., & Burkepile, J. 2006, Space Science Reviews, 123, 13, doi: `10.1007/s11214-006-9009-x`

Hudson, H. S., & Cliver, E. 2001, J. Geophys. Res., 106, 25199

Hudson, M. K., Baker, D. N., Goldstein, J., et al. 2014, Geophys. Res. Lett., 41, 1113, doi: `10.1002/2014GL059222`

Hundhausen, A. J. 1993, J. Geophys. Res., 98, 13,177

Huttunen, K., & Koskinen, H. 2004, Annales Geophysicae, 22, 1729, doi: `10.5194/angeo-22-1729-2004`

Huttunen, K. E. J., Schwenn, R., Bothmer, V., & Koskinen, H. E. J. 2005, Ann. Geophys., 23, 625, doi: `10.5194/angeo-23-625-2005`

Isavnin, A. 2016, The Astrophysical Journal, 833, 267, doi: `10.3847/1538-4357/833/2/267`

Isavnin, A., Vourlidas, A., & Kilpua, E. K. J. 2014, Solar Phys., 289, 2141, doi: `10.1007/s11207-013-0468-4`

Isenberg, P. A., & Forbes, T. G. 2007, The Astrophysical Journal, 670, 1453, doi: `10.1086/522025`

Iucci, N., Parisi, M., Storini, M., & Villoresi, G. 1988, Astron. Astrophys. Suppl. Ser, 72, 369

Izenman, A. J. 1985, Math. Intell., 7, 27

Janoo, L., Farrugia, C. J., Torbert, R. B., et al. 1998, J. Geophys. Res., 103, 17,249

Janvier, M., Winslow, R. M., Good, S., et al. 2019, Journal of Geophysical Research: Space Physics, 124, doi: `10.1029/2018JA025949`

Jian, L. K., Russell, C. T., & Luhmann, J. G. 2011, Solar Phys., 274, 321, doi: `10.1007/s11207-011-9737-2`

Jian, L. K., Russell, C. T., Luhmann, J. G., & Galvin, A. B. 2018, The Astrophysical Journal, 885, 114, doi: `10.3847/1538-4357/aab189`

Jones, G. H., Rees, A., Balogh, A., & Forsyth, R. J. 2002, Geophys. Res. Lett., 11, 1520, doi: `10.1029/2001GL014110`

Joselyn, J. A., & Tsurutani, B. T. 1990, EOS Trans., 71, 1808, doi: `10.1029/90EO00350`

Jurac, S., Kasper, J. C., Richardson, J. D., & Lazarus, A. J. 2002, Geophys. Res. Lett., 29, 1463, doi: `10.1029/2001GL014034`

Kaiser, M. L. 2005, Advances in Space Research, 36, 1483

Kamide, Y., Yokoyama, N., Gonzalez, W., et al. 1998, J. Geophys. Res., 103, 6917, doi: `10.1029/97JA03337`

Kataoka, R., Watari, S., Shimada, N., Shimazu, H., & Marubashi, K. 2005, Geophys. Res. Lett., 32, L12103, doi: `10.1029/2005GL022777`

Kay, C., Gopalswamy, N., Reinard, A., & Opher, M. 2017, The Astrophysical Journal, 835, 10, doi: `10.3847/1538-4357/835/2/117`

Kay, C., Opher, M., & Evans, R. M. 2013, The Astrophysical Journal, 775, 5, doi: `10.1088/0004-637X/775/1/5`

—. 2015, The Astrophysical Journal, 805, 168

Kaymaz, Z., & Siscoe, G. 2006, Solar Phys., 239, 437, doi: `10.1007/s11207-006-0308-x`

Kilpua, E. K. J., Fontaine, D., Moissard, C., et al. 2019, Space Weather, 17, 1257, doi: `10.1029/2019SW002217`

Kilpua, E. K. J., Hietala, H., Koskinen, H. E. J., Fontaine, D., & Turc, L. 2013, Ann. Geophys., 31, 1559, doi: `10.5194/angeo-31-1559-2013`

Kilpua, E. K. J., Jian, L. K., Li, Y., Luhmann, J. G., & Russell, C. T. 2011, J. Atmos. Sol. Terr. Phys., 73, 1228, doi: `10.1016/j.jastp.2010.10.012`

Kilpua, E. K. J., Koskinen, H. E. J., & Pulkkinen, T. I. 2017, Living Reviews in Solar Physics, 14, doi: `10.1007/s41116-017-0009-6`

Kilpua, E. K. J., Lumme, E., Andreeova, K., Isavnin, A., & Koskinen, H. E. J. 2015a, Journal of Geophysical Research: Space Physics, 120, 4112, doi: `10.1002/2015JA021138`

Kilpua, E. K. J., Mierla, M., & Rodriguez, L. 2012, Solar Phys., 279, 477, doi: `10.1007/s11207-012-0005-x`

Kilpua, E. K. J., Pomoell, J., Vourlidas, A., et al. 2009, Annales Geophysicae, 27, 4491, doi: `10.5194/angeo-27-4491-2009`

Kilpua, E. K. J., Hietala, H., Turner, D. L., et al. 2015b, Geophys. Res. Lett., 42, 3076, doi: `10.1002/2015GL063542`

Kilpua, E. K. J., Fontaine, D., Good, S. W., et al. 2020, Ann. Geophys., 38, 999, doi: `10.5194/angeo-38-999-2020`

Kim, K., Lee, D.-Y., Kim, H.-J., Lee, E., & Choi, C. 2010, J. Geophys. Res., 115, doi: `10.1029/2009JA014523`

King, J. H., & Papitashvili, N. E. 2005, J. Geophys. Res., 110, A02104

Klein, L. W., & Burlaga, L. F. 1982, J. Geophys. Res., 87, 613, doi: `10.1029/JA087iA02p00613`

Kliem, B., Török, T., & Thompson, W. T. 2012, Solar Phys., 281, 137

Kopp, R. A., & Pneuman, G. W. 1976, Solar Phys., 50, 85

Lamy, P. L., Floyd, O., & Boclet, B. 2019, Space Science Reviews, 215, 39, doi: `10.1007/s11214-019-0605-y`

Lavraud, B., Ruffenach, A., Rouillard, A. P., et al. 2014, J. Geophys. Res., 119, 26, doi: `10.1002/2013JA019154`

Le, G. M., Cai, Z. U., Wang, H. N., Yin, Z. Q., & Li, P. 2013, Res. Astron. Astrophys., 13, 739, doi: `10.1088/1674-4527/13/6/013`

Lee, C. O., Hara, T., Halekas, J. S., et al. 2017, Journal of Geophysical Research: Space Physics, 122, 2768, doi: `10.1002/2016JA023495`

Leighton, R. B. 1969, The Astrophysical Journal, 156, 1, doi: `10.1086/149943`

Leitner, M., Farrugia, C. J., MöStl, C., et al. 2007, Journal of Geophysical Research: Space Physics, 112, doi: `10.1029/2006JA011940`

Lengyel-Frey, D., Thejappa, G., MacDowall, R. J., Stone, R. G., & Phillips, J. L. 1997, J. Geophys. Res., 102, 2611, doi: `10.1029/96JA02871`

Lepping, R. P., Acuna, M. H., & Burlaga, L. F. 1995, Space Science Reviews, 71, 207, doi: `10.1007/BF00751330`

Lepping, R. P., Wu, C.-C., & Berdichevsky, D. B. 2018, Solar Phys., 293, doi: `10.1007/s11207-018-1273-x`

Lepping, R. P., Wu, C.-C., Berdichevsky, D. B., & Ferguson, T. 2008, Ann. Geophys., 26, 1919, doi: `10.5194/angeo-26-1919-2008`

Lepri, S. T., Zurbuchen, T. H., Fisk, L. A., et al. 2001, J. Geophys. Res., 106, 29231, doi: `10.1029/2001JA000014`

Li, Y., Luhmann, J. G., & Lynch, B. J. 2018, Solar Phys., 293, doi: `10.1007/s11207-018-1356-8`

Lindsay, G. M., Luhmann, J. G., Russell, C. T., & Gosling, J. T. 1999, J. Geophys. Res., 104, 12515, doi: `10.1029/1999JA900051`

Lindsay, G. M., Russell, C. T., Luhmann, J. G., & Gazis, P. 1994, J. Geophys. Res., 99, doi: `10.1029/93JA02666`

Liu, J., Ye, Y., Shen, C., Wang, Y., & Erdélyi, R. 2018, The Astrophysical Journal, 855, 109, doi: `10.3847/1538-4357/aaae69`

Liu, Y., Richardson, J. D., & Belcher, J. W. 2005, Planetary and Space Science, 53, 3, doi: `10.1016/j.pss.2004.09.023`

Liu, Y., Shen, F., & Yang, Y. 2019, The Astrophysical Journal, 887, doi: `10.3847/1538-4357/ab543e`

Liu, Y., Thernisien, A., Luhmann, J. G., et al. 2010, The Astrophysical Journal, 722, 1762, doi: `10.1088/0004-637X/722/2/1762`

Liu, Y. D., Chen, C., & Zhao, X. 2020, Astrophys. Journ. Lett., 897, doi: `10.3847/2041-8213/ab9d25`

Liu, Y. D., Hu, H., Wang, C., et al. 2016, Astrophys. J. Suppl., 222, 23, doi: `10.3847/0067-0049/222/2/23`

Liu, Y. D., Luhmann, J. G., Lugaz, N., et al. 2013, The Astrophysical Journal, 769, 45, doi: `10.1088/0004-637X/769/1/45`

Liu, Y. D., Luhmann, J. G., Kajdič, P., et al. 2014, Nature Communications, 5, doi: `10.1038/ncomms4481`

Lotova, N. A., Obridko, V. N., & Vladimirskii, K. V. 2000, Astron. & Astrophys., 357, 1051

Lugaz, N., Downs, C., Shibata, K., et al. 2011, The Astrophysical Journal, 738, 127, doi: `10.1088/0004-637X/738/2/127`

Lugaz, N., & Farrugia, C. J. 2014, Geophys. Res. Lett., 41, 769, doi: `10.1002/2013GL058789`

Lugaz, N., Farrugia, C. J., Davies, J. A., et al. 2012, The Astrophysical Journal, 759, 68, doi: `10.1088/0004-637X/759/1/68`

Lugaz, N., Farrugia, C. J., Huang, C. L., & Spence, H. E. 2015, Geophys. Res. Lett., 42, 4694, doi: `10.1002/2015GL064530`

Lugaz, N., Farrugia, C. J., Huang, C.-L., et al. 2016a, Nature Communications, 7, 13001, doi: `10.1038/ncomms13001`

Lugaz, N., Farrugia, C. J., Winslow, R. M., et al. 2018, Astrophys. Journ. Lett., 864, 6, doi: `10.3847/2041-8213/aad9f4`

—. 2016b, Journal of Geophysical Research: Space Physics, 121, doi: `10.1002/2016JA023100`

—. 2017a, The Astrophysical Journal, 848, 75, doi: `10.3847/1538-4357/aa8ef9`

Lugaz, N., & Kintner, P. 2013, Solar Phys., 285, 281, doi: `10.1007/s11207-012-9948-1`

Lugaz, N., Manchester, W. B., & Gombosi, T. I. 2005, The Astrophysical Journal, 634, 651, doi: `10.1086/491782`

Lugaz, N., Salman, T. M., Winslow, R. M., et al. 2020a, The Astrophysical Journal, 899, doi: `10.3847/1538-4357/aba26b`

Lugaz, N., Temmer, M., Wang, Y., & Farrugia, C. J. 2017b, Solar Phys., 292, 64, doi: `10.1007/s11207-017-1091-6`

Lugaz, N., Winslow, R. M., & Farrugia, C. J. 2020b, Journal of Geophysical Research: Space Physics, 125, doi: `10.1029/2019JA027213`

Luhmann, J. G., Curtis, D. W., Schroeder, P., et al. 2008, Space Science Reviews, 136, 117, doi: `10.1007/s11214-007-9170-x`

Lynch, B. J., Antiochos, S. K., MacNeice, P. J., Zurbuchen, T. H., & Fisk, L. A. 2004, The Astrophysical Journal, 617, 589, doi: `10.1086/424564`

Lynch, B. J., Li, Y., Thernisien, A. F. R., et al. 2010, J. Geophys. Res., 115, doi: `10.1029/2009JA015099`

Lyot, B. 1939, Monthly Notices of the Royal Astronomical Society, 99, 580, doi: `10.1088/0004-637X/697/2/1918`

Mackay, D. H., Karpen, J. T., Ballester, J. L., Schmieder, B., & Aulanier, G. 2010, Space Science Reviews, 151, 333, doi: `10.1007/s11214-010-9628-0`

Maloney, S. A., Gallagher, P. T., & McAteer, R. T. J. 2009, Solar Phys., 256, 149

Manchester, W., Kilpua, E. K. J., Liu, Y. D., et al. 2017, Space Science Reviews, 212, 1159, doi: `10.1007/s11214-017-0394-0`

Manchester, IV, W. 2007, The Astrophysical Journal, 666, 532, doi: `10.1086/520493`

Manchester, W. B., Gombosi, T. I., Roussev, I., et al. 2004, J. Geophys. Res., 109, 2107

Manchester, W. B., Gombosi, T. I., De Zeeuw, D. L., et al. 2005, The Astrophysical Journal, 622, 1225

Mann, G., Klassen, A., Classen, H. T., et al. 1996, Astronomy & Astrophysics Supplemental, 119, 489

Manoharan, P. K., Gopalswamy, N., Yashiro, S., et al. 2004, J. Geophys. Res., 109, doi: `10.1029/2003JA010300`

Masías-Meza, J. J., Dasso, S., Démoulin, P., Rodriguez, L., & Janvier, M. 2016, Astron. & Astrophys., 592, doi: `10.1051/0004-6361/201628571`

Matzka, J., Stolle, C., Yamazaki, Y., Bronkalla, O., & Morschhauser, A. 2021, Space Weather, 19, doi: `10.1029/2020SW002641`

Maunder, E. W. 1904, Mon. Not. Roy. Astron. Soc., 64, 747

McComas, D. J., Angold, N., Elliott, H. A., et al. 2013, The Astrophysical Journal, 779, 10, doi: `10.1088/0004-637X/779/1/2`

McComas, D. J., Bame, S. J., Barraclough, B. L., & Feldman, W. C. 1998, Geophys. Res. Lett., 25, 1, doi: `10.1029/97GL03444`

McComas, D. J., Ebert, R. W., Elliott, H. A., et al. 2008, Geophys. Res. Lett., 35, 18103, doi: `10.1029/2008GL034896`

McComas, D. J., Gosling, J. T., Bame, S. J., Smith, E. J., & Cane, H. V. 1989, J. Geophys. Res., 94, 1465, doi: `10.1029/JA094iA02p01465`

McComas, D. J., Alexashov, D., Bzowski, M., et al. 2012, Science, 336, 1291, doi: `10.1126/science.1221054`

Michalek, G., Gopalswamy, N., Lara, A., & Manoharan, P. K. 2004, Astron. & Astrophys., 423, 729, doi: `10.1051/0004-6361:20047184`

Michalek, G., Gopalswamy, N., & Yashiro, S. 2017, Solar Phys., 292, doi: `10.1007/s11207-017-1143-y`

Mitalas, R., & Sills, K. R. 1992, The Astrophysical Journal, 401, 759

Mitsakou, E., Babasidis, G., & Moussas, X. 2009, Advances in Space Research, 43, 495, doi: `10.1016/j.asr.2008.08.003`

Mitsakou, E., & Moussas, X. 2014, Solar Phys., 289, 3137, doi: `10.1007/s11207-014-0505-y`

Moissard, C., Fontaine, D., & Savoini, P. 2019, Journal of Geophysical Research: Space Physics, 124, 8208, doi: `10.1029/2019JA026952`

Moore, R. L., Sterling, A. C., Hudson, H. S., & Lemen, J. R. 2001, The Astrophysical Journal, 552, 833

Möstl, C. 2015, Nat. Commun., 6, doi: `10.1038/ncomms8135`

—. 2017, Space Weather, 15, 955, doi: `10.1002/2017SW001614`

Möstl, C., Amerstorfer, T., Palmerio, E., et al. 2018, Space Weather, 16, 216, doi: `10.1002/2017SW001735`

Möstl, C., Farrugia, C. J., Biernat, H. K., et al. 2009a, Solar Phys., 256, 427, doi: `10.1007/s11207-009-9360-7`

Möstl, C., Farrugia, C. J., Miklenic, C., et al. 2009b, J. Geophys. Res., 114, 4102, doi: `10.1029/2008JA013657`

Möstl, C., Amla, K., Hall, J. R., et al. 2014, The Astrophysical Journal, 787, 119, doi: `10.1088/0004-637X/787/2/119`

Müller, D., Marsden, R. G., St. Cyr, O. C., & Gilbert, H. R. 2013, Solar Phys., 285, 25, doi: `10.1007/s11207-012-0085-7`

Nandy, D., Muñoz-Jaramillo, A., & Martens, P. 2011, Nature, 471, 80, doi: `10.1038/nature09786`

Napoletano, G., Forte, R., Moro, D. D., et al. 2018, J. Space Weather Space Clim., 8, A11, doi: `10.1051/swsc/2018003`

Neugebauer, M. 1991, Science, 252, 5004, doi: `10.1126/science.252.5004.404`

Neugebauer, M., & Snyder, C. W. 1966, J. Geophys. Res., 71, 4469, doi: `10.1029/JZ071i019p04469`

Nieves-Chinchilla, T., Colaninno, R., Vourlidas, A., et al. 2012, J. Geophys. Res., 117, 6106, doi: `10.1029/2011JA017243`

Nieves-Chinchilla, T., Vourlidas, A., & Raymond, J. C. 2018, Solar Phys., 293, doi: `10.1007/s11207-018-1247-z`

Odstrcil, D., Pizzo, V. J., & Arge, C. N. 2005, J. Geophys. Res., 110, doi: `10.1029/2004JA010745`

Odstrčil, D., Riley, P., & Zhao, X. P. 2003, Adv. Space Res., 32, 497, doi: `10.1016/S0273-1177(03)00332-6`

—. 2004, J. Geophys. Res., 109, doi: `10.1029/2003JA010135`

Ogilvie, K. W. 1995, Space Science Reviews, 71, 55

Oliveira, D. M. 2017, Braz. J. Phys., 47, 81, doi: `10.1007/s13538-016-0472-x`

Ontiveros, V., & Gonzalez-Esparza, J. A. 2010, J. Geophys. Res., 115, A10244, doi: `10.1029/2010JA015471`

Owens, M. J. 2006, J. Geophys. Res., 111, A12109, doi: `10.1029/2006JA011903`

—. 2020, Solar Phys., 295, 148, doi: `10.1007/s11207-020-01721-0`

Owens, M. J., & Cargill, P. J. 2004, Ann. Geophys., 22, 661, doi: `10.5194/angeo-22-661-2004`

Owens, M. J., Cargill, P. J., Pagel, C., Siscoe, G. L., & Crooker , N. U. 2005, J. Geophys. Res., 110, A01105, doi: `10.1029/2004JA010814`

Owens, M. J., & Forsyth, R. J. 2013, Living Reviews in Solar Physics, 10, doi: `10.12942/lrsp-2013-5`

Owens, M. J., Lockwood, M., & Barnard, L. A. 2017a, Scientific Reports, 7, 4152, doi: `10.1038/s41598-017-04546-3`

Owens, M. J., Riley, P., & Horbury, T. S. 2017b, Solar Phys., 292, 69, doi: `10.1007/s11207-017-1090-7`

Palmerio, E., Kilpua, E. K. J., James, A. W., et al. 2017, Solar Phys.

Palmerio, E., Kilpua, E. K. J., & Savani, N. P. 2016, Ann. Geophys., 34, 313, doi: `10.5194/angeo-34-313-2016`

Parker, E. N. 1955, The Astrophysical Journal, 122, 293, doi: `10.1086/146087`

—. 1958, The Astrophysical Journal, 128, 664, doi: `10.1086/146579`

—. 1993, The Astrophysical Journal, 408, 707, doi: `10.1086/172631`

Patsourakos, S. 2016, The Astrophysical Journal, 817, doi: `10.3847/0004-637X/817/1/14`

Paulson, K. W., Taylor, D. K., Smith, C. W., Vasquez, B. J., & Hu, Q. 2012, Space Weather, 10, doi: `10.1029/2012SW000855`

Phan, T. D., Paschmann, G., Gosling, J. T., et al. 2013, Geophys. Res. Lett., 40, 11, doi: `10.1029/2012GL054528`

Pizzo, V. 1978, Journal of Geophysical Research: Space Physics, 83, 5563, doi: `10.1029/JA083iA12p05563`

Pomoell, J., & Poedts, S. 2018, J. Space Weather Space Clim., 8, A35, doi: `10.1051/swsc/2018020`

Prise, A. J., Harra, L. K., Matthews, S. A., Arridge, C. S., & Achilleos, N. 2015, Journal of Geophysical Research: Space Physics, 120, 1566, doi: `10.1002/2014JA020256`

Pulkkinen, T. I., Partamies, N., Huttunen, K. E. J., Reeves, G. D., & Koskinen, H. E. J. 2007, Geophys. Res. Lett., 34, L02105, doi: `10.1029/2006GL027775`

Reames, D. V. 1999, Space Science Reviews, 90, 413

Regnault, F., Janvier, M., Démoulin, P., et al. 2020, Journal of Geophysical Research: Space Physics, 125, doi: `10.1029/2020JA028150`

Reinard, A. A., Lynch, B. J., & Mulligan, T. 2012, The Astrophysical Journal, 761, 175, doi: `10.1088/0004-637X/761/2/175`

Reiner, M. J., Kaiser, M. L., & Bougeret, J.-L. 2007, The Astrophysical Journal, 663, 1369, doi: `10.1029/2004JA010943`

Richardson, I. G. 2018, Living Reviews in Solar Physics, 15, doi: `10.1007/s41116-017-0011-z`

Richardson, I. G., & Cane, H. V. 1995, Journal of Geophysical Research: Space Physics, 100, 23397, doi: `10.1029/95JA02684`

—. 2010, Solar Phys., 264, 189, doi: `10.1007/s11207-010-9568-6`

—. 2012, J. Space Weather Space Clim, 2, doi: `10.1051/swsc/2012001`

Richardson, I. G., Cliver, E. W., & Cane, H. V. 2001, Geophys. Res. Lett., 28, 2569, doi: `10.1029/2001GL013052`

Riley, P. 2018, Space Weather, 16, 1245, doi: `10.1029/2018SW001962`

Riley, P., Ben-Nun, M., Linker, J. A., & Owens, M. J. 2017, Space Weather, 15, 526, doi: `10.1002/2016SW001589`

Riley, P., & Crooker, N. U. 2004, The Astrophysical Journal, 600, 1035, doi: `10.1086/379974`

Riley, P., & Richardson, I. G. 2012, Solar Phys., 284, 217, doi: `10.1007/s11207-012-0006-9`

Rimmele, T. P., Warner, M., & Keil, S. L. 2020, Solar Phys., 295, doi: `10.1007/s11207-020-01736-7`

Robbrecht, E., Patsourakos, S., & Vourlidas, A. 2009, The Astrophysical Journal, 701, 283, doi: `10.1088/0004-637X/701/1/283`

Rodriguez, L., Masías-Meza, J. J., & Dasso, S. 2016, Solar Phys., 291, 2145, doi: `10.1007/s11207-016-0955-5`

Rodriguez, L., Mierla, M., Zhukov, A., West, M., & Kilpua, E. 2011, Solar Phys., 270, 561, doi: `10.1007/s11207-011-9784-8`

Rollett, T., Möstl, C., & Isavnin, A. 2016, The Astrophysical Journal, 824, 131, doi: `10.3847/0004-637X/824/2/131`

Rosenbauer, H., Schwenn, R., & Marsch, E. 1977, Journal of Geophysics Zeitschrift Geophysik, 42, 561

Ruffenach, A., Lavraud, B., Owens, M. J., et al. 2012, J. Geophys. Res., 117, 9101, doi: `10.1029/2012JA017624`

Ruffenach, A., Lavraud, B., Farrugia, C. J., et al. 2015, J. Geophys. Res., 120, 43, doi: `10.1002/2014JA020628`

Russell, C. T., Ginskey, M., Petrinec, S., & Le, G. 1992, Geophys. Res. Lett., 19, 1227

Russell, C. T., McPherron, R. L., & Burton, R. K. 1974, J. Geophys. Res., 79, 1105

Russell, C. T., & Mulligan, T. 2002, Planetary and Space Science, 50, 527, doi: `10.1016/s0032-0633(02)00031-4`

Sachdeva, N., Subramanian, P., Colaninno, R. C., & Vourlidas, A. 2015, The Astrophysical Journal, 809, 158, doi: `10.1088/0004-637X/809/2/158`

Saez, F., Zhukov, A. N., Lamy, P., & Llebaria, A. 2005, Astron. & Astrophys., 442, 351, doi: `10.1051/0004-6361:20042016`

Salman, T. M., Lugaz, N., Farrugia, C. J., et al. 2018, Space Weather, 16, doi: `10.1029/2018SW002056`

—. 2020a, The Astrophysical Journal, 904, doi: `10.3847/1538-4357/abbdf5`

Salman, T. M., Winslow, R. M., & Lugaz, N. 2020b, Journal of Geophysical Research: Space Physics, 125, doi: `10.1029/2019JA027084`

Sanchez, S., Fournier, A., & Aubert, J. 2014, The Astrophysical Journal, 781, doi: `10.1088/0004-637X/781/1/8`

Sarp, V., Kilcik, A., Yurchyshyn, V., Rozelot, J. P., & Ozguc, A. 2018, Monthly Notices of the Royal Astronomical Society, 481, 2981, doi: `10.1093/mnras/sty2470`

Savani, N. P., Owens, M. J., Rouillard, A. P., Forsyth, R. J., & Davies, J. A. 2010, Astrophys. Journ. Lett., 714, L128, doi: `10.1088/2041-8205/714/1/L128`

Savani, N. P., Owens, M. J., Rouillard, A. P., et al. 2011, The Astrophysical Journal, 732, 117, doi: `10.1088/0004-637X/732/2/117`

Savani, N. P., Vourlidas, A., Szabo, A., et al. 2015, Space Weather, 13, 374, doi: `10.1002/2015SW001171`

Sawyer, C. 1968, Annual Review of Astronomy and Astrophysics, 6, 115

Schwabe, S. H. 1843, Astron. Nachr., 20, 283

Schwenn, R., dal Lago, A., Huttunen, E., & Gonzalez, W. D. 2005, Ann. Geophys., 23, 1033

Schwenn, R., Rosenbauer, H., & Miggenrieder, H. 1975, Raumfahrtforschung, 19, 226

Scolini, C., Rodriguez, L., Mierla, M., Pomoell, J., & Poedts, S. 2019, Astron. & Astrophys., 626, A122, doi: `10.1051/0004-6361/201935053`

Shen, C., Wang, Y., Ye, P., et al. 2007, The Astrophysical Journal, 670, 849

Shen, F., Shen, C., Wang, Y., Feng, X., & Xiang, C. 2013, Geophys. Res. Lett., 40, 1457, doi: `10.1002/grl.50336`

Shiota, D., & Kataoka, R. 2016, Space Weather, 14, 56, doi: `10.1002/2015SW001308`

Siscoe, G., Crooker, N. U., & Clauer, C. R. 2006, Adv Space Res, 38, 173, doi: `10.1016/j.asr.2005.02.102.`

Siscoe, G., & Odstrcil, D. 2008, J. Geophys. Res., 113, A00B07, doi: `10.1029/2008JA013142`

Spiegel, E. A., & Zahn, J. P. 1992, Astron. & Astrophys., 265, 106

Spreiter, J. R., & Stahara, S. S. 1985, American Geophysical Union Geophysical Monograph, Washington DC, 35, 85, doi: `10.1029/GM035p0085`

Stone, E. C., & Cummings, A. C. 2001, Proceedings of the 27th International Cosmic Ray Conference. 07-15 August, 2001. Hamburg, Germany. Under the auspices of the International Union of Pure and Applied Physics (IUPAP), 4263

Stone, E. C., Cummings, A. C., & Heikkila, B. C. 2019, Nat. Astron., 3, 1013, doi: `10.1038/s41550-019-0928-3`

Strong, K. T., Schmelz, J. T., Saba, J. L. R., & Kucera, T. A. 2017, Bulletin of the American Meteorological Society, 98, 2387, doi: `10.1175/BAMS-D-16-0191.1`

Sturrock, P. A. 1966, Nature, 211, 695

Subramanian, P., Lara, A., & Borgazzi, A. 2012, Geophys. Res. Lett., 39, L19107, doi: `10.1029/2012GL053625`

Sudar, D., Vršnak, B., & Dumbović, M. 2016, Mon. Not. R. Astron. Soc., 456, 1542, doi: `10.1093/mnras/stv2782`

Syed Ibrahim, M., Joshi, B., & Cho, K.-S. 2019, Solar Phys., 294, 54, doi: `10.1007/s11207-019-1443-5`

Takahashi, T., & Shibata, K. 2017, Astrophys. Journ. Lett., 837, doi: `10.3847/2041-8213/aa624c`

Taktakishvili, A.and Kuznetsova, M., MacNeice, P., Hesse, M., et al. 2009, Space Weather, doi: `10.1029/2008SW000448`

Temmer, M., Dumbović, M., Holzknecht, L., et al. 2021, Journal of Geophysical Research: Space Physics, 126, doi: `10.1029/2020JA028380`

Temmer, M., Rollett, T., Möstl, C., et al. 2011, The Astrophysical Journal, 743, 101, doi: `10.1088/0004-637X/743/2/101`

Temmer, M., Veronig, A. M., Peinhart, V., & Vršnak, B. 2014, The Astrophysical Journal, 785, doi: `10.1088/0004-637X/785/2/85`

Temmer, M., Vršnak, B., Rollett, T., et al. 2012, The Astrophysical Journal, 749, 57, doi: `10.1088/0004-637X/749/1/57`

Thompson, W. T. 2011, J. Atmos. Sol. Terr. Phys., 73, 1138, doi: `10.1016/j.jastp.2010.07.005`

Thompson, W. T., Kliem, B., & Török, T. 2012, Solar Phys., 276, 241, doi: `10.1007/s11207-011-9868-5`

Tokumaru, M., Kojima, M., & Fujiki, K. 2010, Journal of Geophysical Research: Space Physics, 115, doi: `10.1029/2009JA014628`

Török, T., Berger, M. A., & Kliem, B. 2010, Astron. & Astrophys., 516, A49, doi: `10.1051/0004-6361/200913578`

Török, T., & Kliem, B. 2005, Astrophys. Journ. Lett., 630, L97, doi: `10.1086/462412`

Török, T., Kliem, B., & Titov, V. S. 2004, Astron. & Astrophys., 413, L27, doi: `10.1051/0004-6361:20031691`

Tsurutani, B. T. 1995, J. Geophys. Res., 100, 717

Tsurutani, B. T., Gonzalez, W. D., Gonzalez, A. L. C., et al. 2006, J. Geophys. Res., 111, doi: `10.1029/2005JA011273`

Tsurutani, B. T., Gonzalez, W. D., Tang, F., & Akasofu, S. I. Smith, E. J. 1988, J. Geophys. Res., 93, 8519

Tsurutani, B. T., Russell, C. T., King, J. H., Zwickl, R. D., & Lin, R. P. 1984, Geophys. Res. Lett., 11, 339

Turner, D. L., Shprits, Y., Hartinger, M., & Angelopoulos, V. 2012, Nature Physics, 8, 208, doi: `10.1038/nphys2185`

Ulrich, R. K. 2010, The Astrophysical Journal, 725, 658, doi: `10.1088/0004-637X/725/1/658`

Upton, L. A., & Hathaway, D. H. 2018, Geophys. Res. Lett., 45, 8091, doi: `10.1029/2018GL078387`

Usoskin, I. G. 2008, Living Reviews in Solar Physics, 5

Žic, T., Vršnak, B., & Temmer, M. 2015, The Astrophysical Journal, 218, doi: `10.1088/0067-0049/218/2/32`

Žic, T., Vršnak, B., Temmer, M., & Jacobs, C. 2008, Solar Phys., 253, 237, doi: `10.1007/s11207-008-9173-0`

Vourlidas, A. 2015, Space Weather, 13, 197, doi: `10.1002/2015SW001173`

Vourlidas, A., Colaninno, R. C., Nieves-Chinchilla, T., & Stenborg, G. 2011, Astrophys. Journ. Lett., 733, L23, doi: `10.1088/2041-8205/733/2/L23`

Vourlidas, A., Howard, R. A., & Esfandiari, E. 2010, The Astrophysical Journal, 722, 1522, doi: `10.1088/0004-637X/722/2/1522`

Vourlidas, A., Lynch, B. J., Howard, R. A., & Li, Y. 2013, Solar Phys., 284, 179

Vourlidas, A., Patsourakos, S., & Savani, N. P. 2019, Phil. Trans. R. Soc. A, 377, doi: `10.1098/rsta.2018.0096`

Vršnak, B. 2001, Solar Phys., 202, 173

Vršnak, B., & Gopalswamy, N. 2002, J. Geophys. Res., 107, doi: `10.1029/2001JA000120`

Vršnak, B., Maričič, D., Stanger, A. L., et al. 2007, Solar Phys., 241, 85, doi: `10.1007/s11207-006-0290-3`

Vršnak, B., Ruždjak, D., Sudar, D., & Gopalswamy, N. 2004, Astron. & Astrophys., 423, 717, doi: `10.1051/0004-6361:20047169`

Vršnak, B., Sudar, D., & Ruždjak, D. 2005, Astron. & Astrophys., 435, 1149, doi: `10.1051/0004-6361:20042166`

Vršnak, B., Žic, T., Falkenberg, T. V., et al. 2010, Astron. & Astrophys., 512, A43, doi: `10.1051/0004-6361/200913482`

Vršnak, B., Žic, T., Vrbanec, D., et al. 2013, Solar Phys., 285, 295, doi: `10.1007/s11207-012-0035-4`

Vršnak, B., Amerstorfer, T., Dumbović, M., et al. 2019, The Astrophysical Journal, 877, doi: `10.3847/1538-4357/ab190a`

Wang, C., Du, D., & Richardson, J. D. 2005, J. Geophys. Res., 110, A10107, doi: `10.1029/2005JA011198`

Wang, Y., Shen, C., Wang, S., & Ye, P. 2004, Solar Phys., 222, 329, doi: `10.1023/B:SOLA.0000043576.21942.aa`

Wang, Y., Wang, B., Shen, C., Shen, F., & Lugaz, N. 2014, Journal of Geophysical Research: Space Physics, 119, 5117, doi: `10.1002/2013JA019537`

Wang, Y., Shen, C., Liu, R., et al. 2018, Journal of Geophysical Research: Space Physics, 123, 3238, doi: `10.1002/2017JA024971`

Wang, Y. M., & Sheeley Jr., N. R. 1990, The Astrophysical Journal, 355, 726, doi: `10.1086/168805`

Wang, Y.-M., Sheeley Jr., N. R., & Rich, N. B. 2000, Geophys. Res. Lett., 27, 149, doi: `10.1029/1999GL010698`

Webb, D. F., & Howard, T. A. 2012, Living Reviews in Solar Physics, 9, doi: `10.12942/lrsp-2012-3`

Webb, D. F., & Vourlidas, A. 2016, Solar Phys., 291, 3725, doi: `10.1007/s11207-016-0988-9`

Wenzel, K. P., Marsden, R. G., Page, D. E., & Smith, E. J. 1992, Astron. Astrophys. Suppl. Ser, 92, 207

Wild, J. P. 1950, Australian Journal of Scientific Research A: Physical Sciences, 3, 541

Wild, J. P., & Smerd, S. F. 1972, Ann. Rev. Astron. Astrophys., 10, 159, doi: `10.1146/annurev.aa.10.090172.001111`

Wilson, R. M. 1987, Planetary and Space Science, 35, 329, doi: `10.1016/0032-0633(87)90159-0`

Winslow, R. M., Lugaz, N., Philpott, L. C., et al. 2015, Journal of Geophysical Research: Space Physics, 120, 6101, doi: `10.1002/2015JA021200`

Winslow, R. M., Lugaz, N., Scolini, C., & Galvin, A. B. 2021a, The Astrophysical Journal, 916, doi: `10.3847/1538-4357/ac0821`

Winslow, R. M., Philpott, L., Paty, C. S., et al. 2017, Journal of Geophysical Research: Space Physics, 122, 4960, doi: `10.1002/2016JA023548`

Winslow, R. M., Scolini, C., Lugaz, N., & Galvin, A. B. 2021b, The Astrophysical Journal, 916, doi: `10.3847/1538-4357/ac0439`

Winslow, R. M., Lugaz, N., Schwadron, N. A., et al. 2016, Journal of Geophysical Research: Space Physics, 121, 6092, doi: `10.1002/2015JA022307`

Winslow, R. M., Schwadron, N. A., Lugaz, N., et al. 2018, The Astrophysical Journal, 856, 139, doi: `10.3847/1538-4357/aab098`

Winslow, R. M., Lugaz, N., Philpott, L., et al. 2020, The Astrophysical Journal, 889, doi: `10.3847/1538-4357/ab6170`

Wold, A. M., Mays, M. L., Taktakishvili, A., et al. 2018, J. Space Weather Space Clim., 8, A17, doi: `10.1051/swsc/2018005`

Xiang, Z., Tu, W., Li, X., et al. 2017, Journal of Geophysical Research: Space Physics, 122, 9858, doi: `10.1002/2017JA024487`

Yashiro, S., Gopalswamy, N., Michalek, G., et al. 2004, Journal of Geophysical Research: Space Physics, 109, A10102, doi: `10.1029/2003JA010282`

Yermolaev, Y. I., Nikolaeva, N. S., Lodkina, I. G., & Yermolaev, M. Y. 2010, Annales Geophysicae, 28, 2177, doi: `10.5194/angeo-28-2177-2010`

Yurchyshyn, V. 2008, Astrophys. Journ. Lett., 675, L49, doi: `10.1086/533413`

Zhang, J., & Dere, K. P. 2006, The Astrophysical Journal, 649, 1100, doi: `10.1086/506903`

Zhang, J., Liemohn, M. W., Kozyra, J. U., Lynch, B. J., & Zurbuchen, T. H. 2004, J. Geophys. Res., 109, A09101, doi: `10.1029/2004JA010410`

Zhang, J., Richardson, I. G., Webb, D. F., et al. 2007, J. Geophys. Res., 112, A10102, doi: `10.1029/2007JA012321`

Zhao, J., Bogart, R. S., Kosovichev, A. G., Duvall Jr., T. L., & Hartlep, T. 2013, Astrophys. Journ. Lett., 774, doi: `10.1088/2041-8205/774/2/L29`

Zhao, J., & Kosovichev, A. G. 2004, The Astrophysical Journal, 603, doi: `10.1086/381489`

Zhao, X. H., Feng, X. S., Feng, H. Q., & Li, Z. 2017, The Astrophysical Journal, 849, 79, doi: `10.3847/1538-4357/aa8e49`

Zharkov, S., Green, L. M., Matthews, S. A., & Zharkova, V. V. 2011, Astrophys. Journ. Lett., 741, L35, doi: `10.1088/2041-8205/741/2/L35.arXiv:1110.2005`

Zhou, Y. F., & Feng, X. S. 2013, Journal of Geophysical Research: Space Physics, 118, 6007, doi: `10.1002/2013JA018976`

Zhuang, B., Wang, Y., Hu, Y., et al. 2019, The Astrophysical Journal, 876, 73, doi: `10.3847/1538-4357/ab139e`

APPENDIX A

CME conjunction catalog

Table A.1 lists 47 CME events observed in longitudinal conjunction between MESSENGER, *Venus Express*, STEREO, and *Wind*/ACE, as described in Chapter 6.

In Table A.1:

Column 1 is the event tag associated with each conjunction event. The first digit represents the chronological order of appearance of an event in the catalog and the last four digits refer to the year of occurrence. **Column 2** is the month and day the CME was launched from the Sun. **Column 3** is the hour, minute, and second the CME was launched from the Sun (average CME onset time as calculated in the CDAW catalog for LASCO observations or the time of the first STEREO/COR image containing the CME for STEREO observations). **Column 4** is the 2nd order non-linear CME speed (in $\mathrm{km\,s^{-1}}$) listed in the CDAW catalog (second-order polynomial fit to the height-time measurements evaluated when the CME was at a height of 20 R_s) or the maximum speed (in $\mathrm{km\,s^{-1}}$) listed in the CACTus catalog. **Column 5** is the initial/abbreviation of the two spacecraft in longitudinal conjunction (M=MESSENGER, VEx= *Venus Express*, STA= STEREO-A, STB= STEREO-B). **Column 6** is the longitudinal separation (in degress) between the two spacecraft in conjunction in Heliographic Inertial (HGI) coordinates. **Column 7** is the month, day, hour, and minute (for the year refer to the last four digits of the event tag) the CME arrived at SC1. **Column 8** is the month, day, hour, and minute the ME leading-edge arrived at SC1. **Column 9** is the month, day, hour, and minute the CME ended at SC1. **Column 10** is the heliocentric distance (in AU) of SC1 from the Sun at the CME onset time. **Column 11** is the month, day, hour, and minute (for the year refer to the last four digits of the event tag) the CME arrived at SC2. **Column 12** is the month, day, hour, and minute the ME leading-edge arrived at SC2. **Column 13** is the month, day, hour, and minute the CME ended at SC2. **Column 14** is the heliocentric distance (in AU) of SC2 from the Sun at the CME onset time.

Table A.1: List of 47 CMEs observed in conjunction in the inner heliosphere.

Event No-Yr	CME LASCO/COR2 Appearance		CME Speed	SC1-SC2	LS	SC1				SC2			
	MM/DD	HH:MM:SS	km s^{-1}	Name	Degrees	T$_{shock/dis}$	T$_{le}$	T$_{te}$	R$_1$	T$_{shock/dis}$	T$_{le}$	T$_{te}$	R$_2$
1-2011	6/4	22:05:02	2281	M-VEx	6.6	6/5 3:31	6/5 4:30	6/5 12:46	0.32	6/5 13:29	6/5 15:13	6/5 22:31	0.72
2-2011	10/14	12:24:05	750	M-VEx	-1.6	10/15 8:27	10/15 11:14	10/16 6:43	0.46	10/16 0:50	10/16 6:06 to 7:49	10/17 9:39	0.73
3-2011	11/3	23:30:05	946	M-VEx	23.1	11/4 15:09	11/4 17:23	11/5 15:41	0.44	11/5 3:42	11/5 6:56 to 11:04	11/5 15:49	0.73
4-2012	3/7	0:24:06	2594	M-VEx	-1.1	3/7 4:38	3/7 6:11	3/7 18:01	0.32	3/7 13:26	3/7 20:14	3/8 11:43	0.72
5-2013	10/25	15:12:09	1015	M-VEx	16	10/26 11:07	10/26 13:21	10/26 19:24	0.35	10/27 11:14	10/28 1:49	10/29 5:05	0.73
6-2011	6/4	22:05:02	2281	M-STA	44.2	6/5 3:31	6/5 4:30	6/5 12:46	0.32	6/5 18:59	6/6 12:22	6/7 11:15	0.96
7-2011	9/6	5:24:05	716	M-STA	-22.4	9/6 23:34	9/7 1:35	9/7 9:57	0.31	9/8 16:02	9/9 0:05	9/11 8:52	0.97
8-2011	11/3	23:30:05	946	M-STB	-4.8	11/4 15:09	11/4 17:23	11/5 15:41	0.44	11/6 5:11	11/6 22:50	11/9 4:00	1.09
9-2011&12	2011 12/29	16:24:05	756	M-STA	-4.6	2011 12/30 16:27	2011 12/30 18:14	2011 12/31 9:20	0.42	2012 1/1 13:22	2012 1/1 17:00	2012 1/2 4:00	0.96
10-2012	1/2	15:12:40	1109	M-STA	4.4	1/3 17:57	1/3 20:10	1/4 11:21	0.44	1/5 20:40	1/5 20:40	1/6 12:56	0.96
11-2012	5/17	1:48:05	1473	M-STA	15.5	5/17 12:10	5/17 12:58	5/17 15:39	0.34	5/18 12:43	5/18 21:22	5/19 9:12	0.96
12-2012	10/21	20:57:28	528	M-STB	31.7	10/23 9:55	10/23 10:37	10/23 18:54	0.43	10/25 19:10	10/26 4:00	10/27 10:00	1.08
13-2013	4/20	6:00:07	851	M-STA	-31.4	4/21 6:42	4/21 13:35	4/22 5:12	0.42	4/22 10:08	4/23 0:00	4/23 19:30	0.96
14-2013	4/30	1:36:21	699	M-STA	-2.9	5/1 5:46	5/1 8:52	5/2 0:52	0.36	5/2 21:02	5/3 5:50	5/4 16:10	0.96
15-2013	8/19	23:12:11	900	M-STA	15	8/20 12:41	8/20 14:34	8/21 20:31	0.33	8/22 7:05	8/22 23:15	8/24 23:25	0.97
16-2013	9/11	8:48:05	668	M-STB	9.4	9/12 23:37	9/13 2:21	9/13 15:29	0.45	9/15 16:20	9/16 4:20	9/17 0:25	1.04
17-2013	11/29	17:24:25	719	M-STA	-26.8	11/30 14:26	11/30 16:13	12/1 4:10	0.41	12/1 22:29	12/2 6:00	12/4 7:40	0.96
18-2013	12/26	3:24:05	1015 @ 13.76Rs	M-STB	-32.3	12/27 4:14	12/27 5:36	12/27 15:28	0.46	12/28 17:06	12/29 4:12	12/30 14:00	1.09
19-2012	7/12	16:54:26	1249 @ 15Rs	M-ACE	-30.7	7/13 10:53	7/13 13:44	7/14 2:46	0.47	7/14 18:09	7/15 6:00	7/17 5:00	1.00
20-2012	11/20	12:00:07	639	M-ACE	17.8	11/21 6:07	11/21 9:16	11/22 2:05	0.31	11/23 21:52	11/24 12:00	11/25 10:00	1.00
21-2013	7/9	15:54:19	694 @ 15Rs	M-ACE	3.1	7/11 1:05	7/11 1:57	7/11 23:14	0.45	7/12 17:14	7/13 5:00	7/15 0:00	1.00
22-2014	2/12	12:54:00	750 @ 15Rs	M-ACE	-11.8	2/13 4:51	2/13 8:19	2/13 16:56	0.33	2/15 13:16	2/16 5:00	2/16 16:00	1.00
23-2014	2/16	10:24:00	625 @ 15 Rs	M-ACE	4.8	2/17 4:17	2/17 7:03	2/17 12:14	0.35	2/19 3:48	2/19 12:00	2/20 3:00	1.00
24-2008	12/27	5:30:04	562	VEx-STB	-8.5	-	12/29 20:46	12/30 4:58	0.72	12/31 2:00	12/31 2:00	1/1 7:20	1.03
25-2009	5/29	9:30:03	318	VEx-STA	-9.2	-	6/2 18:39	6/3 12:20	0.73	6/03 0:00	6/03 6:42	6/04 22:40	0.96
26-2009	7/5	14:06:03	177	VEx-STA	10.6	-	7/10 10:38	7/11 6:24	0.73	7/11 23:10	7/11 23:10	7/13 5:45	0.96
27-2010	6/2	21:54:05	401	VEx-STB	-21.3	6/6 13:39	6/6 14:36	6/7 0:45	0.72	6/7 4:08	6/7 22:21	6/8 12:30	1.02
28-2010	8/1	3:39:00	1031	VEx-STB	16.5	8/1 14:41	8/1 23:11	8/2 5:56	0.73	-	-	-	-
28-2010	8/1	8:24:00	1932	VEx-STB	17.3	8/2 11:30	8/2 12:42	8/2 16:05	0.73	8/3 5:00	8/3 5:00	8/3 9:50	1.06
28-2010	-	-	-	VEx-STB	17.3	-	8/2 22:06	8/3 14:30	0.73	8/3 14:20	8/3 14:20	8/4 7:09	1.06
29-2011	3/16	19:12:07	743	VEx-STA	-4.2	3/18 20:47	3/19 3:19 to 3/19 5:57	3/19 11:54	0.73	3/19 11:25	3/19 23:34	3/21 1:30	0.96
30-2011	-	-	-	VEx-STA	5.5	-	4/5 17:12	4/6 15:03	0.73	4/5 21:43	4/6 9:40	4/6 23:41	0.96
31-2011	4/9	15:48:06	824	VEx-STA	8.7	-	4/11 11:04	4/11 17:33	0.73	4/11 12:08	4/11 18:14	4/12 10:40	0.96
31-2011	4/9	18:00:08	643	VEx-STA	8.7	-	4/11 11:04	4/11 17:33	0.73	4/11 12:08	4/11 18:14	4/12 10:40	0.96
32-2011	4/16	12:12:05	282 @ 15Rs	VEx-STA	13.4	-	4/20 6:52	4/20 22:00	0.73	4/21 7:12	4/21 7:12	4/22 10:58	0.96
33-2011	4/17	19:00:05	313	VEx-STA	13.9	-	4/21 11:20	4/22 11:27	0.73	4/23 10:00	4/23 10:00	4/24 7:32	0.96
34-2011	6/4	22:05:02	2281	VEx-STA	37.6	6/5 13:29	6/5 15:13	6/5 22:31	0.72	6/5 18:59	6/6 12:22	6/7 11:15	0.96
35-2011	11/3	23:30:05	946	VEx-STB	-27.2	11/5 3:42	11/5 6:56 to 11/5 11:04	11/5 15:49	0.73	11/6 5:11	11/6 22:50	11/9 4:00	1.09
35-2011	11/4	1:25:29	716	VEx-STB	-27.2	11/5 3:42	11/5 6:56 to 11/5 11:04	11/5 15:49	0.73	11/6 5:11	11/6 22:50	11/9 4:00	1.09
36-2011	11/17	20:36:05	1005	VEx-STB	-17	11/19 3:48	11/19 7:39 to 11/19 10:49	11/20 3:19	0.73	11/20 13:39	11/20 22:40	11/22 1:10	1.09
37-2011	12/23	18:36:05	656	VEx-STB	9.6	-	12/26 2:50	12/26 22:38	0.73	12/26 23:51	12/27 7:00	12/28 11:00	1.08
37-2011	12/24	8:48:06	429	VEx-STB	9.6	-	12/26 2:50	12/26 22:38	0.73	12/26 23:51	12/27 7:00	12/28 11:00	1.08
38-2012	11/8	11:00:08	917	VEx-STA	-28.6	11/10 15:39	11/10 21:56	11/11 1:55 to 11/11 3:22	0.72	11/11 21:19	11/12 15:24	11/13 15:05	0.97
39-2012	11/10	14:12:05	556	VEx-STA	-26.9	11/13 10:48	11/13 17:31	11/14 6:27	0.72	11/13 20:57	11/14 10:42	11/16 8:45	0.97
40-2012	11/23	8:12:05	619 @ 13.18Rs	VEx-STA	-19.9	11/25 1:02	11/25 5:17	11/25 11:20	0.72	11/26 7:58	11/26 15:00	11/28 1:22	0.96
40-2012	11/23	23:24:05	1134	VEx-STA	-19.9	11/25 1:02	11/25 5:17	11/25 11:20	0.72	11/26 7:58	11/26 15:00	11/28 1:22	0.96
41-2013	1/6	6:39:59	736	VEx-STA	4.9	1/8 9:23	1/8 15:24	1/9 19:48	0.73	1/9 2:25	1/9 10:38	1/10 17:17	0.96
42-2013	2/14	21:17:41	816	VEx-STA	26.5	-	2/17 10:55	2/17 20:51	0.73	2/19 7:44	2/19 7:44	2/20 6:11	0.96
43-2013	4/25	8:48:06	744	VEx-STB	-20	4/27 14:38	4/28 1:45	4/29 13:54	0.72	4/28 19:38	-	4/29 16:50	1.01
44-2012	6/14	14:12:07	1272 @ 15Rs	VEx-Wind	5.7	-	6/15 19:26	6/16 8:28	0.73	6/16 20:19	6/16 23:00	6/17 12:00	1.00
45-2012	7/4	17:24:04	657 @ 15Rs	VEx-Wind	19.6	-	7/7 20:20	7/8 1:02 to 4:08	0.73	7/8 8:00	7/9 0:00	7/9 14:00	1.00
46-2013	11/27	22:12:27	565	VEx-Wind	-25.3	11/30 4:31	11/30 14:00	12/1 16:00	0.72	11/30 20:00	12/1 11:00	12/2 23:00	1.00
47-2013	12/12	6:24:05	695	VEx-Wind	-16.9	12/14 3:07	12/14 14:33	12/14 23:40	0.72	12/15 13:00	12/15 16:00	12/16 5:00	1.00

APPENDIX B

CMEs with and without shocks and sheaths

Tables B.1 to B.3 list the 106 Cat-I CMEs (with shocks and sheaths), 36 Cat-II CMEs (with sheaths but no shocks), and 46 Cat-III CMEs (with no shocks and sheaths), respectively, measured by STEREO near 1 AU, as categorized in Chapter 4.

In Table B.1:

$\mathbf{T}_{CME}$, $\mathbf{T}_{le}$, and $\mathbf{T}_{te}$ are the arrival timings of the shock, ME leading-edge, and ME trailing-edge at STEREO (in UT). $\mathbf{T}_{sheath}$ is the sheath duration (in h), $\mathbf{T}_{model}$ is the ASIA predicted sheath duration (in h), and $\mathbf{T}_{ME}$ is the ME duration (in h). No value in the $\mathbf{T}_{model}$ column indicates that the ASIA did not identify any sheath upstream of the ME. $\mathbf{M}_{ms}$ is the shock magnetosonic Mach number. $\mathbf{v}_{sw}$ is the upstream solar wind speed (in $\mathrm{km\,s^{-1}}$). $\mathbf{N}_{sheath}$ is the average sheath density (in $\mathrm{cm^{-3}}$), $\mathbf{B}_{sheath}$ is the average sheath magnetic field (in nT), $\mathbf{v}_{sheath}$ is the average sheath speed (in $\mathrm{km\,s^{-1}}$), and $\mathbf{P}_{sheath}$ is the average sheath dynamic pressure (in nPa). $\mathbf{v}_{le}$ is the ME leading-edge speed (in $\mathrm{km\,s^{-1}}$).

Table B.2 is almost similar to Table B.1, but $\mathbf{T}_{CME}$ represents the start of the sheath (as Cat-II CMEs do not have associated shocks).

In Table B.3, $\mathbf{T}_{CME}$ is the start of the ME because Cat-III CMEs do not have shocks and sheaths. $\mathbf{N}_{ME}$ is the average ME density (in $\mathrm{cm^{-3}}$), $\mathbf{B}_{ME}$ is the average ME magnetic field (in nT), $\mathbf{v}_{ME}$ is the average ME speed (in $\mathrm{km\,s^{-1}}$), and $\mathbf{v}_{le}$ is the ME leading-edge speed (in $\mathrm{km\,s^{-1}}$).

Table B.1: Cat-I CMEs with shocks and sheaths

SC	Year	T$_{CME}$	T$_{le}$	T$_{te}$	T$_{sheath}$	T$_{model}$	T$_{ME}$	M$_{ms}$	v$_{sw}$	N$_{sheath}$	B$_{sheath}$	v$_{sheath}$	P$_{sheath}$	v$_{le}$
ST-A	2007	8/25 20:30	8/25 23:27	8/26 16:00	2.95	2.08	16.55	1.21	290	39.64	8.89	317	7.99	333
ST-B	2008	4/29 14:10	4/29 15:34	4/30 07:00	1.40	2.08	15.43	1.45	340	19.03	11.11	422	6.77	434
ST-B	2008	6/6 15:36	6/6 22:15	6/7 12:32	6.65	3.25	14.28	1.34	328	15.13	9.14	402	4.88	404
ST-B	2009	08/05 22:35	08/06 04:39	08/07 05:25	6.07	4.58	24.75	1.43	332	17.08	8.33	374	4.78	379
ST-B	2009	08/30 02:50	08/30 16:20	08/31 05:40	13.50	12.33	13.33	1.17	309	12.47	7.04	347	3.01	349
ST-B	2009	10/02 15:42	10/03 05:48	10/04 04:32	14.10	13.17	22.73	1.17	269	12.83	8.54	310	2.47	335
ST-A	2009	10/16 14:57	10/16 21:35	10/17 22:16	6.63	5.67	24.69	1.36	309	5.72	7.54	344	1.36	336
ST-A	2009	12/8 23:38	12/9 9:00	12/10 23:13	9.37	8.58	38.21	1.72	272	29.66	8.49	322	6.13	327
ST-A	2010	2/5 3:33	2/5 12:40	2/6 2:00	9.12	8.17	13.33	2.24	331	21.37	10.82	384	6.31	397
ST-A	2010	4/23 00:35	4/23 6:27	4/23 14:06	5.87	5.08	7.65	0.67	373	12.65	6.90	402	4.09	417
ST-A	2010	5/30 15:00	5/31 00:26	5/31 14:00	9.43	9.00	13.57	1.39	401	13.07	8.92	425	4.71	403
ST-A	2010	6/3 8:36	6/3 12:30	6/4 02:46	3.90	2.83	14.26	1.7	329	27.83	6.65	362	7.29	372
ST-A	2010	8/20 16:14	8/20 22:22	8/21 13:14	6.13	5.33	14.87	2.11	337	15.52	20.08	528	8.65	543
ST-A	2010	9/11 6:59	9/11 16:45	9/13 5:55	9.77	8.17	37.16	1.23	365	12.64	14.04	575	8.35	581
ST-A	2010	9/17 22:34	9/18 6:22	9/19 6:21	7.80	7.42	23.98	0.97	352	19.94	9.89	406	6.56	408
ST-B	2010	11/19 20:26	11/20 6:34	11/21 9:10	10.13	9.08	26.60	0.9	413	7.90	7.06	458	3.31	452
ST-B	2011	1/17 15:46	1/18 0:0	1/18 9:38	8.23	7.33	9.63	1.94	322	9.66	7.45	389	2.93	363
ST-A	2011	3/19 11:25	3/19 23:34	3/21 1:30	12.17	10.92	25.92	1.42	392	6.14	12.10	478	2.81	499
ST-B	2011	3/28 8:53	3/28 17:48	3/29 18:48	8.92	8.08	24.99	1.03	425	6.50	14.71	558	4.05	628
ST-B	2011	3/31 23:39	4/1 4:00	4/1 13:50	4.37	3.17	9.83	3.55	413	18.40	18.55	598	13.17	571
ST-A	2011	4/11 12:08	4/11 18:14	4/12 10:40	6.10	5.50	16.43	2.27	614	5.18	7.83	626	4.06	607
ST-A	2011	6/5 18:59	6/6 12:22	6/7 11:15	17.39	17.25	22.88	1.76	625	6.07	12.48	823	8.21	949
ST-B	2011	6/17 7:40	6/17 7:40	6/18 4:00	10.70	10.42	20.33	0.83	365	16.71	12.67	568	10.79	531
ST-A	2011	8/6 12:43	8/6 16:38	8/7 19:38	3.93	3.25	27.00	1.54	444	13.98	10.71	486	6.61	516
ST-A	2011	9/8 16:02	9/9 00:05	9/11 8:51	8.07	7.67	56.75	1.36	286	28.84	10.59	350	7.08	371
ST-B	2011	9/24 9:06	9/24 12:36	9/24 19:28	3.50	7.00	6.87	1.39	553	19.43	25.51	683	18.13	740
ST-B	2011	10/3 22:23	10/4 02:00	10/4 12:40	3.62	3.67	10.66	4.02	375	18.91	18.89	634	15.21	641
ST-A	2011	10/25 4:51	10/25 15:47	10/26 16:00	10.93	10.75	24.22	1.48	357	17.49	11.20	409	5.84	401
ST-B	2011	11/6 5:11	11/6 22:50	11/9 4:00	17.67	16.75	53.16	0.06	487	5.36	9.71	630	4.26	617
ST-B	2011	11/20 13:39	11/20 22:40	11/22 1:10	9.03	7.33	26.50	0.88	300	15.77	11.67	423	5.66	501

Cat-I CMEs with shocks and sheaths (...continued)

SC	Year	T_{CME}	T_{le}	T_{te}	T_{sheath}	T_{model}	T_{ME}	M_{ms}	v_{sw}	N_{sheath}	B_{sheath}	v_{sheath}	P_{sheath}	v_{le}
ST-A	2011	11/26 18:09	11/27 00:20	11/28 05:00	6.18	5.67	28.67	1.37	420	11.37	7.67	480	5.24	481
ST-A	2011	11/28 14:51	11/28 19:20	11/29 22:10	4.48	3.83	26.83	1.71	425	12.08	14.48	488	5.75	483
ST-A	2011	12/6 22:44	12/7 6:55	12/7 18:00	8.20	7.25	11.08	1.96	294	15.22	8.56	375	4.28	349
ST-B	2011	12/26 23:51	12/27 7:00	12/28 11:00	7.17	6.42	28.00	1.67	308	13.48	5.96	329	2.92	336
ST-A	2012	1/1 13:22	1/1 17:00	1/2 4:00	3.47	2.83	11.16	1.93	351	25.92	9.30	440	10.03	440
ST-B	2012	1/16 9:49	1/17 7:30	1/18 9:00	21.68	20.33	25.50	1.34	318	14.68	6.89	369	3.99	382
ST-B	2012	3/10 21:17	3/11 1:34	3/12 21:51	4.29	3.75	44.27	1.54	594	3.98	6.01	678	3.66	675
ST-A	2012	3/18 19:31	3/19 4:38	3/19 16:00	9.12	8.25	11.36	1.5	413	18.21	12.97	465	7.86	477
ST-B	2012	3/26 16:31	3/26 17:45	3/28 3:52	1.25	2.08	34.12	2.12	324	25.47	11.46	458	10.69	491
ST-B	2012	4/17 3:37	4/17 9:40	4/18 9:05	6.07	5.25	23.41	0.6	530	1.30	8.40	642	1.07	671
ST-B	2012	5/8 14:55	5/8 18:35	5/9 10:16	3.67	2.58	15.68	0.73	397	41.25	22.77	423	14.77	419
ST-B	2012	5/12 23:09	5/13 3:00	5/14 4:30	3.87	3.17	25.50	0.55	315	13.32	8.99	352	3.30	342
ST-A	2012	5/18 12:43	5/18 21:22	5/19 9:12	8.66	8.58	11.82	3.5	624	6.04	14.32	787	7.48	-
ST-A	2012	5/28 2:48	5/28 9:00	5/29 4:22	6.20	5.25	19.36	2.37	407	21.29	28.71	761	24.66	796
ST-B	2012	6/11 21:06	6/12 3:00	6/12 19:21	5.90	5.42	16.35	0.81	371	15.92	12.52	425	5.75	430
ST-B	2012	7/4 6:57	7/4 11:40	7/5 12:50	4.73	3.75	25.17	3.68	426	23.81	25.74	675	21.68	600
ST-A	2012	7/10 18:55	7/11 9:10	7/13 4:00	14.25	13.08	42.83	1.42	568	12.14	9.27	630	9.63	620
ST-A	2012	7/20 22:43	7/21 11:40	7/22 2:30	12.95	-	14.83	1.98	556	15.25	10.82	687	14.40	648
ST-B	2012	7/23 21:21	7/24 20:00	7/25 12:00	22.65	22.33	15.99	1.28	338	10.85	6.67	346	2.59	330
ST-B	2012	7/28 14:59	7/28 17:08	7/29 1:00	2.15	2.08	7.87	1.12	353	12.29	8.92	430	4.55	443
ST-A	2012	8/5 15:37	8/6 4:00	8/7 6:00	12.38	11.42	26.00	1.1	427	9.25	6.68	490	4.44	476
ST-A	2012	9/19 21:46	9/20 14:22	9/21 22:36	16.62	-	32.21	0.89	331	14.55	6.74	422	5.17	429
ST-B	2012	9/23 8:44	9/23 23:38	9/24 9:46	14.90	14.33	10.13	1.92	349	35.96	16.06	407	11.92	391
ST-A	2012	9/23 14:29	9/23 21:00	9/24 11:00	6.53	5.83	14.00	1.49	451	13.92	10.83	541	8.14	516
ST-B	2012	9/25 16:26	9/26 3:21	9/28 16:55	10.92	-	61.56	1.7	518	3.07	11.16	647	2.57	713
ST-A	2012	10/5 2:51	10/5 16:10	10/7 12:00	13.32	13.25	43.83	1.05	342	9.51	8.72	412	3.23	440
ST-B	2012	10/17 6:57	10/17 11:20	10/18 21:15	4.38	3.08	33.92	0.95	274	8.03	7.49	309	1.53	316
ST-B	2012	10/25 19:10	10/26 4:00	10/27 10:00	8.83	8.08	30.00	1.29	279	19.49	11.94	371	5.36	399
ST-A	2012	11/10 22:30	11/11 00:45	11/11 13:18	2.25	2.08	12.55	2.37	324	15.29	12.99	508	7.89	490
ST-A	2012	11/13 20:57	11/14 10:42	11/16 8:45	13.75	9.08	46.05	1.36	398	16.32	8.78	487	7.75	490

Cat-I CMEs with shocks and sheaths (...continued)

SC	Year	T_{CME}	T_{le}	T_{te}	T_{sheath}	T_{model}	T_{ME}	M_{ms}	v_{sw}	N_{sheath}	B_{sheath}	v_{sheath}	P_{sheath}	v_{le}
ST-B	2012	11/19 9:50	11/19 12:30	11/20 0:26	2.67	2.08	11.93	1.46	305	30.98	11.80	472	13.82	455
ST-A	2012	11/23 18:28	11/23 22:20	11/25 14:26	3.88	4.42	40.10	1.35	348	11.20	12.57	413	3.82	424
ST-A	2012	11/26 7:58	11/26 15:00	11/28 1:22	7.05	6.17	34.37	0.67	389	15.23	11.75	488	7.25	518
ST-B	2012	11/28 3:36	11/28 7:37	11/29 7:00	4.02	3.50	23.38	0.99	299	8.67	4.61	326	1.85	316
ST-A	2013	1/9 2:25	1/9 10:38	1/10 17:17	8.22	6.75	30.65	1.15	356	19.37	9.71	455	8.02	470
ST-A	2013	2/8 7:44	2/8 18:22	2/10 3:20	10.64	10.25	32.95	0.61	272	19.92	7.02	314	3.93	323
ST-B	2013	2/18 3:06	2/18 8:24	2/19 18:00	5.30	4.08	33.59	1.34	277	35.95	14.82	336	8.13	359
ST-A	2013	2/28 21:14	3/1 13:30	3/5 20:25	16.27	15.83	102.90	1.4	328	20.34	11.73	397	6.41	396
ST-B	2013	3/7 12:23	3/8 8:00	3/10 8:45	19.62	19.00	48.74	1.92	421	12.51	9.85	511	6.54	459
ST-A	2013	3/26 2:46	3/26 9:16	3/26 20:55	6.52	5.67	11.64	1.25	362	15.47	10.75	469	6.80	469
ST-A	2013	4/22 10:08	4/23 0:0	4/23 19:30	13.87	13.67	19.49	1.52	448	9.29	10.09	555	5.73	621
ST-A	2013	4/27 4:20	4/27 6:55	4/27 23:00	2.60	2.08	16.08	0.83	324	6.59	7.68	378	1.88	401
ST-A	2013	5/2 21:02	5/3 5:50	5/4 16:10	8.80	7.42	34.33	1.17	446	14.45	9.78	538	8.37	549
ST-B	2013	5/4 4:52	5/4 15:00	5/6 9:40	10.13	9.83	42.67	0.94	306	15.37	13.73	370	4.20	415
ST-A	2013	5/12 23:30	5/13 16:00	5/15 12:36	16.50	16.42	44.60	1.15	460	5.18	6.87	541	3.03	554
ST-B	2013	5/15 13:34	5/16 1:16	5/16 16:00	11.70	11.17	14.73	1.24	431	11.14	14.64	599	7.99	618
ST-B	2013	6/2 6:09	6/2 12:15	6/6 8:52	6.10	5.25	92.62	0.62	369	9.52	6.25	396	2.99	376
ST-A	2013	8/10 9:16	8/10 17:24	8/12 7:00	8.13	6.75	37.60	1.41	341	7.68	8.96	415	2.64	430
ST-B	2013	9/3 15:50	9/3 22:30	9/4 22:47	6.67	6.42	24.28	1.98	343	13.87	14.38	494	6.76	581
ST-B	2013	9/9 14:32	9/10 6:52	9/10 22:53	16.33	16.08	16.02	0.03	364	7.07	7.87	466	3.07	429
ST-B	2013	10/8 4:54	10/8 17:25	10/9 23:35	12.52	11.83	30.16	1.55	359	12.98	7.70	456	5.40	454
ST-A	2013	11/4 8:56	11/4 20:00	11/6 01:30	11.07	9.75	29.49	1.54	387	11.41	15.55	556	7.06	623
ST-B	2013	11/6 2:00	11/6 13:38	11/7 14:00	11.63	11.58	24.37	1.73	383	11.24	18.14	598	8.05	621
ST-A	2013	11/11 10:31	11/12 2:00	11/13 3:00	15.48	-	25.00	0.85	356	15.37	5.21	381	4.47	377
ST-A	2013	12/1 22:29	12/2 6:00	12/4 7:40	7.52	6.42	49.66	1.71	336	13.74	19.74	596	9.77	555
ST-B	2013	12/8 18:22	12/9 2:25	12/10 18:40	8.05	7.67	40.24	1.44	341	3.87	6.44	419	1.36	420
ST-B	2013	12/17 13:29	12/18 2:05	12/20 15:00	12.60	11.42	60.91	1.18	377	5.97	6.60	414	2.05	427
ST-B	2013	12/28 17:06	12/29 4:12	12/30 14:00	11.10	10.75	33.79	1.86	354	21.91	17.74	470	9.67	512
ST-A	2014	1/9 13:17	1/9 16:00	1/10 13:33	2.72	2.50	21.54	1.17	487	29.73	15.92	544	17.60	535
ST-B	2014	1/29 5:20	1/29 17:14	1/31 9:00	11.90	14.33	39.77	1.16	593	2.85	5.85	663	2.51	671

Cat-I CMEs with shocks and sheaths (...continued)

SC	Year	T_{CME}	T_{le}	T_{te}	T_{sheath}	T_{model}	T_{ME}	M_{ms}	v_{sw}	N_{sheath}	B_{sheath}	v_{sheath}	P_{sheath}	v_{le}
ST-A	2014	2/7 20:59	2/8 6:36	2/9 2:27	9.62	8.42	19.84	1	364	10.13	13.42	414	3.46	448
ST-A	2014	2/16 7:50	2/16 15:06	2/17 16:15	7.27	-	25.15	1.34	434	7.23	12.30	620	5.56	582
ST-A	2014	2/22 23:06	2/23 10:15	2/23 17:18	11.15	11.67	7.05	1.14	402	6.52	6.99	432	2.43	430
ST-A	2014	2/25 12:16	2/26 00:38	2/26 8:26	12.38	-	7.80	0.99	355	9.17	5.15	370	2.51	394
ST-B	2014	3/8 4:41	3/8 20:00	3/9 10:00	15.32	14.33	13.99	3.12	321	15.71	12.65	500	7.84	535
ST-A	2014	3/11 9:37	3/12 2:49	3/14 1:16	17.20	17.50	46.45	1.77	395	5.28	9.22	540	3.08	546
ST-A	2014	3/14 16:38	3/15 1:15	3/15 14:25	8.63	-	13.17	0.69	471	2.30	7.56	608	1.70	683
ST-B	2014	3/14 23:10	3/15 5:15	3/16 18:12	6.08	5.25	36.95	5.5	342	21.22	16.57	548	12.76	500
ST-A	2014	3/30 21:38	3/31 1:05	3/31 13:20	3.46	2.25	12.24	2.31	403	24.09	20.27	610	17.93	672
ST-A	2014	4/9 13:08	4/10 6:05	4/10 15:35	16.97	16.17	9.49	0.62	321	15.02	10.19	407	4.97	404
ST-B	2014	4/12 2:27	4/12 20:46	4/15 7:13	18.32	17.25	58.44	2	315	17.78	14.02	424	6.41	445
ST-B	2014	5/8 1:37	5/8 21:00	5/10 8:23	19.38	19.33	35.39	0.95	363	11.37	10.66	408	3.79	440
ST-A	2014	5/11 12:34	5/11 18:00	5/13 6:00	5.46	4.92	35.98	1.12	447	19.31	14.45	566	12.37	615
ST-B	2014	6/27 18:27	6/28 15:20	6/29 19:45	20.88	20.25	28.41	1.18	321	5.88	8.08	379	1.69	362
ST-B	2014	7/1 12:51	7/1 20:15	7/2 18:48	7.40	7.08	22.55	2.63	392	20.54	14.84	494	10.02	516
ST-A	2014	7/4 16:53	7/4 22:27	7/5 8:51	5.57	4.17	10.39	1.38	300	4.10	4.62	327	0.88	338

Table B.2: Cat-II CMEs with sheaths

SC	Year	T_{CME}	T_{le}	T_{te}	T_{sheath}	T_{model}	T_{ME}	v_{sw}	N_{sheath}	B_{sheath}	v_{sheath}	P_{sheath}	v_{le}
ST-B	2007	5/21 23:44	5/22 04:20	5/22 22:00	4.60	3.58	17.67	494	12.88	6.19	490	6.18	471
ST-B	2007	10/23 10:35	10/23 16:50	10/24 00:07	6.25	5.83	7.28	318	17.79	6.85	380	5.13	395
ST-B	2008	2/5 13:37	2/5 20:37	2/7 10:50	7.00	5.50	38.22	354	3.87	4.43	373	1.07	368
ST-A	2008	3/21 06:40	3/21 08:33	3/21 18:39	1.88	2.58	10.10	447	8.91	6.02	447	3.56	448
ST-B	2008	8/15 05:36	8/15 12:00	8/15 22:00	6.40	5.08	10.00	311	7.91	3.67	330	1.72	342
ST-A	2008	9/4 05:25	9/4 13:30	9/5 12:00	8.08	6.42	22.50	299	13.76	4.38	324	2.89	335
ST-A	2009	07/11 12:10	07/11 23:10	07/13 05:45	11.00	11.42	30.58	328	9.31	4.42	340	2.15	332
ST-B	2009	08/25 07:16	08/25 09:40	08/26 13:27	2.40	3.17	27.78	301	7.17	3.86	338	1.64	357
ST-B	2009	09/09 06:17	09/09 17:17	09/11 04:13	11.00	15.75	34.93	289	8.43	3.95	320	1.72	320
ST-B	2009	11/10 09:36	11/10 18:48	11/11 11:00	9.20	8.92	16.20	314	6.18	5.05	339	1.42	347
ST-A	2009	11/14 8:00	11/14 20:00	11/15 21:30	12.00	9.92	25.50	284	17.61	8.02	303	3.24	313
ST-B	2009	12/29 17:15	12/30 1:50	12/30 09:20	8.58	-	7.50	286	6.05	8.30	313	1.19	330
ST-B	2010	1/20 09:20	1/20 20:20	1/21 22:48	11.00	10.67	26.47	334	5.24	3.25	334	1.17	344
ST-B	2010	9/16 00:20	9/16 10:50	9/17 7:12	10.50	11.58	20.37	316	13.41	6.55	399	4.27	394
ST-B	2010	12/2 2:40	12/2 9:55	12/3 11:11	7.25	8.33	25.27	323	8.75	5.35	345	2.08	354
ST-A	2011	1/16 2:10	1/16 5:40	1/17 10:10	3.50	6.08	28.50	461	10.92	7.45	457	4.57	446
ST-A	2011	1/31 19:19	2/1 10:25	2/2 18:40	15.10	9.17	32.25	357	4.57	4.80	395	1.42	384
ST-B	2011	2/26 8:28	2/26 16:00	2/27 23:00	7.53	6.92	31.00	532	7.63	9.12	617	5.81	688

Cat-II CMEs with sheaths (...continued)

SC	Year	T_{CME}	T_{le}	T_{te}	T_{sheath}	T_{model}	T_{ME}	v_{sw}	N_{sheath}	B_{sheath}	v_{sheath}	P_{sheath}	v_{le}
ST-B	2011	3/20 15:46	3/21 10:00	3/22 3:00	18.23	16.08	17.00	339	14.86	7.63	388	4.47	415
ST-A	2011	4/5 21:43	4/6 9:40	4/6 23:41	11.95	11.25	14.02	405	9.27	11.20	502	4.67	522
ST-A	2011	4/21 01:12	4/21 7:12	4/22 10:58	6.00	8.67	27.77	353	22.13	2.69	346	5.29	339
ST-B	2011	6/1 7:25	6/1 17:35	6/2 18:00	10.17	9.08	24.41	329	27.85	14.01	448	11.17	512
ST-B	2011	9/24 3:58	9/24 5:00	9/24 9:06	1.03	2.08	4.10	538	8.63	13.11	718	8.90	701
ST-B	2011	10/29 04:12	10/29 17:00	10/31 13:23	12.80	7.83	44.38	357	15.88	7.99	425	5.73	438
ST-B	2012	3/29 23:25	3/30 1:37	3/30 8:30	2.20	2.08	6.88	475	5.29	7.12	558	3.29	651
ST-A	2012	4/19 00:07	4/19 10:07	4/19 21:00	10.00	9.42	10.88	380	17.51	8.05	371	4.83	356
ST-B	2012	6/18 8:00	6/18 23:47	6/20 10:00	15.78	14.17	34.22	359	6.46	8.35	451	2.63	497
ST-A	2012	6/20 1:20	6/20 8:20	6/21 4:27	7.00	11.08	20.12	338	4.38	7.85	355	1.10	355
ST-A	2012	9/8 11:19	9/9 00:07	9/9 15:52	12.80	10.83	15.75	298	11.07	5.26	315	2.20	321
ST-A	2013	2/19 1:20	2/19 7:44	2/20 6:11	6.40	5.58	22.45	385	26.30	9.06	401	8.44	409
ST-A	2013	5/29 12:20	5/29 19:00	5/31 6:00	6.67	-	35.00	342	6.08	7.75	406	2.01	417
ST-A	2013	6/20 04:01	6/20 11:13	6/21 9:37	7.20	6.92	22.40	426	9.10	7.24	469	4.00	462
ST-A	2013	7/27 18:52	7/28 1:50	7/28 23:37	6.97	7.00	21.78	438	19.47	10.43	518	10.43	543
ST-A	2013	9/1 1:10	9/1 9:47	9/1 20:08	8.62	12.58	10.35	332	3.86	6.87	370	1.05	367
ST-A	2013	11/26 16:42	11/26 19:30	11/27 7:30	2.80	4.67	12.00	352	14.41	6.25	341	3.35	356
ST-A	2014	6/7 16:14	6/8 1:44	6/9 9:29	9.50	9.08	31.75	317	14.11	4.09	328	3.04	349

Table B.3: Cat-III CMEs with no shocks and sheaths

SC	Year	T_{CME}	T_{le}	T_{te}	T_{ME}	v_{sw}	N_{ME}	B_{ME}	v_{ME}	v_{le}
ST-A	2007	11/19 22:00	11/19 22:00	11/21 3:17	29.27	443	10.18	9.93	419	441
ST-B	2008	5/15 23:00	5/15 23:00	5/16 18:00	18.98	496	2.19	3.39	435	507
ST-B	2008	10/19 01:02	10/19 01:02	10/20 11:32	34.48	349	6.13	6.53	329	345
ST-B	2009	1/13 05:22	1/13 05:22	1/13 22:00	16.62	344	4.90	9.20	377	374
ST-B	2009	07/16 17:08	07/16 17:08	07/17 17:00	23.85	308	7.28	8.12	300	304
ST-B	2009	09/28 03:10	09/28 03:10	09/28 12:15	9.07	329	2.02	5.93	316	319
ST-A	2009	10/30 01:40	10/30 01:40	10/30 20:00	18.32	378	4.72	5.45	384	394
ST-A	2009	11/1 08:00	11/1 08:00	11/3 02:00	41.98	519	1.23	6.21	422	496
ST-B	2010	4/13 22:11	4/13 22:11	4/14 9:46	11.57	404	10.47	11.88	414	411
ST-B	2010	6/15 4:04	6/15 4:04	6/16 14:00	33.92	453	3.51	4.98	398	468
ST-A	2010	6/16 16:20	6/16 16:20	6/18 3:44	35.38	512	4.87	7.48	447	490
ST-B	2010	6/23 8:00	6/23 8:00	6/25 3:30	43.48	556	5.52	6.00	456	541
ST-A	2010	8/30 21:38	8/30 21:38	8/31 9:32	11.88	434	5.27	13.56	451	423
ST-B	2010	9/19 23:22	9/19 23:22	9/20 6:45	7.37	488	0.63	4.73	494	513
ST-B	2010	10/30 17:30	10/30 17:30	10/31 7:20	13.82	361	6.45	8.91	374	352
ST-B	2010	12/25 20:20	12/25 20:20	12/27 06:00	33.65	290	5.59	8.62	305	307
ST-A	2011	1/26 15:09	1/26 15:09	1/27 3:05	11.92	487	1.49	7.66	447	482
ST-A	2011	2/3 17:00	2/3 17:00	2/4 2:48	9.78	333	5.49	7.50	336	311
ST-A	2011	3/12 00:25	3/12 00:25	3/12 16:47	16.35	514	2.29	5.84	478	523
ST-B	2011	4/1 21:00	4/1 21:00	4/2 10:00	12.98	472	2.06	9.26	481	480
ST-B	2011	4/4 17:00	4/4 17:00	4/5 15:07	22.10	428	6.56	6.17	373	420
ST-A	2011	4/15 7:52	4/15 7:52	4/16 9:25	25.53	416	6.80	10.46	414	430
ST-A	2011	4/28 9:00	4/28 9:00	4/29 20:07	35.10	440	3.35	6.83	376	441
ST-B	2011	5/4 19:06	5/4 19:06	5/5 8:25	13.30	390	13.70	13.30	398	406

Cat-III CMEs with no shocks and sheaths (...continued)

SC	Year	T$_{CME}$	T$_{le}$	T$_{te}$	T$_{ME}$	v$_{sw}$	N$_{ME}$	B$_{ME}$	v$_{ME}$	v$_{le}$
ST-A	2011	5/6 22:00	5/6 22:00	5/7 4:11	6.17	447	13.74	13.30	435	468
ST-A	2011	9/4 22:40	9/4 22:40	9/5 11:08	12.45	304	11.69	7.64	324	306
ST-A	2011	12/2 5:45	12/2 5:45	12/2 20:28	14.70	447	1.36	6.15	431	445
ST-A	2012	1/5 20:40	1/5 20:40	1/6 12:56	16.25	509	8.18	19.19	435	492
ST-A	2012	1/25 22:10	1/25 22:10	1/26 22:00	23.82	600	4.41	7.05	505	593
ST-A	2012	3/4 10:34	3/4 10:34	3/4 22:00	11.42	404	7.12	9.38	409	409
ST-A	2012	7/16 00:45	7/16 00:45	7/16 18:00	17.23	347	0.16	6.92	350	351
ST-A	2012	7/17 3:40	7/17 3:40	7/18 00:25	20.73	373	3.14	5.95	347	373
ST-B	2013	3/24 5:20	3/24 5:20	3/24 22:00	16.65	342	5.94	14.19	384	358
ST-B	2013	6/19 15:08	6/19 15:08	6/20 22:00	30.85	619	1.93	8.21	606	598
ST-A	2013	7/14 23:20	7/14 23:20	7/16 13:26	38.08	311	0.94	4.72	297	-
ST-A	2013	10/17 15:15	10/17 15:15	10/19 5:27	38.18	305	2.60	2.81	305	348
ST-B	2013	11/24 3:22	11/24 3:22	11/24 22:12	18.82	373	2.50	7.21	384	383
ST-A	2013	12/27 22:22	12/27 22:22	12/29 3:38	29.25	415	2.00	2.79	384	426
ST-A	2014	1/13 17:17	1/13 17:17	1/16 3:32	58.23	363	4.53	9.34	346	373
ST-A	2014	2/6 11:34	2/6 11:34	2/7 20:30	32.92	438	2.33	7.42	393	430
ST-B	2014	3/3 22:00	3/3 22:00	3/5 17:00	42.98	374	2.03	7.10	350	405
ST-B	2014	3/18 12:00	3/18 12:00	3/19 19:22	31.35	515	0.85	6.57	465	507
ST-A	2014	4/1 13:30	4/1 13:30	4/1 21:43	8.20	468	3.63	8.82	469	490
ST-A	2014	6/23 11:00	6/23 11:00	6/25 11:00	47.98	303	2.31	7.73	298	301
ST-A	2014	6/29 23:30	6/29 23:30	7/1 10:42	35.18	458	1.91	9.45	458	488
ST-B	2014	8/11 6:20	8/11 6:20	8/13 14:47	56.43	527	5.57	8.24	477	596

APPENDIX C

Propagation and expansion sheaths

Tables C.1 and C.2 list the 28 propagation sheaths and 18 expansion sheaths, respectively, as defined in Chapter 5.

In Tables C.1 and C.2:

$\mathbf{T}_{shock}$, $\mathbf{T}_{le}$, and $\mathbf{T}_{te}$ are the arrival timings of the shock, ME leading-edge, and ME trailing-edge at STEREO (in UT). $\mathbf{T}_{sheath}$ and $\mathbf{T}_{ME}$ are the sheath and ME durations, respectively (in h). $\mathbf{M}_{ms}$ is the shock magnetosonic Mach number. $\mathbf{v}_{sw}$ is the upstream solar wind speed (in $\mathrm{km\,s^{-1}}$), $\mathbf{v}_{sheath}$ is the calculated average speed of the sheath (in $\mathrm{km\,s^{-1}}$), and $\mathbf{v}_{ms}$ is the fast magnetosonic speed of the local solar wind (in $\mathrm{km\,s^{-1}}$). Both $\mathbf{v}_{sw}$ and $\mathbf{v}_{ms}$ are calculated as the average in a 2-hr time interval upstream of the shock. $\mathbf{M}_{exp}$ and $\mathbf{M}_{prop}$ are the ME Mach numbers associated with the expansion and propagation of the ME, respectively, with respect to the background solar wind (see Chapter 5).

Table C.1: Selected parameters of 28 CMEs associated with propagation sheaths.

SC	Year	T_{shock}	T_{le}	T_{te}	T_{sheath}	T_{ME}	M_{ms}	v_{sw}	v_{sheath}	v_{ms}	M_{exp}	M_{prop}
ST-A	2007	8/25 20:30	8/25 23:27	8/26 16:00	2.95	16.55	1.21	290	317	26	-0.19	2.31
ST-B	2008	4/29 14:10	4/29 15:34	4/30 07:00	1.4	15.43	1.45	340	422	62	-0.23	1.70
ST-B	2008	6/6 15:36	6/6 22:15	6/7 12:32	6.65	14.28	1.34	328	402	46	0.36	1.34
ST-B	2009	08/05 22:35	08/06 04:39	08/07 05:25	6.07	24.75	1.43	332	374	38	-0.96	1.92
ST-B	2009	08/30 02:50	08/30 16:20	08/31 05:40	13.5	13.33	1.17	309	347	35	-0.52	0.74
ST-A	2010	2/5 3:33	2/5 12:40	2/6 2:00	9.12	13.33	2.24	331	384	42	-0.02	1.67
ST-A	2011	3/19 11:25	3/19 23:34	3/21 1:30	12.17	25.92	1.42	392	478	104	0.31	0.58
ST-A	2011	12:42.663	8/6 16:38	8/7 19:38	3.93	27.00	1.54	444	486	56	-0.87	0.59
ST-A	2011	9/8 16:1.45	9/9 00:05	9/11 8:52	8.07	56.75	1.36	286	350	53	-0.49	2.08
ST-A	2011	12/6 22:44	12/7 6:55	12/7 18:00	8.2	11.08	1.96	294	375	39	0.15	0.98
ST-B	2011	12/26 23:51	12/27 7:00	12/28 11:00	7.17	28.00	1.67	308	329	32	-0.77	1.83
ST-B	2012	1/16 9:49	1/17 7:30	1/18 9:00	21.68	25.50	1.34	318	369	41	0.41	0.67
ST-A	2012	3/18 19:31	3/19 4:38	3/19 16:00	9.12	11.36	1.50	413	465	60	-0.15	1.02
ST-A	2012	7/20 22:43	7/21 11:40	7/22 2:30	12.95	14.83	1.98	556	687	92	0.28	0.79
ST-B	2012	7/28 14:59	7/28 17:08	7/29 1:00	2.15	7.87	1.12	353	430	51	0.17	1.32
ST-B	2012	9/23 8:44	9/23 23:38	9/24 9:46	14.9	10.13	1.92	349	407	34	-0.03	1.01
ST-A	2012	9/23 14:29	9/23 21:00	9/24 11:00	6.53	14.00	1.49	451	541	62	0.09	1.38
ST-B	2012	10/17 6:57	10/17 11:20	10/18 21:15	4.38	33.92	0.95	274	309	43	0.05	0.80
ST-A	2013	1/9 2:25	1/9 10:38	1/10 17:17	8.22	30.65	1.15	356	455	72	0.23	1.29
ST-A	2013	2/8 7:44	2/8 18:22	2/10 3:20	10.64	32.95	0.61	272	314	54	0.22	0.59
ST-A	2013	2/28 21:14	3/1 13:30	3/5 20:25	16.27	102.90	1.40	328	397	80	0.33	0.81
ST-A	2013	3/26 2:46	3/26 9:16	3/26 20:55	6.52	11.64	1.25	362	469	75	0.10	1.08
ST-A	2013	4/27 4:20	4/27 6:55	4/27 23:00	2.6	16.08	0.83	324	378	66	0.23	0.83
ST-B	2013	9/9 14:32	9/10 6:52	9/10 22:53	16.33	16.02	0.03	364	466	74	0.09	0.88
ST-A	2014	2/16 7:50	2/16 15:6	2/17 16:15	7.27	25.15	1.34	434	620	132	0.39	0.92
ST-A	2014	4/9 13:08	4/10 6:5	4/10 15:35	16.97	9.49	0.62	321	407	60	-0.05	1.20
ST-B	2014	7/1 12:51	7/1 20:15	7/2 18:48	7.4	22.55	2.63	392	494	70	-0.39	3.21
ST-A	2014	7/4 16:53	7/4 22:27	7/5 8:51	5.57	10.39	1.38	300	327	41	-0.02	0.59

Table C.2: Selected parameters of 18 CMEs associated with expansion sheaths.

SC	Year	T$_{shock}$	T$_{le}$	T$_{te}$	T$_{sheath}$	T$_{ME}$	M$_{ms}$	v$_{sw}$	v$_{sheath}$	v$_{ms}$	M$_{exp}$	M$_{prop}$
ST-B	2010	11/19 20:26	11/20 6:34	11/21 9:10	10.13	26.60	0.90	413	458	55	0.89	-0.08
ST-B	2011	1/17 15:46	1/18 0:0	1/18 9:38	8.23	9.63	1.94	322	389	46	0.57	0.38
ST-B	2011	11/6 5:11	11/6 22:50	11/9 4:00	17.67	53.16	0.06	487	630	144	0.61	-0.09
ST-B	2012	3/10 21:17	3/11 1:34	3/12 21:51	4.29	44.27	1.54	594	678	78	1.38	-0.20
ST-B	2012	4/17 3:37	108 4/17 9:40	109 4/18 9:05	6.07	23.41	0.60	530	642	134	0.58	0.43
ST-A	2012	7/10 18:55	7/11 9:10	7/13 4:00	14.25	42.83	1.42	568	630	62	1.31	-0.25
ST-A	2012	8/5 15:37	8/6 4:00	8/7 6:00	12.38	26.00	1.10	427	490	56	0.57	-0.10
ST-B	2012	9/25 16:26	9/26 3:21	9/28 16:55	10.92	61.56	1.70	518	647	95	1.86	0.04
ST-A	2012	11/13 20:57	11/14 10:42	11/16 8:45	13.75	46.05	1.36	398	487	66	1.11	-0.26
ST-A	2012	11/26 7:58	11/26 15:00	11/28 1:22	7.05	34.37	0.67	389	488	71	0.85	0.42
ST-A	2013	5/2 21:02	5/3 5:50	5/4 16:10	8.80	34.33	1.17	446	538	98	0.63	0.23
ST-A	2013	5/12 23:30	5/13 16:00	5/15 12:36	16.50	44.60	1.15	460	541	63	1.30	0.32
ST-A	2013	8/10 9:16	8/10 17:24	8/12 7:00	8.13	37.60	1.41	341	415	60	0.80	0.43
ST-B	2013	12/17 13:29	12/18 2:05	12/20 15:00	12.60	60.91	1.18	377	414	48	1.13	-0.47
ST-B	2014	1/29 5:20	1/29 17:14	1/31 9:00	11.90	39.77	1.16	593	663	67	2.00	-1.04
ST-A	2014	3/14 16:38	3/15 1:15	3/15 14:25	8.63	13.17	0.69	471	608	164	0.68	0.44
ST-B	2014	4/12 2:27	4/12 20:46	4/15 7:13	18.32	58.44	2.00	315	424	63	1.14	0.43
ST-B	2014	5/8 1:37	5/8 21:00	5/10 8:23	19.38	35.39	0.95	363	408	65	0.94	0.20